IMPROVED MATERIAL BALANCE EQUATION OF SHALE GAS RESERVES AND PRODUCTION

BY

ADEOLU JULIUS ALAWODE
B.Eng, M.Eng Mechanical Engineering (Ilorin),
M.Sc Petroleum Engineering (Ibadan)
(Matric. No.: 134979)

A Thesis in the Department of Petroleum Engineering,Submitted to the Faculty of Technology in Partial Fulfilment of the Requirement for the Degree of

DOCTOR OF PHILOSOPHY

of the

UNIVERSITY OF IBADAN

DECEMBER, 2018

CERTIFICATION

I certify that this work was carried out by Adeolu Julius Alawode in the Department of Petroleum Engineering, University of Ibadan, Nigeria.

Supervisor

O.A. Falode, B.Sc (Jos), M.Sc, Ph.D (Ibadan)

Department of Petroleum Engineering

University of Ibadan

ABSTRACT

Langmuir adsorption isotherm has been used extensively when incorporating gas desorption into gas Material Balance Equation (MBE) framework. However, it over-estimates adsorbed gas reserves at higher pressures without adsorption saturation pressure (P_s). Previous researches developed modified Z-factors incorporating gas desorption, rendering them complex for routine calculations. Therefore, this study was designed to improve shale gas MBE by developing an isotherm that defines the onset of adsorption saturation pressure, and modifying single-porosity Z-factor to a simpler but accurate dual-porosity free gas Z-factor.

A new adsorption isotherm involving pressure (P), P_s, maximum adsorbed volume (V_{max}), and adsorbate-adsorbent resistance parameter (n) was developed using kinetic approach. The developed and Langmuir isotherms were used in modelling secondary adsorption data of different adsorbents, and the qualities of fit were statistically assessed. The modified Z-factor incorporates ratio of dual porosity to initial matrix porosity (ϕ'_{mat}), and it was statistically correlated with existing dual-porosity Z-factor. The improved MBE is a function of the developed isotherm and the modified Z-factor. Using adsorption and reservoir data of some shale gas formations obtained from literature, variation of cumulative gas production (G_p) with pressure depletion (ΔP) were determined. Effect of fracture porosity (ϕ_{frac}) on G_p was determined. Free and total gas production decline rate models were derived from well production history and average change of G_p with pressure depletion from initial reservoir pressure to wellbore flowing pressure. The results were statistically correlated.

The developed isotherm,

$$V = \begin{Bmatrix} V_{max}\left\{\frac{P}{P_s} + \left(1 - \frac{P}{P_s}\right)\left(\frac{P}{P_s}\right)^n\right\}, for\ P < P_s\ i.e. undersaturated\ adsorption \\ V_{max},\ for\ P \geq P_s\ i.e. saturated\ adsorption \end{Bmatrix}$$

shows that V_{max} is maintained during pressure depletion to P_s, below which gas desorption begins. For secondary low-pressure methane adsorption data of a shale sample from 190 to 2,005 psia at 25 °C, a V_{max} of 0.0450 mmol/g at a P_s of 2,005 psia and Langmuir volume of 0.0548 mmol/g at infinite P_s were predicted by the developed

and Langmuir isotherms with R^2 values of 0.997 and 0.989, respectively. The modified Z-factor is $Z \cdot \left\{1 - \left(1 - \phi_{frac} + \frac{\phi_{frac}}{\phi'_{mat}}\right)\left(\frac{C_w S_{w_i} + C_{matrix}}{S_{g_i}}\right) \cdot \Delta P\right\}^{-1}$ where Z, C_w, S_{w_i}, C_{matrix} and S_{g_i} are Z-factor at P, water compressibility, initial water saturation, matrix compressibility and initial gas saturation, respectively. For a shale formation, correlating the modified Z-factor with Aguilera Z-factor yields a R^2 value of 1.00. With pressure drawdown from 3,500 to 2,285 psig, technically recoverable reserves of 489 Tscf would be depleted in form of free gas G_p; the corresponding developed isotherm-based and Langmuir isotherm-based total gas G_p were estimated as 509.26 and 564.09 Tscf, respectively. Increase in ϕ_{frac} was found to increase G_p. Using a production history of 59 months as base case, the developed isotherm-based decline rate model results offered better correlation than Langmuir isotherm-based model results, with Root Mean Square Errors (RMSE) of 6.680 and 52.646 Mscf/d, respectively. A production forecast of 30 years, using the production history and its projection as base case, yields corresponding RMSE of 5.333 and 42.774 Mscf/d, respectively.

An improved adsorption isotherm that defines the onset of adsorption saturation pressure was established, Z-factor was modified for dual-porosity and an improved material balance equation was formulated for a better production forecast.

Keywords: Shale gas reserves, Langmuir isotherm, Z-factor, Dual-porosity system

Word Count: 499

ACKNOWLEDGEMENTS

I am highly indebted to my supervisor, Dr. O.A. Falode for his painstaking guidance, advice, encouragement and support. I feel honoured and pleased studying and learning under his supervision. Without his love and consistent assessment, the objectives of this study would not have been achieved.

I hereby express appreciation to Prof. S.O. Isehunwa (the Head of Petroleum Engineering Department) and Dr. L.O. Akinpelu for their love and encouragement on the completion of this study. I thank all the members of staff (academic, technical and administrative) of Petroleum Engineering Department, University of Ibadan for sustaining an amiable atmosphere for effective teaching and research to thrive. I appreciate Engr. Samuel Olamijulo for offering training on MAPPLE programming. I am grateful to Dr. I.A. Oladosu (Chemistry Department), Dr. G.M. Ayininuola (Civil Engineering Department) and Dr. B.O. Odedairo (Industrial and Production Engineering Department) for reviewing the Abstract. I also express gratitude to Prof. O.M. Oyewola (Mechanical Engineering Department) for reviewing the corrected version of the Thesis.

I deeply appreciate the love, support and commitment of my family especially my daughter - Maureen OluwadamilolaALAWODE. God bless you abundantly (Amen).

Above all, I give all Honour and Glory to Jehovah God for giving me the grace to start and complete the Ph.D. programme. He is the One who can do for us what we cannot do for ourselves.

ABBREVIATIONS

BHP	: Bottom Hole Pressure
MBA	: Material Balance Analysis
MBE	: Material Balance Equation
OGIP	: Original Gas-In-Place
RMSE	: Root Mean Square Error
WRMS	: Weighted Root Mean Square Deviation
WAAD	: Weighted Average Absolute Deviation
%AAD	: Percent Average Absolute Deviation

NOMENCLATURE

A : Reservoir area (square mile or square kilometer)

b : Ratio of V_{last} to V_{max} (fraction)

b_{k_m} : Slippage factor in the matrix (psi)

B_g : Gas formation volume factor evaluated at pressure P(rcf/scf)

B_{g_i} : Gas formation volume factor evaluated at initial pressure P_i (rcf/scf)

B_w : Water formation volume factor (fraction)

c : Ratio of P_{last} to P_s (fraction)

C : Constant of proportionality

C_{matrix} : Matrix compressibility (psi^{-1})

C_w : Water compressibility(psi^{-1})

$C^*_{p_{mat}}$: Matrix pore volume compressibility (psi^{-1})

$C^*_{p_{frac}}$:Fracture volume compressibility (psi^{-1})

dP : Change in pressure (psi)

E : Interaction energy (i.e., heat or enthalpy of adsorption) between the gas molecules and the solid sites (J/mol)

F : Fluid phase

G : Free gas initially in place i.e. original free gas in place (OGIP) (scf)

$GIP_{adsorbed}$: Adsorbed gas-in-place (scf)

GIP_{free} : Free gas-in-place(scf)

G_p : Cumulative gas production (scf)

$G_{p_{desorbed}}$: Desorbed gas production (scf)

$G_{p_{free}}$: Cumulative free gas production(scf)

$G_{p_{Total}}$: Total gas production (free + desorbed)(scf)

G_{Total} :Total OGIP (free + adsorbed)(scf)

G_{mat} : OGIP in the matrix(scf)

h : Reservoir net thickness (ft.)

J_g : Gas productivity index (scf/psi.d)

J_g^* : Modified gas productivity index in the reservoir matrix (scf/psi.d)

k : Dynamic parameter expressed as: $k = \left(\frac{P}{P_s}\right)^n$ (fraction)

K : Modelfitting factor (ratio of flow rate from field data to flow rate from well forecast) (fraction)

K_{ads_o} : Adsorption rate coefficient at the onset of adsorption

K_{des} : Desorption rate coefficient

K_{eq}^f : Dynamic equilibrium parameter

n : Adsorbate-adsorbent resistance parameter (fraction)

n : Production decline exponent

N : Number of gas specie (1 for pure-component, 2 for binary mixture, etc.)

N : Number of data points

$OGIP_{adsorbed}$: Original adsorbed gas-in-place (scf)

$OGIP_{free}$: Original free gas in place (scf)

P : Equilibrium pressure (psi)

P_a : Pressure deviation from the corresponding linear isotherm pressure (psi)

P_β : Pressure at the inflexion point β where $\Delta\left(\frac{V}{V_{max}}\right) = \Delta\left(\frac{P}{P_s}\right)$(psi)

P_i : Initial reservoir pressure (psi)

P_L : Langmuir pressure (i.e. the pressure at half the Langmuir volume) (psi)

P_{last} : Last$P$ value of the experimental adsorption data (psi)

P_{pc} : Pseudo-critical pressure (psi)

P_{pr} : Pseudo-reduced pressure

P_s : Adsorption saturation pressure (psi)

P_{wf} : Wellbore flowing pressure (Bottomhole pressure) (psi)

q_g : Gas production rate (scf/d)

q_{g_i} : Initial production rate (scf/d)

q_{g_1} : Production rate at first time step (psi/d)

R : Universal gas constant (J/mol/K)

R_{ads} : Rate of adsorption (hr.$^{-1}$)

R_{des} : Rate of desorption (hr.$^{-1}$)

S_{ads} : Occupied adsorption surface site concentration (number/area)

S_{g_i} : Initial gas saturation

S_{vac} : Vacant adsorption surface site concentration (number/area)

S_T : Total adsorption surface site concentration (number/area)

S_{w_i} : Initial water saturation

t : Production time (day)

t_p : Total production period (day)

T : Temperature (C or K or R)

T_{pc} : Pseudo-critical temperature (R)

T_{pr} : Pseudo-reduced temperature

V : Volume of gas adsorbed per unit mass of adsorbent (scf/ton)

V_B : Reservoir bulk volume (scf)

V_β : Adsorbed volume at the inflexion point β where $\Delta\left(\frac{V}{V_{max}}\right) = \Delta\left(\frac{P}{P_s}\right)$(scf/ton)

V_{cal} : Calculated adsorption volume (scf/ton)

V_{exp} : Experimental adsorption volume (scf/ton)

V_i : Volume of the adsorbing specie i in a mixture of gases at an equilibrium pressure P (scf/ton)

V_L : Langmuir volume (maximum adsorbed volume per unit mass of adsorbent at infinite pressure) (scf/ton)

V_{last} : Last$V$ value of experimental adsorption data. (scf/ton)

V_{max} : Maximum adsorbed volume(scf/ton)

$(V_{max})_i$: Maximum adsorbed volume of the adsorbing specie i of 100% concentration(scf/ton)

$(V_{max})_j$: Maximum adsorbed volume of the respective adsorbing specie j of 100% concentration, where $j = 1, \ldots\ldots N$ (scf/ton)

$(V_{100\%})_i$: Volume of the adsorbing specie i of 100% concentration at the corresponding pressure(scf/ton)

W_e : Water influx (barrel)

W_p : Cumulative water produced (stb)

y_i : Gas phase mole fraction (or the feed ratio) of the adsorbing specie i

y_j : Gas phase mole fraction (or the feed ratio) of the respective adsorbing specie j, where $j = 1, \ldots\ldots N$

Z :Dranchuk-Abou-Kassem Z-factor

Z_i : Initial Z-factor

Z^* : Single-porosity gas reservoirs

Z^* : Single-porosity Z-factor

Z'' : Aguilera Z-factor

Z^{**} :Modified Z-factor

Z^i : Initial guess of Z

β_{ads} : Adsorption rate parameter

ω_f : Fraction of OGIP in the fracture system

δ : Volume deviation from the corresponding linear isotherm volume

σ_{exp} : Expected experimental uncertainty

Δt : Change in production time (day)

ΔP : Pressure depletion (psi)

ΔV_m : Pore compaction (barrel or scf)

ΔV_{mw} : Matrix water expansion (barrel or scf)

ϕ : Porosity (fraction)

ϕ'_{mat} : Initial matrix porosity (fraction)

ϕ_{frac} : Fracture porosity (fraction)

ϕ''_{mat} : Matrix porosity after fracturing (fraction)

γ_g : Gas specific gravity (i.e. relative density)

ρ_r : Reduced density

ρ_b : Reservoir bulk density (g/cm^3),

$\psi(P)$: Gas pseudo-pressure (psi^2/cp)

$\psi^*_m(P)$: Modified gas pseudo-pressure $\psi(P)$ in the reservoir matrix (psi^2/cp)

μ : Gas viscosity (cp)

Subscripts

i : Data point

n : Subscript denoting current status of a parameter

$n-1$: Previous status of a parameter

g : Gas

TABLE OF CONTENTS

LIST OF FIGURES

LIST OF TABLES

CHAPTER ONE

INTRODUCTION

1.1 BACKGROUND TO THE STUDY

Growing demand for energy relies heavily on fossil fuels obtained from hydrocarbons, and the need for increasedgas supply resulted in the development of *unconventional* gas resources such as shale gas, tight sand gas, coalbed methane, and gas hydrate. The term *unconventional* refers to the source but not the nature of gas, implying that production from the reservoir involves operational and economic challenges, or both, which would not be ordinarily found in conventional reservoirs. Economic development of resources from unconventional reservoirs is attributed to improvements in drilling and completion technology especially directional drilling and hydraulic fracturing.

The primary method of recovering methane from unconventional reservoirs (especially shale gas, coalbed methane and tight sand gas reservoirs) is normally by means of hydraulic fracturing. Hydraulic fracturing is a well stimulation method that involves pumping pressurised liquid (basically water containing sand and proppants suspended by thickening agents) into a wellbore to the target zone of the reservoirs at a pressure higher than the reservoir pressure. The fluid pressure creates fractures through which the sand flows and sand props open the fractures to maintain permeability. During hydraulic fractures stabilisation and porosity/permeability maintenance, fracture volume compressibility is sustained at a lower level that corresponds to injection water compressibility. After pumping pressure is relieved, the fracture fluid (referred to as "*flowback*") returns to the surface through the wellbore while the hydraulic fractures are still open. Further pumping out of formation water causes reservoir pressure depletion and allows methane production from the reservoir, i.e. *degassing* the reservoir. This practice is simple but often yields total recovery usually less than 50% of the original gas-in-place (OGIP), depending on gas saturation, reservoir permeability, etc. (Rice, 1997).Solid residues produced when pumping water out of the reservoir often raises environmental issues during water disposal.

A more effective process with higher yields than the hydraulic fracturing is enhanced gas recovery which involves injecting liquefied carbon dioxide (CO_2) into the reservoir

to displace methane since CO_2has higher adsorptivitythan methane (Hall, 1993; Hall *et al*., 1994, Stevens *et al*., 1998). From another perspective, injecting CO_2 to displace methane in unconventional reservoirs not only enhance methane recovery but alsosequester CO_2.CO_2 sequestration is a potential environmental benefit against climate change caused by global warming effect of anthropogenic emission of CO_2. Several methods proposed in the 1991 Kyoto Protocol to reduce CO_2 (carbon) emission involves CO_2 capture from various industrial activities and subsequent sequestration in geologic formations such as saline aquifers, depleted oil and gas reservoirs, and unconventional gas reservoirs (UNEP, 2006).

The unconventional gas resources that had received wide attention in recent time for natural gas production is shale gastrapped within fractures and pore spaces, or adsorbed onto organic materials and minerals in low-permeability shale at depths of usually more than 1 km. Shale gas formations are complex rocks, characterised by heterogeneity in composition and structure, and this affects the degree of natural gas recovery (Bustin *et al.*, 2008; Loucks *et al.*, 2009; Wang & Reed, 2009; Sondergeld *et al.*, 2010).

World shale gas reserves are evaluated as 450,000billion cubic meters, i.e. 15,891.6 trillion standard cubic feet (Tscf) (New Scientist, 2012) with large amount of gas reserves in Western Europe and North America (House of Commons Library, 2012). Interest in shale gas is increasing as the demand for gas gradually grows and North Sea gas reserves are declining. About 1.0 Tscf annual production of natural gas had been recorded from over 40,000 shale gas wells in the United States (Jenkins *et al*., 2008). The economic success of shale gas in the United States since year 2000 contributed to increased production of shale gas in Canada, and of recent has stimulated prospects of shale gas production in Europe, Australia and Asia. In Nigeria, the Nkporo shale gas formation contains very high potent organic matter and it spans from Anambra basin to lower Benue trough. The total organic contents (TOC) value shows the presence of abundant gas condensate-prone formations (Ehinola & Sonibare, 2005). Development of shale gas formations in Nigeria will help in increasing global natural gas supply. This is part of the plans in the ongoing reforms at making Nigeria oil and gas sector

more vibrant and attractive to investment as emphasised in the Nigeria's Gas Master Plan.

The economic viability of gas recovery from unconventional gas reservoirs is a function of the amount and distribution of gas, its adsorption/desorption characteristics, and the petrophysical properties such as reservoir thickness, porosity, permeability, water saturation, diffusion, etc. (Arumugan, 2004). Amongst these contributing factors, adsorption/desorption capacity is the major factor affecting gas production.

1.2 PROBLEM STATEMENT

In conventional gas reservoirs, free gas is stored in the pores by compression. However, in unconventional gas (shale gas, coalbed methane and tight-sand gas)reservoirs, apart from the free gas stored in the pores and fracture systems, gas is also stored within the matrix by adsorption. During pressure depletion in shale gas reservoirs, free gas flows from fractures to the wellbore. The pressure drop in the fractures becomes the driving force for transport of free gas from matrix pores to the fractures. Subsequent pressure drop in the matrix poresbelow a threshold weakens the van der Waal's forces (van der Waals, 1873) and causes adsorbed gas to desorb from matrix particles surface into the matrix pores.

However, pressure depletion is slow because of ultra-low formation permeability; hence, remarkable desorption occurs in later time of production when matrix pressure is lower than a threshold pressure called adsorption saturation pressure, and the well is producing under boundary-dominated flow (BDF).

Hence, it is obvious that desorption mechanisms constitute an additional source of natural gas production; and that the traditional gas material balance equation (MBE) underestimates gas-in-place (GIP) and cumulative production (G_p) because it considers only the free gas. Incorporating appropriate gas adsorption isotherm into the framework of gas MBE would result into an accurate evaluation of the GIP and the G_p in unconventional gas reservoirs.

Adsorption in shale gas reservoirs often exists as monolayer because of the nanostructure profile (Merey, 2013; Merey and Sinayuc, 2015). Hence, a better representation of adsorption in shale gas reservoirs is Type I isotherm which is characterised by a progressively increasing adsorption with pressure application until monolayer surface coverage is attainedat adsorption saturation pressureabove which no further adsorption can occur.Most often, due to the ease of application, Langmuir isotherm had been used extensively as the Type I isotherm in modelling gas adsorption in shale gas and coalbed reservoirs despite the fact that it does not feature adsorption saturation pressure thus rendering an overestimation of adsorbed/desorbed gas at higher pressures.To the best of my knowledge, developing a Type I adsorption isothermthat incorporates adsorption saturation pressure into its framework has not been reported in the literature.

Also, Z-factor in single-porosity gas reservoirs with pressure depletion is modified to reflect dual porosity that characterises shale gas reservoirs. The existing Aguilera (2008) dual-porosity free gas Z-factor incorporatesOGIP fractions within fractures and matrix pores. Previous researchers developed modified Z-factors into which gas desorption was lumped, rendering them complex for routine calculations. However, single-porosity Z-factor can be modified to a simpler but accurate dual-porosity Z-factor that correlates well with existing dual-porosityZ-factor. An accurate estimation of free and desorbed gas production will yield an improved MBE for better production forecast.

This research work is inspired by these challenges and it is tailored towards filling these knowledge gaps.

1.3 OBJECTIVES OF THE STUDY

The main objective of this research work is to develop an improved material balance equationof shale gas reserves and production for a better production forecast.

The specific objectives are to:

(i) Develop and generalise an adsorption isotherm that incorporates adsorption saturation pressure into its framework to correct Langmuir isotherm's over estimation of adsorbed/desorbed gas volume at higher pressures.

(ii) Modify single-porosity Z-factorto a simpler but accurate dual-porosity Z-factor that correlates well with existing dual-porosityZ-factor.

(iii) Formulate an improved MBE involving the developed isotherm-based gas desorption and free gas production (that incorporates the modified Z-factor),and compare reserves and production withthose in anMBE that incorporates Langmuir isotherm and the modified Z-factor.

(iv) Analyse effect of fracture porosity on cumulative gas production, and

(v) Derive free and total gas production decline rate models from well production history, and average change of G_p with pressure depletion $\left(\frac{dG_p}{dP}\right)$ from initial reservoir pressure (P_i) to wellbore flowing pressure $\left(P_{wf}\right)$.

1.4 JUSTIFICATION FOR THE STUDY

Accurate reservesand production estimation is an important component of effective production forecast, economic assessment, fiscal planning and decision making in reservoir development. Therefore the findings of this study would assist the industry to make effective decision in shale gas reservoir development.

1.5 SCOPE OF THE STUDY

The primary task in this research work is the development of a truly Type I adsorption isotherm that assumes a monolayer type of adsorption (because of the nanostructure profile of shale gas formations), and offers a correction to Langmuir isotherm's over estimation of adsorbed/desorbed gas volume at higher pressures. This, coupled with modification of single-porosity Z-factor to a simpler but accurate dual-porosity Z-factor, forms the building block for an improved material balance equationof shale gas reserves and production for a better production forecast.

1.6LIMITATIONS OF THE STUDY

The shale gas is considered dry i.e. the wellbore conditions do not encroach into the two-phase envelope (of the pressure-temperature (P-T) diagram) after pressure depletion as experienced in retrograde/condensate and wet gas formations. Also, water production of any form is considered negligible. Actually, the shale formations used as study areas in this work are predominantly of dry gas; however some traces of oil and condensate are found in the Barnett shale formation.

1.7STUDY AREAS

For Nigerian shale formations, laboratory shale gas adsorption isotherm data has not been generated and there is no shale gas production history yet. Hence, the shale formations used as study areas are the Marcellus, Haynesville and Barnett formations.

1.7.1 Marcellus Shale Formation

The Marcellus shale formation is located in eastern North America. It is by far the most extensive shale formation involved in shale gas plays. The shale stretches across 104,000 square miles (269,359 km^2) in Pennsylvania, New York, Ohio and West Virginia in the north-eastern United States (US DoE, 2009). Marcellus shale matrix permeability ranges from 100 to 450 nanodarcy (Zhong, 2011).

1.7.2 Haynesville Shale Formation

The Haynesville shale formation underlies large portion of the Gulf Coast area of the United States. The formation underlies 9,000 square miles (23,310 km^2) running through north-western Louisiana, north-eastern Texas and the south-western tip of Arkansas (US DoE, 2009). The formation is the deepest, the highest pressured and the hottest shale among the prominent shale gas formations in the United States. Hence, it is expected to ultimately out-produce the Barnett shale by the year 2020 (Oil and Gas Journal, 2016). To produce natural gas, wells are drilled to about 10,000 to 13,500 feet deep.

1.7.3 Barnett Shale Formation

The Barnett shale formation is the largest onshore natural gas field in Texas and also one of the largest in the United States. The formation underlies 5,000 square miles (12,950 km^2) area spanning Fort Worth city and at least 17 counties (US DoE, 2009). Barnett formation ranges between 6,500 to 8,500 feet in depth, and it is bounded by Marble and Chappel limestone. It is between 100 to 600 feet thick (US DoE, 2009). Barnett shale is unique because most of it is located in a highly-urbanised area.

CHAPTER TWO

LITERATURE REVIEW

2.1 FLOW EQUATIONS FOR UNCONVENTIONAL GAS RESERVOIRS

In deriving an analytical model for single-phase gas flow in unconventional gas reservoirs, Bumb and McKee (1986) incorporated both free gas compressibility factor C_g and desorbed gas compressibility factor C_d featuring Langmuir isotherm into the radial flow type of diffusivity equation (a semi-analytical model governing flow behaviour).

The model is expressed as:

$$\frac{1}{r}\frac{\partial}{\partial r}\left(r\frac{\partial \Delta m(P)}{\partial r}\right) = \frac{\phi \mu_g}{k}\left\{C_g + \frac{aC_m}{\phi} + C_d\right\}\frac{\partial \Delta m(P)}{\partial t} \tag{2.1}$$

where $m(P)$ is pseudo-pressure, $C_d = \frac{\rho_{gsc} V_L P_L}{\phi \rho_R (P_L + \bar{P})^2}$, total compressibility $C_T = C_g + \frac{aC_m}{\phi} + C_d$, ϕ is rock porosity, μ_g is gas viscosity, a is a constant, C_m is matrix compressibility, ρ_R is rock bulk density, ρ_{gsc} is gas density at standard condition, and $V_L \frac{\bar{P}}{\bar{P}+P_L}$ is Langmuir isotherm whereV_L is Langmuir volume (scf/ton),$\bar{P}$ is average reservoir pressure (psia) and P_L is Langmuir pressure (psia). The semi-analytical model was correlated with numerical simulation results.

Seidle (1991) used real gas pseudo-pressure and Langmuir isotherm in defining gas diffusivity equation for coalbeds flow behaviour; here the dimensionless time and dimensionless $m(P)$ were used. The equation is expressed as:

$$\nabla^2 m(P) = \frac{\phi \mu_g S_g}{k_g}(C_g + C_d)\frac{\partial m(P)}{\partial t} \qquad (2.2)$$

where $m(P)$ is gas pseudo-pressure, ϕ is porosity, μ_g is gas viscosity, S_g is gas saturation, k_g is gas permeability, and C_g is free gas compressibility. The adsorbed gas compressibility $C_d$is expressed as:

$$C_d = 1.7525 + 10^{-4}\frac{B_g V_m \rho_B P_L}{\phi(P+P_L)} \qquad (2.3)$$

where B_g is gas formation volume factor, V_m is volume of gas in the matrix, ρ_B isbulk gasdensity, and $V_L \frac{P}{P+P_L}$ is the Langmuir isotherm. The results of Seidle methodcorrelated with the analytical solution for liquid (adsorbed) gas within lower dimensionless time. Using pseudo-pressure in gas deliverability equation and mass balance, involving adsorbed gas, Seidle (1991) evaluated average gas pressure by iteration to forecast gas production.

Wu *et al*. (2013) showed the gas diffusivity equation for shale gas mixture flow behaviour as:

$$-\nabla(\rho_\beta v_\beta) + q_\beta = \frac{\partial(\phi S_\beta \rho_\beta + \rho_R \rho_g V_{ads})}{\partial t} \qquad (2.4)$$

where ρ_β is density of fluidβ, v_β is volumetric velocity vector of fluidβ determined by Darcy's law or non-Darcy flow model, ϕ is effective porosity, S_β is saturation of fluidβ,ρ_R is rock bulk density, ρ_g is gas density at standard condition, V_{ads} is adsorbed gas content (scf/ton) represented by$V_L \frac{P}{P+P_L}$the Langmuir isotherm, and q_β is the sink or source term offluidβ per unit volume of formation; fluid$\beta = g$ for gas and $\beta = w$ for water.

Thereafter, shale gas flow behaviour modelling had been extended to the consideration of gas storativity, gas transmissibility and a factor that integrates gas slippage (Klinkenberg) effect forinequality inmatrix blocks and fractures pseudo-pressures. Feast *et al*. (2015) expressed the gas diffusivity equation governing shale gas flow behaviour as:

$$\frac{\partial(\rho_g u_g)}{\partial t} + F = \frac{\partial\left(\phi S_g \rho_g + (1-\phi)\rho_R \rho_{g_{sc}} V_{ads}\right)}{\partial t} \tag{2.5}$$

where ρ_g is free gas density, u_g is gas flow rate per unit cross-sectional area, ϕ is rock porosity, S_g is gas saturation, ρ_R is rock bulk density, $\rho_{g_{sc}}$ is the gas density instandard condition, V_{ads} is adsorbed gas content (scf/ton), and the source term $F$is mass influx from matrix blocks to fracturesystem per unit time step. The source term F is expressed as:

$$F = s\beta\left\{1 + \sqrt{\frac{\tilde{\omega}\tilde{\lambda}}{3s}}\, tanh\left(\sqrt{\frac{3\,\tilde{\omega}s}{\tilde{\lambda}}}\right)\right\} \tag{2.6}$$

where s is a Laplace transform-term, β is a factor that integrates gas slippage (Klinkenberg) effect for pseudo-pressure inequality between matrix blocks and fractures,$\tilde{\omega}$ is gas storativity in the matrix and $\tilde{\lambda}$is gas transmissibility in the fractures.

The gas storativity in the matrix blocks is expressed as: $\tilde{\omega} = \frac{\phi_m C_{tm}}{2\phi_f C_f}$ where ϕ_m is matrix porosity, C_{tm} matrix total compressibility, ϕ_f is fracture porosity, and C_f is fracture compressibility. Also, gas transmissibility in the fractures is expressed as: $\tilde{\lambda} = \frac{k_m L}{k_{fi} h_f} L$ where k_m is matrix permeability, L is the characteristic length considered as hydraulic fracture half-length, k_{fi} is initial permeability of fractures, h_f is fracture thickness. The pseudo-pressure inequality factor is expressed as: $\beta = \frac{m(P)_m}{m(P)_f}$ where $m(P)_m$ is matrix pseudo-pressure expressed as: $m(P)_m = 2\int_{P^*}^{P}\left(1 + \frac{b_{k_m}}{P}\right)\frac{P}{\mu z}dP$ and $m(P)_f$ is fracture pseudo-pressure expressed as:$m(P)_m = 2\int_{P^*}^{P}\frac{P}{\mu z}dP$ whereb_{k_m} is slippage factor (psi) in the matrix, μ is gas viscosity, Z is gas compressibility factor and P is reservoir pore pressure.

2.1.1 Klinkenberg (Gas Slippage) Effect

Klinkenberg (1941) found that the permeability of a core sample measured by air (or gas) is relatively higher than that measured by water. This is attributed to a gas slippage at the pore wall; when pore radius attains the mean free path of gas molecules, the rate of collision between gas molecules and pore wall increases. Thegas slippage phenomenon is called Klinkenberg effect.

The Klinkenberg parameter is contained in the modified permeability expressed as:

$$k_{slip} = k_{Darcy}\left(1 + \frac{b_{k_m}}{P}\right) \quad (2.7)$$

where $k_{Darcy} = k_{abs}$ is rock absolute permeability, b_{k_m} is slippage factor (psi) in the matrix.

Ertekin *et al*. (1986) expressed the slippage factorb_{km} (psi) as:

$$b_{km} = \frac{D_g}{k_{abs}} \cdot \mu_g c_g \cdot P \quad (2.8)$$

where $D_g = \frac{31.57}{\sqrt{M_g}} \cdot k_{abs}^{0.67}$; hence,

$$b_{km} = \frac{31.57}{\sqrt{M_g}} \cdot k_{abs}^{-0.33} \cdot \mu_g c_g \cdot P \quad (2.9)$$

where μ_g is gas velocity, c_g is gas compressibility, P is reservoir pressure at current time step, $k_{abs}$is rock absolute permeability, and $M_g$is gas molecular weight.

The correlation of Klinkenberg slippage factor b_k with effective permeability k_{Darcy} has been proposed by many authors. Jones (1972) conducted gas permeability experiments on coresamples for the evaluation of porosity,air permeability k_g, and liquid permeability k_L (absolute permeability). The Klinkenberg slippage factor $b_k$was correlated with effective permeability k_L as:

$$b_k = 6.9k_L^{-0.38} \quad (2.10)$$

Also, experiments were conducted on 100 samples of tight sand gas formations in the United States by Jones and Owens (1980) and the following empirical formula was proposed:

$$b_k = 12.639 k_{Darcy}^{-0.38} \quad (2.11)$$

Also, Civan*et al*. (2010) expressed the slippage factor b_k as:

$$b_k = \frac{4\mu}{r}\sqrt{\frac{\pi R_g T}{2M_w}} (2.12)$$

where r is the pore radius, b_k is the gas slippage factor, R_g is the gas constant, T is the temperature and M_w is the gas molecular mass. This equation is used in estimating the apparent pore radiusafter fitting a straight line to the apparent permeability versus reciprocal pressure plot.

Many empirical and semi-empirical models had been developed to modify Klinkenberg effect for shale reservoirs. These models include the double-slip Klinkenberg equation (a quadratic expression) proposed by Fathi *et al.*(2012) for gas flow in nano-pores using lactic Boltzmann simulation.

$$k_{slip} = k_{Darcy}\left(1 + \left(\frac{b_k}{P}\right)^2 \frac{L_{ke}}{\lambda}\right) \quad (2.13)$$

where L_{ke}accounts for kinetic energy of molecules bouncing back and λ is the mean free path of the gas molecules.

2.2 GAS MATERIAL BALANCE EQUATIONS

Schilthuis (1936) presented an equation called material balance equation (MBE), formulated to consider the reservoir as a single tank characterised by homogeneous rock properties. The equation keeps inventory of all materials entering, leaving and accumulating in the reservoir and was developed as a volume balance in which the underground withdrawal in the form of observedcumulative production is equal to the expansion of the fluids in the reservoir due to pressure depletion. MBE thereafter

became a basic tool often used by reservoir engineers to interpret and predict reservoir performance. When appropriately used, MBE can be utilised to:

(1) Evaluate initial hydrocarbon volumes in place
(2) Forecast reservoir production performance, and
(3) Predict oil and gas recovery under different types of primary driving mechanisms (Ahmed, 1989).

Rock (matrix) compaction is more remarkable in low-permeability reservoirs. If there is negligible rock compaction in a volumetric reservoir (no water influx or water production), the traditional gas MBE is expressed as:

$$\frac{P}{Z} = \frac{P_i}{Z_i}\left(1 - \frac{G_p}{G}\right) \tag{2.14}$$

i.e.

$$\frac{G_p}{G} = 1 - \frac{P/Z}{P_i/Z_i} \tag{2.15}$$

where G_p is cumulative gas produced (scf), G is free gas initially in place (scf), P is reservoir pressure, Z is gas deviation factor (gas compressibility factor), and subscript i denoted condition before expansion. The details of the derivation of gas MBE for non-fractured gas reservoirs, as presented by Schilthuis (1936), is shown in **Appendix A**.

As stated earlier, desorption mechanisms constitute an additional source of gas production; thus the traditional material balance equation (MBE) for gas reservoirs underestimates the values of original gas-in-place (OGIP) because it considers only the free gas. Also, the compressibility factor (Z-factor) in the material balance equation (MBE) should be modified for dual-porosity gas reservoirs where there is significant rock compaction.

King (1990) modified the material balance equation for original gas-in-place (OGIP) evaluation and future performance prediction for wells in coalbed and Devonian shale reservoirs. In the approach, equilibrium condition is assumed for free and adsorbed gases. Also, gas desorption from the matrix blocks to the fracture system is assumed to

be in pseudo-steady state. King's method works just like the traditional MBE, where the straight line plot of P/Z versus cumulative production G_p is used in estimating OGIP.

The MBE presented by King (1990) is expressed as:

$$\left(\frac{G_p}{G}\right)_{Total\ Gas} = 1 - \frac{P/Z^*}{P_i/Z_i^*} \tag{2.16}$$

where $Z^* = Z\Big/\left(S_g + \frac{V_L T P_{sc} Z}{\phi(P + P_L T_{sc} Z_{sc})}\right)$ with the assumption that rock and fluid compressibilities are negligible and water saturation is constant, Z is gas compressibility factor, Z_{sc} is gas compressibility factor at surface condition, S_g is gas saturation, T is reservoir temperature, T_{sc} is temperature at surface condition, P is reservoir pressure, P_{sc} is pressure at surface condition, and $V_L \frac{P_i}{P_i + P_L}$ is the Langmuir isotherm representing adsorbed gas content. A plot of P/Z^* versus cumulative production G_p yields a straight line and can be extrapolated to evaluate OGIP.

For fractured gas reservoirs with no gas adsorption, a dual porosity model is incorporated, where a tank is considered for the matrix pores and another for the fracture systems. Thus, gas material balance equation for fracture gas reservoirs where the effect of gas desorption on production was not considered (Aguilera, 2008) yields:

$$\left(\frac{G_p}{G}\right)_{Free\ Gas} = 1 - \frac{P/Z'}{P_i/Z_i} \tag{2.17}$$

where $Z' = Z\Big/\left\{1 - \left(\left(1 - \omega_f\right)C' + \omega_f C''\right)\Delta P\right\}$, ω_f is OGIP (free gas) fraction within the fractures, $\left(1 - \omega_f\right)$ is OGIP (free gas) fraction within the matrix blocks, ΔP is change in pressure, $C' = \frac{C_{pm} + C_w S_{wm}}{\left(1 - S_{wm}\right)}$, $C'' = \frac{C_f + C_w S_{wf}}{\left(1 - S_{wf}\right)}$, C_w is water compressibility, S_{wm} is water saturation in the matrix and S_{wf} is water saturation in the fracture system.

Moghadam *et al*. (2009) improved on the material balance equation presented by King (1990) and obtained a normalised compressibility factor expressed as:

$$Z^{**} = Z\frac{Z_i}{Z_i^*} \tag{2.18}$$

The plot of P/Z^{**} versus G_p has resemblance with the traditional P/Z versus G_p. The modified material balance equation was reported to be applicable to all kinds of gas reservoirs i.e., unconventional, over-pressure and water-driven. Cumulative gas production G_p can thus be evaluated as:

$$G_{p_{Total}} = \frac{\phi V_B Z_i^2}{B_{g_i} P_i Z_i^*}\left\{\frac{P_i}{Z^{**}} - \frac{P}{Z^{**}}\right\} \tag{2.19}$$

The estimated values of $G_p$were then correlated with G_p values obtained from shale gas production analysis (SGPA) by plotting P/Z versus G_p, and G_p versus time. The results showed good match.

Mengal (2010) used the free and adsorbed gas compressibilities C_g and C_d of Bumb and McKee (1986) to express the change of gas produced G_p with pressure.

$$\frac{dG_p}{dP} = \frac{\phi V_B S_g}{B_g}\{C_g + C_d\} \tag{2.20}$$

hence, production rate

$$q_g = \frac{\phi V_B S_g}{B_g}\left\{C_g + \frac{\rho_{g_{sc}} V_L P_L}{\phi \rho_{g(P_L + \bar{P}^2)}}\right\}\frac{dP}{dt} \tag{2.21}$$

Production rate q_g could be evaluated in terms of the productivity index J_g at any pressure (with corresponding pseudo-pressure) as:

$$q_g = J_g\{m(\bar{P}) - m(P_{wf})\} \tag{2.22}$$

where gas pseudo-pressure is expressed as:

$$m(P) = \int \frac{2P}{\mu Z} dP \tag{2.23}$$

Gas flow rate was obtained as:

$$q_g = q_o \cdot exp\left\{-\frac{2J_g}{\phi V_B(1-S_w)} \cdot \frac{B_g P}{(C_g+C_d)\bar{\mu}\bar{Z}}\right\} \quad (2.24)$$

Evaluating gas rate and correlating with that obtained from SGPA on decline curve plots yielded good match.

Also, Mengal and Wattenbarger (2011) expressed dry shale OGIP as:

$$G = V_B\left\{\left(\frac{\phi S_g}{B_{g_i}}\right) + V_L \frac{P_i}{P_i+P_L}\right\} \quad (2.25)$$

where $V_L = 0.031214\rho_m V_m$; ρ_m and V_m are matrix density and Langmuir maximum adsorbed gas volume respectively. And current gas-in-place was expressed as:

$$G_{current} = V_B\left\{\left(\frac{\phi S_g}{\bar{B}_g}\right) + V_L \frac{\bar{P}}{\bar{P}+P_L}\right\} \quad (2.26)$$

where $\bar{B}_g$ is the gas average formation volume factor, and $\bar{P}$ is reservoir average pressure.

However, Duarte *et al*. (2014) incorporated gas desorption into the Aguilera (2008) MBE for fractured gas reservoirs to yield:

$$\left(\frac{G_p}{G}\right)_{Total\ Gas} = 1 - \frac{P/Z_c}{P_i/Z_i} \quad (2.27)$$

where

$$Z_c = Z\left\{1 - \omega_a - \left(\omega_m C'_{pm} + \omega_f C'_f\right)\Delta P + \omega_m \frac{\rho_b B_g}{35.515\phi(1-S_{wm})} V_{ads}\right\}^{-1} \quad (2.28)$$

and $\omega_a = \frac{OGIP_a}{OGIP_{Total}}$ is the ratio of the adsorbed gas to the original gas-in-place, $\omega_m = \frac{OGIP_m}{OGIP_{Total}}$ is the fraction of the original gas-in-place that is initially stored within the matrix pores, $\omega_f = \frac{OGIP_f}{OGIP_{Total}}$ is the fraction of the original gas-in-place that is initially stored within the fracture network, ρ_b is shale bulk density (g/cm^3), ϕ is porosity and V_{ads} is the adsorbed gas volume. Duarte *et al*. (2014) evaluated V_{ads}using the Langmuir adsorption isotherm$V_{ads} = V_L \frac{P}{P_L+P}$ where V_L is Langmuir

volume (scf/ton), P is average reservoir pressure (psia) and P_L is Langmuir pressure(psia).

2.3 PRODUCTION DECLINE ANALYSIS

Production decline analysis for wells and reservoirs is the analysis of past declining production performance, i.e. the variation of rate with time and the variation of rate with cumulative production (Ahmed & McKinney, 2005). Various methods employed in estimating reserves in tight gas reservoirs (including shale gas reservoirs) range from the basic MBE to production decline and type curve analysis techniques.

2.3.1 Decline Curve Analysis

Decline curves are frequently used in estimating gas reserves and predicting production. The fundamental assumption here is that the past production trend (and the factors affecting it) will continue in the future and thus can be extrapolated and modelled analytically. The production rate and decline curvature are the major indices of decline curve analysis; however, these factors are complex functions of various parameters within the reservoir, well bore, and surface-handling facilities (Ahmed and McKinney, 2005).

The three conditions to be considered when performing production decline curve analysis (Ikoku, 1984) are:

(1) The production decline observed should actually reflect reservoir productivity and not be the consequence of external causes like change in production conditions (choke size, wellhead pressure, etc.) well damage, production controls and equipment failure.
(2) Stable reservoir conditions (i.e. producing mechanisms) must prevail in order to extrapolate decline curve with any degree of reliability. Decline curves comparison could only be done when improved recovery techniques such as infill drilling, fluid injection, and well stimulation are carried out.

(3) Production decline curve analysis is used, in evaluating new investment and auditing previous expenditures. These involve reserves estimation and equipment and facility capacities assessment.

The assumptions made.in carrying out decline curve analysis are:

(1) The well is draining a finite acting reservoir, i.e. the well is under boundary-dominated flow conditions.
(2) The well is produced at or near capacity.
(3) The well is produced at a constant wellbore flowing pressure.

2.3.1.1 Types of Rate Decline

Decline curves are obtained when production rate is plotted versus time or versus cumulative production on Cartesian, semi-log and log-log scales. These decline curves can be used in choosing the production decline model suitable for the hydrocarbon system. Production decline curvatures, according to Arps (1945), can be characterised and expressed mathematically by:

(1) Exponential decline,
(2) Harmonic decline, and
(3) Hyperbolic decline.

Exponential decline yields a straight line when production rate is plotted against time on a semi-log scale, and also when flow rate is plotted against cumulative production on a Cartesian scale; while other types of decline curve have some curvatures.

Harmonic decline yields a straight line when production rate is plotted against cumulative production on a semi-log scale, while other types of decline curves have some curvatures. However, many shifting methods are employed to obtain straight line from the curvature of flow rate versus time plot on log-log scale.

Hyperbolic decline does not exhibit a straight line on any of the plotting scale. However, shifting methods can be used to obtain straight line from the curvature of flow rate versus time plot on log-log scale.

Arps (1945) presented empirical model for production rate versus time for decline curve analysis as:

$$q_t = \frac{q_i}{(1+bD_i t)^{\frac{1}{b}}} \tag{2.29}$$

here $q_t$is gas flow rate (MMscf/d) at time t, q_i is initial gas flow rate (MMscf/d), t is time (day), D_i is initial decline rate (day), b is Arp's decline rate exponent, and the nominal decline rate D is expressed as:

$$D = -\frac{d(Inq)}{dt} = -\frac{1}{q}\frac{dq}{dt} \tag{2.30}$$

The area under the rate-time curve between timest_1 and t_2 is a measure of the cumulative gas production G_p during this period, and it is expressed as: $G_p = \int_{t_1}^{t_2} q_t dt$.

Arp's equations and cumulative gas production for the three types of decline rate are shown in **Table 2.1**:

Table 2.1: Arp's equations and cumulative production for the three types of decline rate (Ahmed & McKinney, 2005)

Parameters	Exponential decline	Hyperbolic decline	Harmonic decline
b	$b = 0$	$0 < b < 1$	$b = 1$
Rate-time relationship	$q_t = q_i exp(-D_i t)$	$q_t = \frac{q_i}{(1 + bD_i t)^{\frac{1}{b}}}$	$q_t = \frac{q_i}{(1 + bD_i t)}$
Cumulative production	$G_{p(t)} = \frac{1}{D_i}(q_i - q_t)$	$G_{p(t)} = \left\{\frac{q_i}{D_i(1-b)}\right\}\left\{1 - \left(\frac{q_t}{q_i}\right)^{1-b}\right\}$	$G_{p(t)} = \frac{q_i}{D_i} In\left(\frac{q_i}{q_t}\right)$

2.4 ADSORPTION AND ITS CLASSIFICATION

Based on the temperature-dependent binding energy of the adsorbate to the adsorbent, adsorption can be grouped as *physisorption* (physical adsorption) or *chemisorption* (chemical adsorption).

2.4.1 Physisorption (Physical Adsorption)

Physisorption is a physical attraction due to non-specific, relatively weak van der Waal\s forces and adsorption energy lower than 80 KJ/mole, the electronic structure of the bonding atom or molecule is hardly affected upon adsorption. Physically adsorbed molecules are not bound to a particular site on the surface. Physisorption is reversible because of its weak bond.

Physisorption occurs on all surfaces having favourable temperature and pressure conditions.Physisorption can result in formation of multiple layers of adsorbed molecules.

2.4.2 Chemisorption (Chemical Adsorption)

However, in chemisorption the structure of bonding atoms or molecules is altered and covalent or ionic bonds form. The strong bond in chemisorption makes it difficult foradsorption to be reversed.

Chemisorption typically continues as long as the adsorbate is in direct contact with the adsorbent; hence, it is a monolayer process. However, multiple layers could form when the adsorbate has high polarity, e.g. ammonia. Physisorption and chemosorption can co-exist on the surface; physisorption overlaying chemisorption. Also, the same surface can exhibit physisorption at lower temperature and chemisorption at elevated temperature. Nitrogen gas, for example, displays physisorption at 77 K but chemosorption at 800 K to form iron nitride (Moore, 1972).

2.5 GAS ADSORPTION AND DESORPTION KINETICS

Gas adsorption occurs when the interaction forces in the region of the phase boundary (i.e., solid surface) is altered. The interaction forces are in the form of:

(1) The van der Waals forces that cause physical attraction
(2) Electrostatic/ionic forces that cause surface charge interaction
(3) Covalent bonding that cause chemical attraction, and
(4) The adsorbent hydrophilic or hydrophobic nature.

The strengths of the electrostatic and covalent forces are comparable to typical chemical bonds. The adsorbate must obtain activation energy before it could be desorbed from the surface and transformed to the gas bulk phase. As stated earlier, adsorption equilibrium occurs when the free gas and adsorbed gas concentrations are dynamically stable. Adsorption equilibrium is established when an adsorbate has been in contact with the adsorbent for sufficient time (Ghiaci *et al*., 2004; Kumar & Sivanesan, 2007).

In pure-component gas adsorption, there is only a single phase gas diffusion and adsorption in the pore structure of the adsorbent. However, in multi-component gas adsorption, a mixture of gases is involved and there are counter-diffusion and a simultaneous/competitive affinity for adsorption based on the proportion of the gas component in the mixture.

Organic matter (such as kerogen and clay) acts as molecular sieve, allowing carbon dioxide having higher molecular interaction energy to accumulate in small pores where other gases like methane cannot access.Thischemical and thermodynamic effects leads to an enhanced adsorption of CO_2 relative to methanesimilar to those of coals in enhanced coalbed methane recovery (ECBM) recovery (Kang*etal*., 2010).

Free gas is also stored in fracture porosity and inter-granular pores. As an unconventional reservoir, the porosity and permeability of shales are remarkably lower than that of conventional reservoirs but have similar features with coalbed reservoirs (Shi & Durucan, 2010; Soeder, 2011; Wang *et al*., 2012). These features include matrix-based storage and fracture-based transport.In a chemically and structurally complex porous medium like a shale gas reservoir, CO_2 sequestration and enhanced gas recovery involve the following processes:

(1) Convective flow of free gas in the fractures
(2) Diffusive gas transport in the matrix pore structure, and
(3) Multi-component sorption (i.e., competitive adsorption) in the micro-pore structure of the shale matrix. (Fathi & Akkutlu, 2013).

Bergen *et al*. (2000) showed that in enhanced coalbed methane (ECBM) recovery, molecules of CO_2 replace molecules of methane in a proportion of 2:1 and 5:1 at about 700 and 1,500 m depth, respectively. Research at Delft University of Technology on coal samples confirmed the CO_2-methane molecular replacement proportion of 2:1 at about 700 m depth of thick coalbed (Lako, 2002).

Also, Nuttall *et al*. (2005) reported CO_2 to have an adsorption capacity roughly 5 times greater than that of methane. Busch *et al*. (2008), and Shi & Durucan (2010) showed that CO_2 adsorptivity of shale is more than that for methane. However, Kang *et al*.

(2010) found CO_2 to adsorb 5 to 10 times more than methane. This is favourable not only for geologic sequestration of CO_2 but alsofor enhanced shale gas recovery(Kang *et al*., 2010; Nuttall *et al*., 2005).

Naturally fractured reservoirs, like shales and coalbeds are usually modelled using the dual porosity idea (Warren & Root, 1963). Gas is physically adsorbed to the surface of the porous shale structure and after desorption, it is transported by diffusion obeying Fick's law. Fractures offer high permeability but low storage conduits to access the low permeability but high storage matrix; transport in the fractures obeys Darcy's law.

In adsorption, the gas loses activation energy at the surface of the adsorbent. Therefore, the apparent gas density near the solid-gas interface increases. The value of adsorbate density depends on its molar composition, temperature and pressure. The methane in-place at discovery has proven that the retention and storage have been effective for millions of years. Hence, the risk of CO_2 leakage in shale gas recovery is very minimal. Gas adsorption in shale gas reservoirs is illustrated in **Figure 2.1**:

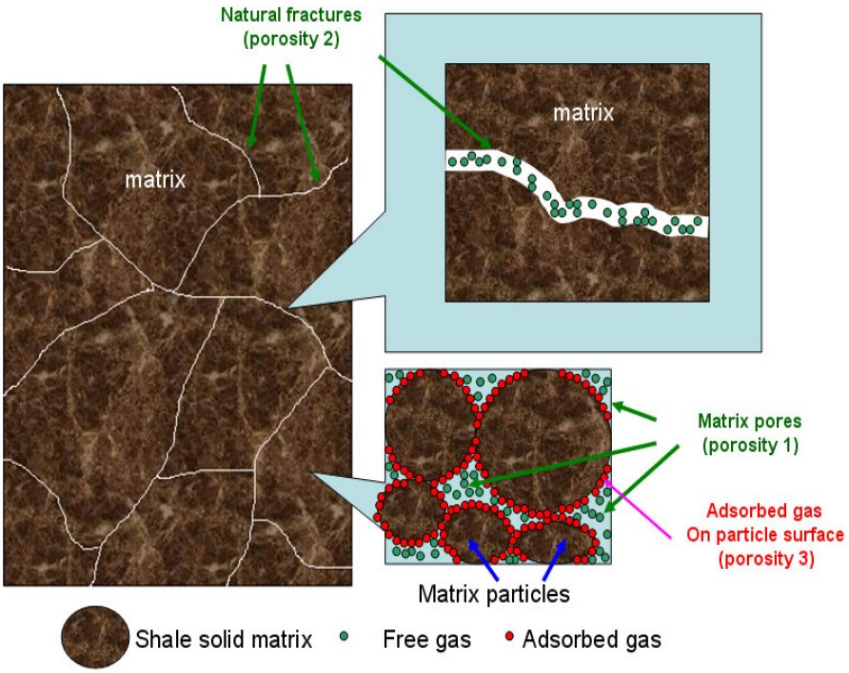

Figure 2.1: Illustration of gas adsorption in shale gas reservoirs (Song *et al*., 2011)

In unconventional gas recovery, gas flows from the fractures (the frontier storage system) to the wellbore and the pressure in the fractures declines. The pressure drop in the fractures becomes the driving force for transport of free gas from the shale matrix pores (the secondary storage system) to the fractures.

Subsequent pressure drop in the matrix pores below a threshold weakens the van der Waal's forces (van der Waals, 1873) causing the adsorbed gas to desorb from the matrix particles surface (the primary storage system) into the matrix pores. The

adsorbed gas molecules at the interface are assumed to be in equilibrium with the free gas molecules within the shale matrix pores.

Thus, adsorption isotherm serves as the boundary condition at the interface of the primary and secondary porosities (Saulsberry *et al*., 1996). However, in low-permeability formations like the shale gas reservoirs, pressure depletion is slow so the effects of desorption may not be appreciable until the well has been producing for a long time. Hence, desorption of gas from shale is a gradual process often described qualitatively as ‘slow bleeding’.

The flow mechanism responsible for production in shale gas reservoirs is shown in **Figure2.2**.

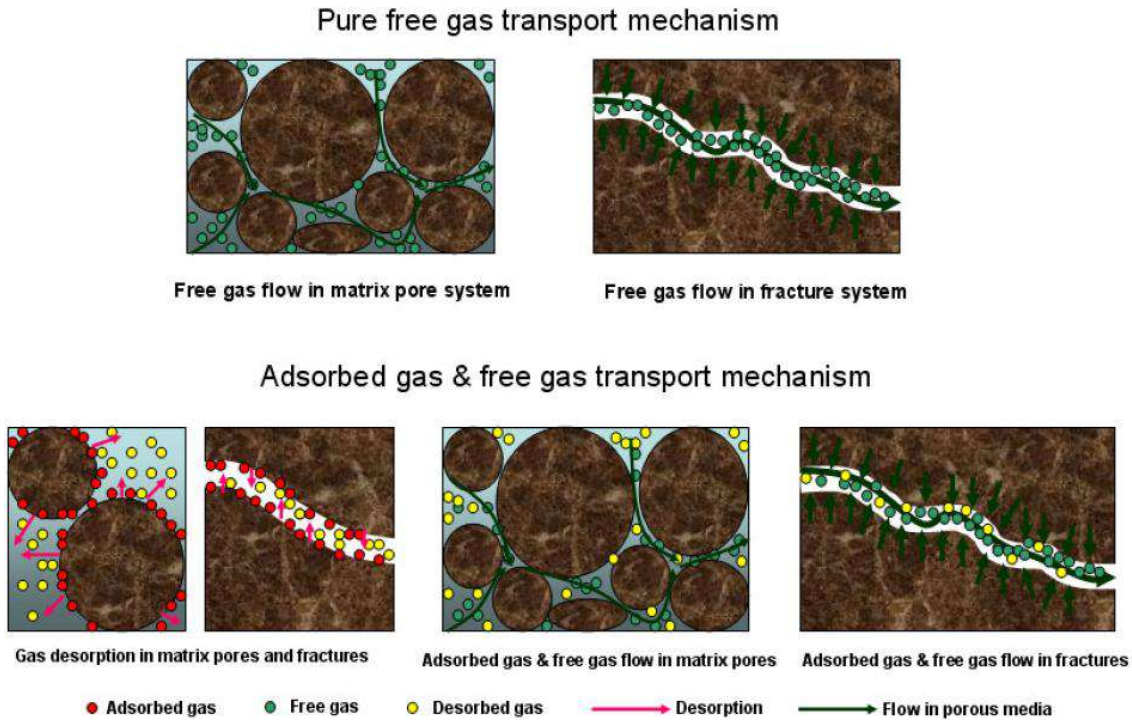

Figure 2.2: Gas transport mechanism in shale gas reservoirs (Song *et al*., 2011)

2.6 GAS ADSORPTION MODELS

The experimentally-observed adsorption isotherms are grouped by the International Union of Pure and Applied Chemistry (IUPAC, 1985) recommendations in six different types I to VI as shown in **Figure 2.3**.The geometry of the adsorption model is guided by the properties of the adsorbate and the adsorbent, and on the shape of the pore-space (Silin & Kneafsey, 2011).

Type I isotherms are characterised by the constant value the mass adsorbed attains and maintains even at very high gas pressures. Type I isotherms are often explained by the Langmuir equation, and it is applicable in microporous materials exhibiting monolayer micropore filling.

Type II isotherms describe typically adsorption in mesoporous materials exhibiting monolayer at low pressures, multilayer at higher pressures near saturation pressurewith pore condensation without hysteresis. Disperse, nonporous or only macroporous solids also feature Type II isotherms. Type II isotherms often can be described by the BET equation (Keller & Staudt, 2005).

Type III isotherms occur in systems where the adsorbate-adsorbate interaction is stronger than the adsorbate-adsorbent interaction. An example is water onhydrophobic zeolites and activated carbon.

Type IV isotherms describe the adsorption behaviour of some mesoporous materials exhibiting pore condensation with hysteresis between adsorption and desorption paths. An example is water vapour from humid air on some hydrophilic zeolites and activated carbons (Keller & Staudt, 2005).

Type V isotherms (unlike the Type IV isotherms) features nearly perpendicular middle portions of the adsorption and the desorption paths often near relative gas pressures. This shows the existence of mesopores in which pore condensation may occur. An example is water on special activated carbons and carbon molecular sieves.

Type VI isotherms are characterised by stepwise multilayer adsorption; the layers often feature at low temperatures. Examples are nonpolar, spherical molecules (noble gases) on planar graphite surfaces, and butanol on aluminium silicate (Keller & Staudt, 2005).

Different models with diverse frameworks have been applied to describe the adsorption behaviour of fluids. These models include linear adsorption isotherm, Langmuir adsorption isotherm, extended Langmuir adsorption isotherm, Freundlich adsorption isotherm, Branauer-Emmett-Teller (BET) adsorption model, Fowler-Guggenheim

adsorption isotherm, Temkin adsorption isotherm, Harkins-Jura adsorption isotherm, Langmuir-Freundlich (or Sips) adsorption isotherm, Koble-Corrigan adsorption isotherm, Kiselev adsorption isotherm, Redlich-Peterson adsorption isotherm, Elovich adsorption isotherm, ideal adsorbed solution (IAS) theory, Dubinin's micropores filling models (Dubinin-Astakhov (D-A) equation and Dubinin-Radushkevich (D-R) equation), Toth adsorption isotherm, multisite occupancy model, Volmer adsorption isotherm, real adsorbed solution (RAS) theory and Flory-Huggins adsorption isotherm.

Here, isotherm refers to the model showing volume of a gas adsorbed on a solid surface as a function of pressure for a particular temperature. Some of these isotherms model physisorption while some model chemisorption processes.

Others gas adsorption models, the theory-based equilibrium physisorption models, applicable to unconventional gas reservoirs are the Ono-Kondo (OK) lattice model, two- dimensional equations of state (2-D EOS) adsorption model (including Hill-de Boer adsorption isotherm), and simplified local density (SLD) models.

Although based on very different theoretical basis, the Ono-Kondo lattice model, the two-dimensional equation-of-state, and the simplified local-density models are good inmodellingadsorption in unconventional gas reservoir systems especially in enhanced coalbed methane recovery (Gasem *et al*., 2003; Gasem *et al*.,2008; Gasem *et al*.,2009).

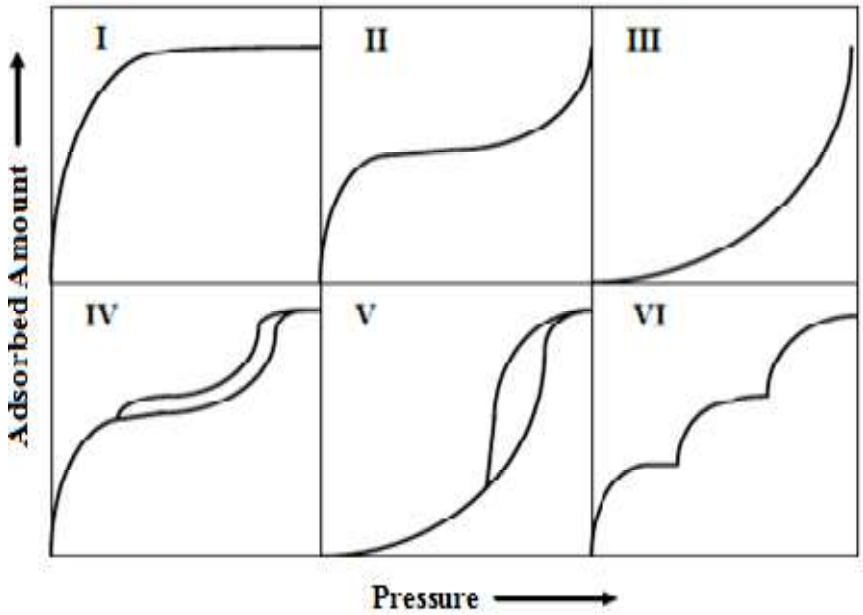

Figure 2.3: Main types of gas physisorption isotherms
(Gregg and Sing, 1982: IUPAC, 1985)

A chronological review of the development and up-to-date modifications of the above-mentioned models are hereby presented:

2.6.1 Linear Adsorption Isotherm

The linear adsorption isotherm is the simplest adsorption isotherm because the amount of the surface adsorbate is expressed as being directly proportional to the partial pressure of the adsorptive gas. The linear adsorption isotherm is expressed as:

$$V = K_H P \tag{2.31}$$

where V is volume of gas adsorbed per unit mass of adsorbent at any given equilibrium partial pressure P; and K_H is Henry's adsorption constant.

For multi-component gas, concentrations are often used instead of the partial pressures. The linear isotherm can serve as basis for many practical isotherms; it is typically applicable to low surface coverage with the assumptions thatthe surface is homogeneous and all sites are identical.

2.6.1.1 Limitation of Linear Adsorption Isotherm

The linear isotherm does not in any way model practical gas adsorption but only serves as basis for many practical isotherms.

2.6.2 Freundlich Adsorption Isotherm

Freundlich isotherm (Freundlich, 1906) describes non-ideal and reversible monolayer and multi-layer adsorption on heterogeneous surface, with non-uniform distribution of adsorption heat. Here, adsorption energy are exponentially decreased upon the completion of adsorption process (Zeldowitsch, 1934; Adamson & Gast, 1997). It was initially referred to as Freundlich-Ostwald-Boedecker (FOB) adsorption isotherm. The isotherm is expressed as:

$$V = kP^{1/n} \tag{2.32}$$

where V is the amount of adsorbed per mass of adsorbent (g/g), P is pressure of adsorbate (psia), k and n are empirical constants (changing with temperature); $k$is an indicator of adsorption capacity; and $1/n$ is a measure of intensity of adsorption (generally $1/n > 1$but at high pressure $1/n$ approaches 0, hence pressure application does not affect adsorption.

To determine the maximum adsorption volume, constant initial concentrationofadsorbateC_o(mg/L) in variable weights of adsorbent; therefor$In\ q_m$ is the extrapolated value of $In\ q$for $C = C_o$. According to Halsey (1952),

$$k = \frac{q_m}{{C_o}^{1/n}} \tag{2.33}$$

where q_m is the Freundlich maximum adsorption capacity (mg/g).

Ahmaruzzaman (2008) stated that Freundlich adsorption isotherm was originally developed for the adsorption of animal charcoal; showing that at different solution concentrations, the ratio of the adsorbate onto a given mass of adsorbent varies. But at present, Freundlich isotherm is used in modelling adsorption in heterogeneous surfaces mainly for organic compounds or activated carbon.

The slope ranges between 0 and 1 is a measure of adsorption intensity or surface heterogeneity, becoming more heterogeneous as its value gets closer to zero. Chemisorption process is characterised by $1/n < 1$, whereas $1/n > 1$ is an indicative of cooperative adsorption (Haghseresht & Lu, 1998).

An example of Freundlich adsorption model fitting to laboratory data is shown in **Figure 2.4**.

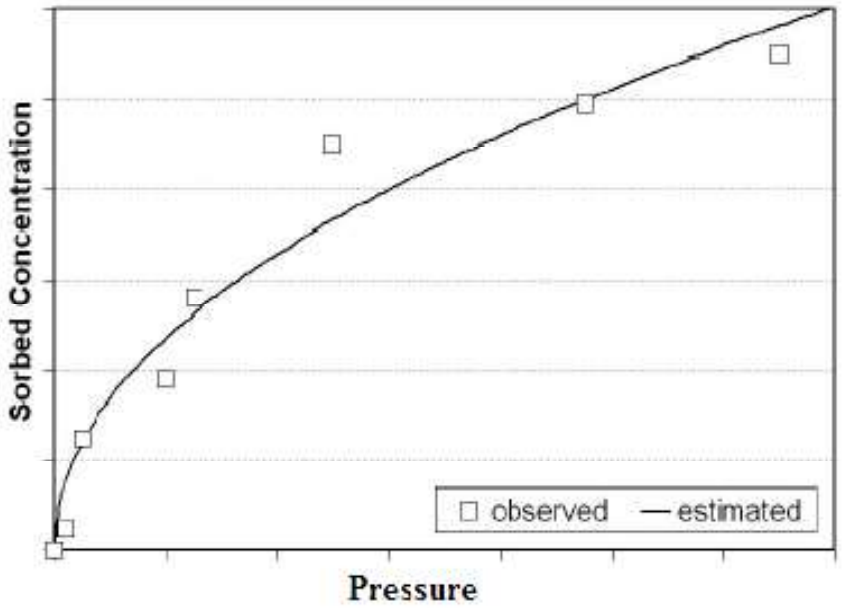

Figure 2.4: Example of Freundlich adsorption model fit
(Matott, 2007)

2.6.2.1 Limitations of Freundlich Adsorption Isotherm

It was experimentally determined that the level of adsorption increases with pressure increase until saturation pressure $P_s$is reached; thus applying higher pressure beyond that point, does not increase adsorption. Freundlich adsorption isotherm is, therefore, not effective for modelling higher-pressure adsorption because the saturation pressure is not definite. Also, Freundlich isotherm has been criticised for its limitation of lacking a fundamental thermodynamic framework, not attaining Henry's law at low concentrations (Ho *et al*., 2002).

2.6.3 Langmuir Adsorption Isotherm

Langmuir (1916) developed a mathematical model describing the dynamic equilibrium between the rate of adsorption and the rate of desorption of anadsorbate on an adsorbent. Langmuir isotherm model expresses a relationship between adsorbed gas content and gas pressure for a single-component gas adsorption (Langmuir, 1916; Langmuir, 1918). The model is called Langmuir isotherm or Hill-Langmuir equation. The Langmuir model is at present the simplest adsorption model of practical relevance, and it is derived from kinetic approach.

The isotherm assumes an ideal surface where:

(1) Solid surface has localised adsorption sites holding only one adsorbate molecule per site
(2) Adsorption sites are energetically equivalent i.e. the surface is homogeneous and all sites are identical
(3) Saturation coverage is attained when all sites are completely occupied
(4) Adsorption coverage is assumed to be independent of the enthalpy of adsorption
(5) There are no adsorbate-adsorbate interactions (including attractive and repulsive forces) between neighbouring adsorption sites
(6) Adsorption of molecules is of monolayer type, and
(7) Adsorption is reversible i.e. desorption occurs during pressure depletion.

The Langmuir isotherm describes a gradually increasing surface adsorption with pressure application until the entire surface area attains monolayer with no further adsorption. Because of its simplicity and ability to represent low-pressure adsorption behaviour, this model is still applied widelyalthough itis restricted to monolayer coverage. The reflection or adsorption of a molecule after hitting a surface depends on availability of vacant site. Langmuir adsorption isotherm is expressed as:

$$V_{ads} = V_L \cdot \left(\frac{P}{P+P_L}\right) \tag{2.34}$$

where V_{ads} is volume of gas adsorbed per unit mass of adsorbent (scf/ton) at any given equilibrium pressure P; V_L is the Langmuir volume i.e., the maximum volume of gas

which can be adsorbed per unit mass of adsorbent (scf/ton) at infinite pressure; and P_L is the Langmuir pressure, which is the pressure at which half the Langmuir volume is adsorbed.

The presumed Langmuir isotherm curve is shown in **Figure 2.5**.

Another form of expressing Langmuir isotherm is:

$$V_{ads} = V_L \cdot \left(\frac{bP}{1+bP}\right) \tag{2.35}$$

where $b = \frac{1}{P_L}$ is Langmuir's constant with unit of inverse pressure, it is a measure of the partitioning of the adsorbate molecules between the adsorbed gas and free gas, and it is dependent on the adsorbent composition, moisture content and temperature (Mohammad, 2009).

An example of Langmuir isotherm fitting to laboratory data is shown in **Figure 2.6**: The details of the derivation of Langmuir adsorption isotherm is shown in **Appendix B**.

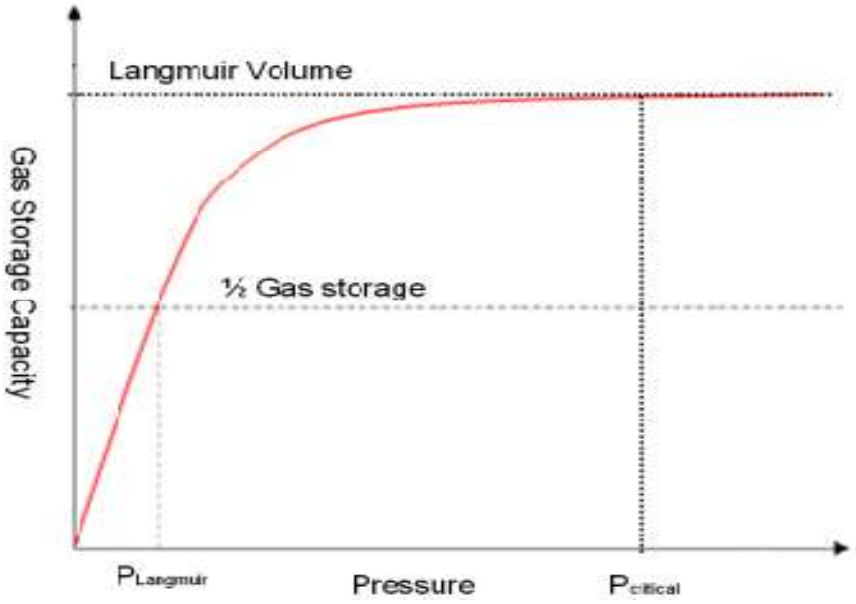

Figure 2.5:The presumed Langmuir isotherm curve
(Song *et al*., 2011)

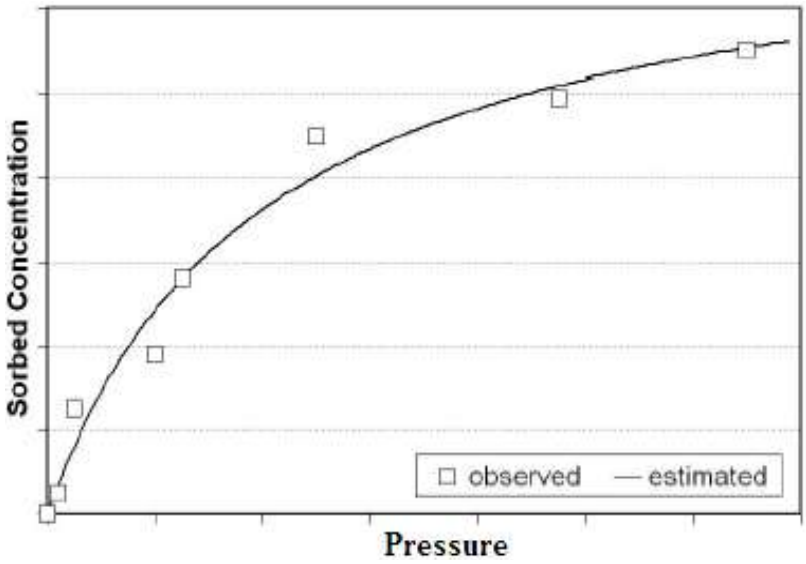

Figure 2.6: Example of Langmuir adsorption model fit(Matott, 2007)

2.6.3.1 Limitations of Langmuir Adsorption Isotherm

Langmuir adsorption isotherm does not have a fixed onset of adsorption saturation pressure because maximum adsorbed volume is obtained at an infinite pressure that is far higher than the Langmuir pressureP_L. Hence, Langmuir isotherm prediction of adsorption is not reliable at high pressures.

The limitations in the assumptions made in Langmuir isotherm include:

(1) Non-consideration of rough inhomogeneous surfaces having multiple site-types of varying parameters such as the heat of adsorption

(2) Ignorance of adsorbate-adsorbate interactions often observed in heat of adsorption data. The adsorbate-adsorbate interactions are of two kinds:
   (i) Direct interaction between neighbouring adsorbed molecules, which favours adsorption near another adsorbate molecule; and
   (ii) Indirect interactions, where the adsorbate changes the surface around the adsorbed site thereby affecting the adsorption of neighbouring molecules.

(3) Langmuir isotherm is valid at low pressures (Merey, 2013) but exhibits an over-estimation of adsorbed/desorbed volume at higher pressures. The ambiguity is due to non-existence of adsorption saturation pressure in Langmuir isotherm framework

2.6.4 Extended Langmuir Adsorption Isotherm

Practically, the gas adsorbed is usually of multi-component nature; each gas does not adsorb/desorb independently, but competes for the same adsorption locations. Hence, mixture adsorption had to be modelled. The extended Langmuir isotherm model was postulated by Markham and Benton (1931) to describe mixture (multi-component) adsorption. Here, the extended model assumes that:

(1) All the sites are equivalent,

(2) The adsorption of molecules is of monolayer type, where each site can hold at most one molecule of either of the gas species, but not both, and

(3) There are no interactions between adsorbate molecules on neighbouring sites. The model can be represented as:

$$\theta_i = \left(\frac{V_{ads}}{V_L}\right)_i = \frac{y_i b_i P}{1+\sum_{j=i}^{N} y_j b_j P} \tag{2.36}$$

where θ_i is the fractional loading of the adsorbing component i;y_i is the gas-phase mole fraction of the adsorbing specie i;$b_i$is equal to $\frac{1}{P_{L_i}}$, the temperature-dependent pure-component Langmuir model parameterof the adsorbing specie i; P is equilibrium pressure; and $j = 1, \ldots N$; $N$is the number of gas component (1 for pure-component, 2 for binary mixture, and 3 for ternary mixture).

The selectivity factorα can be expressed as:

$$\alpha_{ij} = \frac{(x/y)_i}{(x/y)_j} = \frac{l_i b_i}{l_j b_j} \tag{2.37}$$

where x and y are the adsorbed and free gas mole fractions of the mixture, respectively, and l and b are the corresponding single-component model parameters. The equation shows that the extended Langmuir model predictsfor α a constant value independent of pressure and composition.

2.6.4.1 Limitations of Extended Langmuir Adsorption Isotherm

The extended Langmuir adsorption isotherm is characterised by the following:

(1) Non-consideration of rough inhomogeneous surfaces having multiple site-types of varying parameters such as the heat of adsorption
(2) Negligence of adsorbate-adsorbate interactions
(3) Non-considerationof multi-component gas equilibria and system pressure to evaluate mixed-gas adsorption, and
(4) The monolayer type of adsorption.

Hence, the extended Langmuir model isthermodynamically inconsistentand it is an entirely empirical model (Arri & Yee, 1992).

2.6.5 Brunauer-Emmett-Teller (BET) Adsorption Model

The assumptions in Langmuir isotherm are not applicable for relatively flat and non-porous surfaces. Brunauer *et al*. (1938) developed an isotherm (called BET model) that prolonged the Langmuir adsorption model from a monolayer to a multilayer adsorption with the assumptions that:

(1) Gas molecules are physically adsorbed on a solid in layers endlessly,
(2) There is no interaction between each adsorption layer, and
(3) The Langmuir model can be applied to each layer.

Derivation of BET model is more complicated than Langmuir model; BET adsorption isotherm is presented as:

$$\frac{1}{V\left\{\left(\frac{P_s}{P}\right)-1\right\}} = \frac{1}{V_m c} + \frac{c-1}{V_m c}\left(\frac{P}{P_s}\right) \tag{2.38}$$

$$\frac{1}{\left(\frac{P_s-P}{P}\right)} = \frac{V}{V_m c}\left\{1 + (c-1)\frac{P}{P_s}\right\} \tag{2.39}$$

$$V = \frac{V_m c P}{(P_s-P)\left\{1+(c-1)\frac{P}{P_s}\right\}} \tag{2.40}$$

where V is the volume of adsorbed gas at standard conditions, and V_m is the volume of adsorbed gas required to form a monolayer, c is the BET constant related to the heat of adsorption,P and P_s are the equilibrium and the saturation pressure (or vapour pressure) of adsorbates at the temperature T,

$$c = exp\left(\frac{E_1-E_L}{RT}\right) \tag{2.41}$$

where E_1 is the heat of adsorption for the first layer, and E_L is the heat of adsorption for the second and higher layers and is equal to the heat of liquefaction.

The BET adsorption isotherm plot yields a straight line with $\frac{1}{V\left\{\left(\frac{P_s}{P}\right)-1\right\}}$ on the y-axis and $\phi = \frac{P}{P_s}$on the x-axis using laboratory data. Here, linearity is maintained only in the range of $< 0.05\frac{P}{P_s} < 0.35$. The value of the slope J and the y-intercept K are used to calculate the monolayer adsorbed gas volume V_m and the BET constant c.where:

$$V_m = e\frac{1}{J+K} \tag{2.42}$$

and

$$c = 1 + \frac{J}{K} \tag{2.43}$$

The BET model is widely used in surface science for evaluating surface areas of solids by physical adsorption of gas molecules. The total surface area $S_{Total}$and the specific surface area S_{BET} are expressed as:

$$S_{Total} = \frac{V_m N S}{V} \tag{2.44}$$

and

$$S_{BET} = \frac{S_{Total}}{a} \tag{2.45}$$

where V_m is the monolayer adsorbed gas molar volume, N is Avogadro's number, $S$is the adsorption cross section of the adsorbing species, $V$is the adsorbate gas molar volume, and $a$is the mass of the adsorbent. An example of BET adsorption model fitting to laboratory data is shown in **Figure 2.7**.

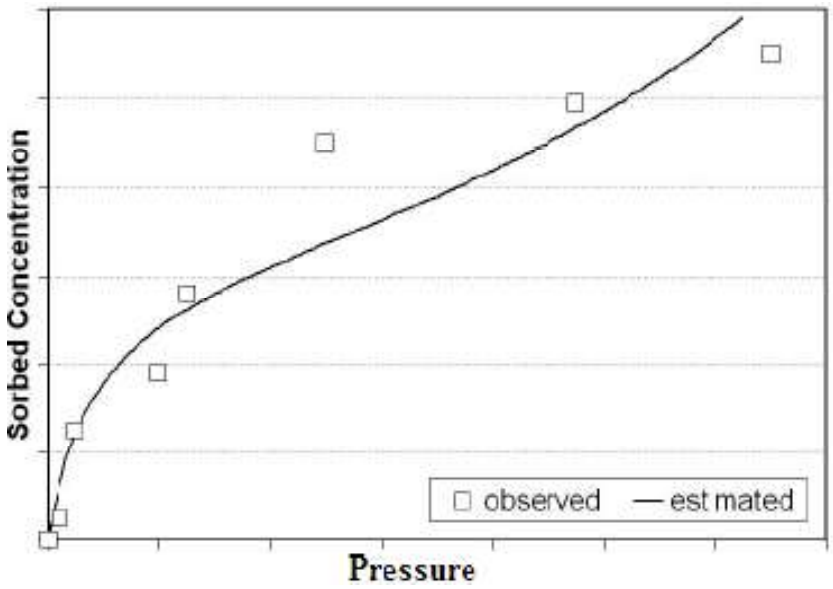

Figure 2.7:Example of BET adsorption model fit
(Matott, 2007)

2.6.6 Fowler-Guggenheim Adsorption Isotherm

Fowler and Guggenheim (1939) developed an adsorption isotherm which considers the lateral interaction of the adsorbed molecules. The isotherm is expressed as:

$$K_{FG} = \frac{\theta}{1-\theta} exp\left(\frac{2\theta\omega}{RT}\right) \tag{2.46}$$

where K_{FG} is the Fowler-Guggenheim equilibrium constant (L/mg), $\frac{V_{ads}}{V_{max}}$ is thefractional coverage, $R$is the universal gas constant (kJ mo$l^{-1}K^{-1}$), $T$is the temperature (K), and ω is the adsorbed molecules interaction energy (kJ mol^{-1}).

Fowler-Guggenheim isotherm is one of the simplest models that consider the lateral interaction. For a positive ω, interaction between the adsorbed molecules is attractive and the heat of adsorption will increase with loading. However, for negativeω, interaction among adsorbed molecules is repulsive and the heat of adsorption decreases with loading. When $\omega = 0$, there is no interaction between adsorbed molecules and the Fowler-Guggenheim equation collapses to the Langmuir equation.

2.6.7 Temkin Adsorption Isotherm

Temkin and Pyzhev (1940) developed an adsorption isotherm for the adsorption of hydrogen onto platinum electrodes in an acidic medium. The isotherm explicitly considers adsorbent-adsorbate interactions. Temkin adsorption isotherm assumes that heat of adsorption of all molecules in the layer would decrease linearly rather than logarithmic withloading irrespective of the level of concentration (Aharoni and Ungarish, 1977). The isotherm assumes a uniform distribution of binding energies up to some maximum levels. Temkin isotherm is very good in predicting free gas equilibrium in a tightly packed structure with having varied orientations (Kim *et al*., 2004). Temkin adsorption isotherm is usually expressed (Aharoni and Sparks, 1991) as:

$$\theta = \frac{V}{V_m}\frac{RT}{\Delta Q} In\ A_T P \qquad (2.47)$$

where θ is the fractional coverage, $T$is the temperature (K), $\Delta Q = -\Delta H$is the variation of adsorption energy (kJ mol^{-1}), A_T is the Temkin equilibrium constant (L/mg) and $R$is the universal gas constant (kJ $mo1^{-1}K^{-1}$).

For Temkin model, the variation of adsorption energy and the Temkin equilibrium constant can be evaluated from the slope and the intercept of the plot of θversus InP.

2.6.7.1 Limitations of Temkin Adsorption Isotherm

Temkin adsorption isotherm is not valid for modelling complex adsorption systems with liquid-phase adsorption (Kim *et al*., 2004).

2.6.8 Harkins-.Jura Adsorption Isotherm

Harkins and Jura (1943) developed an adsorption isotherm expressed as:

$$\frac{1}{V^2} = \frac{B}{A} - \frac{1}{A} logP \quad (2.48)$$

where V is volume of gas adsorbed per unit mass of adsorbent at any given equilibrium pressure P, the isotherm constants A and B are estimated from the linear plot.

2.6.9 Langmuir-Freundlich (or Sips) Adsorption Isotherm

Sips (1948) developed an adsorption isotherm which is a combined form of Langmuir and Freundlich expressions developed for modelling heterogeneous adsorption (Gunay *et al*., 2007) and correcting the rising adsorbate concentration characterising Freundlich isotherm model. The operating conditions governing the model are the changeof pH, temperature and concentration (Perez-Marin *et al*., 2007).

Langmuir-Freundlich adsorption isotherm is expressed as:

$$\frac{V}{V_L} = \frac{bP^{nL}}{(1+bP)^{nL}} \quad (2.49)$$

where n and L are surface specific constants.

2.6.9.1 Limitation of Langmuir-Freundlich Adsorption Isotherm

Variation in adsorbate concentration renders Langmuir-Freundlich adsorption isotherm inconsistent; at low concentrations, the isotherm collapses to Freundlich isotherm but at high concentrations, it models monolayer adsorption (a characteristic of Langmuir isotherm).

2.6.10 Koble-Corrigan Adsorption Isotherm

Koble and Corrigan (1952) developed an adsorption isotherm similar to the Sips (Langmuir-Freundlich) isotherm. Koble-Corrigan isotherm is a three-parameter model, which incorporates both Langmuir and Freundlich isotherm models. Koble-Corrigan isotherm is expressed as:

$$V = \frac{AP^n}{1+BP^n} \tag{2.50}$$

where V is volume of gas adsorbed per unit mass of adsorbent at any given equilibrium pressure P; the isotherm constants A, B and n are estimated from the linear plot with a trial and error optimisation approach.

2.6.11 Kiselev Adsorption Isotherm

Kiselev (1958) developed a model for localised monolayer. Kiselev adsorption isotherm is expressed as:

$$K_K P = \frac{\theta}{(1-\theta)(1+K_n\theta)} \tag{2.51}$$

where $K_K P$ is the Kiselev equilibrium constant (L/mg), θ is the fractional coverage,and K_n is the constant of complex formation between adsorbed molecules.

2.6.12 Redlich-Peterson Adsorption Isotherm

Redlich and Peterson (1959) proposed a three-parameter isotherm which was later modified by Jossens *et al*. (1978) to incorporate features of both the Langmuir and Freundlich equations. The equation is expressed as:

$$\frac{V}{V_L} = \frac{bP}{1+bP^k} \tag{2.52}$$

The isotherm models adsorption equilibria in homogeneous or heterogeneous materials with a linear concentration-dependence in the numerator and an exponential function in the denominator. A minimisation method is usually carried out by maximising the correlation coefficient between the experimental data points and the model predictions using the Microsoft Excel (Wong *et al*., 2004).

2.6.12.1 Limitations of Redlich-Peterson Adsorption Isotherm

Variation in adsorbate concentration renders Redlich-Peterson adsorption isotherm inconsistent; at low concentrations. The Redlich-Peterson isotherm collapses to Henry's law (low concentration limit of the ideal Langmuir condition) and at high concentrations, it reduces to the Freundlich isotherm.

2.6.13 Elovich Adsorption Isotherm

Elovich adsorption isotherm developed by Elovich and Larinov (1962) is based on the kinetic approach assumption that adsorption sites increase exponentially with adsorption, thus yielding a multilayer adsorption. It is expressed as:

$$\frac{V}{V_m} = K_E P \; exp\left(\frac{-V}{V_m}\right) \tag{2.53}$$

where K_E is the Elovich equilibrium constant (L/mg) and V_m is the Elovich maximum adsorption capacity (mg g^{-1}). If the adsorption obeys Elovich equation,V_m and $K_E$can be evaluated from the slopes and the intercepts of the plot $In\ (V/P)$ versus V.

2.6.14 Ideal Adsorbed Solution (IAS) Theory

The ideal adsorbed solution (IAS) theory was developed by Myers and Prausnitz (1965). This theory is an adsorption equilibrium analogue to Raoult's law, which is used in vapour- liquid equilibria. The IAS theory is models multi-component adsorption from pure-component adsorption data. Theassumptions are that the adsorbed gas and free gas phases form ideal solutions, i.e. all activity coefficients are unity. The IAS theory is expressed as:

$$x_i = y_i \frac{P}{[P_{o,i}]_\pi} \tag{2.54}$$

where x_i is the adsorbed gas mole fraction, y_i is gas-phase mole fraction, P is gas pressure, $P_o$is the equilibrium gas pressure that corresponds to the temperature and spreading pressure π of the pure component. The spreading pressure is defined as the surface tension difference between a clean surface and a surface covered with a monolayer adsorbate (Yang, 1987).

The IAS theory extends a pure-component isotherm model to multi-component adsorption. Any pure-component isotherm can be used with the IAS theory, hence numerous authors have used IAS theory in modelling multi-component adsorption. Zhou *et al*. (1994) and Hall *et al.* (1994) utilised a 2-D EoS with the IAS theory to model multi-component adsorption.

Valenzuela *et al*. (1998) employed Langmuiradsorption isotherm with the IAS theory for different adsorptions. Also, Manik (2002) used the IAS theory with the Toth theory in modelling adsorption with compositional coalbed methane simulator.

2.6.15 Dubinin's Micropores Filling Models

Polanyi's potential theory (Polanyi, 1932) was extended by Dubinin (Dubinin, 1960 and Dubinin, 1966) in developing the theory of volume filling of micro-pores (TVFM). The theory is based on the assumption that:

(1) The adsorbate fills the adsorption surface through a pore-filling method, and
(2) A discrete monolayer is never formed in the pores.

Dubinin modelled micro-porous adsorption by pore-filling models (Dubinin-Polanyi approach) rather than surface coverage models such as Langmuir isotherm and others. The two .types of Dubinin's pore-filing isotherms are the Dubinin-Radushkevich (D-R) and Dubinin-Astakhov (D-A) equations.

2.6.15.1 Dubinin-Astakhov (D-A) Equation

The Dubinin-Astakhov (D-A) equation (Dubinin and Astakhov, 1971) is expressed as:

$$\frac{V}{V_o} = exp\left\{-\left(\frac{RT}{\beta E_o} In\frac{P_o}{P}\right)^n\right\} \tag{2.55}$$

2.6.15.2 Dubinin-Radushkevich (D-R) Equation

The Dubinin and Radushlcevich (1977) adsorption isotherm is an empirical model initially meant for the adsorption of subcritical vapours onto micro-pores with pore filling mechanisma Gaussian energy distribution onto a heterogeneous surface (Dabrowski, 2001; Gunay *et al*., 2007).

The Dubinin-Radushkevich (D-R) isotherm is obtained by setting $n = 2$ in the (D-A) equation (Yang, 1987):

$$\frac{V}{V_o} = exp\left\{-\left(\frac{RT}{\beta E_o} In\frac{P_o}{P}\right)^2\right\} \tag{2.56}$$

where V is the adsorbed volume, V_o is the micropore saturation volume that corresponds to adsorption saturated pressure P_o, n is a structuralheterogeneity parameter, $\beta$is an affinity coefficient and E_o is the enthalpy of adsorption. A value of range of 1 to 4 has been reported for n (Clarkson *et al*., 1997) and the values of β have also been compiled from many adsorbates (Wood, 2001).

The model is valid for high solute activities and the intermediate range of concentrations data. Also, one of the unique features of the Dubinin-Radushkevich (1977) isotherm lies on the fact that it is temperature-dependent. Thus when adsorption data at different temperatures are plotted as a function of logarithm of amount adsorbed versus the square of potential energy, all appropriate data will lie on the same curve (called the characteristic curve).

Dubinin's pore-filling isotherms are single-component models, hence they need a mixture theory like the IAS theory for multi-componentadsorption. Several works have established that the pore-filling models is superior to the Langmuir model. Clarkson and Bustin (2000) compared the IAS theory and pore-filling models with the extended Langmuir model; the IAS/D-A model was found to perform better than the IAS/D-R, IAS/Langmuir and extended Langmuir isotherms.

However, none of these models is valid in modelling accurately the selectivity of the adsorbates; thus they yielded either a constant selectivity (applicable to extended Langmuir) or an increasing selectivity with increasing feed composition of the larger adsorbing gas (applicable to IAS/D-R equation). Also, Harpalani *et al*. (2006) modelled data adsorption isotherms data with the Langmuir, D-R and D-A equations and found the D-A equation to be superior to the other two models.

A major characteristic of the D-A equation is the temperature-invariance of the characteristic plot of $In\frac{P_o}{P}$ versus V. This feature can be used in modelling adsorption atdifferent temperatures based on data from a single isotherm; however, the pore-filling models are developed for sub-critical adsorbates. These models particularly use the saturation pressure P_o of the respective isotherms and introduce an empirical modification when in the consideration of pore-filling model for coalbed methane

(CBM) systems. Although, a lot of modifications have been developed (Clarkson *et al*., 1997; Day *et al*., 2008), there seems to be little theoretical justification behind them.

Clarkson *et al*. (1997) used the Langmuirmonolayer, BETmultilayer, and D-R. and D-Apotential theories in high-temperature, high-pressure methane adsorption and low-pressure CO_2adsorption in determining the best fit for laboratory data. The D-A modelwas found to yield the best fit to the high-pressure methane adsorption. It was then concluded that the assumption of energetically homogeneous adsorption surface (observed in Langmuir isotherm) does not apply to coal. It was also observed that, although the adsorption potential theory is valid for low-pressure CO_2 adsorption, high-pressure adsorption isotherms for CO_2 needed further clarification.

2.6.15.3 Limitation of Dubinin's Micropores Filling Models

Despite its advantages, Dubinin-Radushkevich adsorption isotherm has unsatisfactory asymptotic properties (i.e. bonds between molecules become stronger when they are far apart) and does not model Henry's law at low pressures (Altin *et al*., 1998).

2.6.16 Toth Adsorption Isotherm

Toth (1971) utilised potential theory to develop an adsorption isotherm which is valid for heterogeneous adsorptionsuch as phenolic compounds adsorption on carbon. Toth isotherm models low-pressure monolayer adsorption.

Toth adsorption isotherm for pure-component gas is expressed as:

$$\theta^t = \left(\frac{V}{V_\alpha}\right)^t = \frac{(bP)^t}{1+(bP)^t} \tag{2.57}$$

where θ is fractional loading, V_α is the limiting amount of gas adsorbed at infinite pressure, b is Langmuir parameter, and t is Toth parameter describing approximately energetic heterogeneity and fractality of the adsorbent surface, $0 \leq t \leq 1$.

Toth adsorption isotherm, for gas mixture is expressed as:

$$\theta^t = \left(\frac{V_i}{V_{i_\alpha}}\right)^t = \frac{(b_i P_i)^t}{1+\sum_{k=1}^{N}(b_i P_i)^t} \quad (2.58)$$

where $i = 1 \ldots\ldots N$ and $k = 1$.

Toth isotherm correlation assumes thatthe energy of most adsorption sites is less than the peak or mean value (Ho *et al*., 2002). The isotherm is valid for both low and high-end boundary of the concentration (Vijayaraghavan *et al*., 2006).

2.6.17 Multisite Occupancy Model

Nitta *et al.* (1984) developed an adsorption isotherm from a localised monolayer model in which each molecule occupies multi-site on a homogeneous surface. The resultant equation is the same as that of Honig and Mueller (1962) for single-component adsorption derived from a fractured-sized vacancy model. Multisite occupancy model for multi-component adsorption on a homogeneous surface is expressed as:

$$In(n_i K_i P_i) = In\theta_i - n_i In\left(1 - \sum_j \theta_j\right) - \frac{n_i \sum_j \theta_j u_{i,j}}{kT} \quad (2.59)$$

where $i = 1,2, \ldots\ldots, k$; n is the neighbouring sites occupied by a molecule; k is temperature dependence factor; K is an adsorption equilibrium constant; j is theadsorbatemolecules internal and vibrational partition function;T istemperature;$P_i$is partial pressure of component i; θ is degree of surface coverage, i.e.,$\theta = \frac{V}{V_{max}}$; u is adsorbate-adsorbate molecular interaction parameter.

2.6.18 Volmer Adsorption Isotherm

Volmer adsorption isotherm was developed by Volmer (1925). It applies to cases of mobile adsorbates and also takes into account excluded areas per moleculea_m. Volmer isotherm is expressed as:

$$K_{eq,y}P = \frac{\theta}{1-\theta} exp\left(\frac{\theta}{1-\theta}\right) \quad (2.60)$$

where

$$K_{eq,y}P = \left(\frac{h^2}{2\pi m K_B T}\right)^{1/2} \frac{a_m}{V} exp\left(\frac{\Delta G_{ads}}{K_B T}\right) \quad (2.61)$$

Contrary to the Langmuir adsorption isotherm where localised adsorbates are considered, in Volmer adsorption model, a plot of $\frac{1}{\theta}$ versus $\frac{1}{P}$ does not result in a straight line.

2.6.19 Real Adsorbed Solution (RAS) Theory

Unlike in the ideal adsorbed solution theory where adsorbed gas activity coefficients are assumed to be equal to, the real adsorbed solution theory requires the real values of adsorbed gas activity coefficients. Considering the activity coefficients, the real adsorbed solution (RAS) theory is obtained as follows (Stevenson *et al*., 1991):

$$x_i = \frac{y_i}{\gamma_i} \frac{P}{(P_i^o)_{\pi,T}} \frac{\varphi_i}{\varphi_{i\ i}^o} \quad (2.62)$$

where x_i is the adsorbed gas mole fraction, y_i is gas-phase mole fraction, γ_i is the activity coefficient of the component i in the adsorbed phase, P is gas pressure, φ_i is the gas-phase fugacity coefficient of the single component i , $\varphi_{i\ i}^o$ is the gas-phase fugacity coefficient of the single component i at its reference pressure P_i^o. The adsorbed-phase reference pressure is defined as the pressure exerted by the single-component adsorbate at the same temperature and spreading pressure π as the mixture, i.e., $P_i^o = (P_i^o)_{\pi,T}$. The adsorbed gas activity coefficients are functions of temperature, pressure and composition.

The spreading pressure is an intensive thermodynamic variable; hence, the spreadingpressure group ψ is defined as: $\psi = \frac{\pi A}{RT}$where A is surface area of the absorbent. Relating the Gibbs adsorption equation to the spreading pressure group, the spreading pressure of mixtures can be obtained as follows (Stevenson *et al*., 1991):

$$d\psi = \sum_{i=1}^{N_c} n_i dIn(Py_i\varphi_i) - \frac{n_T}{\rho_a RT} dP \quad (2.63)$$

where n_i and n_T are the amount of gas component i adsorbed and the total amount of adsorbed gas, respectively, while$\rho_a$is the molar density of the adsorbed phase.

When modelling multi-component adsorption with the IAS and RAS theories, Stevenson *et al*. (1991) found that the theory was more reliable than the RAS theory at higher pressures where the activity coefficients are approximately equal to one. Therefore, the use of the RAS theory has been very limited.

2.6.20 Flory-Huggins Adsorption Isotherm

As stated by Horsfall and Spiff (2005), Flory-Huggins isotherm model models the level of surface loading of adsorbate onto adsorbent in determining spontaneous nature of an adsorption process. Flory-Huggins isotherm is expressed as:

$$\theta = \frac{V}{V_m} = V_o K_{FH}(1-\theta)^{n_{FH}} \tag{2.64}$$

where θ is degree of surface coverage,V_m is maximum adsorbate concentration (mg/L),V_o is adsorbate initial concentration (mg/L), K_{FH} is Flory-Huggins isotherm equilibrium constant, and n_{FH} is Flory-Huggins isotherm model exponent. The free Gibbs energy is evaluated as:

$$\Delta G^o = -RTInK_{FH} \tag{2.65}$$

where ΔG^o is Gibbs energy change, R is universal gas constant (J/mol/K) and T is temperature (K) (Vijayaraghavan *et al*., 2006).

2.6.21 Two-Dimensional Equations of State (2-D EoS) Adsorption Model

The method of modelling conventional oil and gas reservoirs throughvapour-liquid equilibria estimation using three-dimensional equations of state(3-D EoS) models is also applied to modelling unconventional gas reservoirs using two-dimensional equations of state (2-D EoS) models.

DeGance (1992) indicated the assumptions made in developing 2-D EoS models as:

(1) the adsorbent surface is a two-dimensionalsurface withunique thermodynamic properties

(2) the adsorbent is thermodynamically inert
(3) the adsorbent surface area is temperature-invariant and it is accessible equally to all adsorbate molecules, and
(4) the adsorbent surface is homotattic, i.e., it consists of many homogeneous sub-regions.

Zhou *et al*. (1994) stated the advantages of the 2-D EoS models to include:

(1) allowing simultaneous estimation of equilibrium adsorption and volumetric properties
(2) using suitable mixing rule to applysingle-component isotherms in modelling multicomponent adsorption
(3) amenable to model-parameter generalisation, and
(4) utilising proven and similar model format for use in reservoir simulations.

As stated earlier, the 2-D EoS was developed as an equivalent of the 3-D EoS. A generalised form of the cubic (3-D) EoS used in vapour-liquid equilibrium estimationis expressed as:

$$\left\{P + \frac{a\rho^2}{1+Ub\rho+(b\rho)^2}\right\}(1 - b\rho) = \rho RT \tag{2.66}$$

where a and b are the EoS parameters and values of U and W are specified to give various forms of the 3-D EoS. The 2-D EoS was developed simply by replacing two terms in the 3-D EoS, i.e., the bulk pressure P with the spreading pressure π, and the bulk density ρ with the absorbent specific surface density σ.

The generalised 2-D equivalent of the 3-D EoS is then expressed as:

$$\left\{\pi + \frac{a_2\sigma^2}{1+Ub_2\sigma+(b_2\sigma)^2}\right\}\{1 - (b_2\sigma)^n\} = \sigma RT \tag{2.67}$$

or

$$\left\{A\pi + \frac{\alpha\omega^2}{1+U\beta\omega \quad (\beta\omega)^2}\right\}\{1 - (b_2\sigma)^n\} = \sigma RT \tag{2.68}$$

where A is the adsorbent specific surface area, $\pi$is the spreading pressure, σ is the absorbent specific surface density, $\omega = \sigma A$ is the specific amount adsorbed, $\alpha = \frac{a_2}{A}$and $\beta = \frac{b_2}{A}$ are the 2-D EoS model parameters and m is an added parameter used to give more flexibility to the model. The model coefficients U, ω and m are specified or set to obtain a particular form of the 2-D EoS equivalent of the 3-D EoS. For instance, for the van der Waals (VDW) EoS, $m = 1$and$U = W = 0$; for the Soave-Redlich-Kwong (SRK) EoS, $m = U = 1$and $W = 0$; for the Peng-Robinson (PR) EoS, $m = 1$, $U = 2$and$W = -1$; for the Eyring EoS, $m = \frac{1}{2}$and $U = W = 0$; and for the Zhou-Gasem-Robinson (ZGR)EoS, $m = \frac{1}{3}$ and $U = W = 0$ (Zhou *et al*., 1994).

Using van der 2-D Waals EoS,Hill (1946) and de Boer (1953) correlated single-component adsorption; Hoory and Prausnitz (1967) used mixing rule to extend the van der Waals 2-D EoS to multicomponent adsorption. DeGance (1992) correlated high-pressure, single-component adsorption using the 2-D Virial and Eyring EoS. Zhou *et al*. (1994) used the 2-D EoS model to model single- and multi-component adsorptions. Pan (2004) incorporated Gibbs free energy mixing rules into the 2-D Peng- Robinson EoS framework and developed temperature-dependent relations for modelling high-pressure supercritical single-component adsorption.

2.6.21.1 Hill-de Boer Adsorption Isotherm

As stated previously, Hill (1946) and de Boer (1953) correlatedsingle-component adsorption using the van der Waals EoS and developed an adsorption isotherm. The isotherm modelsmobile adsorption with lateral interaction between adsorbate molecules. Hill-de Boer adsorption isotherm is expressed as:

$$K_{Hb}P = \frac{\theta}{1-\theta} exp\left(\frac{\theta}{1-\theta} - \frac{K_{e\theta}}{RT}\right) \tag{2.69}$$

where K_{Hb} is the Hill-de Boer constant (L/mg), $\theta = \frac{V}{V_m}$ is the fractional coverage, R isthe universal gas constant (kJ $mol^{-1}K^{-1}$), T is the temperature (K), and K_e is the adsorbate molecules interaction energy constant (kJ mol^{-1}).

Attraction between adsorbed species yields a positive K_e,and repulsion yields a negative value. Non-interaction yields $K_e = 0$ making Hill-de Boer model to collapse to Volmer equation.

2.6.22 Simplified Local Density (SLD) Model

The simplified local density (SLD) model is a simplified version of the more computationally-intensive local density theory. The model is termed "local" because it considers thermodynamic properties of a fluid at a local point z, where an average single density value $\rho(z)$ is evaluated (Rangarajan*et al*., 1995). The total energy function depends on all point densities and their spatial derivatives and minimised to obtain the density profile(Henderson, 1992).

Hence, the SLD model utilises mean-field theory in evaluating the chemical potential within the micropores (of slit geometry). Also, the chemical potential of the fluid molecules is considered as a function of its proximity to the adsorbent molecular wall (Fitzgerald *et al*., 2004; Fitzgerald *et al*.,2005; Fitzgerald, 2005).

The advantages of SLD framework include:

(1) Accounting for adsorbate-adsorbate (fluid-fluid) and adsorbate-adsorbent (fluid-solid) molecular interactions
(2) Relating adsorbent structural properties to physical geometries of the adsorbent
(3) Modelling adsorbed-phase density to evaluate absolute gas adsorption, and
(4) Modelling multicomponentgas adsorption using single-component isotherms.

Adsorbent structures can be modelledby different shapes such as cylindrical pores (Subramanian *et al*., 1995), rectangular slits (Chen *et al*., 1997; Gasem *et al*., 2003), flat surfaces (Gasem *et al*., 2003), etc. The pore geometry widely used in a local densitymodel for carbon adsorbents is a slit. Using the slit geometry, the SLD model

assumes theadsorbate molecules reside within a two-surface rectangular-shaped slit. The distancebetween the slit surfaces is L and the distance of a molecule from the nearest slit wall is z, where z is orthogonal to the solid surface.Within the slit, the adsorbate molecule interacts with both the slit surfaces and the free gasmolecules. **Figure 2.8** shows the slit geometry of the SLD model. The details and concept of the SLD model slit geometry is further shown in **Figure 2.9**.

The assumptions made in developing the SLD model (Rangarajan *et al*., 1995) include:

(1) The chemical potential at any point near the adsorbent surface is equal to the free gas chemical potential which is the sum of the fluid-fluid and fluid-solid interactions, and
(2) The attractive potential between fluid and solid at a point does not depend the number of molecules at and around that point.

The models illustrating intermolecular potential energy functions in fluid-solid interactions are the hard-sphere model, the Sutherland potential and the Leonard-Jones potential (Koretsky, 2004). In the hard sphere model, the molecules are considered impenetrable; however, in the Sutherland model, van der Waals attraction is incorporated into the hard sphere model. The Lennard-Jones potential is a more "realistic" model which combines van der Waals attraction and quantum (repulsive) effects; the model features the concepts that molecules are really not rigid but rather are bounded by diffuse electron clouds whose overlap (when the molecules get so close) causes coulombic repulsion.

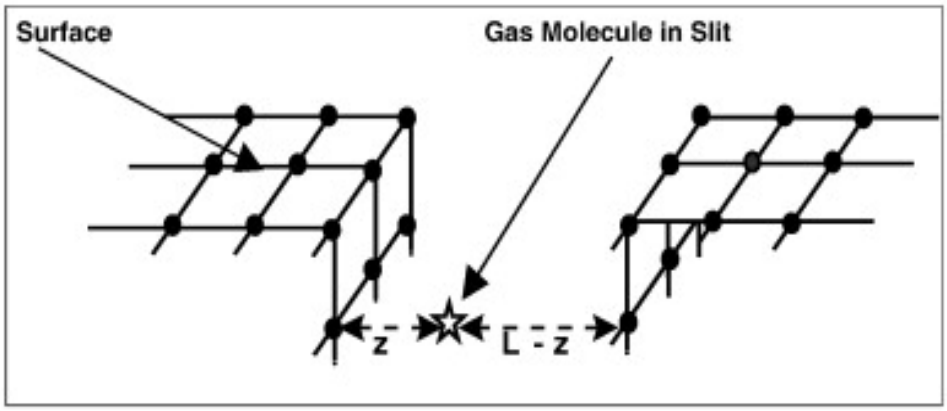

Figure 2.8: Slit Geometry of the SLD Model(Chen, 2007)

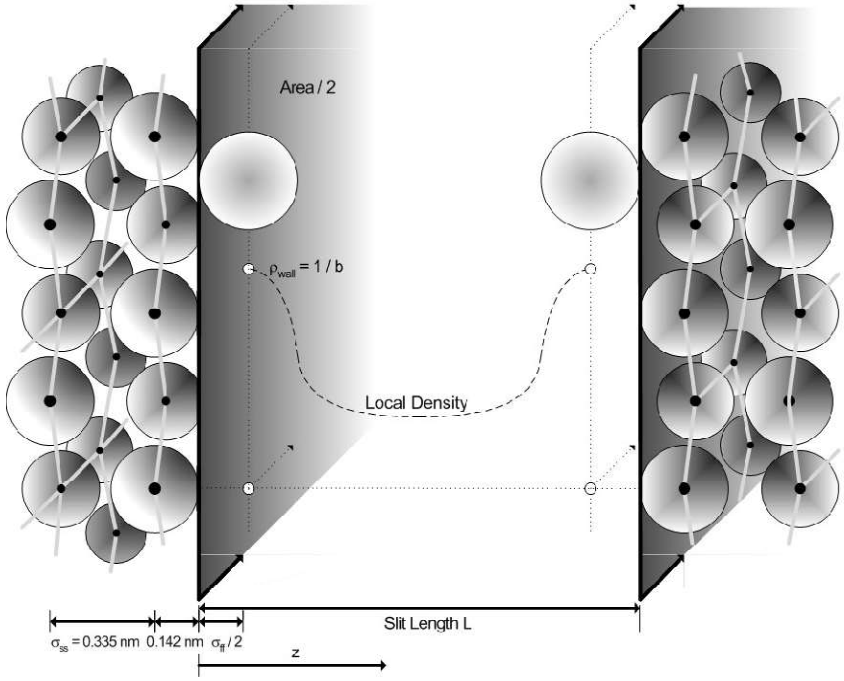

Figure 2.9: Details of Slit Geometry for SLD Model (Fitzgerald, 2005)

A form of the Lennard-Jones model designed for fluid-wall (fluid-solid) system is termed 10-4 Lennard-Jones potential (Lee, 1988). Hence, the fluid-solid interactions in the SLD model are often modelled through the 10-4 Lennard-Jones potential. Rangarajan *et al*. (1995) used the 10-4 Lennard-Jones potential with the van der Waals EoS to provide the fluid-solid and fluid-fluid interactions information in developing the SLD model. However, any EoS with suitable modifications can be used within the SLD framework.

Thereafter, researchers have used Peng-Robinson (PR) EoS (Chen *et al*., 1997; Fitzgerald *et al*., 2003; Fitzgerald, 2005), Elliot-Suresh-Donohue ESD EoS (Soule, 1998; Soule *et al*., 2001), and Bender EoS (Ustinov *et al*., 2002) within the SLD theoretical framework for high-pressure gas adsorption.

2.6.22.1 SLD//Lennard Jones Framework for Pure-Gas Adsorption on Dry Samples

Considering the slit geometry of the SLD model shown in **Figure 2.8** and **Figure 2.9**, laboratory data regression for the slit length L are 2 to 5 times the value of σ_{ff}(the distance at which the attractive and repulsive potentials of two fluid molecules are equal); σ_{ff} is characterized by the fluid molecular diameter or size (Fitzgerald, 2005).

The equilibrium chemical potential of the bulk fluid at a position z is equal to the summation of the chemical potentials from fluid-fluid and fluid-solid interactions:

$$\mu_{bulk} = \mu_{ff}(z) + \mu_{fs}(z) \tag{2.70}$$

Fugacity f is defined as the pressure of a real gas whose chemical potential is the same asthat of an ideal gas. Fugacity coefficient $\frac{f}{P}$ is the ratio of the fugacity of a real gas to thepressure of an ideal gas of the same chemical potential. The chemical potential of the bulk fluid and fluid-fluid interactions (functions of temperature and local density) are expressed in terms of fugacity as:

$$\mu_{bulk} = \mu_o + RTIn\left(\frac{f_{bulk}}{f_o}\right) \tag{2.71}$$

and

$$\mu_{ff} = \mu_o + RTIn\left(\frac{f_{ff}}{f_o}\right) \tag{2.72}$$

where μ_o is the standard state chemical potential, R is universal gas constant, f_{bulk}, $f_{ff}$and f_o are the bulk fluid, fluid-fluid and standard condition fugacities respectively. Note that μ_{ff} and $f_{ff}$are functions of the position z while μ_{bulk}, f_{bulk}, $\mu_o$and $f_o$are not. The fluid-fluid interactions are modelled through an EoS (e.g. van der Waals, Peng-

Robinson, etc.). The attractive parameter in the EoS is modified to account for the presence of the adsorbent wall.

The chemical potential due to contributions from fluid-solid interaction is expressed as:

$$\mu_{fs}(z) = \mu_{fs_1}(z) + \mu_{fs_2}(L-z) = \mu_{bulk} - \mu_{ff}(z) \tag{2.73}$$

where subscripts ff, fs_1, fs_2 and $bulk$ refer to fluid-fluid interactions, fluid-solid interactions on the first wall surface, fluid-solid interactions on the second wall surface, and bulk phase interactions respectively.

The fluid-solid interactions are modelled through a potential function such as the 10-4 Lennard-Jones potential ψ(Lee, 1988); and the chemical potential of the fluid-solid interactions is expressed on a molecular basis as:

$$\mu_{fs}(z) = \mu_{fs_1}(z) + \mu_{fs_2}(L-z) = N_A\{\psi(z) + \psi(L-z)\} = N_A\psi_T(z) \tag{2.74}$$

where N_A is Avogadro's number, and $\psi_T(z) = \psi(z) + \psi(L-z)$ respectively reflects the 10-4 Lennard-Jones potential with reference to the first and second wall surfaces from position z. Note that μ_{fs} is a function of the position z.

From **Equation (2.70)** to **(2.74)**,

$$\mu_{fs}(z) = RT\left\{In\left(\frac{f_{bulk}}{f_o}\right) - In\left(\frac{f_{ff}}{f_o}\right)\right\} = N_A\psi_T(z) \tag{2.75}$$

$$RT\left\{In\left(\frac{f_{ff}}{f_o}\right) - In\left(\frac{f_{bulk}}{f_o}\right)\right\} = -N_A\{\psi(z) + \psi(L-z)\} \tag{2.76}$$

i.e.

$$In\left(\frac{f_{ff}}{f_{bulk}}\right) = -\left\{\frac{\psi(z)+\psi(L-z)}{kT}\right\} \tag{2.77}$$

Note that $k = \frac{R}{N_A}$is independent of position z within the pore and ψ_T is dependent on position only, i.e.

$$f_{ff}\left(T, \rho_{ads}(z)\right) = f_{bulk}(T, \rho_{bulk}) exp\ \frac{-\{\psi(z)+\psi(L-z)\}}{kT} \tag{2.78}$$

The bulk gas fugacity f_{bulk} can be evaluatedeasily since it is not a function of the gas molecule position z. The equations of state often used to express gas fugacity are the van der Waals EoS (Rangarajan*et al*., 1995), Peng-Robinson EoS (Chen *et al*., 1997; Fitzgerald *et al*., 2003), the Elliot-Suresh-Donohue EoS (Soule *et al*., 2001) and the Bender EoS (Ustinov *et al*., 2002).

The 10-4 Lennard-Jones' potential with reference to the first wall surface is expressed as:

$$\psi(z) = 4\pi\rho_c\varepsilon_{fs}\sigma_{fs}^2\left\{\frac{\sigma_{fs}^{10}}{5(z')^{10}} - \frac{1}{2}\sum_{i=1}^{4}\frac{\sigma_{fs}^4}{\{z'+(i-1)\sigma_{ss}\}^4}\right\} \tag{2.79}$$

In a similar way, the 10-4 Lennard-Jones potential with reference to the second wall surface is expressed as:

$$\psi(L-z) = 4\pi\rho_c\varepsilon_{fs}\sigma_{fs}^2\left\{\frac{\sigma_{fs}^{10}}{5((L-z)')^{10}} - \frac{1}{2}\sum_{i=1}^{4}\frac{\sigma_{fs}^4}{\{(L-z)'+(i-1)\sigma_{ss}\}^4}\right\} \tag{2.80}$$

where $\rho_c = 0.382\text{atoms/Å}^2$ is the number of carbon plane atoms per square Angstrom(Lee, 1988), ε_{fs} is the fluid-solid interaction energy parameter, $\varepsilon_{fs} = \sqrt{\varepsilon_{ff} \times \varepsilon_{ss}}$; $\varepsilon_{ff}$is the fluid- fluid interaction energy parameter and ε_{ss} is the solid-solid energy interaction parameter. σ_{ss} is the carbon inter-planar distance. The carbon inter-planar distance is considered to be that of graphite, i.e. $\sigma_{ss} = 0.335nm$or 3.35 Å.

The fluid-solid diameter σ_{fs}, and the dummy coordinates z' and $(L-z)'$ are respectively defined as:

$$\sigma_{fs} = \frac{\sigma_{ff}+\sigma_{ss}}{2} \tag{2.81}$$

$$z' = z + \frac{\sigma_{ss}}{2} \tag{2.82}$$

and

$$(L-z)' = (L-z) + \frac{\sigma_{ss}}{2} \tag{2.83}$$

For the slit geometry considered, the SLD model is developed in terms of the Gibbs adsorptionn_{ads}^{Gibbs}defined as the excess number of moles per unit mass of adsorbent. TheSLD model is expressed as:

$$n_{ads}^{Gibbs} = \frac{A}{2}\int_{\frac{\sigma_{ff}}{2}}^{L-\frac{\sigma_{ff}}{2}} (\rho_{ads\ at\ z} - \rho_{bulk})dz \tag{2.84}$$

where A is the surface area per unit weight of adsorbent (m^2/g) ($\frac{A}{2}$ is indicated in theequation because both walls contribute to the total surface area),ρ_{ads} at z is the local density, ρ_{bulk} is the bulk density, σ_{ff} is the Leonard-Jones diameter of the fluid, the lowerlimit of integration$\frac{\sigma_{ff}}{2}$ is the location of the centre of an adsorbed molecule touching the left plane surface, and the upper limit of integration $L - \frac{\sigma_{ff}}{2}$ is the location of the centre of an adsorbed molecule touching the right plane surface. Here, fluid closer to the wall than $z = \frac{\sigma_{ff}}{2}$is ignored i.e. its local density near the wall is considered to be zero.

The adsorbate molecular diameter and fluid-fluid interaction energy parameter of some shale gas fluids are shown in **Table 2.2**.

Table 2.2: Physical fluid parameters of some shale gas fluids (Mohammad, 2009)

Parameters	**Methane**	**CO_2**	**Nitrogen**	**Water**
$\boldsymbol{\sigma_{ff}}$	0.3758	0.3941	0.3798	0.2641
$\boldsymbol{\varepsilon_{fs}/k}$ **(K)**	148.6	195.2	71.4	809.1

2.6.22.2: Steps Involved in SLD/Lennard-Jones Pure-Gas Adsorption Modelling

1. At specific temperature and pressure, solve the equation of state to obtain the bulk phase densityρ_{bulk}.

2. Evaluate the corresponding bulk phase fugacity f_{bulk} from the ρ_{bulk} values.
3. Considering the position z spanning from $\frac{\sigma_{ff}}{2}$ to $L-\frac{\sigma_{ff}}{2}$ within two homogeneous parallel walls that contribute to the surface area of the slit, sub-divide half the slit length into 50 intervals and determine the corresponding 10-4 Lennard-Jones fluid-solid potential.
4. Calculate adsorbed (local) phase fugacity $f_{ff}(z)$ at each position z from f_{bulk} and $\frac{\psi_T}{k}$.
5. Obtain adsorbed (local) phase density $\rho_{ads}(z)$ from $f_{ff}(z)$ by any iteration technique and determine the local density profile across the entire slit length.
6. Integrate $(\rho_{ads}(z)-\rho_{bulk})$ in the exact geometry form over the entire length using the modified Simpson's rule to yield Gibbs (excess void) adsorption and the corresponding absolute (total) adsorption.
7. Plot Gibbs adsorptions versus pressure at each temperature to show the adsorption isotherms for the respective gases.
8. Generalise the adsorption models by modification of the original SLD model (via the co-volume b) to conform to experimental data, and correlate with Langmuir and other related models.
9. Plot the corresponding absolute (total) adsorptions versus pressure at each temperature for the respective gases.

2.6.22.3 Modification of Attraction and Repulsion Parameter in SLD Model

In accounting for the fluid-fluid interaction in the slit, the original SLD gas adsorption model incorporates an EoS attractive term (in terms of fugacity) for the adsorbed phase a_{ads} on activated carbon developed by Chen *et al*. (1997) as a function of ratio of the slit length L to the molecular diameter σ_{ff} (Fitzgerald *et al*., 2003; Fitzgerald 2005; Mohammad *et al*., 2009).

The adsorbed density ρ_{ads} near the wall attains the reciprocal of the co-volume b. Compared to the attraction parameter, the co-volume b is the principal factor determining the profile of the adsorbed density at high-pressure; hence its accuracy is important.

The adsorbed phase densities calculated from the SLD model having original EoS are usually higher than the experimental data (Cheng *et al*., 1997; Fitzgerald *et al*., 2003; Fitzgerald, 2005; Mohammad *et al*., 2009). Hence, obtaining reliable SLD model for higher-pressure adsorption involves modifying the co-volume b by the parameterA_b by empirical approach:

$$b_{ads} = b(1 + A_b) \tag{2.85}$$

For gases in activated carbons, typical values of A_b range from 0.52 to 0.56 (Fitzgerald, 2005); and for coalbeds gases, the values range from -0.4 to 0.0 (Mohammad, 2009). The trend of the A_b range is attributed to the fact that activated carbon have significantly higher surface areas than thecoals.

Therefore, in the SLD adsorption model, when applying Peng-Robinson EoS, the adsorbed fluid fugacity is given as:

$$In\, f_{ff} = \frac{b\rho_{ads}}{1-b\rho_{ads}} - \frac{a_{ads}\rho_{ads}}{RT}\left(\frac{1}{1+2b\rho_{ads}-b^2\rho_{ads}^2}\right) - In\left(\frac{1-b\rho_{ads}}{\rho_{ads}RT}\right) - \frac{a_{ads}}{2\sqrt{2}bRT}\cdot In\left(\frac{1+(1+\sqrt{2})b\rho_{ads}}{1+(1-\sqrt{2})b\rho_{ads}}\right) \tag{2.86}$$

Thus the modified adsorbed fluid fugacity is:

$$In\, f_{ff} = \frac{b_{ads}\rho_{ads}}{1-b_{ads}\rho_{ads}} - \frac{a_{ads}\rho_{ads}}{RT}\left(\frac{1}{1+2b_{ads}\rho_{ads}-b_{ads}^2\rho_{ads}^2}\right) - In\left(\frac{1-b_{ads}\rho_{ads}}{\rho_{ads}RT}\right) - \frac{a_{ads}}{2\sqrt{2}bRT}\cdot In\left(\frac{1+(1+\sqrt{2})b_{ads}\rho_{ads}}{1+(1-\sqrt{2})b_{ads}\rho_{ads}}\right) \tag{2.87}$$

2.6.23 Ono-Kondo (OK) Lattice Model

The Ono-Kondo (OK) model developed by Ono and Kondo (1960) is a monolayer and multilayer gas adsorption model, It is based on lattice theory. Since then, Aranovich and Donohue (1996; 1997; 2001) had generalised the model for the adsorption of solutes in liquid solutions. Sudibandriyo (2003) generalised the OK model parameters for multi-component adsorption in coalbed methane reservoirs. Arumugam (2004)

implemented and further refined these model generalisations for gas adsorption on dry Argonne premium coals.

The assumptions used in developing the Qno-Kondo lattice model (Sudibandriyo, 2003) are:

1. The fluid system consists of one or more layers of lattice cells that contain fluid molecules and vacancies
2. Molecular interactions exist only between the nearest adjacent molecules
3. Adsorption equilibrium between the adsorbed layers and the free gas is given by the equality of the chemical potential in each layer and the free gas.

The major features of Ono-Kondo model include:

1. Providing a layering analogue to adsorption
2. Generating independent estimates for the adsorbed-phase densities to evaluate absolute gas adsorption
3. Reducing the correlative burden on adsorption modelling by incorporating accurate density estimates from equation of state models
4. Modelling multicomponent gas adsorption using single-component isotherms without the use of binary interaction parameters.

In this model, only one fluid molecule can be absorbed on an adsorption site. Because of the molecular interactions with the adsorbent surface, more fluid molecules are located in the cells of the adsorbed-phase layers than in the cells of the free gas layers. This is illustrated in **Figure 2.10**.

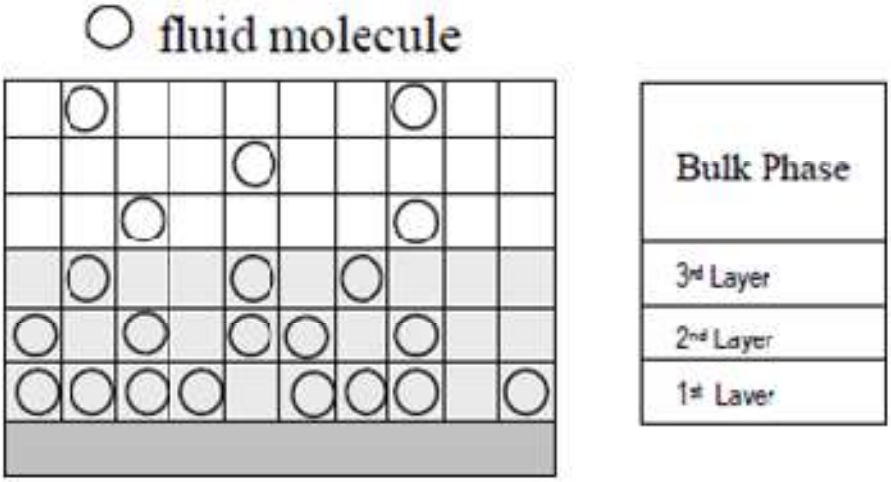

Figure 2.10: Ono-Kondo Lattice Model of Adsorption
(Sudibandriyo *et al*., 2003; Merey, 2013)

2.6.23.1 Ono-Kondo Lattice Model for Pure Gas

For single-component gas adsorption, thermodynamic equilibrium between bulk gas phase and multilayer adsorbed gas phase is modelled (Sudibandriyo *et al*., 2003) as:

$$In\left\{\frac{x_{i_{ads}}(1-x_{bulk})}{x_{bulk}(1-x_{i_{ads}})}\right\}+\frac{\varepsilon'_{ff}}{kT}\{z_o(x_{i_{ads}}-x_{bulk})+z_2(x_{i+1_{ads}}-2x_{i_{ads}}+x_{i-1_{ads}})\}=0 \quad (2.88)$$

where $x_{i_{ads}}$ is the reduced density (i,e. fraction of sites occupied by adsorbed molecules inlayer$l=2,3,\ldots\ldots m$), x_{bulk} is the fraction of sites occupied by fluid molecules in the bulkphase, m is the maximum number of adsorbed layers obtained from the adsorption data, ε'_{ff} is the fluid-fluid interaction energy parameter, and T is absolute temperature. For a hexagonal configuration of lattice cells, the coordination numbers (denotingneighbourhood molecules arrangement filling the cells) $z_o$and z_1 are 8 and 6 respectively and by definition,$z_2=\frac{z_o-z_1}{2}$; hence, $z_2=1$ and $z_o-z_1=2$.

Applying boundary conditions for layer 1 yields:

$$In\left\{\frac{x_{1_{ads}}(1-x_{bulk})}{x_{bulk}(1-x_{1_{ads}})}\right\}+\frac{\varepsilon'_{ff}}{kT}(z_o x_{1_{ads}}-z_o x_{bulk}+x_{2_{ads}}-2x_{1_{ads}})+\frac{\psi_{fs}}{kT}=0 \quad (2.89)$$

where ψ_{fs} is the 12-6 Lennard-Jones fluid-solid inter-molecular interaction potential, $k=\frac{R}{N_A}$ is Boltzman's constant. Since $z_o-2=z_1$and $x_{1_{ads}}=x_{2_{ads}}$, in modelling the adsorption inside a slit, thermodynamic equilibrium for a monolayer yields:

$$In\left\{\frac{x_{1_{ads}}(1-x_{bulk})}{x_{bulk}(1-x_{1_{ads}})}\right\}+\frac{\varepsilon'_{ff}}{kT}((z_1+1)x_{1_{ads}}-z_o x_{bulk})+\frac{\psi_{fs}}{kT}=0 \quad (2.90)$$

The Gibbs (excess void) adsorption in the Ono-Kondo model is expressed as:

$$n_{ads}^{Gibbs}=C\sum_{n=1}^{m}(x_{ads}-x_{bulk})=C\sum_{n=1}^{m}\left(\frac{\rho_{ads}}{\rho_{mc}}-\frac{\rho_{bulk}}{\rho_{mc}}\right) \quad (2.91)$$

where C is known as a prefactor related to the capacity of the adsorbent for a specific gas i.e. an index signifying number of active pores or other structural properties of the adsorbent. The reduced densities x_{ads} and $x_{bulk}$are expressed as $\frac{\rho_{ads}}{\rho_{mc}}$and $\frac{\rho_{bulk}}{\rho_{mc}}$respectively, where ρ_{ads} and ρ_{bulk} are respectively the adsorbed and the bulk

densities of the gas, and ρ_{mc} is the maximum adsorbed-phase density. Fluid-solid interaction energy determines the number of layers m obtainable. Establishing the number of layer for the model involves choosing a number that yields the best fit for experimental adsorption isotherm data.

Here, the Gibbs (excess void) adsorption expression for the OK monolayer model becomes:

$$n_{ads}^{Gibbs} = 2C\left(\frac{\rho_{ads}}{\rho_{mc}} - \frac{\rho_{bulk}}{\rho_{mc}}\right) \quad (2.92)$$

2.6.23.2 Estimation of Ono-Kondo Model Parameters

The model parameters to be estimated are ρ_{mc}, $\frac{\varepsilon'_{ff}}{kT}$, $\frac{\psi_{fs}}{kT}$ and C . Two conventional ways of evaluating the adsorbed-phase density are to use the saturated liquid density at ambient pressure (normal boiling point) (Arri & Yee, 1992), or the reciprocal of the van der Waals co-volume b (Gasem*et al*., 2003; Sudibandriyo *et al*., 2010). Also, Hocker *et al*. (1999) used a theoretical value of the density of close-packed molecules. The approach equating ρ_{mc} to $\frac{1}{b}$ is preferred because the adsorbed-phase density valuesgenerated by the OK model were found to be less than the boiling point estimates but closer to the reciprocal the co-volume b (Gasem*et al*., 2003; Sudibandriyo *et al*., 2010; Merey, 2013). Also, these values are close to the Gibbs adsorption isotherm estimates.

In Ono Kondo model, a correlation was derived for the fluid-fluid interaction energy parameter ε'_{ff} as being proportional to the Lennard-Jones potentialwell depthfluid-fluid interaction energy parameter ε_{ff}(Sudibandriyo *et al*., 2010). The correlation is expressed thus:

$$\varepsilon'_{ff} = 0.432\varepsilon_{ff} \quad (2.93)$$

The physical properties of adsorbates and adsorbents are shown in **Table 2.3**:

Table 2.3: Physical properties of adsorbates and adsorbents (Reid *et al*., 1987)

Adsorbates/ Adsorbents	**Normal Boiling Point (K)**	**Reciprocal of van der Waals co-volume (mol/L)**	$\frac{\varepsilon_{ff}}{k}$ **(K)**
H_2	20.4	38.16	59.7
N_2	77.3	25.89	71.4
H_2S	212.8	23.08	301.1
CO_2	216.6	23.34	195.2
CH_4	111.7	23.37	148.6
C_2H_4	184.6	15.41	215.7
C_3H_8	231.1	11.07	237.1
i-C_4H_{10}	261.4	8.60	330.1
Carbon	-	3.40	28.00
O (zeolite)	-	3.04	139.96

For model generalisation, ρ_{mc} and ε'_{ff} estimates are applied for modelling of selected gas adsorption, and the12-6 Lennard-Jones fluid-solid inter-molecular interaction potential $\psi_{fs}$is regressed for each adsorption system while the parameter C is regressed for each adsorption isotherm.

2.6.23.3 Steps Involved in Ono-Kondo Single-Component Gas Adsorption Modelling

1. At specific temperature and pressure, solve the equation of state (here, PR EoS) by any iteration technique to obtain the bulk phase density ρ_{bulk}:

$$P = \frac{\rho_{bulk}RT}{1-b\rho_{bulk}} - \frac{a\rho_{bulk}^2}{1-2b\rho_{bulk}-b^2\rho_{bulk}^2} \tag{2.94}$$

2. For each pressure, evaluate the corresponding bulk phase fugacity f_{bulk} from the ρ_{bulk} values as:

$$Inf_{bulk} = \frac{\rho_{bulk}RT}{1-b\rho_{bulk}} - \frac{a\rho_{bulk}}{RT}\left(\frac{1}{1-2b\rho_{bulk}-b^2\rho_{bulk}^2}\right) - In\left(\frac{1-b\rho_{bulk}}{\rho_{bulk}RT}\right) - \frac{a}{2\sqrt{2}RT}\cdot In\left(\frac{1+(1+\sqrt{2})b\rho_{bulk}}{1+(1-\sqrt{2})b\rho_{bulk}}\right) \tag{2.95}$$

3. By selecting typical values of $x_{ads} = \frac{\rho_{ads}}{\rho_{mc}}$ within the range $0 \leq x_{ads} \leq 1$, evaluate thefluid-solid potential ψ_{fs} for the isothermal monolayer adsorption system, from the expression:

$$In\left\{\frac{x_{1_{ads}}(1-x_{bulk})}{x_{bulk}(1-x_{1_{ads}})}\right\} + \frac{\varepsilon'_{ff}}{kT}\left((z_1+1)x_{1_{ads}} - z_o x_{bulk}\right) + \frac{\psi_{fs}}{kT} = 0 \tag{2.96}$$

and obtain an average value of the reduced form of 12.6 Lennard Jones potential ψ_{fs} for the density range as a function of $\pi\rho_c\varepsilon_{fs}\sigma_{fs}^2$; i.e. $\psi_{fs} = \pi\rho_c\varepsilon_{fs}\sigma_{fs}^2$ where A is a constant, $\rho_c = 0.382$ atoms/Å^2 is the number of carbon plane atoms per square Angstrom (Lee, 1988), ε_{fs} is the fluid-solid interaction energy parameter; in the Ono-Kondo model, $\varepsilon_{fs} = \sqrt{\varepsilon'_{ff} \times \varepsilon_{ss}}$; where $\varepsilon'_{ff} = 0.432$,$\varepsilon_{ff}$ is the Lennard-Jones fluid-fluid energyinteraction parameter and ε_{ss} is the solid-solid interaction energy parameter. The fluid-solid diameter (i.e. the adsorbate-carbon collision diameter) σ_{fs} is defined as: $\sigma_{fs} = \frac{\sigma_{ff}+\sigma_{ss}}{2}$where σ_{ff} is the molecular diameter of the adsorbate

and σ_{ss} is the carbon (or graphite) inter-planar distance i.e. $\sigma_{ss} = 0.335$ nm or 3.35 Å.

4. For each pressure, evaluate the corresponding adsorbed phase density fugacity f_{ff} from f_{bulk} and $\frac{\psi_{fs}}{kT}$:

$$f_{ff}(T, \rho_{ads}) = f_{bulk}(T, \rho_{ads}) exp\left(\frac{-\psi_{fs}}{kT}\right) \quad (2.97)$$

5. For each pressure, obtain adsorbed phase density ρ_{ads} from f_{ff} by any iteration technique, and determine the local density profile across the pressure range.

$$In\, f_{ff} = \frac{b\rho_{ads}}{1-b\rho_{ads}} - \frac{a_{ads}\rho_{ads}}{RT}\left(\frac{1}{1+2b\rho_{ads}-b^2\rho_{ads}^2}\right) - In\left(\frac{1-b\rho_{ads}}{\rho_{ads}RT}\right) - \frac{a_{ads}}{2\sqrt{2}bRT} \cdot In\left(\frac{1+(1+\sqrt{2})b\rho_{ads}}{1+(1-\sqrt{2})b\rho_{ads}}\right) \quad (2.98)$$

6. Evaluate and plot $\left(\frac{\rho_{ads}}{\rho_{mc}} - \frac{\rho_{bulk}}{\rho_{mc}}\right)$ versus pressure at each temperature for the respective gases.

7. With reference to the expression $n_{ads}^{Gibbs} = 2C\left(\frac{\rho_{ads}}{\rho_{mc}} - \frac{\rho_{bulk}}{\rho_{mc}}\right)$, transform the plots to appropriate adsorption models by choosing a suitable value of C to perfect the curve fit so that the average absolute percent deviation (%AAD) in each isotherm is minimum.

8. Evaluate the corresponding absolute (total) adsorption

$$n_{ads}^{Absolute} = n_{ads}^{Gibbs}\left(\frac{\rho_{ads}}{\rho_{ads}-\rho_{bulk}}\right) \quad (2.99)$$

9. Correlate the adsorption isotherms with Langmuir isotherm and other related models.

2.6.23.4 Ono-Kondo Lattice Model for Gas Mixtures

For monolayer adsorption of binary gas mixture having components A and B Sudibandriyo *et al*., 2011), the Ono-Kondo lattice model is expressed for component Aas:

$$In\left\{\frac{x_{A_{ads}}(1-x_{A_{bulk}}-x_{B_{bulk}})}{x_{A_{bulk}}(1-x_{A_{ads}}-x_{B_{ads}})}\right\} + \frac{\varepsilon'_{AA}}{kT}\left((z_1+1)x_{A_{ads}} - z_o x_{A_{bulk}}\right) + \frac{\varepsilon'_{AB}}{kT}\left((z_1+1)x_{B_{ads}} - z_o x_{B_{bulk}}\right) + \frac{\psi_{fs}}{kT} = 0 \quad (2.100)$$

While for component B, the Ono-Kondo lattice model is expressed as:

$$In\left\{\frac{x_{B_{ads}}(1-x_{A_{bulk}}-x_{B_{bulk}})}{x_{B_{bulk}}(1-x_{A_{ads}}-x_{B_{ads}})}\right\}+\frac{\varepsilon'_{BB}}{kT}\left((z_1+1)x_{B_{ads}}-z_o x_{B_{bulk}}\right)+\frac{\varepsilon'_{AB}}{kT}\left((z_1+1)x_{A_{ads}}-z_o x_{A_{bulk}}\right)+\frac{\psi_{fs}}{kT}=0 \quad (2.101)$$

Hence, for monolayer adsorption of gas mixture, the generalised equation for each component is expressed as:

$$In\left\{\frac{x_{i_{ads}}\left(1-\sum_{j=1}^{n}x_{j_{bulk}}\right)}{x_{i_{bulk}}\left(1-\sum_{j=1}^{n}x_{j_{ads}}\right)}\right\}+\sum_{j=1}^{n}\left\{\frac{\varepsilon'_{ij}}{kT}\left((z_1+1)x_{j_{ads}}-z_o x_{j_{bulk}}\right)\right\}+\frac{\psi_{fs}}{kT}=0 \quad (2.102)$$

where the summation n is over all the components.

The interaction energy between molecules of components i and j is evaluated by a geometric combination rule thus: ^

$$\varepsilon'_{ij}=\left(1+C_{ij}\right)\sqrt{\varepsilon'_{ii}\varepsilon'_{jj}} \quad (2.103)$$

where C_{ij} a binary interaction is incorporated to facilitate evaluation of interaction energy between dissimilar molecules. In such cases, C_{ij} is determined by regression of the available adsorption data.

At each pressure, evaluate the corresponding adsorbed phase fugacity $\left[f_{ff}\right]_i$ from $[f_{bulk}]_i$ and $\left[\frac{\psi_{fs}}{kT}\right]_i$ as:

$$\left[f_{ff}\right]_i=[f_{bulk}]_i exp\left(\frac{-\psi_{fs}}{kT}\right) \quad (2.104)$$

Also, at each pressure, obtain adsorbed phase density $\rho_{i_{ads}}$ from $\left[f_{ff}\right]_i$, by any iteration technique, and determine the local density profile across the pressure range.

$$In\left[f_{ff}\right]_i=\frac{b\rho_{i_{ads}}}{1-b\rho_{i_{ads}}}-\frac{a_{ads}\rho_{i_{ads}}}{RT}\left(\frac{1}{1+2b\rho_{i_{ads}}-b^2\rho_{i_{ads}}^2}\right)-In\left(\frac{1-b\rho_{i_{ads}}}{\rho_{i_{ads}}RT}\right)-\frac{a_{ads}}{2\sqrt{2}bRT}\cdot In\left(\frac{1+(1+\sqrt{2})b\rho_{i_{ads}}}{1+(1-\sqrt{2})b\rho_{i_{ads}}}\right) \quad (2.105)$$

Generally, Gibbs (excess void) adsorption for each component is evaluated as:

$$\left[n_{ads}^{Gibbs}\right]_i = 2C_i\left(x_{i_{ads}} - x_{i_{bulk}}\right) = 2C_i\left(\frac{\rho_{i_{ads}}}{\rho_{mc_{ij}}} - \frac{\rho_{i_{bulk}}}{\rho_{mc_{ij}}}\right) \quad (2.106)$$

where C_i is the prefactor related to the capacity of the adsorbent for adsorbate gas specie i obtained in the pure gas modelling.

and

$$\frac{1}{\rho_{mc_{ij}}} = \frac{x_{A_{ads}^{Absolute}}}{\rho_{mc_A}} + \frac{x_{B_{ads}^{Absolute}}}{\rho_{mc_B}} \quad (2.107)$$

Thus

$$\left[n_{ads}^{Absolute}\right]_i = \left[n_{ads}^{Gibbs}\right]_i \left[\frac{\rho_{i_{ads}}}{\rho_{i_{ads}} - \rho_{i_{bulk}}}\right] \quad (2.108)$$

2.6.24 Comparison between SLD and Ono-Kondo Models

Both simplified local density (SLD) and Ono-Kondo (OK) adsorption models predict adsorption from the adsorbed gas density at the super-critical pressure and bulk gas density at the sub-critical pressure. However, the SLD model is more cumbersome because of the numerous intervals considered in the slit width when evaluating the 10-4 Lennard Jones solid-fluid interaction energy potential.

2.7 GIBBS AND ABSOLUTE GAS ADSORPTION MEASUREMENT

Laboratory gas adsorption in reservoir core samples are evaluated as Gibbs (excess void) adsorption and further determined as "*absolute adsorption*". The experimental method employs the principle of mass balance. The experimental set-up shown in **Figure 2.11** had been used successfully in previous measurements (Hall *et al*., 1994; Sudibandriyo *et al*., 2003;Gasem *et al*., 2003; Arumugam, 2004; Fitzgerald *et al*., 2005; Mohammad, 2009).

The entire apparatus is maintained at isotherm air bath condition and the cell is placed under vacuum prior to gas injection. To determine the void volume of the adsorbent, from the calibrated pump helium (an inert gas) is injected into the equilibrium cell

filled with the crushed absorbent to avoid the prolonged time encountered before attaining equilibrium when using intact core sample of ultra-low permeability.

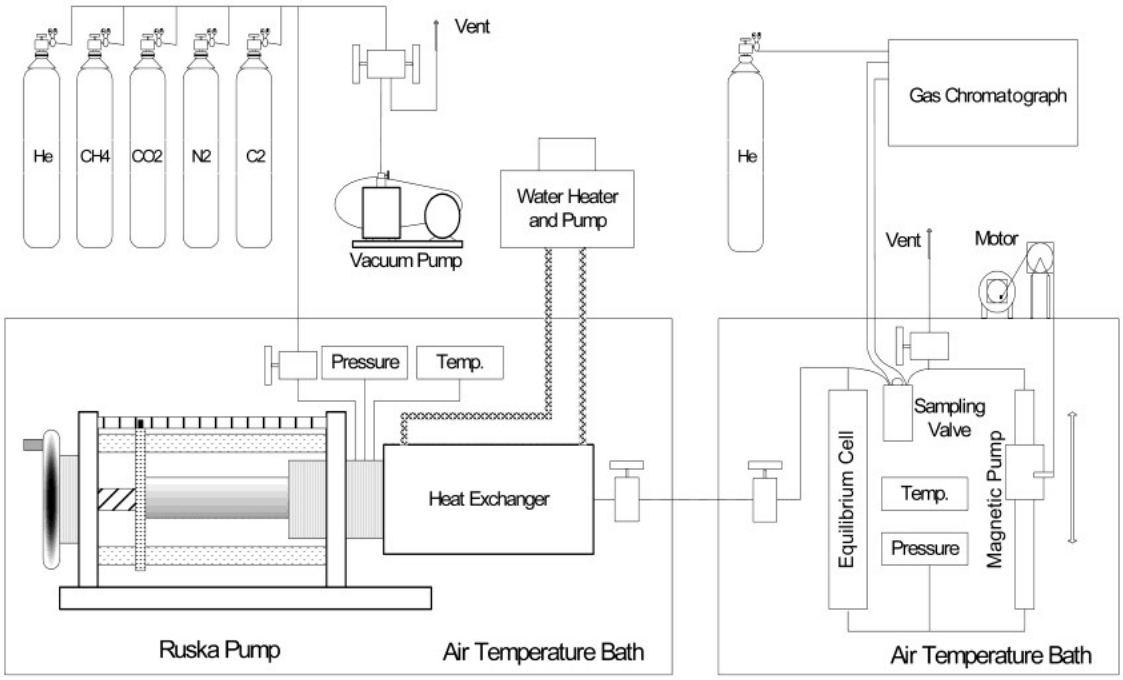

Figure 2.11: Schematic Diagram of Adsorption Apparatus(Sudibandriyo *et al*., 2003)

2.7.1 Pure-Gas Adsorption Measurement for Dry Samples

2.7.1.1 Gibbs (or Excess Void) Gas Adsorption Measurement for Dry Samples

At first stage of helium gas injection, mole of gas injected n_{inj}equals moles of gas in celln_{cell}:

$$\left(\frac{PV}{zRT}\right)_{pump} = \left(\frac{PV_{void}}{zRT}\right)_{cell} \tag{2.109}$$

$$V_{void} = \left(\frac{PV}{zRT}\right)_{pump} \Big/ \left(\frac{P}{zRT}\right)_{cell} \tag{2.110}$$

where P,V,z,R, T are pressure, volume, gas compressibility factor, universal gas constant, and temperature respectively. The void volume includes all the volume of the cell section excluding the adsorbent volume which is impenetrable to the helium gas. Helium gas injection into the adsorbent is done sequentially at different pressures to confirm the value of the adsorbent void volume; equilibrium is attained at each stage of injection before increasing the pressure.

At subsequent stages of injections, additional moles of gas injected Δn_{inj} equals the moles of gas in cell at final stage minus moles of gas in cell at initial stage:

$$\left(\frac{P\Delta V}{zRT}\right)_{pump} = V_{void}\left(\frac{P_f}{z_f RT} - \frac{P_i}{z_i RT}\right)_{cell} \tag{2.111}$$

$$V_{void} = \left(\frac{P\Delta V}{zRT}\right)_{pump} \Big/ \left(\frac{P_f}{z_f RT} - \frac{P_i}{z_i RT}\right)_{cell} \tag{2.112}$$

From literature, over a range of pressure, the void volume evaluated at several sequential injections of helium gas is usually of consistent value (Hall *et al*., 1994; Sudibandriyo *et al*., 2003; Gasem *et al*., 2003; Arumugam, 2004; Fitzgerald *et al*.,

2005; Mohammad, 2009). After void volume .evaluation, the equilibrium cell is then placed under vacuum to remove helium gas from the crushed sample and the void space. This paves the way for an effective and reliable measurement of the Gibbs adsorption value of gases such as CO_2, methane and nitrogen.

For single-component gas adsorption, a known quantity n_{inj} of gas from the pump is injected at given temperature and pressure into the cell; some of the gas is adsorbed n_{ads}^{Gibbs} while the unadsorbed n_{unads}^{Gibbs}s exist at equilibrium in the pore space in the cell. The equilibrium pressure in the cell is attained when no further change in pressure is observed (it usually takes about 6 to 12 hours, depending on the adsorption capacity of the adsorbent).

The amount adsorbed is usually expressed as an intensive property of the adsorbent (mol/g). Applying mass balance, moles of gas adsorbed equals moles of gas injected minus moles of gas unadsorbed:

$$n_{ads}^{Gibbs} = n_{inj} - n_{unads}^{Gibbs} \tag{2.113}$$

$$n_{ads}^{Gibbs} = \left(\frac{PV}{zRT}\right)_{pump} - \left(\frac{PV_{void}}{zRT}\right)_{cell} \tag{2.114}$$

Gas injection into the adsorbent is then continued sequentially at higher pressures to yield a complete adsorption isotherm. The experiment shows that Gibbs adsorption can be estimated directly from the laboratory measurement of temperature, pressure, and volume coupled with independent knowledge of the gas compressibility factor z.

In determining void volume, helium compressibility factor is evaluated as:

$$Z_{He} = 1 + \left\{\frac{\left(1.471*10^{-3}\right) - \left(4.779*10^{-6}T\right) + \left(4.927*10^{-9}T^2\right)}{P}\right\} \tag{2.115}$$

where T is temperature (K) and P is pressure (atmosphere). This empirical equation is based on laboratory data from the National Bureau of Standards Technical Note 631 for helium (McCarty, 1972) and as used by Hall (1993), Fitzgerald (2005) and Mohammad (2009).

However, compressibility factors of pure methane, CO_2 and nitrogen is often evaluated from accurate equations of state (Angus *et al*., 1978; Angus *et al*., 1979: Wagner, 1996).

2.7.1.2 Absolute (or Total) Gas Adsorption Measurement for Dry Samples

It should be noted that there was minimal adsorptionduring the injection of helium. The Gibbs adsorption estimation neglects the volume occupiedby the adsorbed phase in evaluating the amount of unadsorbed gas. Thus, this void volume would really be over-estimated if it is considered in the adsorption of gases like methane, CO_2 and nitrogen. This is because some portion of the Helium void volume would now be occupied by the adsorbed phase; in fact, the gas penetrates the adsorbent volume which is impenetrable to helium. Failure to make correction for this portion of the Helium void volume would result in an under-prediction of the adsorbed volume. When this correction is effected, the adsorption evaluated is termed "*absolute or total adsorption*". Hence, absolute adsorption is more than the Gibbs adsorption.

Applying mass balance to evaluate the amount adsorbed (mol/g), moles of gas injected equals moles of gas adsorbed plus moles of gas unadsorbed.

For the concept of helium injection process,

$$n_{inj} = n_{ads}^{Gibbs} + V_{void} \cdot \rho_{gas} \tag{2.116}$$

where ρ_{gas} is the density of the bulk gas phase. For gases such as CO_2, methane and nitrogen yields, the actual pore volume gas phase accounts for the reduction of volume accessible to the gas as a result of the volume occupied by the adsorbed phases:

$$n_{inj} = n_{ads}^{Absolute} + V_{gas} \cdot \rho_{gas} \tag{2.117}$$

Equating **Equations 2.116** and **2.117** gives:

$$n_{ads}^{Absolute} = n_{ads}^{Gibbs} + \left(V_{void} - V_{gas}\right)\rho_{gas} \tag{2.118}$$

However, the volume of the adsorbed phase V_{ads} can be expressed as:

$$V_{ads} = V_{void} - V_{gas} \tag{2.119}$$

V_{ads}can also be expressed in terms of the amount adsorbed and the average density of the adsorbed phase pads as:

$$V_{ads} = {n_{ads}^{Absolute}}/{\rho_{ads}} \tag{2.120}$$

Combining **Equations 2.118**, **2.119** and **2.120** yields:

$$n_{ads}^{Absolute} = n_{ads}^{Gibbs} + \frac{n_{ads}^{Absolute}}{\rho_{ads}} \cdot \rho_{gas} \tag{2.121}$$

$$n_{ads}^{Absolute}\left\{1 - \frac{\rho_{gas}}{\rho_{ads}}\right\} = n_{ads}^{Gibbs} \tag{2.122}$$

This shows that:

$$n_{ads}^{Gibbs} = V_{ads}(\rho_{ads} - \rho_{gas}) \tag{2.123}$$

Equation 2.121 clearly illustrates that absolute adsorption is more than the Gibbs adsorption.It should be noted that at low pressures, the correction from the Gibbs to the absolute adsorption is insignificant $(\rho_{ads} \ll \rho_{gas})$ but at higher pressures it becomes significant.

After making the correction on Gibbs adsorption and obtaining absolute adsorption, the data can be fit to one of several isotherm models that incorporate the concept of an adsorbed-phase volume (Heller & Zoback, 2014) to predict the adsorbed volume at any pressure. Examples of such models are the SLD approaches using Peng-Robinson EOS(Fitzgerald, 2005; Chen, 2007; Mohammad, 2009), the Elliott-Suresh-Donohue (ESD) EOS (Soule *et al*., 2001), and the Bender EoS (Ustinov *et al*., 2002).

2.7.2 Concept of Adsorbed Water for Modelling Wet Adsorption of Gas

The moisture content in shale (and coal) are categorised as adsorbed water in the micropores and the capillary water in the pores. ASTM Standard D3302 considers

water contentin principle as “not chemically combined”. Hence, for the purpose of modelling, any capillary water can also be considered as adsorbed though the SLD adsorption framework does not address capillary process separately.

2.7.3 Pure-Gas Adsorption Measurement for Wet Samples (Consideration of Gas Solubility in Water)

2.7.3.1 Gibbs and Absolute Gas Adsorption Measurement for Wet Samples

Here, the term “wet” is used to indicate saturation of core sample with adsorbed equilibrium moisture content and absence of water in the bulk gas phase (i.e. gas phase mole fraction $y_{water} = 0$). As usual, a known quantity of gas $n_{inj}$from the pump is injected at given temperature and pressure into the cell. However, apart from the adsorbed gas$n_{ads}^{Gibbs}$and the unadsorbed gas n_{unads}^{Gibbs}existing in the equilibrium bulk phase (gas) inthe cell, some of the gas n_{sol} are soluble in water/moisture.

Applying mass balance:

$$n_{ads}^{Gibbs} = n_{inj} - n_{unads}^{Gibbs} - n_{sol} \quad (2.124)$$

This shows that the amount of gas adsorbed in wet samples are lower when compared to that in dry samples. The mole fraction of gas soluble in water is expressed as:

$$x_{gas} = \frac{n_{sol}}{n_{water}} \quad (2.125)$$

where n_{water} is number of moles of water (mol/g). To evaluate the amount of gas soluble in water as a function of pressure, an empirical modelfor temperatures at 318.2 K or 319.3 K obtained from Amoco Corporationis often used (Mohammad, 2009):

$$x_{gas} = \frac{P}{a+bP+c^{\ 2}} \quad (2.126)$$

The values of the parameters a, b and c for each gas are listed in **Tables 2.4** and **2.5**. Methane and nitrogen exhibit small solubility in water while CO_2 displays remarkable solubility; hence, when evaluating gas solubility at other temperatures, **Equation 2.126**

and the parameters in **Tables 2.4** and **2.5** can be used for methane and nitrogen but not CO_2.

Table 2.4: Parameters for Gas Solubility in Water at 115 °F(Fitzgerald, 2005)

Gas	**Constants**		
	a (psia)	b	c (1/psia)
Methane	769000	150.4	-0.005369
Nitrogen	1480000	127.3	-0.000635
CO_2	39840	9.452	0.00833

Table 2.5: Parameters for Gas Solubility in Water at 318.2 Kor 319.3 K(Mohammad, 2009)

Gas	**Constants**		
	a (MPa)	b	c (1/MPa)
Methane	5302.07	150.4	-0.078
Nitrogen	10204.24	127.3	-0.09
CO_2	276.69	9.452	1.21

Gasem *et al*. (2003) and Mohammad (2009)used literature data (Weibe & Gaddy, 1940; King & Coan, 1971; Dhima *et al*., 1999)in constructing an empirical relationship for temperature range of 313.2 K to 383.2 K and pressure range of 0 to 15 MPa to evaluate the amount of CO_2 soluble in water at other temperatures. The data represented in the empirical function have average absolute deviation of 1.5%. The empirical relationship is expressed as:

$$x_{gas} = \frac{P}{a+(b_1+b_oT)P+(c_1+c_oT)P^2} \qquad (2.127)$$

The values of the parameters a, b_1, b_o, $c_1$and $c_o$are listed in **Tables 2.6** and **2.7**. After obtaining x_{gas}, n_{sol} is evaluated to arrive atn_{ads}^{Gibbs}. Note that the relationship of

$n_{ads}^{Gibbs}$and n_{ads}^{Gibbs} for dry samples holds also for wet samples.

Table 2.6: Parameters for CO_2-Water Solubility at104 °F to 167°F (Fitzgerald, 2005)

Gas	**Constants**				
	a (psia)	b_1	b_o(1/K)	c_1(1/psia)	c_o (1/psia.K)
CO_2	39480	-332.637	1.06683	0.132207	-0.000386758

Table 2.7: Parameters for $C0_2$-Water Solubility at 313.2 Kto 383.2 K (Mohammad, 2009)

Gas	**Constants**				
	a (MPa)	b_1	b_o(1\K)	c_1(1/MPa)	c_o (1/MPa.K)
CO_2	272.21	-332.637	1.06683	19.18	-0.05609

2.7.4 Gas Mixture Adsorption Measurement for Dry Samples

A molar amount $n^{total}$of a gas mixture having certain feedstock composition of each component a_i are prepared and injected into the equilibrium cell.

Similar to a single-component gas, multicomponent gas also occupies volume space either in the adsorbed or unadsorbed phase volume; i.e., **Equation 2.113** still holds and n_{ads}^{Gibbs} is determined. Thereafter, the composition of the gas mixture remaining in the void volume at equilibrium is determined by gas chromatographic (GC) analysis; about 20 $\mu L$of gas mixture sample is sent for GC analysis by a pneumatically-controlled sampling device in the air bath at the cell temperature. The mole fractions y_i of the unadsorbed gas mixture are determined; this paves the way for determining the molar fractions x_i of the adsorbed gas mixture. The compressibility factors of the injected gas mixture and unadsorbed gas mixture phases are evaluated using mixing rules.

For each component of the gas mixture, applying mass balance, moles of gas injected equals moles of gas adsorbed plus moles of gas unadsorbed:

$$a_i n^{total} = x_I(V_{ads}\rho_{ads}) + y_I\left(V_{unads}\rho_{gas}\right) \tag{2.128}$$

Thus it is evident that:

$$n_i^{Absolute} = x_I(V_{ads}\rho_{ads}) + y_I\left(V_{unads}\rho_{gas}\right) \tag{2.129}$$

After making the correction on Gibbs adsorption and obtaining absolute adsorption, the data can be fit to any EoS or the SLD approach using the ESDEoS.

2.7.5 Gas Mixture Adsorption Measurement for Wet Samples

As usual, apart from the adsorbed gas n_{ads}^{Gibbs} and the unadsorbed gas n_{unads}^{Gibbs}existing in the equilibrium bulk phase (gas) in the cell, some of the gas n_{sol} are soluble in water/moisture.

Applying mass balance:

$$a_i n^{total} = x_I(V_{ads}\rho_{ads}) + y_I\left(V_{unads}\rho_{gas}\right) - n_{sol} \qquad (2.130)$$

Gas-water solubility n_{sol} is evaluated to arrive at n_{ads}^{Gibbs}. As stated earlier, the relationship of $n_{ads}^{Gibbs}$and $n_{ads}^{Absolute}$ for dry samples holds also for wet samples.

2.8 EVALUATION OF GAS COMPRESSIBILITY FACTOR (Z-FACTOR)

Standing and Katz (1942) presented a generalised Z-factor chart which is a graphical correlation of Z-factor for natural gases as a function of the pseudo-reduced pressure and pseudo-reduced temperature. The ranges considered in Standing and Katz chart are $1.05 \leq T_{pr} \leq 3.0$ and $0 \leq P_{pr} \leq 15$. For the purpose of improving accuracy, many empirical equations and equations of state have been fit to the original Standing and Katz chart. These correlations are: Wichert and Aziz (1972) correlation (that considers effect of H_2S and CO_2 contaminants), Hall and Yarborough (1973) correlation (that offers an accurate representation of the Standing and Katz chart), Beggs and Brills(1974) correlation, Dranchuk-Purvis-Robinson (1974) correlation, Dranchuk and Abou-Kassem (1975) (that fits an eleven-constant EoS to the Standing and Katz data, and extrapolated this correlation to higher reduced pressures of the range $0 \leq P_{pr} \leq 20$) and Takacs (1976) correlation. Based on Takacs (1976) comparison of eight correlations representing the Standing and Katz (1942) chart, the Hall and Yarborough (1973), and the Dranchuk and Abou-Kassem (1975) equations give the most accurate representation for a wide range of temperatures and pressures. Both equations are valid for $1 \leq T_{pr} \leq 3$ and $0.2 \leq P_{pr} \leq 25\ to\ 30$. The Hall and Yarborough or Dranchuk and Abou-Kassem equation is recommended for the evaluation of the Z-factor of most natural gases. For sour gas, gas deviation factor can be calculated using Piper *et aI*. (1993) correlation, and Elsharkawy and Elkamel (2001) correlation.

The correlations developed for calculating pseudo-critical properties (pseudo-critical pressure and pseudo-critical temperature) are Standing (1981) correlation developed only for low molecular weight natural gases with minor amount of non-hydrocarbon gases; Sutton (1985) correlation for a wide range of natural gas (it considers high molecular weight natural gases which are rich in heptane plus with minor concentration of carbon dioxide and nitrogen, and no hydrogen sulphide); Ahmed (1989) correlation applicable for mixture with impurities such as N_2,CO_2, H_2S; Elsharkawy *et al*. (2000) correlation suitable for retrograde gases (gas condensates); and Guo and Ghalambor (2005) correlation valid for H_2S < 3%, N_2< 5%, and total content of inorganic compounds less than 7%.

Standing(1981) correlation gives consideration to both dry and wet hydrocarbon gases. For dry hydrocarbon gases ($\gamma_g < 0.75$) the correlation is stated as:

$$P_{pc} = 667 + 15.0\gamma_g - 37.5{\gamma_g}^2 \quad (2.131)$$

$$T_{pc} = 168 + 325\gamma_g - 12.5{\gamma_g}^2 \quad (2.132)$$

For wet hydrocarbon gases ($\gamma_g \geq 0.75$) the correlation is stated as:

$$P_{pc} = 706 + 51.7\gamma_g - 11.1{\gamma_g}^2 \quad (2.133)$$

$$T_{pc} = 187 + 330\gamma_g - 71.5{\gamma_g}^2 \quad (2.134)$$

where P_{pc} is in psi, T_{pc} is in ^{o}R and γ_g is the gas specific gravity which is expressed as the ratio of gas molecular weight to air molecular weight.

Sutton (1985) correlation is valid for $0.57 < \gamma_g < 1.68$ based on 264 different gas samples. Pseudo-critical pressure and pseudo-critical temperature in Sutton correlation are stated as:

$$P_{pc} = 756.8 - 131.0\gamma_g - 3.6{\gamma_g}^2 \quad (2.135)$$

$$T_{pc} = 169.2 + 349.5\gamma_g - 74.0{\gamma_g}^2 \quad (2.136)$$

Given the size of the database used in its development, Sutton's correlation is a good representative for all gas reservoirs (Blasingame, 1988).

Shale gas processing is often guided by gas compositions across a field (Bullin & Krouskop, 2008). Therefore, ethane and propane levels should be considered in choosing either Standing (1981) correlation or Sutton (1985) correlation for shale gas pseudo-critical properties evaluation.

2.9SHALE COMPOSITION

Shale gas reservoirs are defined as fine-grained,low- permeability sedimentary rocks rich in organic contents. Major components of shale formations are shale (containing fossil materials), mudstone (containing non-fossil materials), siltstone, fine-grained sandstone laminated with shale or mudstone, carbonate rocks, clay minerals and otherssuch as calcite and quartz (Crain, 2011). The different colours of shale samples are characterised by different clay contents, organic contents and other minerals. **Figure 2.12** shows shale samples in different colours.

Adsorbed gas constitutes a major portion of gas-in-place in shale gas reservoirs; capacities ranging from 20 to 85 % (Lancaster *et al.*, 1993). Clay content in shale formations (from 30 to 50 %) plays a major role in increasing adsorption capacity than the total organic carbon (TOC) content (often less than 5 %) (Ross & Bustin, 2008; Heller & Zoback, 2011).

The range of TOC content and adsorption status of tight-sand, shale and coalbed methane (CBM) gas reservoirs are shown in **Figure 2.13**.

Figure 2.12: Shale samples of different colours
(Merey, 2013)

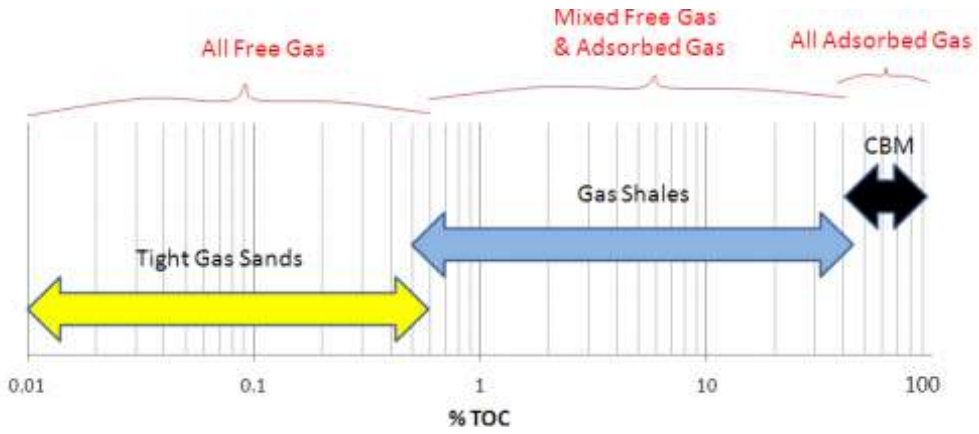

Figure 2.13: Ranges of TOC in tight-sand, shale and coalbed methane gas reservoirs (Promote UK, 2011)

2.10WORLD SHALE RESOURCE ASSESSMENTS

China leads the world in shale gas reserves, with over 1,115 Tscf, followed by Argentina, and Algeria(US EIA, 2015). However, United States and Canada lead the global production of shale gas. Other countries in the Americas with shale resources are Mexico and Argentina. Aside China, other countries in Asia with shale resources are Turkey, India, Indonesia and Pakistan. In Europe, countries with shale resources are Austria, Bulgaria, Denmark, France, Germany, Hungary, Ireland, Netherlands, Poland, Romania, Sweden, United Kingdom and Ukraine.In Africa, South Africa and Nigeria are prominent countries with shale gas reserves.

The major shale resource in South Africa is the Karoo Basin in central and southern regions. The Karoo basin extends across about two-thirds of the country(Catuneanua*et al*., 2005: Wickens & Cole, 2018).

In Nigeria shale gas resources are found mostly in the inland basins edge ofsouth-eastern and north-eastern regions i.e. the Benue trough and Borno basin (Avbovbo & Ayoola, 1981; Idowu & Ekweozor, 1993; Obaje & Abaa, 1996; Obaje *et al*., 2004). The Benue trough consists of the lower Benue (i.e. Anambra basin), the middle Benue and the upper Benue (i.e. Gongola and Yola sub-basins). Also, there are potential shale resources in the Niger Delta and Benin (Dahomey) basins. Recent studies show thatEze Aku and Ekenkpon shalesare found to be potential shale resources in the Abakaliki Fold Belt and Calabar Flank of the southeastern Nigeria (Oluwajana & Ehinola, 2018).

2.11 TECHNICALLY RECOVERABLE (NATURAL GAS) RESERVES IN THE UNITED STATES

The technically recoverable natural gas reserves base of the United States, as of the end of 2012, was reported to be 2,689 Tscf (Potential Gas Committee, 2013; National Energy Technology Laboratory, 2013). Shale gas contribution to this total was estimated as 1,073 Tscf.

The technically recoverable natural gas reserves in the United States are shown in **Figure 2.14**.

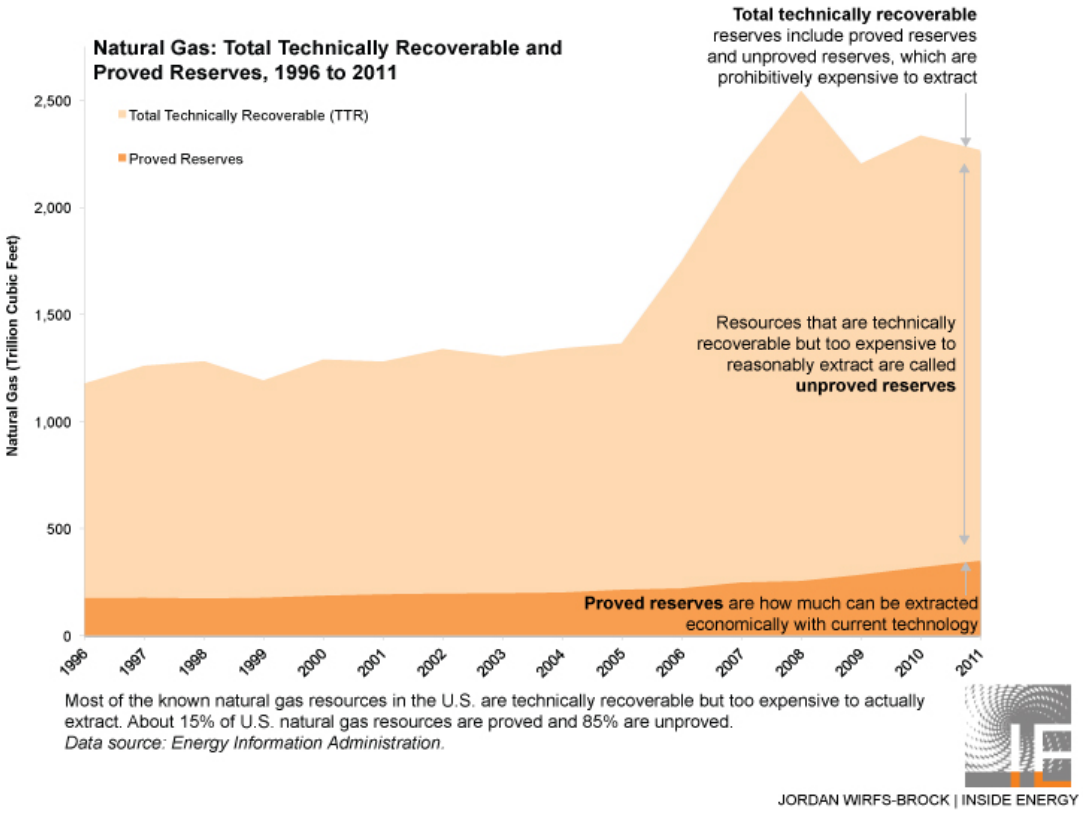

Figure 2.14: Technically recoverable natural gas reserves in the United States (U.S. Energy Information Administration, 2012)

2.12 OVERVIEW OF SOME U.S. SHALE GAS FORMATIONS

Because of the low-permeability nature of shale gas reservoirs, the use of hydraulic fracturing and horizontal drilling increases gas production. Thus it was projected that shale gas will be the major contributor to natural gas production in the United States (US EIA, 2013) as shown in **Figure 2.15**.

The reservoir characteristics and production history data used in this work are obtained from the Marcellus, Haynesville and Barnett shale gas fields; all in the UnitedStates of America. **Figure 2.16**shows an overview of the important United States shale formations. Though the distribution of oil and gas shale formations across the United States is much larger than those shown in the map, only a relatively small number of these are currently being developed (3-Legs Resources, 2011). **Figure 2.17**shows U.S. dry shale gas production.

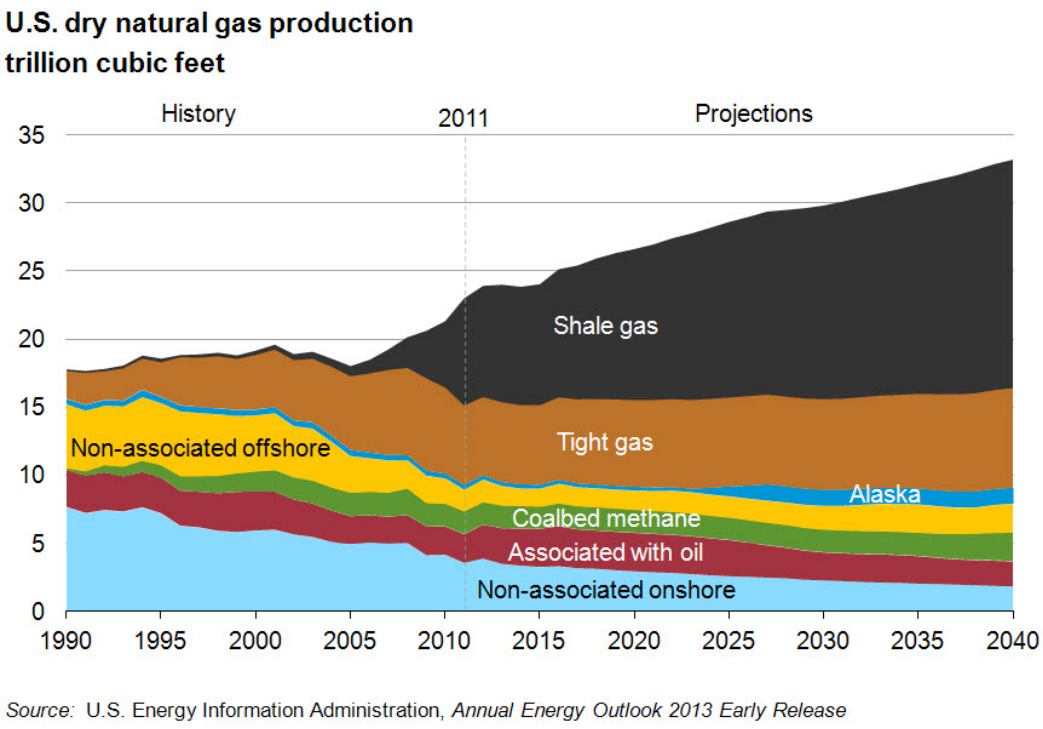

Source: U.S. Energy Information Administration, *Annual Energy Outlook 2013 Early Release*

Figure 2.15: Dry Natural Gas Production (Tscf) by Source in the United States (U.S. Energy Information Administration, 2013)

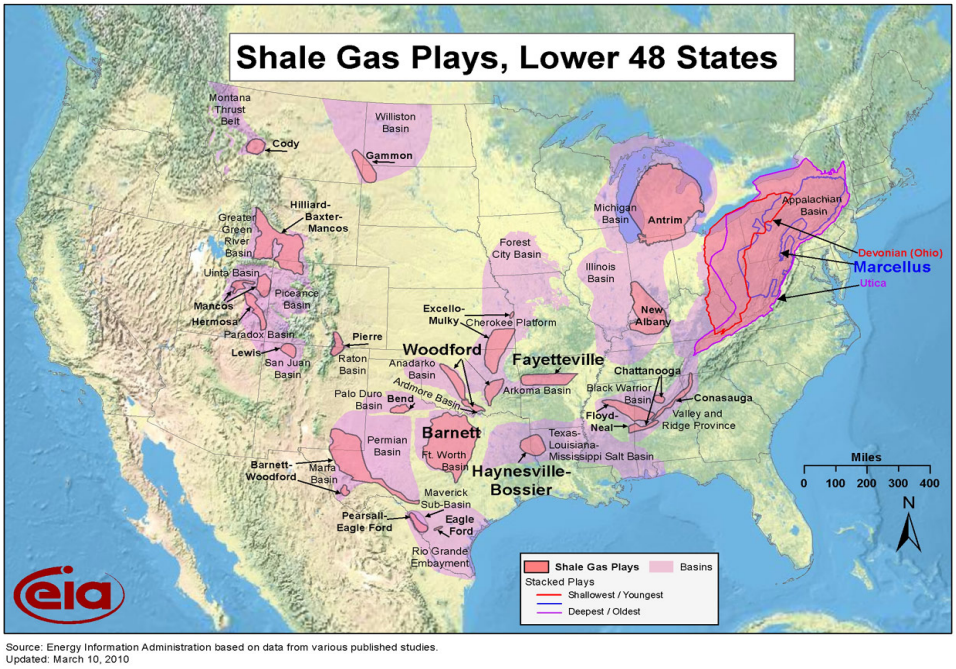

Source: Energy Information Administration based on data from various published studies.
Updated: March 10, 2010

Figure 2.16: Overview of Key US Shales
(U.S. Energy Information Administration.Updated: March 10, 2010)
Here, sedimentary basins, current plays and prospectivefuture plays are highlighted in purple,redand orange respectively.

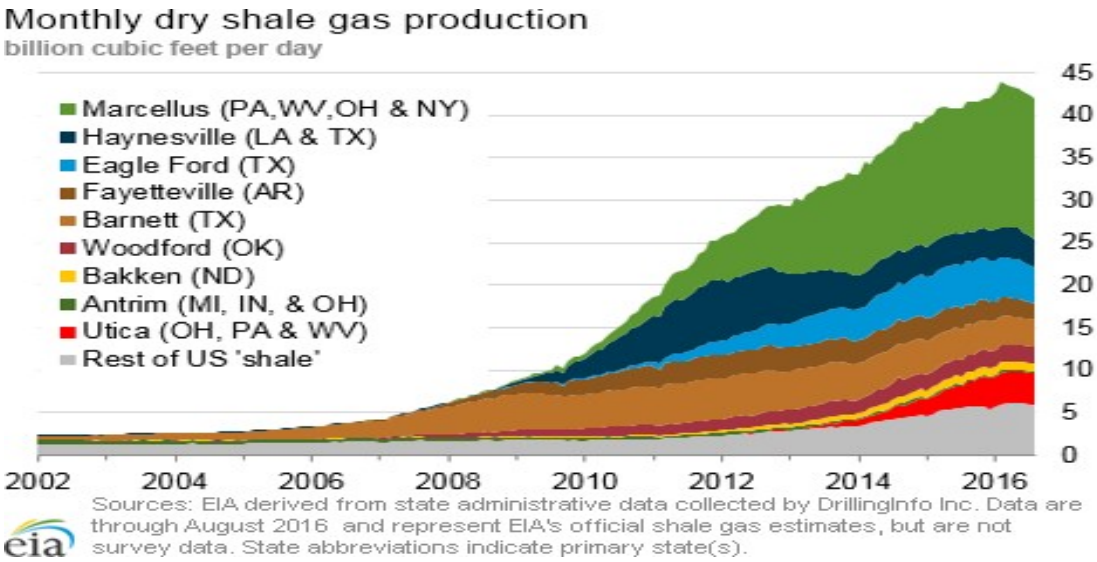

Figure 2.17: U.S. Dry Shale Gas Production
(US Energy Information Administration, 2016)

2.12.1 Marcellus Shale Formation

The-Marcellus shale formation consists of sedimentary rocks dating from the Middle Devonian age (387.7± 2.7 million years ago). It is located in eastern North America andderived its nomenclature from a distinctive outcrop near the village of Marcellus, New York, in the United States. Marcellus shale stretches across 104,067 square miles (US EIA, 2012) or 104,000 square miles (State Impact, 2017) in Pennsylvania, New York, Ohio and West Virginia in the north-eastern United States.Marcellus shale extends throughout much of the Appalachian Basin. Marcellus shale formation contains an estimated 1,500 Tscf of original free gas-in-place (US DoE, 2009). Matrix permeability ranges from 100 to 450 nanodarcy (Zhong, 2011).

Marcellus shale is a good candidate for energy development and export due to its nearness to the high-demand markets along the East Coast of the United States(Bailey, 2008). The depth is typically between 4000 to 8500 ft. Fracture porosity in the Marcellus formation ranges from 2.0% to 7.0%. Marcellus shale is bounded by the Hamilton group shale above and Tristates Group limestone below. It is between 50 to 200 feet thick. The very hilly terrain of the Appalachians poses a challenge in finding appropriate areas to drill in the Marcellus shale.

Black shale is the dominant lithology of the Marcellus shale formation; however, it also contains lighter shales and interbedded limestone layers (Harper *et al*., 2004). The black shale was deposited in comparatively deep water devoid of oxygen, and most fossils are contained in the limestone layers. The black shales also contain iron ore, uranium and pyrite. The geographical map of Marcellus shale formation is shown in **Figure 2.18**, while sampled shale gas composition is shown in **Table 2.8** (the compositions have been normalised to the reported compounds).

Figure 2.18:Geographical Map of Marcellus Shale Formation
(US Energy Information Administration, 2016)

Table 2.8: Marcellus shale gas composition (Hill *et al*., 2007; Bullin & Krouskop, 2008)

Well	Gas Composition (%)				
	C1	**C2**	**C3**	**CO_2**	**N_2**
1	79.4	16.1	4.0	0.1	0.4
2	82.1	14.0	3.5	0.1	0.3
3	83.8	12.0	3.0	0.9	0.3
4	95.5	3.0	1.0	0.3	0.2

2.12.2 Haynesville Shale Formation

The Haynesville shale formation is a black, organic-rich shale of Upper Jurassic age underlying considerable part of the Gulf Coast area of the United States. It was deposited about 150 million years ago in a shallow offshore environment. The formation runs through north-western Louisiana, north-eastern Texas and the south-western tip of Arkansas. It is underlain by the Smackover formation and overlain by rocks of the Cotton Valley group. (Geoscience News and Information, 2016).

Haynesville shale stretches across 9,000 square miles (US DoE, 2009). Haynesville shaleformation contains an estimated 717 Tscf of original free gas-in-place (US DoE, 2009). The Haynesville is the deepest, hottest, and highest pressured shale among the four big shale formations (the others are Barnett, Fayetteville and Marcellus). In Haynesville shale formation, wells are drilled to approximately 10,000 feet to 13,500 feet deep. Due to its very deep and thick formation, the Haynesville shale is expected to produce more than the Barnett shale by the year 2020 (Oil and Gas Journal, 2016). The geographical map of Haynesville shale formation is shown in **Figure 2.19**, while field average shale gas composition is shown in **Table 2.9** (the compositions have been normalised to the reported compounds).

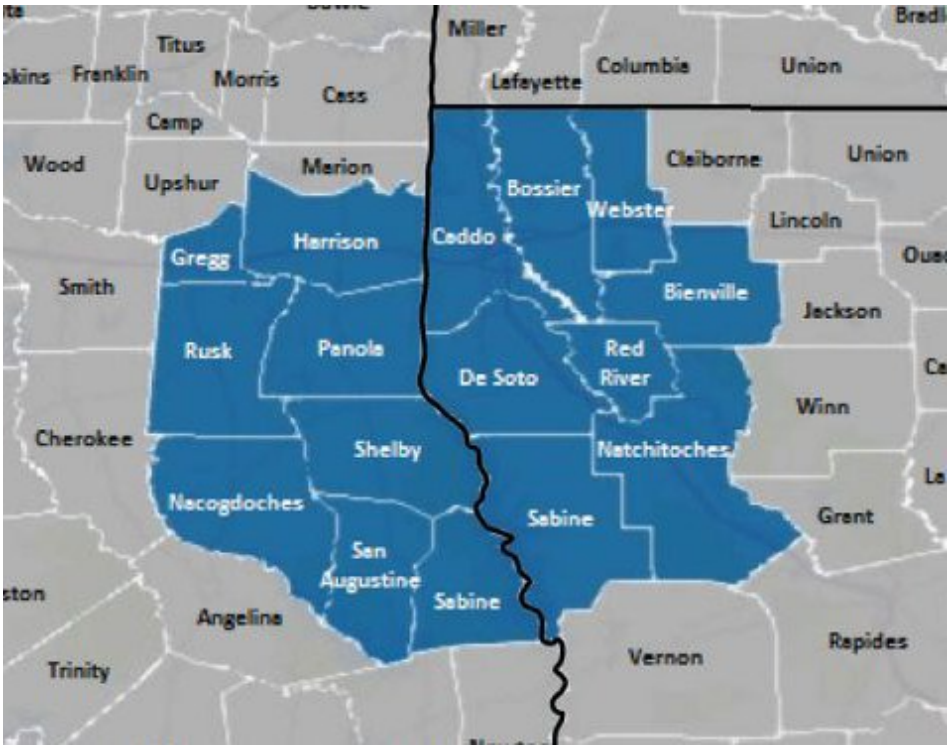

Figure 2.19: Geographical Map of Haynesville Shale Formation
(Energy Information Administration, 2016)

Table 2.9: Haynesville shale gas composition
(Hill *et al*., 2007; Bullin & Krouskop, 2008)

Well	**Gas Composition (%)**				
	C1	**C2**	**C3**	**CO_2**	**N_2**
Average	95.0	0.1	0	4.8	0.1

2.12.3 Barnett Shale Formation

The Barnett shale formation is located in the Bend Arch-Fort Worth Basin. North Texas, in the United States. It consists of sedimentary rocks dating from the Mississippi an period (354 to 323 million years ago). The formation underlies 5,000 square miles spanning the city of Fort Worth and at least 17 counties (US DoE, 2009). Barnett shaleformation contains an estimated 327 Tscf of original free gas-in-place (US DoE, 2009). Barnett shale ranges between 6500 to 8500 feet in depth. Barnett shale is bounded by Marble and Chappel limestone. It is between 100 to 600 feet thick. The Barnett shale is the largest active onshore natural gas field in Texas and one of the largest in the United States. Barnett shale is predominantly a natural gas field; however, it also contains some oil and condensate. One unique feature of the Barnett shale is that much of it is located in a highly urbanised area.The geographical map of Barnett shale formation is shown in **Figure 2.20**, while sampled shale gas composition is shown in **Table 2.10** (the compositions have been normalised to the reported compounds).

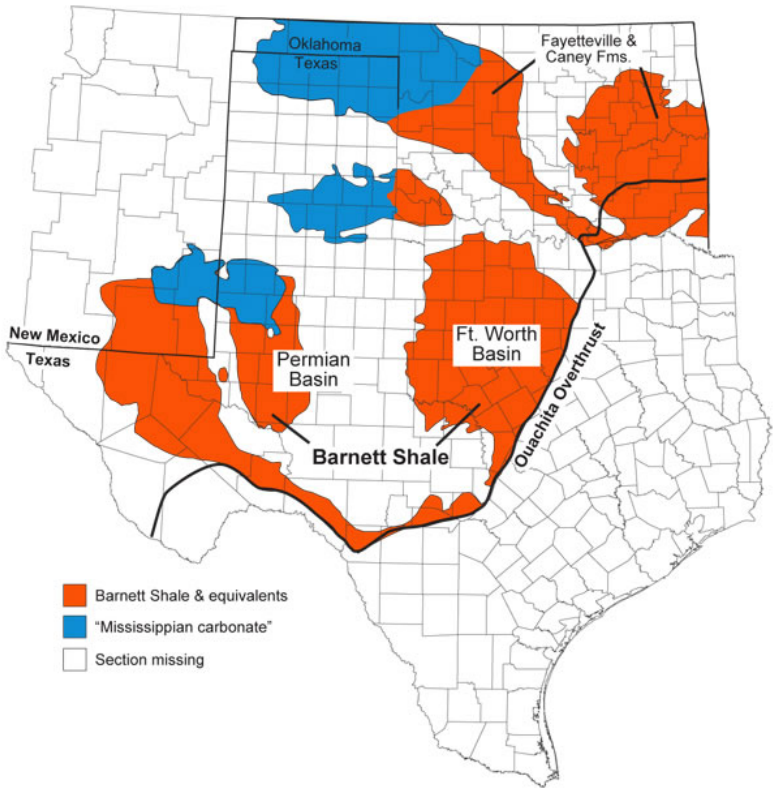

Figure 2.20: Geographical Map of Barnett Shale Formation
(US Energy Information Administration, 2016)

Table 2.10: Barnett shale gas composition (Hill *et al*., 2007; Bullin & Krouskop, 2008)

Well	Gas Composition (%)				
	C1	**C2**	**C3**	**CO_2**	**N_2**
1	80.3	8.1	2.3	1.4	7.9
2	81.2	11.8	5.2	0.3	1.5
3	91.8	4.4	0.4	2.3	1.1
4	93.7	2.6	0.0	2.7	1.0

2.12.4 Comparison of Gas Shale and Shale Gas Data

Reservoir volumetric data for the Marcellus, Haynesville and Barnett gas shales are shown in **Table 2.11** (Note that 1 square mile = 2.58998811 square kilometers). Also, the decline curves (well production history) of major shale formations in the United States are shown in **Figure 2.21**.

Table 2.11: Comparison of data for Marcellus, Haynesville and Barnett gas shales (US DOE, 2009;State Impact, 2017)

Gas Shale Basin	Marcellus	Haynesville	Barnett
Reservoir Area (mile^2)	104,000	9,000	5,000
Reservoir Area (km^2)	268,359	23,310	12,950
Depth (ft.)	4,000 – 8,500	10,500 – 13,500	6,500 – 8,000
Net Thickness (ft.)	25 – 250	100 – 300	100 – 600
Total Organic Carbon (%)	3 – 12	0.5 – 4.0	4.5
Total Porosity (%)	10	8 – 9	4 – 5
Gas Content (scf/ton)	60 – 100	100 - 330	300 – 350
OGIP (Free Gas) (Tscf)	1,500	717	327

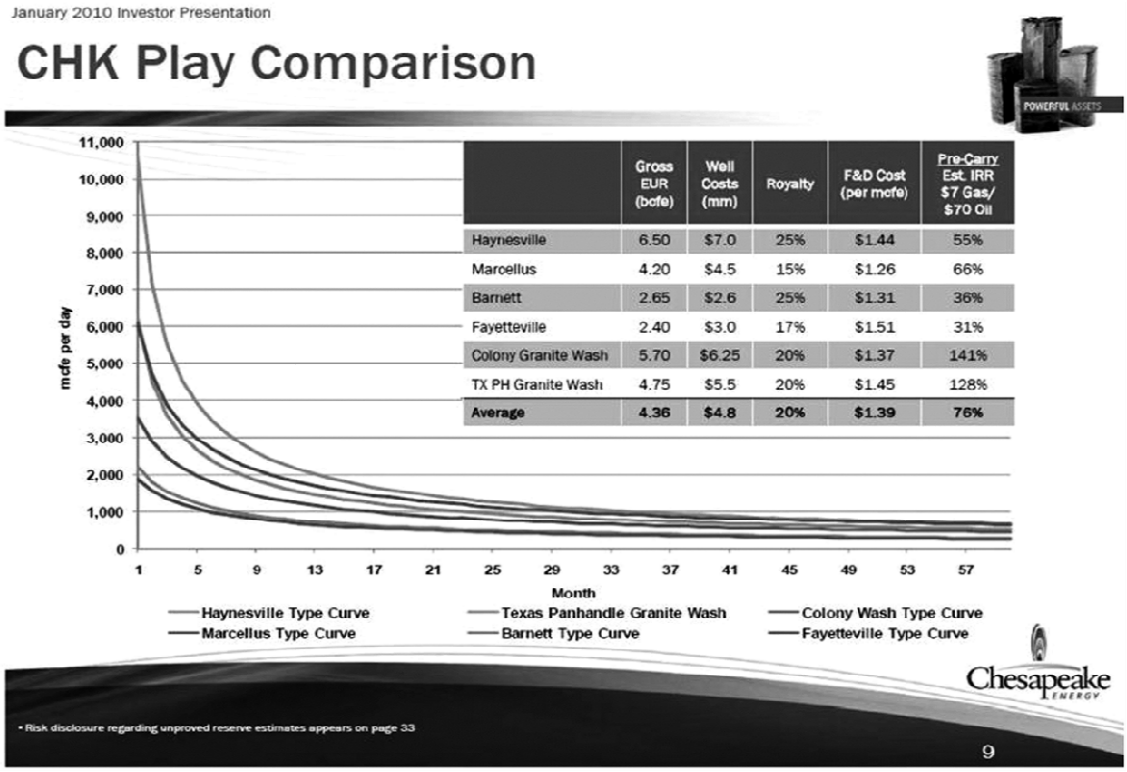

	Gross EUR (bcfe)	Well Costs (mm)	Royalty	F&D Cost (per mcfe)	Pre-Carry Est. IRR $7 Gas/ $70 Oil
Haynesville	6.50	$7.0	25%	$1.44	55%
Marcellus	4.20	$4.5	15%	$1.26	66%
Barnett	2.65	$2.6	25%	$1.31	36%
Fayetteville	2.40	$3.0	17%	$1.51	31%
Colony Granite Wash	5.70	$6.25	20%	$1.37	141%
TX PH Granite Wash	4.75	$5.5	20%	$1.45	128%
Average	**4.36**	**$4.8**	**20%**	**$1.39**	**76%**

Figure 2.21: Well Production History of Major Shale Formations in the United States (Chesapeake Energy, 2010)

2.13 CONCLUDING REMARKS ON LITERATURE REVIEW

From the literature review, it has been stated that Langmuir isotherm (representing Type I Isotherm) is the only isotherm used in modelling monolayer adsorptions, and also most often used when incorporating gas desorption into gas Material Balance Equation (MBE) despite the fact that it could not define the onset of adsorption saturation pressure (P_s)thereby yielding over-estimation at higher pressures thus contradicting the description of Type I isotherm. Here, higher pressures refer to pressures above the adsorption saturation pressure.

To correct the overestimation of adsorbed/desorbed volume that Langmuir isotherm presents, a truly Type I gas adsorption isotherm that incorporates adsorption saturation pressure into its framework should be developed. To the best of my knowledge, developing aType I gas adsorption isotherm that incorporates adsorption saturation pressure has not been reported in literature; thus the task is considered in this study.

Coupled with the proposed adsorption isotherm, modification of the gas deviation factor (Z-factor) in the traditional material balance equation (MBE) is needed to give a true account of the geomechanic effects of matrix porosity before fracturing (ϕ'_{mat}) and fracture porosity (ϕ_{frac})on gas production.

Further, decline rate model obtained from shale gas well production history, and average change of cumulative gas production with pressure depletion in the material balance analysis should be used in developing the proposed isotherm-based and Langmuir isotherm-based rate decline models for production performance forecast correlation.

In this work, local content consideration would have been preferred. However, laboratory shale gas adsorption isotherm data has not been generated for Nigerian shale

formationsand there is no shale gas production history yet. Hence, shale gas formations in the United States are considered.

CHAPTER THREE

METHODOLOGY

3.1 DEVELOPMENT OF THE NEW GAS ADSORPTION ISOTHERM

3.1.1 Basis for Developing a Truly Type I Adsorption Isotherm

As stated earlier, in unconventional gas reservoirs, flow of free gas from the fracture system into the wellbore causes gas transport into the fractures from the matrix pores. Subsequent pressure drop below a threshold weakens the van der Waal's forces and adsorption energy causinggas desorption from the matrix surface into the matrix pores.

This shows that a constant value of the adsorbed volume is maintained during pressure depletion from the initial reservoir pressure P_i down to the adsorption saturation pressure P_s; and gas desorption commences when the pressure is lower than P_s. This is depicted by Type I adsorption isotherm.

Langmuir isotherm (the only Type I adsorption isotherm in use) states that the adsorbed volume:

$$V = V_L \cdot \left(\frac{P}{P+P_L}\right) \tag{3.1}$$

where V is volume of gas adsorbed per unit mass of adsorbent (scf/ton) at any given equilibrium pressure P; V_L is the Langmuir volume (the maximum adsorbed volume per unit mass of adsorbent (scf/ton); and P_L is the Langmuir pressure(i.e.the pressure at half the Langmuir volume, $\frac{V_L}{2}$).

This implies that V_L is attained when $P \gg P_L$,i.e. at infinite P. Hence, Langmuir isotherm exhibits an over-estimation of adsorbed/desorbed volume at higher pressures. The ambiguity surrounding the onset of adsorption saturation pressure in Langmuir isotherm does not reflect the practical reservoir conditions (as explained above).

3.1.2 Physical Depiction of Adsorption in the New Model

The physical depiction (schematic) of adsorption of the molecules of a fluid F in the new model is shown in **Figure 3.1**.

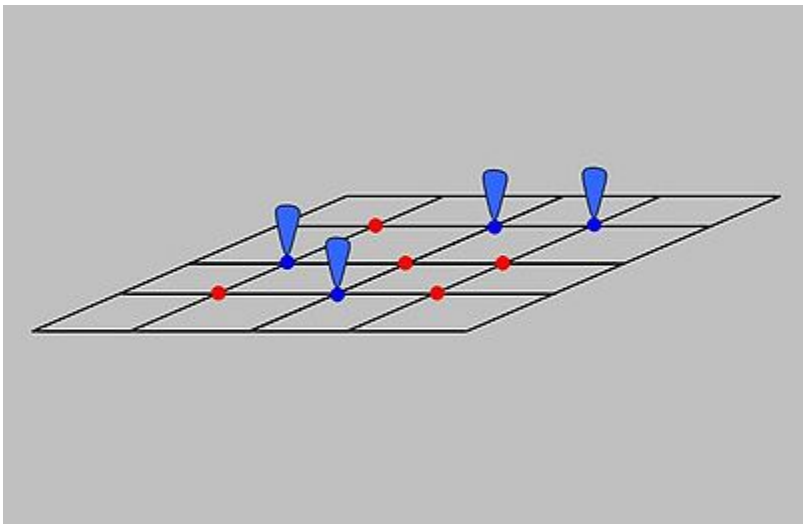

Figure 3.1: Schematic of adsorption in the newmodel (Langmuir, 1916). Here, the occupied surface sites are denoted as blue clips while vacant surface sites are denoted as red spots on the surface.

3.1.3 Assumptions

The basic assumptions made here are similar to those of Langmuir isotherm. The model assumes an ideal surface where:

1. Solid surface is composed of localised adsorption sites, and each site can only hold one adsorbate molecule
2. Adsorption sites are energetically equivalent i.e. the surface is homogeneous and all sites are identical
3. Saturation coverage is attained when all sites are completely occupied
4. Adsorption of molecules is of monolayer type, and
5. Adsorption is reversible i.e. desorption occurs during pressure depletion

However, Langmuir isotherm's assumptions of no adsorbate-adsorbate interactions and adsorption coverage being independent of the heat (enthalpy) of adsorptionare faulted in the new isotherm. Hence, additional (major) assumptions included are:

1. Adsorbate-adsorbate interactions exist between neighbouring adsorption sites.
2. Consideration of dynamic equilibrium parameter as not being constant (as opposed to Langmuir isotherm's assumption)because adsorption coverage actually depends on the enthalpy of adsorption (and saturation pressure is an index of adsorption coverage).
3. Attainment of a definite adsorption saturation pressure - the threshold pressure of remarkable significance for both gas adsorption (as pressure increases) and the commencement of gas desorption (during pressure depletion).

3.1.4Development of the New Adsorption Isotherm: Kinetic Approach

In the adsorption of the molecules of a fluid phase$F$, the concentration of the occupied surface site is denoted as $[S_{ads}]$ (number/area) while the vacant surface sites concentration is denoted as $[S_{vac}]$.

Total site concentration is:

$$[S_T] = [S_{ads}] + [S_{vac}] \text{ (number/area).} \tag{3.2}$$

Rate of adsorption R_{ads} is proportional to the adsorption potential of the fluid (at pressure P) towards saturation coverage of the surface. The saturation coverage is of course attained when all sites $[S_T]$ are completely occupied.Attractive interactions causing adsorption are characterised by adsorbates losing activation energy, thus adsorption is an exothermic reaction. Hence,

$$R_{ads} = \beta_{ads} \cdot P[S_T] \tag{3.3}$$

where adsorption rate parameter β_{ads} is expressed as an Arrhenius relation:

$$\beta_{ads} = K_{ads_o} \cdot exp\left(\frac{-E}{RT}\right) \tag{3.4}$$

and K_{ads_o} is adsorption rate coefficient at the onset of adsorption, E is interaction energy (i.e., heat or enthalpy of adsorption) between the gas molecules and the solid sites, R is universal gas constant and T is temperature.

On the other hand, rate of desorption R_{des} is proportional to the difference between the desorption potential of the fluid (at the adsorption saturation pressureP_s) towards partial coverage of the surface$[S_{ads}]$, and the adsorption potential at a lower pressure P.

$$R_{des} = K_{des} \cdot \{P_s[S_{ads}] - P[S_T]\} \tag{3.5}$$

whereK_{des} is desorption rate coefficient,P_s is the adsorption saturation pressure, the pressure at which adsorbed volume saturation is attained (as pressure increases) and the commencement of gas desorption (during pressure depletion).

The dynamic equilibrium parameter is expressed as:

$$K_{eq}^{f} = \frac{\beta_{ads}}{K_{des}} = \frac{K_{ads_o}}{K_{des}} \cdot exp\left(\frac{-E}{RT}\right) \tag{3.6}$$

It should be noted that K_{eq}^{f} is only constant if adsorption coverage is assumed to be independent of the enthalpy of adsorption$E$as done in Langmuir isotherm derivation. However, here, K_{eq}^{f} is not considered constant because adsorption coverage actually depends on the enthalpy of adsorption$E$ (adsorption saturation pressure isan index of adsorption coverage).

At dynamic equilibrium, rate of adsorption equals rate of desorption. Hence, the dynamic equilibrium parameter is expressed as:

$$K_{eq}^{f} = \frac{\beta_{ads}}{K_{des}} = \frac{\{P_s[S_{ads}] - P[S_T]\}}{P[S_T]} \tag{3.7}$$

$$K_{eq}^{f} = \frac{P_s[S_{ads}]}{P[S_T]} - 1 \tag{3.8}$$

$$\frac{P_s[S_{ads}]}{P[S_T]} = 1 + K_{eq}^{f} \tag{3.9}$$

$$\frac{[S_{ads}]}{[S_T]} = \frac{P\left(1+K_{eq}^{f}\right)}{P_s} \tag{3.10}$$

Expressing the occupied sites $[S_{ads}]$ as the adsorbed volume V at pressure P, and the concentration of all sites $[S_T]$ as the maximum adsorbed volume V_{max} at and above the onset of adsorption saturation pressure i.e. $P \geq P_s$; then

$$\frac{V}{V_{max}} = \frac{P\left(1+K_{eq}^{f}\right)}{P_s} \tag{3.11}$$

where K_{eq}^{f} is a measure of the pressure deviation from the corresponding linear isotherm pressure.

$$V = V_{max}\left(\frac{P+K_{eq}^{f}P}{P_s}\right) \tag{3.12}$$

Expressing $K_{eq}^{f}P$ as P_a the pressure deviation from the corresponding linear isotherm pressure, then

$$V = V_{max}\left(\frac{P}{P_s} + \frac{P_a}{P_s}\right) \quad (3.13)$$

(1) For under-saturated adsorption, i.e. when $0 \leq P < P_s$

The pressure deviation from the corresponding linear isotherm pressure is proportional to pressure deviation from the adsorption saturated pressure:

$$P_a = k(P_s - P) \quad (3.14)$$

where k is a dynamic parameter expressed as:

$$k = \left(\frac{P}{P_s}\right)^n \quad (3.15)$$

and n is adsorbate-adsorbent resistance parameter.

Hence,

$$P_a = (P_s - P)\left(\frac{P}{P_s}\right)^n \quad (3.16)$$

And K_{eq}^f is further simplified as:

$$K_{eq}^f = \left(\frac{P}{P_s}\right)^{n-1} - \left(\frac{P}{P_s}\right)^n \quad (3.17)$$

This shows that the dynamic equilibrium parameterK_{eq}^f is a function of pressure P and adsorption saturation pressure P_s: as P changes, K_{eq}^f also changes unlike the case in Langmuir isotherm derivation where K_{eq}^f is considered constant irrespective of the level of$P$.

It should be noted that when there is no adsorption, $P = 0$ and thus $P_a = 0$. Also, at the onset of adsorption saturation pressure $P = P_s$ and thus $P_a = 0$. Substituting **Equation 3.16** into **Equation 3.13** gives:

$$V = V_{max}\left\{\frac{P}{P_s} + \left(1 - \frac{P}{P_s}\right)\left(\frac{P}{P_s}\right)^n\right\} \quad (3.18)$$

where V is the adsorbed volume at pressure P, V_{max} is the maximum adsorbed volume at and above the saturation pressure, and n is adsorbate-adsorbent resistanceparameter (n ranges from 0.30 to 1.15).

(2) For saturated adsorption, i.e. when $P \geq P_s$

The adsorption saturated pressure P_s is the effective pressure while additional increase in pressure is latent; hence, the heat of adsorption $E = 0$. Thus

$$V = V_{max} \tag{3.19}$$

3.1.5Statement of the Developed Adsorption Isotherm

The developed adsorption isotherm is stated as follows:

$$V = \begin{Bmatrix} V_{max}\left\{\frac{P}{P_s} + \left(1 - \frac{P}{P_s}\right)\left(\frac{P}{P_s}\right)^n\right\}, for\ P < P_s\ i.e. undersaturated\ adsorption \\ V_{max}, \quad for\ P \geq P_s\ i.e. saturated\ adsorption \end{Bmatrix}$$

(3.20)

where V is the adsorbed volume at equilibrium pressure P, P_s is the adsorption saturation pressure at which the maximum adsorbed volume V_{max} is attained, n is adsorbate-adsorbent resistance parameter (n ranges from 0.30 to 1.15).

3.1.6Establishment of Boundary Conditions for the Developed Adsorption Isotherm

The graphical analysis of establishing boundary conditions for the developed adsorption isotherm is shown in **Figure 3.2**.

For an adsorbed volume V, point C on the isotherm is projected downwards to meet line $\overline{OA}$ at D and the pressure axis at E. The volume deviation from the corresponding linear isotherm volume is $\overline{CD} = \delta$.

Along $\overline{OA}$,

$$slope = \frac{\overline{DE}}{\overline{OE}} = \frac{\overline{AB}}{\overline{OB}} \tag{3.21}$$

but

$$\overline{DE} = \overline{CE} - \overline{CD} \tag{3.22}$$

i.e.

$$\overline{DE} = V - \delta \tag{3.23}$$

Hence,

$$slope = \frac{V-\delta}{P} = \frac{V_{max}}{P_s} \tag{3.24}$$

$$\frac{V-\delta}{V_{max}} = \frac{P}{P_s} \tag{3.25}$$

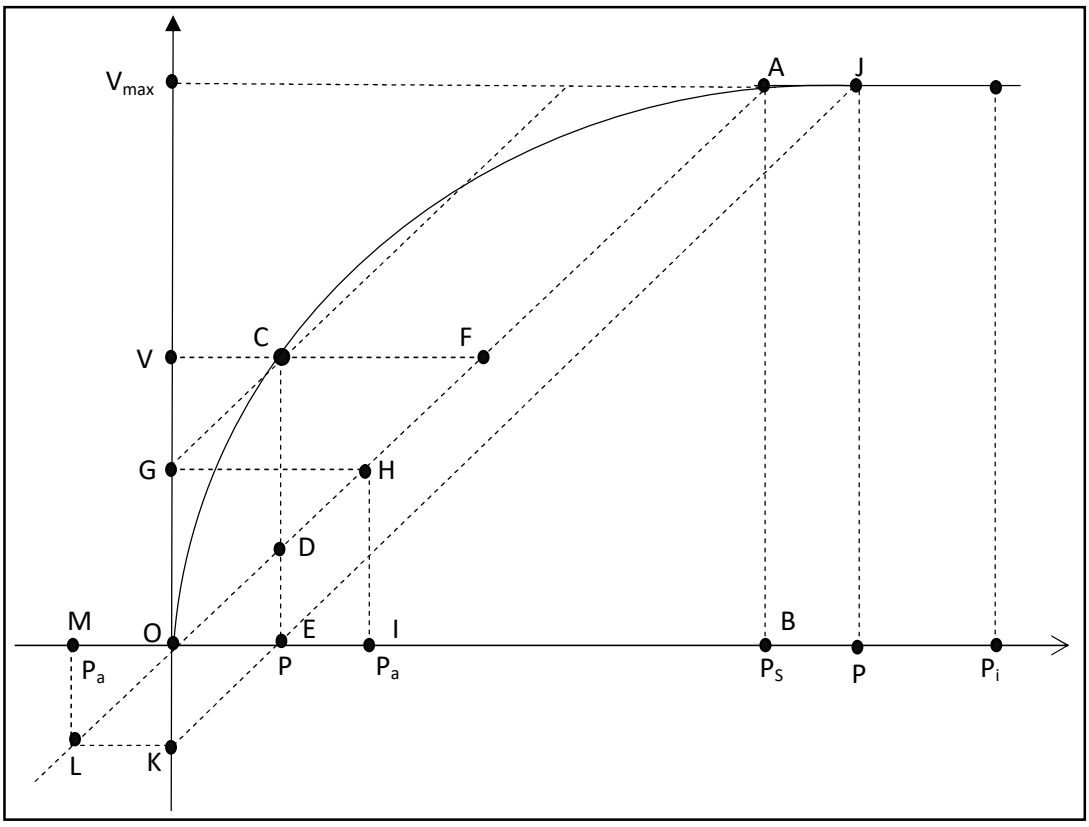

Figure 3.2: Graphical analysis of the developed adsorption isotherm

$$\frac{V}{V_{max}} = \frac{P}{P_s} + \frac{\delta}{V_{max}} \tag{3.26}$$

Point C on the isotherm is again projected horizontally to meet $\overline{OA}$ at F. Also, at C a line of equal slope as $\overline{OA}$ is projected to intercept the volume axis at G, and meet $\overline{OA}$ and the pressure axis atH and I respectively. The pressure deviation from the corresponding linear isotherm pressure is $\overline{CF} = P_a$.

$$P_a = \overline{CF} = \overline{GH} = \overline{OI} \tag{3.27}$$

Also,

$$\delta = \overline{CD} = \overline{GO} = \overline{HI} \tag{3.28}$$

Along $\overline{OA}$,

$$slope = \frac{\overline{HI}}{\overline{OI}} = \frac{\overline{AB}}{\overline{OB}} \tag{3.29}$$

$$\frac{\delta}{P_a} = \frac{V_{max}}{P_s} \tag{3.30}$$

$$\frac{\delta}{V_{max}} = \frac{P_a}{P_s} \tag{3.31}$$

Substituting **Equation 3.30** into **Equation 3.25** gives:

$$\frac{V}{V_{max}} = \frac{P}{P_s} + \frac{P_a}{P_s} \tag{3.32}$$

i.e.

$$V = V_{max}\left(\frac{P+P_a}{P_s}\right) \quad (3.33)$$

3.1.6.1 Establishment of Boundary Conditions for P_a

Boundary conditions forP_a, the pressure deviation from the corresponding linear isotherm, is highlighted thus:

1. $P_a = 0$ at $P = 0$ and $P = P_s$
2. $P_a > 0$ within the pressure range $0 < P < P_s$
3. P_a is maximum ($\frac{dP_a}{dP} = 0$) i.e.

$$\frac{d}{dP}\left\{(P_s - P)\left(\frac{P}{P_s}\right)^n\right\} = 0 \quad (3.34)$$

at the inflexion point β of the isotherm within the pressure range $0 < P < P_s$. At the inflexion point β,

$$\Delta\left(\frac{V}{V_{max}}\right) = \Delta\left(\frac{P}{P_s}\right) \quad (3.35)$$

4. For saturated adsorption, i.e. when $P > P_s$, at J (see **Figure 3.2**), a line of equal slope as $\overline{OA}$ is projected to intercept the volume axis at K and meet $\overline{OA}$ extension and the pressure axis at L and M respectively.

$$P_a = \overline{OM} = \overline{KL} = -\overline{AJ} \quad (3.36)$$

$$P_a = -(P - P_s) \quad (3.37)$$

$$P_a = P_s - P \quad (3.38)$$

and

$$V = V_{max} \quad (3.39)$$

3.1.7Plot of Relative Adsorbed Volume versus Relative Pressure for the Developed Adsorption Isotherm

For pressure range below adsorption saturation pressure ($P < P_s$), the developed adsorption isotherm

$$\frac{V}{V_{max}} = \left\{\frac{P}{P_s} + \left(1 - \frac{P}{P_s}\right)\left(\frac{P}{P_s}\right)^n\right\} \quad (3.40)$$

could be expressed as:

$$Y = \{X + (1 - X)(X)^n\} \quad (3.41)$$

A plot of Y versus X is shown in **Figure 3.3**.The major representatives of Type I adsorption isotherm pressure-volume data (below the adsorption saturation pressure) arecaptured and depicted by the adsorbate-adsorbent resistance parameter n ranging from 0.30 to 1.15.

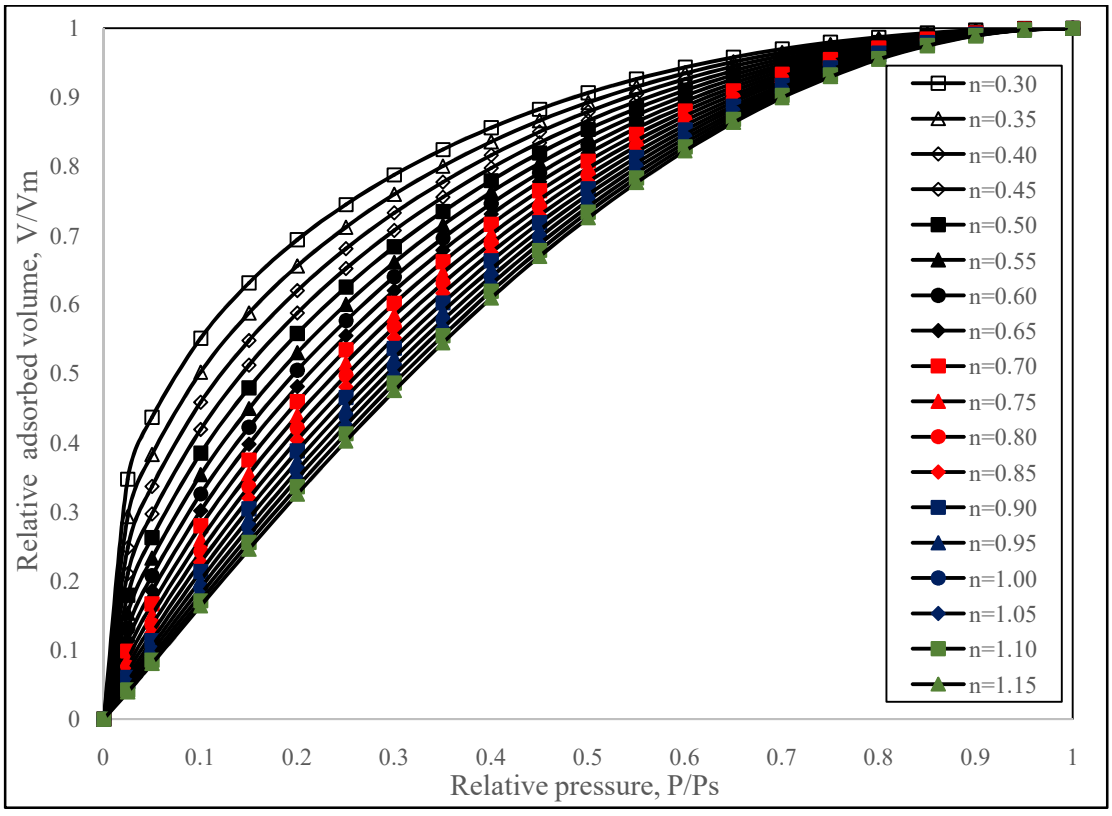

Figure 3.3: Plot of relative adsorbed volume (V/V_{max}) versus relative

pressure(P/P_s) for the developed adsorption isotherm

3.2PARAMETERISATION OF EXPERIMENTAL ADSORPTION DATA

3.2.1 Parameterisation of Experimental Adsorption Data using the Developed Isotherm

The steps involved in the developed isotherm parameters evaluation from experimental data are as highlighted below:

1. Produce the experimental adsorption isotherm by plotting the adsorbed volume V versus pressure P.
2. Compare and match the experimental isotherm with the relative adsorbed volume–relative pressure curve (see **Figure 3.3**) and select a few adsorbate-adsorbent resistance parameter$n$ of closer range.
3. For each n selected, feature the corresponding parameters

$$b = \frac{V_{last}}{V_{max}} \tag{3.42}$$

and

$$c = \frac{P_{last}}{P_s} \tag{3.43}$$

(see **Tables 3.1, 3.2** and **3.3**) where P_{last}, V_{last} are the last P,V values of the experimental adsorption data.Thus evaluate the corresponding

$$V_{max} = \frac{V_{last}}{b} \tag{3.44}$$

and

$$P_s = \frac{P_{last}}{c} \tag{3.45}$$

and the pressure P_β, and adsorbed volume V_β at the inflexion point β where

$$\Delta\left(\frac{V}{V_{max}}\right) = \Delta\left(\frac{P}{P_s}\right) \tag{3.46}$$

on the proposed isotherm (see **Table 3.4**). Note that

$$\frac{V_{last}}{V_{max}} = \left\{\frac{P_{last}}{P_s} + \left(1 - \frac{P_{last}}{P_s}\right)\left(\frac{P_{last}}{P_s}\right)^n\right\} \qquad (3.47)$$

The details of the derivation of the pressure P_β, and adsorbed volume V_β at the inflexion point β where $\Delta\left(\frac{V}{V_{max}}\right) = \Delta\left(\frac{P}{P_s}\right)$ on the developed isotherm are shown in **Appendix C**.

Table 3.1: Table of adsorption saturation data for establishingthe boundary conditions of the developed isotherm ($n = 0.30$ to $n = 0.55$)

$\boldsymbol{b = \frac{V_{last}}{V_{max}}}$	$\boldsymbol{c = \frac{P_{last}}{P_s}}$					
	$n = 0.30$	$n = 0.35$	$n = 0.40$	$n = 0.45$	$n = 0.50$	$n = 0.55$
0.920	0.5339	0.5621	0.5853	0.6049	0.6218	0.6365
0.925	0.5470	0.5746	0.5974	0.6166	0.6331	0.6474
0.930	0.5607	0.5877	0.6100	0.6287	0.6448	0.6588
0.935	0.5751	0.6014	0.6231	0.6413	0.6570	0.6706
0.940	0.5901	0.6157	0.6368	0.6545	0.6697	0.6830
0.945	0.6060	0.6308	0.6512	0.6684	0.6831	0.6959
0.950	0.6227	0.6467	0.6664	0.6830	0.6972	0.7095
0.955	0.6405	0.6636	0.6825	0.6984	0.7120	0.7238
0.960	0.6594	0.6815	0.6996	0.7148	0.7278	0.7390
0.965	0.6799	0.7009	0.7180	0.7324	0.7447	0.7553
0.970	0.7021	0.7218	0.7380	0.7514	0.7629	0.7730
0.975	0.7265	0.7449	0.7598	0.7723	0.7830	0.7922
0.980	0.7539	0.7706	0.7842	0.7956	0.8052	0.8136
0.985	0.7855	0.8002	0.8122	0.8222	0.8307	0.8381

0.990	0.8235	0.8358	0.8458	0.8541	0.8612	0.8673
0.005	0.8739	0.8829	0.8902	0.8962	0.9013	0.9057
1.000	1.0000	1.0000	1.0000	1.0000	1.0000	1.0000

Table 3.2: Table of adsorption saturation data for establishingthe boundary conditions of the developed isotherm ($n = 0.60$ to $n = 0.85$)

$\boldsymbol{b = \frac{V_{last}}{V_{max}}}$	$\boldsymbol{c = \frac{P_{last}}{P_s}}$					
	$n = 0.60$	$n = 0.65$	$n = 0.70$	$n = 0.75$	$n = 0.80$	$n = 0.85$
0.920	0.6495	0.6610	0.6714	0.6808	0.6893	0.6972
0.925	0.6601	0.6714	0.6815	0.6907	0.6990	0.7066
0.930	0.6711	0.6821	0.6920	0.7009	0.7090	0.7165
0.935	0.6826	0.6933	0.7029	0.7116	0.7194	0.7266
0.940	0.6946	0.7050	0.7142	0.7226	0.7303	0.7372
0.945	0.7071	0.7171	0.7261	0.7342	0.7416	0.7483
0.950	0.7203	0.7299	0.7385	0.7463	0.7534	0.7599
0.955	0.7342	0.7434	0.7517	0.7591	0.7659	0.7721
0.960	0.7489	0.7577	0.7656	0.7727	0.7791	0.7850
0.965	0.7647	0.7730	0.7804	0.7871	0.7932	0.7988
0.970	0.7817	0.7895	0.7964	0.8027	0.8084	0.8136
0.975	0.8003	0.8075	0.8139	0.8197	0.8249	0.8297
0.980	0.8210	0.8274	0.8333	0.8385	0.8432	0.8476
0.985	0.8445	0.8502	0.8553	0.8599	0.8641	0.8679

0.990	0.8727	0.8774	0.8816	0.8854	0.8889	0.8920
0.005	0.9096	0.9130	0.9161	0.9188	0.9213	0.9236
1.000	1.0000	1.0000	1.0000	1.0000	1.0000	1.0000

Table 3.3: Table of adsorption saturation data for establishingthe boundary conditions of the developed isotherm ($n = 0.90$ to $n = 1.15$)

$\boldsymbol{b = \frac{V_{last}}{V_{max}}}$	$\boldsymbol{c = \frac{P_{last}}{P_s}}$					
	$n = 0.90$	$n = 0.95$	$n = 1.00$	$n = 1.05$	$n = 1.10$	$n = 1.15$
0.920	0.7044	0.7110	0.7172	0.7230	0.7283	0.7334
0.925	0.7136	0.7202	0.7262	0.7318	0.7370	0.7420
0.930	0.7233	0.7296	0.7355	0.7409	0.7460	0.7508
0.935	0.7333	0.7394	0.7451	0.7504	0.7553	0.7600
0.940	0.7437	0.7496	0.7551	0.7602	0.7650	0.7695
0.945	0.7545	0.7602	0.7665	0.7705	0.7751	0.7794
0.950	0.7658	0.7713	0.7764	0.7812	0.7856	0.7898
0.955	0.7778	0.7830	0.7879	0.7925	0.7967	0.8006
0.960	0.7904	0.7954	0.8000	0.8044	0.8084	0.8121
0.965	0.8039	0.8086	0.8130	0.8170	0.8208	0.8244
0.970	0.8184	0.8228	0.8268	0.8306	0.8342	0.8375
0.975	0.8341	0.8382	0.8419	0.8454	0.8487	0.8517
0.980	0.8516	0.8552	0.8586	0.8618	0.8647	0.8675
0.985	0.8714	0.8746	0.8776	0.8803	0.8829	0.8853
0.990	0.8949	0.8976	0.9000	0.9023	0.9045	0.9065

0.005	0.9257	0.9276	0.9293	0.9310	0.9325	0.9399
1.000	1.0000	1.0000	1.0000	1.0000	1.0000	1.0000

Table 3.4: Table of pressure and adsorbed volume at point β where $\Delta\left(\frac{V}{V_{max}}\right) = \Delta\left(\frac{P}{P_s}\right)$

	$n = 0.30$	$n = 0.35$	$n = 0.40$	$n = 0.45$	$n = 0.50$
$P_\beta = \frac{n}{n+1}P_s$	$\frac{3}{13}P_s$	$\frac{7}{27}P_s$	$\frac{2}{7}P_s$	$\frac{9}{29}P_s$	$\frac{1}{3}P_s$
V_β	$0.7262V_{max}$	$0.7211V_{max}$	$0.7185V_{max}$	$0.7177V_{max}$	$0.7182V_{max}$
	$n = 0.55$	$n = 0.60$	$n = 0.65$	$n = 0.70$	$n = 0.75$
$P_\beta = \frac{n}{n+1}P_s$	$\frac{11}{31}P_s$	$\frac{3}{8}P_s$	$\frac{13}{33}P_s$	$\frac{7}{17}P_s$	$\frac{3}{7}P_s$
V_β	$0.7197V_{max}$	$0.7220V_{max}$	$0.7247V_{max}$	$0.7278V_{max}$	$0.7312V_{max}$
	$n = 0.80$	$n = 0.85$	$n = 0.90$	$n = 0.95$	$n = 1.00$
$P_\beta = \frac{n}{n+1}P_s$	$\frac{4}{9}P_s$	$\frac{17}{37}P_s$	$\frac{9}{19}P_s$	$\frac{19}{39}P_s$	$\frac{1}{2}P_s$
V_β	$0.7348V_{max}$	$0.7385V_{max}$	$0.7423V_{max}$	$0.7462V_{max}$	$0.7500V_{max}$
	$n = 1.05$	$n = 1.10$	$n = 1.15$		
$P_\beta = \frac{n}{n+1}P_s$	$\frac{21}{41}P_s$	$\frac{11}{21}P_s$	$\frac{23}{43}P_s$		

V_β	$0.7538V_{max}$	$0.7576V_{max}$	$0.7614V_{max}$		

4. Choose the P_β, V_β values that correlate with the experimental adsorption isotherm, and thus consider the corresponding n, P_s and V_{max} as the parameters of the proposed adsorption isotherm for the experimental adsorption data.
5. Model the adsorption data as:

$$V = \begin{Bmatrix} V_{max}\left\{\frac{P}{P_s} + \left(1 - \frac{P}{P_s}\right)\left(\frac{P}{P_s}\right)^n\right\}, for\ P < P_s\ i.e.\ undersaturated\ adsorption \\ V_{max}, \quad for\ P \geq P_s\ i.e.\ saturated\ adsorption \end{Bmatrix} \quad (3.48)$$

where V is the adsorbed volume at equilibrium pressure P, P_s is the adsorption saturation pressure at which the maximum adsorbed volume V_{max} is attained, n is a parameter that defines the adsorbent resistance to the adsorbate (n ranges from 0.30 to 1.15).

3.2.2 Parameterisation of Experimental Adsorption Data using Langmuir Isotherm

The steps involved in Langmuir isotherm parameters evaluation from experimental data are as highlighted below:

1. Obtain the parameters V_L and P_L (Langmuir volume and Langmuir pressure respectively) by arranging the isotherm

$$V = V_L \frac{P}{P + P_L} \quad (3.49)$$

as:

$$\frac{P}{V} = \frac{1}{V_L}P + \frac{1}{V_L}P_L \qquad (3.50)$$

2. Plot $\frac{P}{V}$ versus $P$to yield the equation of a straight line $Y = mX + C$, where slope

$$m = \frac{1}{V_L} \qquad (3.51)$$

and Y-axis intercept

$$C = \frac{1}{V_L}P_L \qquad (3.52)$$

are obtained from the best fit line.

3. Model the experimental adsorption data using the two parameters V_L and $P_L$as:

$$V = V_L\frac{P}{P+P_L} \qquad (3.53)$$

3.3GENERALISATION OF THE DEVELOPED ISOTHERM

The steps involved are as follows:

1. Plot V versus P for the experimental data, the developed isotherm data and Langmuir isotherm data
2. Correlate the developed isotherm with Langmuir isotherm and validate with experimental isotherm using statistical deviation (error) parameters.

3.4STATISTICAL DEVIATION (ERROR) PARAMETERS USED

The statistical deviation (error) parameters used in assessing the quality of fit in the adsorption model representation are the weighted root mean square (WRMS) deviation, the weighted average absolute deviation (WAAD), the percent average absolute deviation (%AAD) and the root mean square error (RMSE). These parameters are expressed as follows:

$$WRMS = \sqrt{\frac{1}{N}\cdot\sum_{n=1}^{N}\left(\frac{V_{cal}-V_{exp}}{\sigma_{exp}}\right)_i^2} \qquad (3.54)$$

$$WAAD = \frac{1}{N}\cdot\sum_{n=1}^{N} abs\left(\frac{V_{cal}-V_{exp}}{\sigma_{exp}}\right)_i \qquad (3.55)$$

$$\%AAD = \frac{1}{N}\cdot\sum_{n=1}^{N} abs\left(\frac{V_{cal}-V_{exp}}{V_{exp}}\right)_i \times 100\% \qquad (3.56)$$

and

$$RMSE = \sqrt{\frac{1}{N} \cdot \sum_{n=1}^{N} \left(V_{cal} - V_{exp}\right)_i^2} \quad (3.57)$$

Here i is the data point, N is the number of data points, V_{exp} is the experimental adsorption volume, V_{cal} is the calculated adsorption volume and σ_{exp} is the expected experimental uncertainty.

3.5STATEMENT OF DEVELOPED ADSORPTION ISOTHERM FOR GAS MIXTURE

With reference to the pure-component adsorption isotherm developed in this study, the volume of the adsorbing specie i in a mixture of gases at an equilibrium pressure P is expressed as:

$$V_i = \frac{y_i (V_{max})_i}{\sum_{j=1}^{N} y_j (V_{max})_j} (V_{100\%})_i \quad (3.58)$$

wherey_i is the gas phase mole fraction (or the feed ratio) of the adsorbing specie i; $(V_{max})_i$ is the maximum adsorbed volume of the adsorbing specie i of 100% concentration; y_j is the gas phase mole fraction (or the feed ratio) of the respective adsorbing specie j; $(V_{max})_j$ is the maximum adsorbed volume of the respective adsorbing specie j of 100% concentration; $j = 1, \ldots\ldots N$; N is the number of gas specie (1 for pure-component, 2 for binary mixture, and 3 for ternary mixture); $(V_{100\%})_i$ is the volume of the adsorbing specie i of 100% concentration at the corresponding pressure.

3.6 CORRELATION OF THE DEVELOPED ISOTHERM FOR GAS MIXTURE WITH THE EXTENDED LANGMUIR ISOTHERM

The mixing rule for the developed adsorption isotherm (for gas mixture) is correlated with the extended Langmuir isotherm expressed as:

$$V_i = (V_L)_i \frac{y_i b_i P}{\left(1+\sum_{j=1}^{N} y_j b_j P\right)} \tag{3.59}$$

where y_i is the gas-phase mole fraction of the adsorbing specie i; b_i is equal to $1/P_{L_i}$, the temperature-dependent pure-component Langmuir model parameter;; P is equilibrium pressure; and $j = 1, \ldots . N$; N is the number of gas component (1 for pure-component, 2 for binary mixture, and 3 for ternary mixture).

3.7IMPROVED MATERIAL BALANCE EQUATION

3.7.1 Modification of Gas Deviation Factor (Z-Factor) for Fractured Gas Reservoirs

The original gas material balance equation (MBE) (Schilthuis, 1936) is stated as:

$$G \cdot \left(B_g - B_{g_i}\right) + \Delta V_m + \Delta V_{mw} + W_e = G_p B_g + W_p B_w \tag{3.60}$$

where $G \cdot \left(B_g - B_{g_i}\right)$ is gas expansion, G is free gas initially in place i.e. original gas in place (OGIP) (scf), B_{g_i} is gas formation volume factor (rcf/scf) evaluated at initial pressure P_i i.e. before expansion, B_g is gas formation volume factor (rcf/scf) evaluated at pressure P i.e. after expansion, ΔV_m is pore compaction, ΔV_{mw} is matrix water expansion, W_e is water influx, G_p is cumulative gas production (scf), W_p is cumulative water produced (stb) and B_w is water formation volume factor.

Assuming a volumetric gas reservoir (i.e. where there is no water influx or water produced), $W_e = W_p = 0$; and also an insignificant rock compaction effect, $\Delta V_m = 0$. Then,

$$G \cdot \left(B_g - B_{g_i}\right) = G_p B_g \tag{3.61}$$

which is further analysed to yield:

$$\frac{G_p}{G} = 1 - \frac{P/Z}{P_i/Z_i} \qquad (3.62)$$

where $Z_i$and Z are therespective Z-factors at initial pressure$P_i$and pressure Pin a single-porosity (or non-fractured) reservoir with insignificant rock compaction. The derivation of **Equation 3.62** is shown in **Appendix A**.

3.7.1.1 Basis for Z-Factor Modification

Z-factor in single-porosity gas reservoirs with pressure depletion had been modified to reflect dual-porosity system that characterises shale gas reservoirs.Previous works done to modify gas MBE include King (1990), Aguilera (2008), Moghadam *et al*. (2009), and Duarte *et al.* (2014) (see **Equations 2.16;2.17;2.19;**and **2.27** respectively).

King (1990), Moghadam *et al*. (2009) and Duarte *et al.* (2014) MBEs featured the model:

$$\left(\frac{G_p}{G}\right)_{Total} = 1 - \frac{P/Z^*}{P_i/Z_i} \qquad (3.63)$$

where Z^* is the modified Z-factor into which gas desorption was lumped. Thus their MBEs work just like the traditional MBE, where the straight line plot of P/Z versus cumulative production G_p is used in estimating OGIP.

The existing Aguilera (2008) dual-porosity Z-factor incorporatesOGIP fractions within fractures and matrix pores. King (1990), Moghadam *et al*. (2009) and Duarte *et al.* (2014) developed modified Z-factors into which gas desorption was lumped, rendering them complex for routine calculationsbecause cumulative free gas production should feature Z-factor while cumulative gas desorption should feature adsorption isotherm.

Total gas production is the sum of cumulative free gas production and cumulative gas desorption, i.e. $G_{p_{Total}} = G_{p_{free}} + G_{p_{desorbed}}$as done by Mengal and Wattenbarger (2011) (see **Equations 2.25** and **2.26**).An accurate estimation of free and desorbed gas production will yield an improved MBE for better production forecast.Furthermore, single-porosity Z-factor can be modified to a simpler but accurate dual-porosity free gas Z-factor.

3.7.1.2 Development of Z-Factor for Single Porosity Gas Reservoirs with Rock Compaction

For single-porosity gas reservoirs (i.e. no fractures), the MBE is as follows:

$$G_{mat}\left(B_g - B_{g_i}\right) + \left(G_{mat}B_{g_i}\right)\left(\frac{C_w S_{w_i} + C_{matrix}}{S_{g_i}}\right)\Delta P + W_e = G_p B_g + W_p B_w \quad (3.64)$$

where G_{mat} is the OGIP in the matrix, $C_{mat}$is matrix compressibility, C_w is water compressibility, $S_{w_i}$is initial water saturation,C_{matrix} is matrix compressibility,$S_{g_i}$is initial gas saturation and $\Delta P$is pressure depletion.

For volumetric gas reservoirs (no water influx or water production), the MBE is expressed as:

$$G_{mat}\left(B_g - B_{g_i}\right) + \left(G_{mat}B_{g_i}\right)\left(\frac{C_w S_{w_i} + C_{matrix}}{S_{g_i}}\right)\Delta P = G_{p_{mat}} B_g \quad (3.65)$$

$$1 - \frac{B_{g_i}}{B_g} + \left(\frac{B_{g_i}}{B_g}\right)\left(\frac{C_w S_{w_i} + C_{matrix}}{S_{g_i}}\right)\Delta P = \frac{G_{p_{mat}}}{G_{mat}} \quad (3.66)$$

$$\frac{G_{p_{mat}}}{G_{mat}} = 1 - \frac{B_{g_i}}{B_g} \cdot \left\{1 - \left(\frac{C_w S_{w_i} + C_{matrix}}{S_{g_i}}\right)\Delta P\right\} \quad (3.67)$$

But

$$\frac{B_{g_i}}{B_g} = \frac{Z_i}{P_i}\frac{P}{Z} \quad (3.68)$$

Hence,

$$\left(\frac{G_p}{G}\right)_{Free} = 1 - \frac{P/Z}{P_i/Z_i} \cdot \left\{1 - \left(\frac{C_w S_{w_i} + C_{matrix}}{S_{g_i}}\right)\Delta P\right\} \quad (3.69)$$

Equation 3.69 is the MBE developed for single-porosity gas reservoirs withrock compaction after pressure depletion, and the corresponding Z-factor is:

$$Z^* = Z \cdot \left\{1 - \left(\frac{C_w S_{w_i} + C_{matrix}}{S_{g_i}}\right)\Delta P\right\}^{-1} \quad (3.70)$$

where Z is single porosity Z-factor at pressure Pwithout pore compaction.

3.7.1.3 Modification ofSingle-Porosity Z-Factor to Dual-Porosity Z-Factor

For fractured gas reservoirs without adsorption, the derivation of Aguilera (2008) gas MBE is as follows:

With reference to **Equation 3.65**, for the matrix blocks in the dual-porosity system,

$$G_{mat}\left(B_g - B_{g_i}\right) + \left(G_{mat}B_{g_i}\right)\left(\frac{C_w S_{w_i} + C_{matrix}}{S_{g_i}}\right)\Delta P = G_{p_{mat}}B_g \qquad (3.71)$$

where G_{mat}, $G_{p_{mat}}$and $\left(\frac{C_w S_{w_i} + C_{matrix}}{S_{g_i}}\right)$are OGIP within the matrix, cumulative gas production from the matrix and matrix pore volume compressibility respectively.

However, for the fractures,

$$G_{frac}\left(B_g - B_{g_i}\right) + \left(G_{frac}B_{g_i}\right)\left(\frac{C_w S_{w_i} + C_{frac}}{S_{g_i}}\right)\Delta P = G_{p_{frac}}B_g \qquad (3.72)$$

where G_{frac}, $G_{p_{frac}}$, $\left(\frac{C_w S_{w_i} + C_{frac}}{S_{g_i}}\right)$are OGIP withinthe fractures, cumulative gas production from the fractures and fracture volume compressibilityrespectively.

Expressing $\left(\frac{C_w S_{w_i} + C_{matrix}}{S_{g_i}}\right)$ and $\left(\frac{C_w S_{w_i} + C_{frac}}{S_{g_i}}\right)$ as $C^*_{p_{mat}}$ and $C^*_{p_{frac}}$ respectively, and adding **Equations 3.71** and **3.72** to obtain dual-porosity gas MBE (i.e. after fracturing) gives:

$$\left(G_{mat} + G_{frac}\right)\left(B_g - B_{g_i}\right) + \left(G_{mat}C^*_{p_{mat}} + G_{frac}C^*_{p_{frac}}\right)B_{g_i}\Delta P = \left(G_{p_{mat}} + G_{p_{frac}}\right)B_g \qquad (3.73)$$

However, G(OGIP) is constant, i.e. $G = G_{mat} + G_{frac}$. Also, $G_{p_{mat}} + G_{p_{frac}} = G_p$. Hence,

$$G\left(B_g - B_{g_i}\right) + \left(G_{mat}C^*_{p_{mat}} + G_{frac}C^*_{p_{frac}}\right)B_{g_i}\Delta P = G_p B_g \qquad (3.74)$$

$$\left(B_g - B_{g_i}\right) + \left(\frac{G_{mat}}{G}C^*_{p_{mat}} + \frac{G_{frac}}{G}C^*_{p_{frac}}\right)B_{g_i}\Delta P = \frac{G_p}{G}B_g \qquad (3.75)$$

$$\left(B_g - B_{g_i}\right) + \left(\left(1 - \omega_f\right)C^*_{p_{mat}} + \omega_f C^*_{p_{frac}}\right)B_{g_i}\Delta P = \frac{G_p}{G}B_g \qquad (3.76)$$

where ω_f is fraction of OGIP (free gas) in the fracture system and $(1-\omega_f)$ is fraction of OGIP (free gas) in the matrix.

$$\left(\frac{G_p}{G}\right)_{Free} = 1 - \frac{B_{g_i}}{B_g} + \left((1-\omega_f)C^*_{p_{mat}} + \omega_f C^*_{p_{frac}}\right)\frac{B_{g_i}}{B_g}\Delta P \tag{3.77}$$

Hence,

$$\left(\frac{G_p}{G}\right)_{Free} = 1 - \frac{P/Z}{P_i/Z_i}\cdot\left(1-\left(1-\omega_f\right)C^*_{p_{mat}} + \omega_f C^*_{p_{frac}}\right)\Delta P \tag{3.78}$$

where the modified Z-factor (Z'') is expressed as:

$$Z'' = Z\cdot\left\{1-\left(\left(1-\omega_f\right)C^*_{p_{mat}} + \omega_f C^*_{p_{frac}}\right)\cdot\Delta P\right\}^{-1} \tag{3.79}$$

where Z is single porosity Z-factor at pressure Pwithout pore compaction. **Equation 3.78** is the Aguilera (2008) gas MBE for fractured gas reservoirs without adsorption and **Equation 3.79** is the Aguilera (2008) dual-porosity Z-factor.

However, from the concept of porosity, this work expresses Aguilera (2008) dual-porosity Z-factor as:

$$Z'' = Z\cdot\left\{1-\left(\left(\frac{\phi''_{mat}}{\phi''_{mat}+\phi_{frac}}\right)C^*_{p_{mat}} + \left(\frac{\phi_{frac}}{\phi''_{mat}+\phi_{frac}}\right)C^*_{p_{frac}}\right)\cdot\Delta P\right\}^{-1} \tag{3.80}$$

whereϕ_{frac} is fracture porosity,$\phi''_{mat} = (1-\phi_{frac})\phi'_{mat}$ is matrix porosity after fracturing andϕ'_{mat} is initial matrix porosity.

During hydraulic fractures stabilisation and porosity/permeability maintenance before pressure depletion, fracture volume compressibility$\left(C^*_{p_{frac}}\right)$ is sustained at a lower level that corresponds to injection water compressibility $\left(C_{w_{Inj}}\right)$. Hence, $C^*_{p_{frac}}$ is assumed to be equal to $C_{w_{Inj}}$.

In this work, a different approach of developing dual porosity MBE is considered. Incorporating the ratio of dual porosity to initial matrix porosity into single-porosity gas MBE yields dual-porosity MBE. The approach is as follows:

With reference to **Equation 3.65**),

$$G\left(B_g - B_{g_i}\right) + G\left(\frac{Dual\ Porosity}{Initial\ Matrix\ Porosity}\right)\left(\frac{C_w S_{w_i} + C_{matrix}}{S_{g_i}}\right) \cdot B_{g_i} \Delta P = G_p \cdot B_g \tag{3.81}$$

$$\left(B_g - B_{g_i}\right) + \left(\frac{Dual\ Porosity}{Initial\ Matrix\ Porosity}\right)\left(\frac{C_w S_{w_i} + C_{matrix}}{S_{g_i}}\right) \cdot B_{g_i} \Delta P = \frac{G_p}{G} B_g \tag{3.82}$$

$$\left(B_g - B_{g_i}\right) + \left(\frac{\phi''_{mat}}{\phi'_{mat}} + \frac{\phi_{frac}}{\phi'_{mat}}\right)\left(\frac{C_w S_{w_i} + C_{matrix}}{S_{g_i}}\right) \cdot B_{g_i} \Delta P = \frac{G_p}{G} B_g \tag{3.83}$$

$$\frac{G_p}{G} = 1 - \frac{B_{g_i}}{B_g} + \left(\frac{B_{g_i}}{B_g}\right)\left(\frac{(1-\phi_{frac})\phi'_{mat}}{\phi'_{mat}} + \frac{\phi_{frac}}{\phi'_{mat}}\right)\left(\frac{C_w S_{w_i} + C_{matrix}}{S_{g_i}}\right) \cdot \Delta P \tag{3.84}$$

$$\left(\frac{G_p}{G}\right)_{Free} = 1 - \frac{P/Z}{P_i/Z_i} \cdot \left\{1 - \left(1 - \phi_{frac} + \frac{\phi_{frac}}{\phi'_{mat}}\right)\left(\frac{C_w S_{w_i} + C_{matrix}}{S_{g_i}}\right) \Delta P\right\} \tag{3.85}$$

and the modified Z-factor for dual porosityis:

$$Z^{**} = Z \cdot \left\{1 - \left(1 - \phi_{frac} + \frac{\phi_{frac}}{\phi'_{mat}}\right)\left(\frac{C_w S_{w_i} + C_{matrix}}{S_{g_i}}\right) \cdot \Delta P\right\}^{-1} \tag{3.86}$$

where Z is single porosity Z-factor at pressure Pwithout pore compaction.

3.7.1.4Evaluation of Z-Factor

As stated earlier, shale gas processing is often influenced by gas compositions across a field (Bullin & Krouskop, 2008). Hence, the choice of using either Standing (1981) correlation or Sutton (1985) correlation for shale gas pseudo-critical properties evaluationdepends on ethane and propane levels consideration.

In this work, Sutton (1985) correlation ($0.57 < \gamma_g < 1.68$) is used in calculating pseudo-critical pressure P_{pc} and pseudo-critical temperature T_{pc} for Marcellus shale formation (having average of 85.2% C1). However, Standing (1981) correlation ($\gamma_g < 0.75$) is used in calculating P_{pc} and T_{pc} for Haynesville shale formation (having average of 95.0 % C1) and Barnett shale formation (having average of 86.75% C1).

The pseudo-reduced pressure P_{pr} and pseudo-reduced temperature T_{pr} are then calculated as $P_{pr} = {}^{P}/_{P_{pc}}$ and $T_{pr} = {}^{T}/_{T_{pc}}$, Thereafter, the single porosity Z-factors at different pressure levels without pore compaction areevaluated using the Dranchuk-Abou-Kassem (1975) eleven-constant equation of state (EoS) expressed as:

$$Z = 1 + C_1(T_{pr}) \cdot \rho_r + C_2(T_{pr}) \cdot \rho_r^2 - C_3(T_{pr}) \cdot \rho_r^5 - C_4(\rho_r, T_{pr}) \quad (3.87)$$

where

$$\rho_r = \frac{0.27 P_{pr}}{Z T_{pr}} \quad (3.88)$$

$$C_1(T_{pr}) = A_1 + \frac{A_2}{T_{pr}} + \frac{A_3}{{T_{pr}}^3} + \frac{A_4}{{T_{pr}}^4} + \frac{A_5}{{T_{pr}}^5} \quad (3.89)$$

$$C_2(T_{pr}) = A_6 + \frac{A_7}{T_{pr}} + \frac{A_8}{{T_{pr}}^2} \quad (3.90)$$

$$C_3(T_{pr}) = A_9\left(\frac{A_7}{T_{pr}} + \frac{A_8}{{T_{pr}}^2}\right) \quad (3.91)$$

$$C_4(\rho_r, T_{pr}) = A_{10}(1 + A_{11}\rho_r^2)\left(\frac{\rho_r^2}{{T_{pr}}^3}\right) exp(-A_{11}\rho_r^2) \quad (3.92)$$

where $A_1 = 0.3265$, $A_2 = -1.0700$, $A_3 = -0.5339$, $A_4 = 0.01569$, $A_5 = -0.05165$, $A_6 = 0.5475$, $A_7 = -0.7361$, $A_8 = 0.1844$, $A_9 = 0.1056$, $A_{10} = 0.6134$, and $A_{11} = 0.7210$.

The Dranchuk-Abou-Kassem (1975) EoS must be solved iteratively since the Z-factor is on both sides of the equation. This task could be executed using the Newton-Raphson iteration method. Rearranging **Equation 3.87** for this purpose yields:

$$F(Z) = Z - \{1 + C_1(T_{pr}) \cdot \rho_r + C_2(T_{pr}) \cdot \rho_r^2 - C_3(T_{pr}) \cdot \rho_r^5 - C_4(\rho_r, T_{pr})\} \quad (3.93)$$

where

$$\left(\frac{\partial F(Z)}{\partial Z}\right)_{T_{pr}} = 1 + C_1(T_{pr}) \cdot \frac{\rho_r}{Z} + 2C_2(T_{pr}) \cdot \frac{\rho_r^2}{Z} - 5C_3(T_{pr}) \cdot \frac{\rho_r^5}{Z} + \left(\frac{2A_{10}\rho_r^2}{{T_{pr}}^3 Z}\right)\{1 + A_{11}\rho_r^2 - (A_{11}\rho_r^2)^2\} exp(-A_{11}\rho_r^2) \quad (3.94)$$

The steps involved in evaluating Z are highlighted as follows:

1. Use Standing and Katz Z-factor Z_{SK} as initial guess Z^i
2. Evaluate the new improved estimate of Z as:

$$Z^{i+1} = Z^i - \frac{F(Z^i)}{F'(Z^i)} \tag{3.95}$$

where

$$F'(Z^i) = \left(\frac{\partial F(Z^i)}{\partial Z}\right)_{T_{pr}} \tag{3.96}$$

3. Repeat step 2 several times n until the error i.e. $abs(Z^n - Z^{n+1}) \approx 0$, such that $Z^n = Z^{n+1}$ at a convergence criterion of 10^{-4}.

A MAPPLE code for evaluating Z at different pressure levels is indicated in **Appendix D**.

3.7.2Material Balance Equation for Volumetric Dry Shale Gas Reservoirs

3.7.2.1 Free Gas MBE Based on the Modified Z-Factor

The original free gas in place $OGIP_{free}(scf)$ is expressed as:

$$OGIP_{free}(scf) = \frac{V_B}{B_{g_i}} \cdot \phi'_{mat} \cdot S_{g_i} \tag{3.97}$$

where V_B is reservoir bulk volume (rcf) and B_{g_i} is initial formation volume factor (rcf/scf).

However, in field unit,

$$OGIP_{free}(scf) = \frac{10{,}763{,}911Ah}{B_{g_i}} \cdot \phi'_{mat} \cdot S_{g_i} \tag{3.98}$$

where A is reservoir area (sq. km), h is reservoir net thickness (ft.), $Ah = V_B$ is reservoir bulk volume, B_{g_i} is initial formation volume factor (rcf/scf), ϕ'_{mat} is reservoir matrix porosity before fracturing, S_{g_i} is initial gas saturation and 10,763,911 is the conversion factor of km^2 to ft^2.

Free gas-in-place during pressure depletion is determined as:

$$GIP_{free}(scf) = \frac{10{,}763{,}911Ah}{B_{g_i}} \cdot \phi'_{mat} \cdot S_{g_i} \cdot \left(\frac{B_{g_i}}{B_g}\right) \tag{3.99}$$

But for dual porosity, $\left(\frac{B_{g_i}}{B_g}\right)$ is expressed as:

$$\frac{B_{g_i}}{B_g} = \frac{Z_i}{P_i}\frac{P}{Z^{**}} \tag{3.100}$$

where Z_i is the Z-factor at P_i, Z^{**} is the modified Z-factor for fractured reservoirs at pressure P expressed as: $Z^{**} = Z \cdot \left\{1 - \left(1 - \phi_{frac} + \frac{\phi_{frac}}{\phi'_{mat}}\right)\left(\frac{C_w S_{w_i} + C_{matrix}}{S_{g_i}}\right) \cdot \Delta P\right\}^{-1}$, ϕ'_{mat} is matrix porosity before fracturing, and ϕ_{frac} is fracture porosity

Hence,

$$GIP_{free}(scf) = \frac{10{,}763{,}911Ah}{B_{g_i}} \cdot \phi'_{mat} \cdot S_{g_i} \cdot \left(\frac{Z_i}{P_i}\frac{P}{Z^{**}}\right) \tag{3.101}$$

Therefore, free gas production (the difference between $OGIP_{free}$ and GIP_{free}) is:

$$G_{p_{free}}(scf) = \frac{10{,}763{,}911Ah}{B_{g_i}} \cdot \phi'_{mat} \cdot S_{g_i} \cdot \left(1 - \frac{Z_i}{P_i}\frac{P}{Z^{**}}\right) \tag{3.102}$$

3.7.2.2 Adsorbed Gas MBE Based on the Developed Isotherm

The original adsorbed gas-in-place based on the developed isotherm is expressed as:

$$OGIP_{adsorbed}(scf) = 10{,}763{,}911Ah\frac{\rho_b}{35.515} \cdot V_{max} \tag{3.103}$$

where ρ_b is reservoir bulk density (g/cm^3), V_{max} is the maximum adsorbed volume (scf/ton) attained at and above the adsorption saturation pressure P_s, and $\frac{1}{35.515}$ is unit similitude factor for $\rho_b \cdot V_{max}$.

However, adsorbed gas-in-place at a pressure Pbelow the adsorption saturation pressure P_s is expressed as:

$$GIP_{adsorbed}(scf) = 10{,}763{,}911Ah\frac{\rho_b}{35.515} \cdot V_{max}\left\{\frac{P}{P_s} + \left(1 - \frac{P}{P_s}\right)\left(\frac{P}{P_s}\right)^n\right\} \tag{3.104}$$

where n is adsorbate-adsorbent resistance parameter (n ranges from 0.30 to 1.15).

Therefore, desorbed gas production (the difference between $OGIP_{adsorbed}$ and $GIP_{adsorbed}$) is

$$G_{p_{desorbed}}(scf) = 10{,}763{,}911Ah\frac{\rho_b}{35.515}\cdot V_{max}\left\{1-\left\{\frac{P}{P_s}+\left(1-\frac{P}{P_s}\right)\left(\frac{P}{P_s}\right)^n\right\}\right\} \quad (3.105)$$

However, for $P_s \le P \le P_i$, the relative pressure $\frac{P}{P_s} = 1$ since the pressure difference $(P - P_s)$ is latent and has no effect on gas adsorption and desorption.

3.7.2.3 Total Gas MBE Based on the Modified Z-Factor and the Developed Isotherm

Considering the modified Z-factor and the developed isotherm, total gas-in-place (the addition of GIP_{free} and $GIP_{adsorbed}$) is:

$$GIP_{Total}(scf) = 10{,}763{,}911Ah\left\{\frac{\phi'_{mat}\cdot S_{g_i}}{B_{g_i}}\cdot\left(\frac{Z_i}{P_i}\frac{P}{Z^{**}}\right)+\frac{\rho_b}{35.515}\cdot V_{max}\left\{\frac{P}{P_s}+\left(1-\frac{P}{P_s}\right)\left(\frac{P}{P_s}\right)^n\right\}\right\} \quad (3.106)$$

Equation 3.106 is the improved material balance equation for shale gas reserves.

Also, total gas production (the addition of $G_{p_{free}}$ and $G_{p_{desorbed}}$) is:

$$G_{p_{Total}}(scf) = 10{,}763{,}911Ah\left\{\frac{\phi'_{mat}\cdot S_{g_i}}{B_{g_i}}\cdot\left(1-\frac{Z_i}{P_i}\frac{P}{Z^{**}}\right)+\frac{\rho_b}{35.515}\cdot V_{max}\left\{1-\left\{\frac{P}{P_s}+\left(1-\frac{P}{P_s}\right)\left(\frac{P}{P_s}\right)^n\right\}\right\}\right\} \quad (3.107)$$

Equation 3.107 is the improved material balance equation for shale gas production.

However, for $P_s \le P \le P_i$, the relative pressure $\frac{P}{P_s} = 1$ since the pressure difference $(P - P_s)$ has no effect on gas adsorption and desorption.

3.7.2.4 Adsorbed Gas MBE Based on Langmuir Isotherm

The original adsorbed gas-in-place based on Langmuir isotherm is expressed as:

$$OGIP_{adsorbed}(scf) = 10{,}763{,}911Ah\frac{\rho_b}{35.515}\cdot V_L\left(\frac{P_i}{P_i+P_L}\right) \quad (3.108)$$

where V_L is the Langmuir volume representing the maximum volume of gas that can be adsorbed per unit mass of adsorbent (scf/ton) at infinite pressure, P_i is the initial reservoir pressure, and P_L is the Langmuir pressure, which is the pressure at which half the Langmuir volume is adsorbed.

However, adsorbed gas-in-place at a pressure *P*is expressed as:

$$GIP_{adsorbed}(scf) = 10{,}763{,}911Ah\frac{\rho_b}{35.515}\cdot V_L\left(\frac{P}{P+P_L}\right) \quad (3.109)$$

Therefore, desorbed gas production (the difference between $OGIP_{adsorbed}$ and $GIP_{adsorbed}$) is

$$G_{p_{desorbed}}(scf) = 10{,}763{,}911Ah\frac{\rho_b}{35.515}\cdot V_L\left(\frac{P_i}{P_i+P_L}-\frac{P}{P+P_L}\right) \quad (3.110)$$

3.7.2.5 Total Gas MBE Based on the Modified Z-Factor and Langmuir Isotherm

Considering the modified Z-factor and Langmuir isotherm, material balance equation for shale gas reserves (the addition of GIP_{free} and $GIP_{adsorbed}$) is:

$$GIP_{Total}(scf) = 10{,}763{,}911Ah\left\{\frac{\phi'_{mat}\cdot S_{g_i}}{B_{g_i}}\cdot\left(\frac{Z_i}{P_i}\frac{P}{Z^{**}}\right)+\frac{\rho_b}{35.515}\cdot V_L\left(\frac{P}{P+P_L}\right)\right\} \quad (3.111)$$

Also, total gas production (the addition of $G_{p_{free}}$ and $G_{p_{desorbed}}$) yields the material balance equation for shale gas production as:

$$G_{p_{Total}}(scf) = 10{,}763{,}911Ah\left\{\frac{\phi'_{mat}\cdot S_{g_i}}{B_{g_i}}\cdot\left(1-\frac{Z_i}{P_i}\frac{P}{Z^{**}}\right)+\frac{\rho_b}{35.515}\cdot V_L\left(\frac{P_i}{P_i+P_L}-\frac{P}{P+P_L}\right)\right\} \quad (3.112)$$

3.7.2.6 Comparison of Free Gas OGIP with the Developed and Langmuir Isotherms-Based OGIPs

The variation of G_p versus $\frac{P}{Z^{**}}$ is plotted to compare $OGIP_{free}$ and $OGIP_{Total}$ (for both free and adsorbed gases) based on the developed and Langmuir isotherms; the straight line yields $OGIP_{free}$ as the Y-intercept and $\frac{P_i}{Z_i}$ as the X-intercept.

3.7.2.7 Effect of Fracture Porosity on Gas Production

In this work, fracture porosity $\phi_{frac}$of 0.04 is adopted for stimulated reservoir volumes (SRV) in Marcellus and Haynesville shale gas formations considering initial matrix porosities $\phi'_{mat}$of 0.10 and 0.085 respectively. However, ϕ_{frac} of 0.02 is adapted for SRV in Barnett shale gas formation consideringϕ'_{mat} of 0.045. To analyse the effect of fracture porosity variation on gas production,ϕ_{frac} of 0.02, 0.04 and 0.06 are compared with ϕ_{frac} of 0.

3.8 GAS PRODUCTION PERFORMANCE PREDICTION

3.8.1 Evaluation of Cumulative Gas Production within the Production History

The cumulative gas production G_p (MMscf) for the respective gas production rate q_g(Mscf/d) is evaluated as:

$$G_{p_n} = G_{p_{n-1}} + \frac{1}{2}\left(q_{g_{n-1}} + q_{g_n}\right)\Delta t \tag{3.113}$$

where subscripts n and $n-1$ denote the current and previous status of the parameters, and change in production timeΔt is in days.

3.8.2Development of Decline Rate Exponent as a Function of the Variation of G_p with Pressure Depletion

Gas production rate q_g is expressed as:

$$q_g = \frac{dG_p}{dP} \cdot \frac{dP}{dt} \tag{3.114}$$

where G_p is the cumulative gas production, P is pressure and t is production time.

For a stabilised flow with constant bottomhole pressure P_{wf}, production rate (at pressure P_p) is expressed as a function of the gas productivity index J_g:

$$q_g = J_g\{\psi(P_p) - \psi(P_{wf})\} \quad (3.115)$$

where gas pseudo-pressure $\psi(P)$ is expressed as:

$$\psi(P) = 2\int_0^P \frac{P}{\mu Z} dP \quad (3.116)$$

Hence,

$$q_g = J_g\left\{\frac{P_p^2}{\mu_i Z_i} - \frac{P_{wf}^2}{(\mu Z)_{P_{wf}}}\right\} \quad (3.117)$$

However, Feast *et al*. (2005) modified the gas pseudo-pressure $\psi(P)$ in the reservoir matrix by incorporating slippage (Klinkenberg) effect into it to yield:

$$\psi_m^*(P) = 2\int_0^P \frac{P\left(1+\frac{b_{km}}{P}\right)}{\mu Z} dP \quad (3.118)$$

$$\psi_m^*(P) = 2\int_0^P \frac{(P+b_{km})}{\mu Z} dP \quad (3.119)$$

where b_{k_m} is slippage factor (psi) in the matrix.

Thus

$$q_g = 2J_g^*\left\{\frac{\frac{P_p^2}{2}+P_p b_{km}}{\mu Z^{**}} - \frac{\frac{P_{wf}^2}{2}+P_{wf} b_{km}}{(\mu Z^{**})_{P_{wf}}}\right\} \quad (3.120)$$

$$q_g = J_g^*\left\{\frac{P_p^2+2P_p b_{km}}{\mu Z^{**}} - \frac{P_{wf}^2+2P_{wf} b_{km}}{(\mu Z^{**})_{P_{wf}}}\right\} \quad (3.121)$$

Thus initial production rate (at initial reservoir pressure P_i) is expressed as:

$$q_{g_i} = J_g^*\left\{\frac{P_i^2+2P_i b_{km}}{\mu_i Z_i^{**}} - \frac{P_{wf}^2+2P_{wf} b_{km}}{(\mu Z^{**})_{P_{wf}}}\right\} \quad (3.122)$$

and

$$dq_g = -2J_g^*\left(\frac{P_i+b_{km}}{\mu Z^{**}}\right) dP \quad (3.123)$$

With reference to **Equations 3.114** and **3.123**,

$$\frac{dq_g}{q_g} = -\frac{2J_g^*(P_i+b_{km})}{\mu_i Z_i^{**}\left(\frac{dG_p}{dP}\right)}dt \quad (3.124)$$

However, production decline is governed by the model:

$$q_g = q_{g_1} t^{-n} \quad (3.125)$$

where q_{g_1} is the production rate at the first time step and n is an exponent

i.e.

$$In\ q_g = In\ q_{g_1} - nIn\ t \quad (3.126)$$

$$\int_{q_{g_1}}^{q_g} \frac{dq_g}{q_g} = -n\int_1^t \frac{dt}{t} \quad (3.127)$$

$$\frac{dq_g}{q_g} = -n\frac{dt}{t} \quad (3.128)$$

Hence, comparing **Equations 3.124** and **3.128** yields:

$$n = \left(\frac{2J_g^*(P_i+b_{km})}{\mu_i Z_i^{**}\left(\frac{dG_p}{dP}\right)}\right) \cdot t_p \quad (3.129)$$

where $\left(\frac{dG_p}{dP}\right)$ is obtained for pressure depletion from initial reservoir pressure P_i to the bottom hole pressure P_{wf}, and t_p is the total production period.

Hence,

$$n = \frac{C}{\left(\frac{dG_p}{dP}\right)} \quad (3.130)$$

where C is a constant of proportionality.

3.8.3 Steps Developed for Shale Gas Production Performance Prediction

The steps involved in gas production performance prediction for the shale gas well in this work are as follows:

1. From the rate decline curve of a gas well in the shale formation (for this work, see **Figure 2.20**), evaluate cumulative gas production G_p for the respective production rate q_g as:

$$G_{p_n} = G_{p_{n-1}} + \frac{1}{2}\left(q_{g_{n-1}} + q_{g_n}\right)\Delta t \tag{3.131}$$

where subscripts n and $n-1$ denote the current and previous status of the parameters, and change in production time Δt is in days.

2. Modelthe variation of actual gasq_g with timeas:

$$q_{g_{Well\ Forecast}}^{Actual\ Gas\ Production} = q_{g_1} t^{-n_{Well\ Forecast}^{Gas\ Production}} \tag{3.132}$$

where q_{g_1} is the production rate at the first time step,$n$is decline rate exponent.

3. Evaluate

$$\left(\frac{Actual\ OGIP}{Predicted\ OGIP}\right)_{Free\ Gas} \tag{3.133}$$

as a constant $\alpha$and determine

$$\left(\frac{dG_p}{dP}\right)_{Free\ Gas}^{Actual} = \alpha \left(\frac{dG_p}{dP}\right)_{Free\ Gas}^{MBA-Predicted} \tag{3.134}$$

for pressure depletion from initial reservoir pressure P_i to the wellbore flowing pressureP_{wf}, where MBA denotes material balance analysis.

4. The developed adsorption isotherm has been established to truly represent Type I isotherm and predict actual adsorption or desorption,i.e.

$$V_{Gas\ Desorption}^{Experimental} \approx V_{Gas\ Desorption}^{Developed\ Isotherm} \tag{3.135}$$

and

$$G_{p_{Total\ Gas}}^{Actual} = G_{p_{Free\ Gas}}^{Actual} + G_{p_{Desorbed\ Gas}}^{Developed\ Isother} \tag{3.136}$$

where

$$G_{p_{Free\ Gas}}^{Actual} = \alpha\, G_{p_{Free\ Gas}}^{MBA-Predicted} \tag{3.137}$$

Therefore, for pressure depletion from initial reservoir pressure P_i to the wellbore flowing pressure P_{wf} evaluate

$$\left(\frac{dG_p}{dP}\right)_{Total\ Gas}^{Actual} = \frac{G_{p_{Total\ Gas}}^{Actual}\ at\ P_{wf}}{(P_i - P_{wf})} \tag{3.138}$$

5. Decline rate exponent,

$$n = \frac{C}{\left(\frac{dG_p}{dP}\right)} \tag{3.139}$$

where $C$is a constant of proportionality thus with reference to the total gas forecast for the well($n_{Well\ Forecast}^{Actual\ Total\ Gas}$). Thus obtain

$$n_{Well\ Forecast}^{Actual\ Free\ Gas} = n_{Well\ Forecast}^{Actual\ Total\ Gas} \times \left(\frac{\left(\frac{dG_p}{dP}\right)_{Total\ Gas}^{Actual}}{\left(\frac{dG_p}{dP}\right)_{Free\ Gas}^{Actual}} \right) \tag{3.140}$$

$$n_{Well\ Forecast}^{(Developed\ Isotherm)\ Total\ Gas} = n_{Well\ Forecast}^{Actual\ Total\ Gas} \times \left(\frac{\left(\frac{dG_p}{dP}\right)_{Total\ Gas}^{Actual}}{\left(\frac{dG_p}{dP}\right)_{Formation\ Total\ Gas\ (Developed\ Isotherm)}^{MBA-Predicted}} \right) \tag{3.141}$$

and

$$n_{Well\ Forecast}^{(Langmuir\ Isotherm)\ Total\ Gas} = n_{Well\ Forecast}^{Actual\ Total\ Gas} \times \left(\frac{\left(\frac{dG_p}{dP}\right)_{Total\ Gas}^{Actual}}{\left(\frac{dG_p}{dP}\right)_{Formation\ Total\ Gas\ (Langmuir\ Isotherm)}^{MBA-Predict}} \right) \tag{3.142}$$

6. To correlate the production rate forecast with the production rate from field data, the respective model fitting factors

$$K = \left(\frac{q_{g_{Field\ Data}}^{Actual\ Total\ Gas}}{q_{g_{Well\ Forecast}}^{Actual\ Total\ Gas}} \right) \tag{3.143}$$

after the first time step must be considered. Thus obtain the variations of respective q_g with time as:

$$q_{g_{Well\ Forecast}}^{Actual\ Free\ Gas} = K\left(q_{g_1} t^{-n_{Well\ Forecast}^{Actual\ Free\ Gas}} \right) \tag{3.144}$$

$$q_{g_{Well\ Forecast}}^{(Developed\ Isotherm)\ Total\ Gas} = K\left(q_{g_1} t^{-n_{Well\ Forecast}^{(Developed\ Isotherm)\ Total\ Gas}} \right) \tag{3.145}$$

and

$$q_{g_{Well\ Forecast}}^{(Langmuir\ Isotherm)\ Total\ Gas} = K\left(q_{g_1} t^{-n_{Well\ Forecast}^{(Langmuir\ Isotherm)\ Total\ Gas}} \right) \tag{3.146}$$

Beyond the production history, the last value of K is retained.

7. On the same chart, plot q_g versus $t$within the production history period for (i) well production history (serving as base case for validation), (ii) the model results for actual free gas production (no desorption), (iii) the model results for actual total gas production based on the developed isotherm, and (iv) the model results for actual total gas production based on Langmuir isotherm.
8. Forthe whole production performance forecast (i.e. within and beyond the production history), plot q_g versus $t$on the same chart for (i) well production history and its projection (serving as base case), (ii) the model results for actual free gas production (no desorption), (iii) the model results for actual total gas production based on the proposed isotherm, and (iv) the model results for actual total gas production based on Langmuir isotherm.
9. For the second time step, evaluate cumulative production for free gas and total gas (based on the developed and Langmuir isotherms) as:

$$G_p = \left(\frac{q_{g_{Forecast}}}{q_{g_{Field\ Data}}^{Actual\ Total\ Gas}}\right) \times G_{p_{Field\ Data}}^{Actual\ Total\ Gas} \tag{3.147}$$

However, for subsequent time steps, do the evaluation as:

$$G_{p_n} = G_{p_{n-1}} + \frac{1}{2}\left(q_{g_{n-1}} + q_{g_n}\right)\Delta t \tag{3.148}$$

where the parameters retain their usual meaning.

10. Plot respective $G_p$versus t on the same chart.

CHAPTER FOUR

RESULTS AND DISCUSSION

4.1 EXPERIMENTAL PURE GAS ADSORPTION DATA USED FOR GENERALISATION OF THE DEVELOPED ISOTHERM

The experimental pure gas adsorption data (secondary data) used for generalising the developed isotherm are shown in **Tables 4.1** to **4.6**.

Table 4.1: Pure carbon dioxide adsorption on BPL activated carbon sample at 28.3 ^{o}C (Merey, 2013)

Pressure, P (psia)	**Gibbs adsorption, V (mmol/g)**	**Absolute uncertainty, σ_{Exp} (mmol/g)**
5	0.773	0.056
34	2.418	0.057
89	4.182	0.060
187	5.672	0.070
293	6.600	0.083
419	7.124	0.131

Table 4.2: Pure methane adsorption on BPL activated carbon sample at 28.3 ^{o}C (Merey, 2013)

Pressure,	**Gibbs**	**Absolute**

P (psia)	adsorption, V (mmol/g)	uncertainty, σ_{Exp} (mmol/g)
23	0.946	0.032
58	1.603	0.033
128	2.496	0.032
229	3.284	0.031
303	3.663	0.033
380	3.936	0.034
443	4.015	0.035

Table 4.3: Pure methane adsorption on Turkey's shale sample at 25 ^{o}C (Merey, 2013)

Pressure, P (psia)	Gibbs adsorption, V (mmol/g)	Absolute uncertainty, σ_{Exp} (mmol/g)
190	0.0197	0.0024
403	0.0265	0.0037
602	0.0325	0.0050
805	0.0361	0.0063
1002	0.0394	0.0077
1201	0.0412	0.0092
1403	0.0437	0.0107
1598	0.0446	0.0122
1798	0.0447	0.0137
2005	0.0450	0.0153

Table 4.4: Pure nitrogen adsorption on dryactivated carbon sample at 328.2 K (Mohammad, 2009)

Pressure, P (MPa)	**Absolute adsorption, V (mmol/g)**	**Absolute uncertainty, σ_{Exp}(mmol/g)**
0.81	1.015	0.041
1.46	1.473	0.040
2.93	2.075	0.039
4.19	2.407	0.039
5.53	2.651	0.039
6.98	2.834	0.039
8.36	2.946	0.039
9.69	3.018	0.040
11.08	3.068	0.039
12.54	3.100	0.040
13.70	3.108	0.040

Note: 1 mmol/g = 758.98 scf/ton

Table 4.5: Pure methane adsorption on dry Tiffany mixed coal sample at 130 ^{o}F (Gasem *et al*., 2002)

Pressure, P (psia)	**Absolute adsorption, V (scf/ton)**	**Absolute uncertainty, σ_{Exp}(scf/ton)**
266.9	117.0	3.510
824.9	243.9	7.317
1210.2	283.6	8.608
1796.9	316.6	9.498

Note: σ_{Exp} are evaluated basedon average expected experimental uncertainty of 6%.

Table 4.6: Pure nitrogen adsorption on dry Tiffany mixed coal sample at 130 ^{o}F (Gasem *et al*., 2002)

Pressure, P (psia)	Absolute adsorption, V (scf/ton)	Absolute uncertainty, σ_{Exp}(scf/ton)
106.6	18.1	1.086
202.9	29.9	1.794
406.0	52.9	3.174
602.7	69.7	4.182
795.6	88.1	5.286
1000.2	102.3	6.138
1202.5	113.9	6.834
1410.9	126.6	7.596
1604.9	138.0	8.280
1806.2	147.2	8.832

Note: σ_{Exp} are evaluated based on average expectedexperimental uncertainty of 6%.

4.2 PARAMETERISATTION OF EXPERIMENTAL ADSORPTION DATA AND GENERALISATION OF THE DEVELOPED ISOTHERM

4.2.1Pure Carbon Dioxide Adsorption on BPL Activated Carbon Sample at 28.3 ^{o}C

4.2.1.1 Parameterisation of Pure Carbon Dioxide Adsorption on BPL Activated Carbon Sample at 28.3 ^{o}Cusing the Developed Isotherm

Plotting the experimental isotherm from **Table 4.1** and matching it with the relative adsorbed volume-relative pressure curve (see **Figure 3.3**) shows the adsorbate-adsorbent resistance parameter n to be in the range of 0.45 to 0.55.

For each n, the corresponding parameters $b = \frac{V_{last}}{V_{max}}$ and $c = \frac{P_{last}}{P_s}$ were featured. Using *Excel* spreadsheet, the corresponding $V_{max} = \frac{V_{last}}{b}$ and $P_s = \frac{P_{last}}{c}$, and the pressure and adsorbed volume P_β, V_β at the inflexion point β where $\Delta\left(\frac{V}{V_{max}}\right) = \Delta\left(\frac{P}{P_s}\right)$ on the isotherms were evaluated. The parameter n = 0.50 yields the P_β, V_β values (see **Table 4.7**) that correlate with the experimental adsorption isotherm as shown in **Figure 4.1**.

The $\boldsymbol{P_\beta}$, $\boldsymbol{V_\beta}$ values of **140 psia** and **5.116 mmol/g** correlate with the experimental isotherm (see **Figure 4.1**), and the corresponding $\boldsymbol{P_s}$, $\boldsymbol{V_{max}}$ values of **419 psia** and **7.124 mmol/g** are thus considered as the developed isotherm parameters for the experimental adsorption data.

Table 4.7: Adsorption saturation data for establishing the boundary conditions of the developed isotherm for pure carbon dioxide adsorption on BPL activated carbon sample at 28.3 ^{o}C. (Here, V_{last} = 7.124 mmol/g and P_{last} = 419 psia)

$b = \frac{V_{last}}{V_{max}}$	$n = 0.50$				
	$c = \frac{P_{last}}{P_s}$	$V_{max} = \frac{V_{last}}{b}$ (mmol/g)	$P_s = \frac{P_{last}}{c}$ (psia)	$V_\beta = 0.7182 V_{max}$ (mmol/g)	$P_\beta = \frac{1}{3} P_s$ (psia)
0.955	0.7120	7.460	588	5.358	196
0.960	0.7278	7.421	576	5.330	192
0.965	0.7447	7.382	562	5.302	187
0.970	0.7629	7.344	549	5.274	183
0.975	0.7830	7.307	535	5.248	178
0.980	0.8052	7.269	520	5.221	173
0.985	0.8307	7.232	504	5.194	168
0.990	0.8612	7.196	486	5.168	162
0.005	0.9013	7.160	464	5.142	155
1.000	1.0000	**7.124**	**419**	**5.116**	**140**

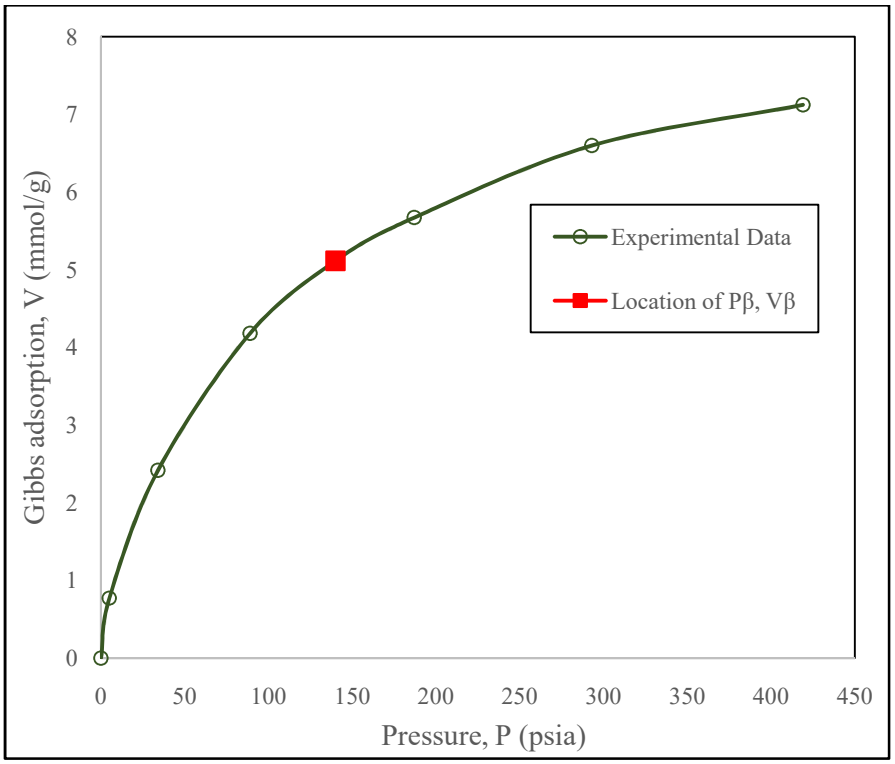

Figure 4.1: Location of P_β, V_β correlation on the experimental isotherm for pure carbon dioxide adsorption on BPL activated carbon sample at 28.3 ^{o}C

Hence, pure carbon dioxide adsorption on BPL activated carbon sample at 28.3 ^{o}C is modelled as:

$$\boldsymbol{V(mmol/g)} = \begin{Bmatrix} \mathbf{7.142}\left\{\frac{\boldsymbol{P}}{\mathbf{419}} + \left(\mathbf{1} - \frac{\boldsymbol{P}}{\mathbf{419}}\right)\left(\frac{\boldsymbol{P}}{\mathbf{419}}\right)^{\mathbf{0.50}}\right\}, for\ P < 419\ psia \\ \mathbf{7.142},\ for\ P \geq 419\ psia \end{Bmatrix} \quad (4.1)$$

where maximum adsorbed volume V_{max} = 7.142 mmol/g, adsorption saturation pressure P_s = 419 psia, and n = 0.50 is a parameter that defines BPL activated carbonresistance to pure carbon dioxide adsorption at 28.3 ^{o}C.

4.2.1.2 Prediction of Pure Carbon Dioxide Adsorption on BPL Activated Carbon Sample at 28.3 ^{o}Cusing the Developed Isotherm

Prediction of pure carbon dioxide adsorption on BPL activated carbon sample at 28.3 ^{o}C using the developed isotherm, and the corresponding deviation (error) analysis parameters are presented in **Table 4.8.**

Here, weighted root mean square, WRMS = 1.4488, weighted average absolute deviation, WAAD = 1.2275, percent average absolute deviation, %AAD = 3.1000, root mean square error, RMSE = 0.1036 mmmol/g and R^2 value = 0.9986.

Table 4.8: Prediction of pure carbon dioxide adsorption on BPL activated carbon sample at 28.3 ^{o}C using the developed isotherm

Pressure, P (psia)	Gibbs adsorption, V (mmol/g)		Deviation (Error) Analysis			
	Experimental	Developed Isotherm	σ_{Exp} (mmol/g)	V_{Cal} - V_{Exp} (mmol/g)	$\frac{V_{Cal} - V_{Exp}}{\sigma_{Exp}}$	$\frac{V_{Cal} - V_{Ex}}{V_{Exp}}$
5	0.773	0.854	0.056	0.081	1.446	0.105
34	2.418	2.443	0.057	0.025	0.438	0.010
89	4.182	4.099	0.060	-0.083	-1.383	-0.020
187	5.672	5.815	0.070	0.143	2.014	0.025
293	6.600	6.773	0.083	0.173	2.084	0.026
419	7.124	7.124	0.131	0	0	0

4.2.1.3 Parameterisation of Pure Carbon Dioxide Adsorption on BPL Activated Carbon Sample at 28.3 ^{o}Cusing Langmuir Isotherm

The variation of P/V with P for pure carbon dioxide adsorption on BPL activated carbon sample at 28.3 ^{o}C is shown in **Table 4.9** and the best fit line of the plot of P/V versus P (shown in **Figure 4.2**) yields the equation:

$$y = 0.1215x + 8.8721 \qquad (4.2)$$

where

$$\text{slope } m = 0.1215 = {}^{1}/_{V_L} \tag{4.3}$$

and

y-axis intercept

$$C = 8.8721 = \left(\frac{1}{V_L}\right) P_L \tag{4.4}$$

Here, Langmuir volume $\boldsymbol{V_L}$ and Langmuir pressure $\boldsymbol{P_L}$ are respectively obtained as **8.230 mmol/g** and**73.021 psia**. Hence, pure carbon dioxide adsorption on BPL activated carbon sample at 28.3 ^{o}C is modelled as:

$$\boldsymbol{V(mmol/g) = 8.230\left(\frac{P}{P+73.021}\right)} \tag{4.5}$$

where P is pressure (psia) and Langmuir constant

$$b = \frac{1}{P_L} = 0.01369 \text{ psia}^{-1} \tag{4.6}$$

Table 4.9: Parameters for plotting Langmuir isotherm for purecarbon

dioxide adsorption on BPL activated carbon sample at 28.3 ^{o}C

Experimental		$\frac{Pressure}{Volume}$, P/V (psia/mmol/g)
Pressure, P (psia)	**Gibbs adsorption, V (mmol/g)**	
5	0.773	6.468
34	2.418	14.061
89	4.182	21.283
187	5.672	32.969
293	6.600	44.394
419	7.124	58.815

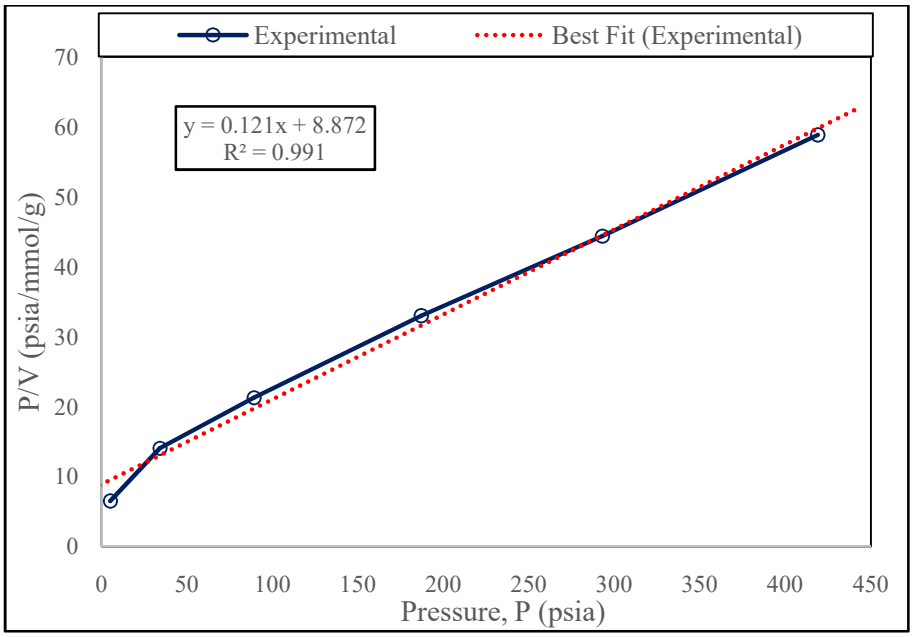

Figure 4.2: Plot of P/V versus P for pure carbon dioxide adsorption on BPL activated carbon sample at 28.3 ^{o}C

4.2.1.4 Prediction of Pure Carbon Dioxide Adsorption on BPL Activated Carbon Sample at 28.3 ^{o}Cusing Langmuir Isotherm

Prediction of pure carbon dioxide adsorption on BPL activated carbon sample at 28.3 ^{o}C using Langmuir isotherm, and the corresponding deviation (error) analysis parameters are presented in **Table 4.10**.

Here, weighted root mean square, WRMS = 3.5686, weighted average absolute deviation, WAAD = 3.0085, percent average absolute deviation, %AAD = 9.0333, root mean square error, RMSE = 0.2193 mmmol/g and R^2 value = 0.9920.

Table 4.10: Prediction of pure carbon dioxide adsorption on BPL activated carbon sample at 28.3 ^{o}C using Langmuir isotherm

Pressure, P (psia)	Gibbs adsorption, V (mmol/g)		Deviation (Error) Analysis			
	Experimental	Langmuir Isotherm	σ_{Exp} (mmol/g)	V_{Cal} - V_{Exp} (mmol/g)	$\frac{V_{Cal} - V_{Exp}}{\sigma_{Exp}}$	$\frac{V_{Cal} - V_{Exp}}{V_{Exp}}$
5	0.773	0.527	0.056	-0.246	-4.393	-0.318
34	2.418	2.615	0.057	0.197	3.456	0.081
89	4.182	4.521	0.060	0.339	5.650	0.081
187	5.672	5.919	0.070	0.247	3.529	0.044
293	6.600	6.588	0.083	-0.012	-0.145	-0.002
419	7.124	7.009	0.131	-0.115	-0.878	-0.016

4.2.1.5 Generalisation of the Developed Isotherm for Pure Carbon Dioxide Adsorption on BPL Activated Carbon Sample at 28.3 ^{o}C

To validate and generalise the developed isotherm, adsorption predictions by Langmuir and the developed isotherm are correlated with the experimental data. The generalisation of the developed isotherm for pure carbon dioxide adsorption on BPL activated carbon sample at 28.3 ^{o}C is shown in **Table 4.11** and **Figure 4.3**.

Table 4.11: Generalisation of the developed isotherm for purecarbon dioxide adsorption on BPL activated carbon sample at 28.3 ^{o}C

Pressure, P (psia)	**Gibbs adsorption, *V* (mmol/g)**		
	Experimental	**Developed Isotherm**	**Langmuir Isotherm**
5	0.773	0.854	0.527
34	2.418	2.443	2.615
89	4.182	4.099	4.521
187	5.672	5.815	5.919
293	6.600	6.773	6.588
419	7.124	7.124	7.009

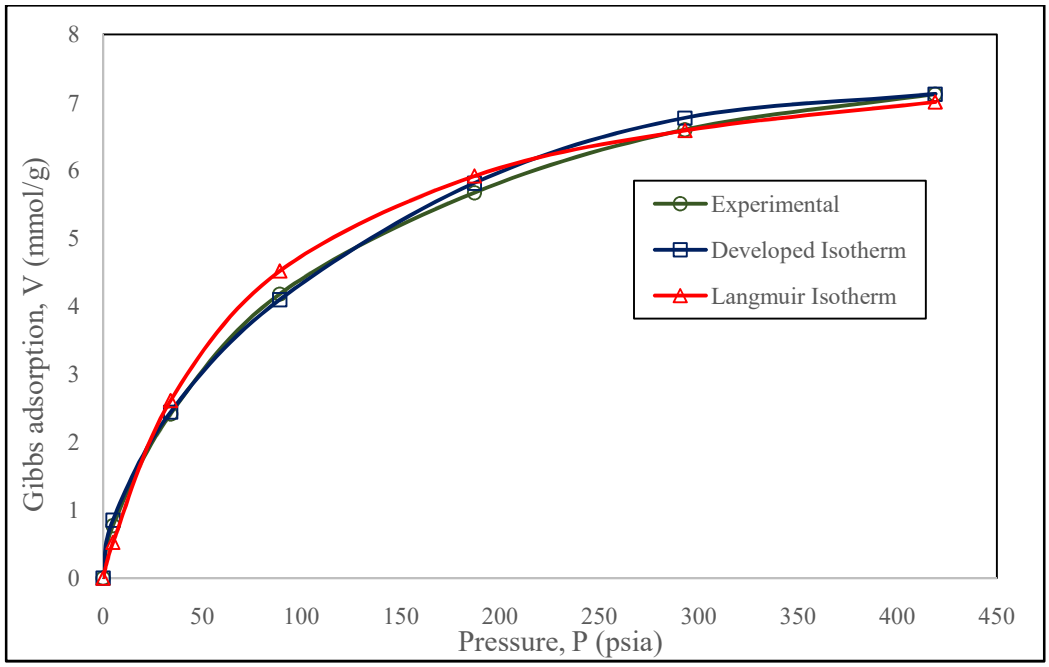

Figure 4.3: Generalisation of the developed isotherm for pure carbon dioxide adsorption on BPL activated carbon sample at 28.3 ^{o}C

4.2.1.6 Comparison of High-Pressure Adsorption Prediction for Pure Carbon Dioxide Adsorption on BPL Activated Carbon Sample at 28.3 ^{o}C

Langmuir and the developed isotherms predictions of pure carbon dioxide adsorption on BPL activated carbon sample at 28.3 ^{o}C for high-pressure range are compared in **Table 4.12** and **Figure 4.4**.

The developed isotherm predicts a maximum adsorbed volume of **7.124 mmol/g** at an adsorption saturation pressure of **419psia**. However, by Langmuir isotherm prediction, a maximum adsorbed volume of **8.230mmol/g** is attained at an infinite adsorption saturation pressure. **Figure 4.4** shows that adsorption prediction by Langmuir isotherm

is not reliable at higher pressures because of its inefficiency in defining the onset of adsorption saturation pressure; this contributes to an overestimation of maximum adsorbed volume.

Table 4.12: Langmuir and the developed isotherms predictions of pure carbon dioxide adsorption on BPL activated carbon sample at 28.3 ^{o}C for high-pressure range

Pressure, P (psia)	Gibbs adsorption, V (mmol/g)	
	Developed Isotherm	Langmuir Isotherm
5	0.854	0.527
34	2.443	2.615
89	4.099	4.521
187	5.815	5.919
293	6.773	6.588
419	7.124	7.009
500	7.124	7.181
700	7.124	7.452
900	7.124	7.612
1100	7.124	7.718
1300	7.124	7.792
1500	7.124	7.848

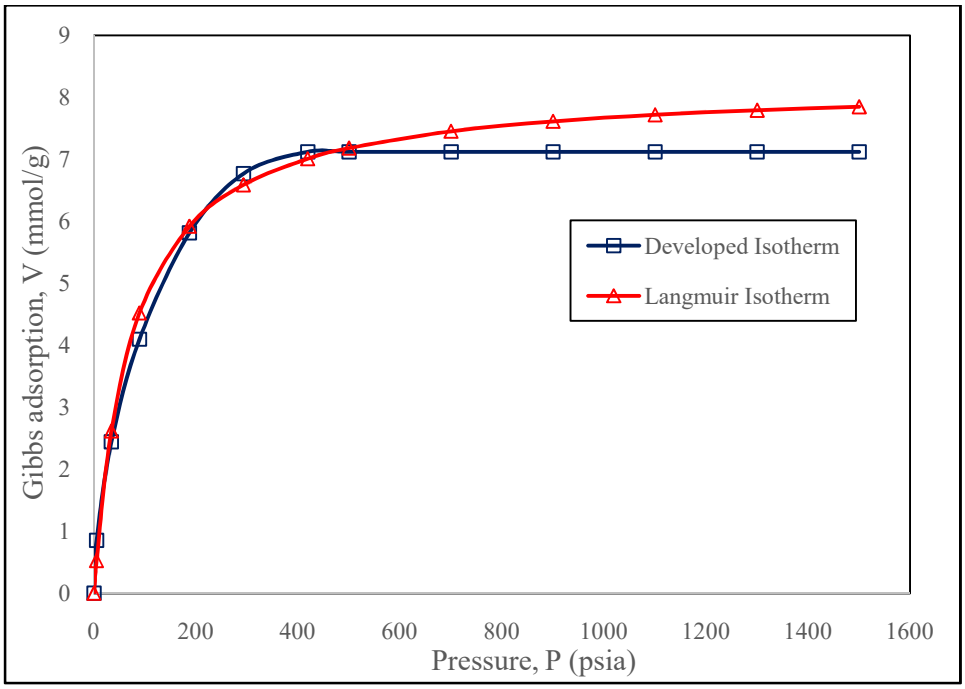

Figure 4.4: Langmuir and the developed isotherms predictions of pure carbon dioxide adsorption on BPL activated carbon sample at 28.3 ^{o}C for high-pressure range

4.2.2Pure Methane Adsorption on BPL Activated Carbon Sample at 28.3 ^{o}C

4.2.2.1 Parameterisation of Pure Methane Adsorption on BPL Activated Carbon Sample at 28.3 ^{o}Cusing the Developed Isotherm

Plotting the experimental isotherm from **Table 4.2** and matching it with the relative adsorbed volume-relative pressure curve (see **Figure 3.3**) shows the adsorbate-adsorbent resistance parameter n to be in the range of 0.45 to 0.55.

For each n, the corresponding parameters $b = \frac{V_{last}}{V_{max}}$ and $c = \frac{P_{last}}{P_s}$ were featured. Using *Excel* spreadsheet, the corresponding $V_{max} = \frac{V_{last}}{b}$ and $P_s = \frac{P_{last}}{c}$, and the pressure and adsorbed volume P_β, V_β at the inflexion point β where $\Delta\left(\frac{V}{V_{max}}\right) = \Delta\left(\frac{P}{P_s}\right)$ on the isotherms were evaluated. The parameter n = 0.50 yields the P_β, V_β values (see **Table 4.13**) that correlate with the experimental adsorption isotherm as shown in **Figure 4.5**.

The $\boldsymbol{P_\beta}$, $\boldsymbol{V_\beta}$ values of **178 psia** and **2.928 mmol/g** correlate with the experimental isotherm (see **Figure 4.5**), and the corresponding $\boldsymbol{P_s}$, $\boldsymbol{V_{max}}$ values of **533 psia** and **4.076 mmol/g** are thus considered as the developed isotherm parameters for the experimental adsorption data.

Hence, pure methane adsorption on BPL activated carbon sample at 28.3 ^{o}C is modelled as:

$$\boldsymbol{V(mmol/g)} = \begin{Bmatrix} \mathbf{4.076}\left\{\frac{P}{533} + \left(1 - \frac{P}{533}\right)\left(\frac{P}{533}\right)^{\mathbf{0.50}}\right\}, for\ P < 533\ psia \\ \mathbf{4.076},\ for\ P \geq 533\ psia \end{Bmatrix} \quad (4.7)$$

where maximum adsorbed volume V_{max} = 4.076 mmol/g, adsorption saturation pressure P_s = 533 psia, and n = 0.50 is a parameter that defines BPL activated carbon sample resistance to methane adsorption at 28.3 ^{o}C.

Table 4.13: Adsorption saturation data for establishing the boundary conditions of the developed isotherm for pure methane adsorption on BPL activated carbon sample at 28.3 °C. (Here, V_{last} = 4.015 mmol/g and P_{last} = 443 psia)

$b = \frac{V_{last}}{V_{max}}$	n = 0.50				
	$c = \frac{P_{last}}{P_s}$	$V_{max} = \frac{V_{last}}{b}$ (mmol/g)	$P_s = \frac{P_{last}}{c}$ (psia)	$V_\beta = 0.7182 V_{max}$ (mmol/g)	$P_\beta = \frac{1}{3} P_s$ (psia)
0.955	0.7120	4.204	622	3.020	207
0.960	0.7278	4.182	609	3.004	203
0.965	0.7447	4.161	595	2.988	198
0.970	0.7629	4.139	581	2.973	194
0.975	0.7830	4.118	566	2.958	189
0.980	0.8052	4.097	550	2.942	183
0.985	0.8307	**4.076**	**533**	**2.928**	**178**
0.990	0.8612	4.056	514	2.913	171
0.005	0.9013	4.035	492	2.898	164
1.000	1.0000	4.015	443	2.884	148

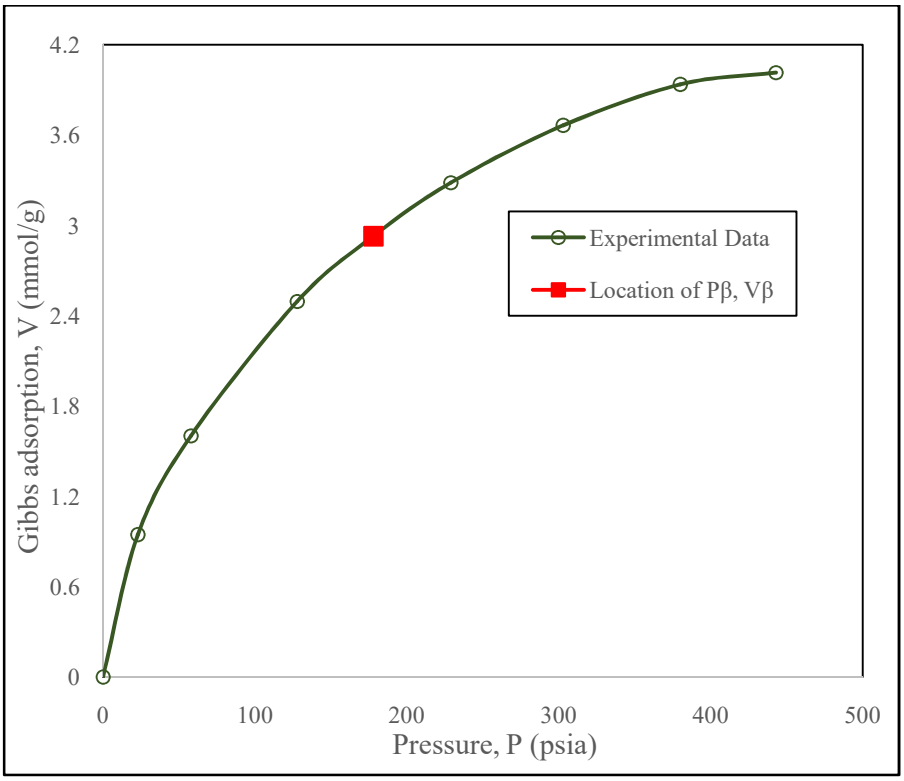

Figure 4.5: Location of P_β, V_β correlation on the experimental isotherm for pure methane adsorption on BPL activated carbon sample at 28.3 ^{o}C

4.2.2.2 Prediction of Pure Methane Adsorption on BPL Activated Carbon Sample at 28.3 ^{o}Cusing the Developed Isotherm

Prediction of pure methane adsorption on BPL activated carbon sample at 28.3 ^{o}C using the developed isotherm, and the corresponding deviation (error) analysis parameters are presented in **Table 4.14.**

Here, weighted root mean square, WRMS = 0.8398, weighted average absolute deviation, WAAD = 0.6563, percent average absolute deviation, %AAD = 1.2000, root mean square error, RMSE = 0.0277 mmmol/g and R^2 value = 0.9999.

Table 4.14: Prediction of pure methane adsorption on BPL activated carbon sample at 28.3 ^{o}C using the developed isotherm

Pressure, P (psia)	Gibbs adsorption, V (mmol/g)		Deviation (Error) Analysis			
	Experimental	Developed Isotherm	σ_{Exp} (mmol/g)	$V_{Cal} - V_{Exp}$ (mmol/g)	$\frac{V_{Cal} - V_{Exp}}{\sigma_{Exp}}$	$\frac{V_{Cal} - V_{Exp}}{V_{Exp}}$
23	0.946	0.986	0.032	0.040	1.250	0.042
58	1.603	1.642	0.033	0.039	1.182	0.024
128	2.496	2.497	0.032	0.001	0.031	0
229	3.284	3.275	0.031	-0.009	-0.290	-0.002
303	3.663	3.643	0.033	-0.020	-0.606	-0.005
380	3.936	3.894	0.034	-0.042	-1.235	-0.011
443	4.015	4.015	0.035	0	0	0

4.2.2.3 Parameterisation of Pure Methane Adsorption on BPL Activated Carbon Sample at 28.3 ^{o}Cusing Langmuir Isotherm

The variation of $^{P}/_{V}$ with P for pure methane adsorption on BPL activated carbon sample at 28.3 ^{o}C is shown in **Table 4.15** and the best fit line of the plot of $^{P}/_{V}$ versus P (shown in **Figure 4.6**) yields the equation:

$$y = 0.1962x + 23.456 \quad (4.8)$$

where

$$\text{slope } m = 0.1962 = {}^{1}/_{V_L} \quad (4.9)$$

andy-axis intercept

$$C = 23.456 = \left(\frac{1}{V_L}\right) P_L \quad (4.10)$$

Here, Langmuir volume $\boldsymbol{V_L}$ and Langmuir pressure $\boldsymbol{P_L}$ are respectively obtained as **5.0968 mmol/g** and**119.55 psia**. Hence, pure methane adsorption on BPL activated carbon sample at 28.3 ^{o}C is modelled as:

$$\boldsymbol{V(mmol/g) = 5.0968\left(\frac{P}{P+119.55}\right)} \quad (4.11)$$

where P is pressure (psia) and Langmuir constant

$$b = \frac{1}{P_L} = 0.008365 \text{ psia}^{-1} \quad (4.12)$$

Table 4.15: Parameters for plotting Langmuir isotherm for pure methane adsorption on BPL activated carbon sample at 28.3 ^{o}C

Experimental		$\frac{Pressure}{Volume}$, P/V
Pressure, P (psia)	**Gibbs adsorption, V (mmol/g)**	**(psia/mmol/g)**
23	0.946	24.313
58	1.603	36.182
128	2.496	51.282
229	3.284	69.732
303	3.663	82.719
380	3.936	96.545
443	4.015	110.336

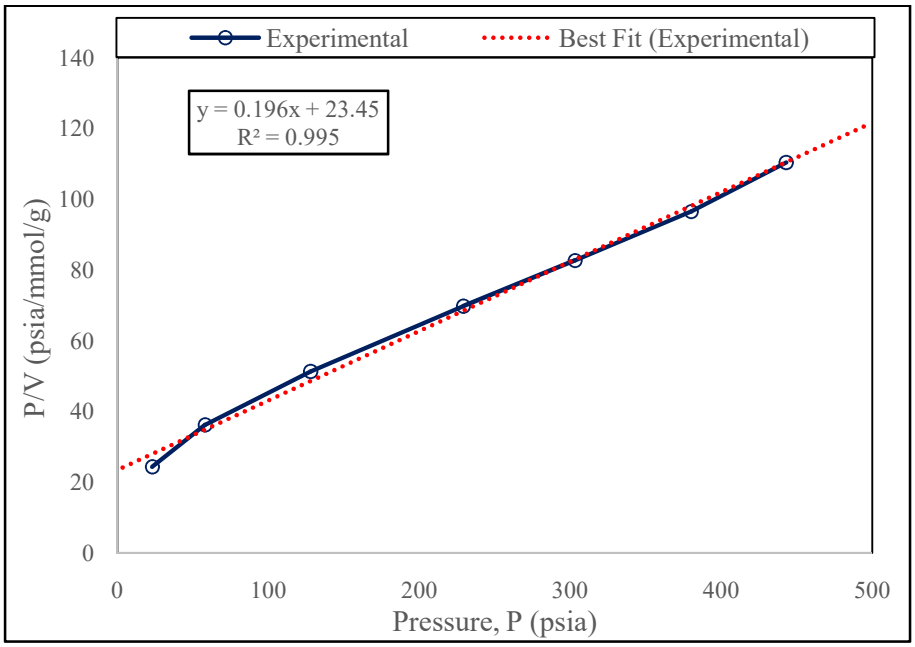

Figure 4.6: Plot of P/V versus P for pure methane adsorption on BPL activated carbon sample at 28.3 ^{o}C

4.2.2.4 Prediction of Pure Methane Adsorption on BPL Activated Carbon Sample at 28.3 ^{o}Cusing Langmuir Isotherm

Prediction of pure methane adsorption on BPL activated carbon sample at 28.3 ^{o}C using Langmuir isotherm, and the corresponding deviation (error) analysis parameters are presented in **Table 4.16**.

Here, weighted root mean square, WRMS = 2.5322, weighted average absolute deviation, WAAD = 2.0287, percent average absolute deviation, %AAD = 3.7600, root mean square error, RMSE = 0.0813 mmmol/g and R^2 value = 0.9949.

Table 4.16: Prediction of pure methane adsorption on BPL activated carbon sample at 28.3 ^{o}C using Langmuir isotherm

Pressure, P (psia)	Gibbs adsorption, V (mmol/g)		Deviation (Error) Analysis			
	Experimental	Langmuir Isotherm	σ_{Exp} (mmol/g)	$V_{Cal} - V_{Exp}$ (mmol/g)	$\frac{V_{Cal} - V_{Exp}}{\sigma_{Exp}}$	$\frac{V_{Cal} - V_{Exp}}{V_{Exp}}$
23	0.946	0.822	0.032	-0.124	-3.875	-0.131
58	1.603	1.665	0.033	0.062	1.879	0.039
128	2.496	2.635	0.032	0.139	4.344	0.056
229	3.284	3.349	0.031	0.065	2.097	0.020
303	3.663	3.655	0.033	-0.008	-0.242	0.002
380	3.936	3.877	0.034	-0.059	-1.735	0.015
443	4.015	4.014	0.035	-0.001	-0.029	0.0002

4.2.2.5 Generalisation of the Developed Isotherm for Pure Methane Adsorption on BPL Activated Carbon Sample at 28.3 ^{o}C

To validate and generalise the developed isotherm, adsorption predictions by Langmuir and the developed isotherm are correlated with the experimental data. The generalisation of the developed isotherm for pure methane adsorption on BPL activated carbon sample at 28.3 ^{o}C is shown in **Table 4.17** and **Figure 4.7**.

Table 4.17: Generalisation of the developed isotherm for pure methane adsorption on BPL activated carbon sample at 28.3 ^{o}C

Pressure, P (psia)	Gibbs adsorption, *V* (mmol/g)		
	Experimental	Developed Isotherm	Langmuir Isotherm
23	0.946	0.986	0.822
58	1.603	1.642	1.665
128	2.496	2.497	2.635
229	3.284	3.275	3.349
303	3.663	3.643	3.655
380	3.936	3.894	3.877
443	4.015	4.015	4.014

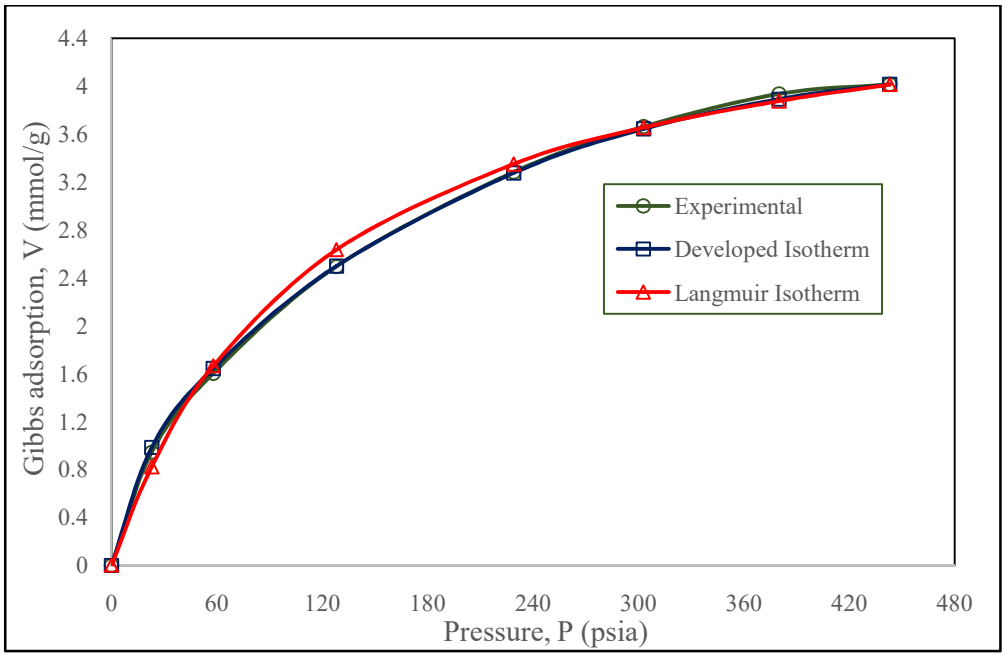

Figure 4.7: Generalisation of the developed isotherm for pure methane adsorption on BPL activated carbon sample at 28.3 ^{o}C

4.2.2.6 Comparison of High-Pressure Adsorption Prediction for Pure Methane Adsorption on BPL Activated Carbon Sample at 28.3 ^{o}C

Langmuir and the developed isotherms predictions of pure methane adsorption on BPL activated carbon sample at 28.3 ^{o}Cfor high-pressure range are compared in **Table 4.18** and **Figure 4.8**.

The developed isotherm predicts a maximum adsorbed volume of **4.076 mmol/g** at an adsorption saturation pressure of **533psia**. However, by Langmuir isotherm prediction, a maximum adsorbed volume of **5.097mmol/g** is attained at an infinite adsorption

saturation pressure. **Figure 4.8** shows that adsorption prediction by Langmuir isotherm is not reliable at higher pressures because of its inefficiency in defining the onset of adsorption saturation pressure; this contributes to an overestimation of maximum adsorbed volume.

Table 4.18: Langmuir and the developed isotherms predictions

of pure methane adsorption on BPL activated carbon sample at 28.3 ^{o}Cfor high-pressure range

Pressure, P (psia)	**Gibbs adsorption, V (mmol/g)**	
	Developed Isotherm	**Langmuir Isotherm**
23	0.986	0.822
58	1.642	1.665
128	2.497	2.635
229	3.275	3.349
303	3.643	3.655
380	3.894	3.877
443	4.015	4.014
533	4.076	4.163
650	4.076	4.305
750	4.076	4.396
850	4.076	4.468
950	4.076	4.527
1050	4.076	4.576

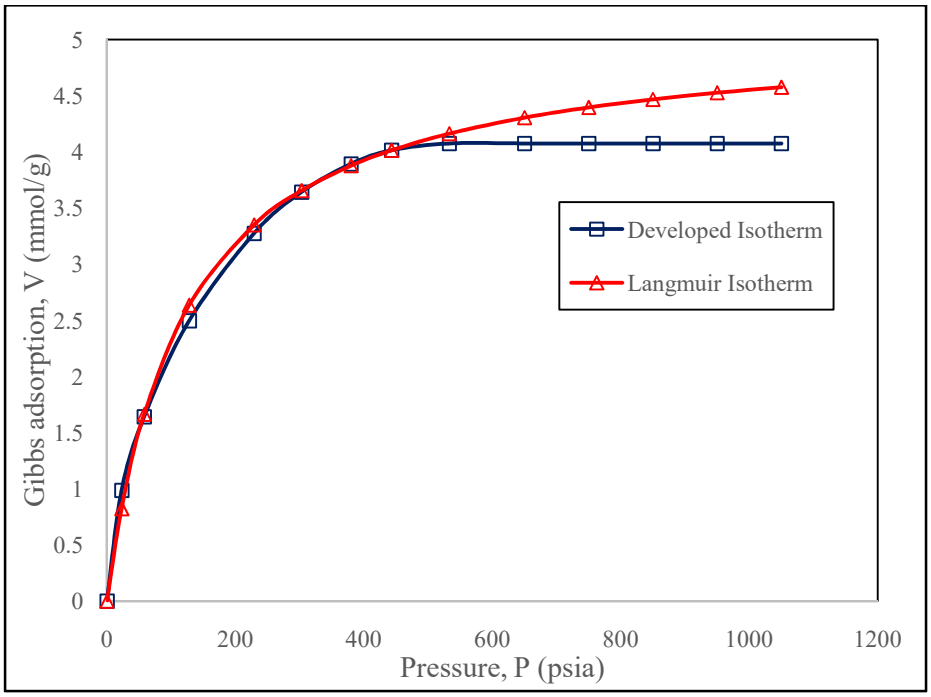

Figure 4.8: Langmuir and the developed isotherms predictions of pure methane adsorption on BPL activated carbon sample at 28.3 ^{o}Cfor high-pressure range

4.2.3Pure Methane Adsorption on Turkey's Shale Sample at 25^{o}C

4.2.3.1 Parameterisation of Pure Methane on Turkey's Shale Sample at 25^{o}C using the Developed Isotherm

Plotting the experimental isotherm from **Table 4.3** and matching it with the relative adsorbed volume-relative pressure curve (see **Figure 3.3**) shows the adsorbate-adsorbent resistance parameter n to be in the range of 0.35 to 0.45.

For each n, the corresponding parameters $b = \frac{V_{last}}{V_{max}}$ and $c = \frac{P_{last}}{P_s}$ were featured. Using *Excel* spreadsheet, the corresponding $V_{max} = \frac{V_{last}}{b}$ and $P_s = \frac{P_{last}}{c}$, and the pressure and adsorbed volume P_β, V_β at the inflexion point β where $\Delta\left(\frac{V}{V_{max}}\right) = \Delta\left(\frac{P}{P_s}\right)$ on the isotherms were evaluated. The parameter n = 0.40 yields the P_β, V_β values (see **Table 4.19**) that correlate with the experimental adsorption isotherm as shown in **Figure 4.9**.

The $\boldsymbol{P_\beta}$, $\boldsymbol{V_\beta}$ values of **572 psia** and **0.0323 mmol/g** correlate with the experimental isotherm (see **Figure 4.9**), and the corresponding $\boldsymbol{P_s}$, $\boldsymbol{V_{max}}$ values of **2005 psia** and **0.0450 mmol/g** are thus considered as the developed isotherm parameters for the experimental adsorption data.

Hence, pure methane adsorption on Turkey's shale sample at 25 ^{o}C is modelled as:

$$\boldsymbol{V(mmol/g)} = \begin{Bmatrix} \mathbf{0.0450}\left\{\frac{\boldsymbol{P}}{\mathbf{2005}} + \left(\mathbf{1} - \frac{\boldsymbol{P}}{\mathbf{2005}}\right)\left(\frac{\boldsymbol{P}}{\mathbf{2005}}\right)^{\mathbf{0.40}}\right\}, for\ P < 2005\ psia \\ \mathbf{0.0450},\ for\ P \geq 2005\ psia \end{Bmatrix} \quad (4.13)$$

where maximum adsorbed volume V_{max} = 0.0450 mmol/g, adsorption saturation pressure P_s = 2005 psia, and n = 0.40 is a parameter that defines Turkey's shale sample resistance to methane adsorption at 25 ^{o}C.

Table 4.19: Adsorption saturation data for establishing the boundary conditions of the developed isotherm for pure methane adsorption on Turkey's shale sample at 25 °C. (Here, V_{last} = 0.0450 mmol/g and P_{last} = 2,005psia)

$b = \frac{V_{last}}{V_{max}}$	n = 0.40				
	$c = \frac{P_{last}}{P_s}$	$V_{max} = \frac{V_{last}}{b}$ (mmol/g)	$P_s = \frac{P_{last}}{c}$ (psia)	$V_\beta = 0.7185 V_{max}$ (mmol/g)	$P_\beta = \frac{2}{7} P_s$ (psia)
0.955	0.6825	0.0471	2938	0.0338	839
0.960	0.6996	0.0469	2866	0.0337	819
0.965	0.7180	0.0466	2793	0.0335	798
0.970	0.7380	0.0464	2717	0.0333	776
0.975	0.7598	0.0461	2639	0.0331	754
0.980	0.7842	0.0459	2557	0.0330	731
0.985	0.8122	0.0457	2469	0.0328	705
0.990	0.8458	0.0454	2371	0.0326	677
0.005	0.8902	0.0452	2252	0.0325	643
1.000	1.0000	**0.0450**	**2005**	**0.0323**	**572**

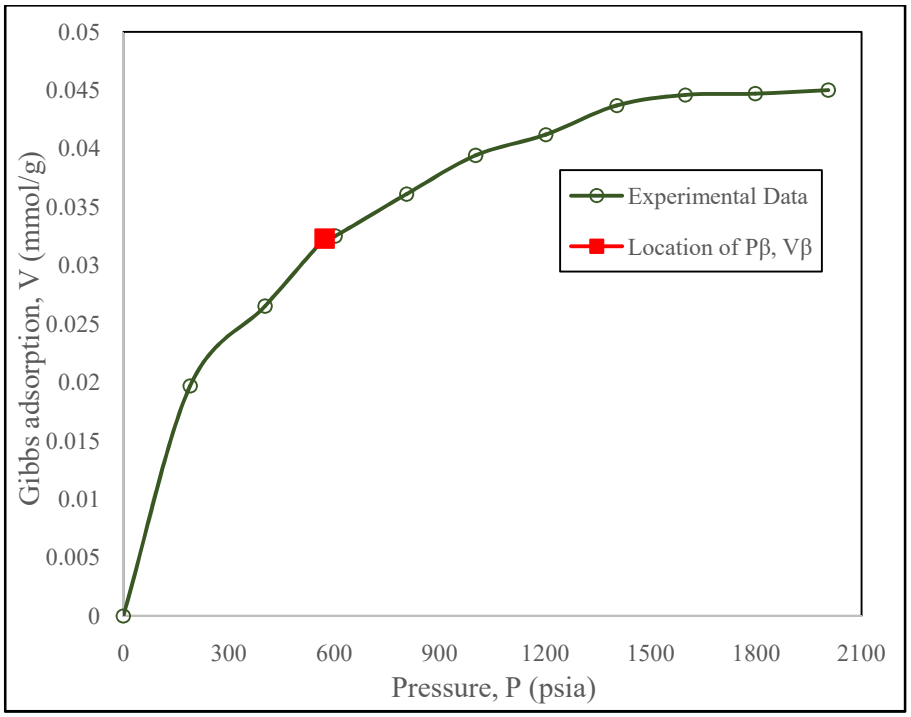

Figure 4.9: Location of P_β, V_β correlation on the experimental isotherm for pure methane adsorption on Turkey's shale sample at 25 ^{o}C

4.2.3.2 Prediction of Pure Methane Adsorption on Turkey's Shale Sample at 25^{o}C using the Developed Isotherm

Prediction of pure methane adsorption on Turkey's shale sample at 25 ^{o}C using the developed isotherm, and the corresponding deviation (error) analysis parameters are presented in **Table 4.20.**

Here, weighted root mean square(WRMS) = 0.1486, weighted average absolute deviation (WAAD) = 0.0937, percent average absolute deviation (%AAD) = 1.4890, root mean square error (RMSE) = 0.0006 mmmol/g and R^2 value = 0.9973.

Table 4.20: Prediction of pure methane adsorption on Turkey's shale sample at 25 ^{o}C using the developed isotherm

Pressure, P (psia)	Gibbs adsorption, V (mmol/g)		Deviation (Error) Analysis			
	Experimental	Developed Isotherm	σ_{Exp} (mmol/g)	V_{Cal} - V_{Exp} (mmol/g)	$\frac{V_{Cal} - V_{Exp}}{\sigma_{Exp}}$	$\frac{V_{Cal} - V_{Exp}}{V_{Exp}}$
190	0.0197	0.0201	0.0024	0.0004	0.1667	0.0203
403	0.0265	0.0280	0.0037	0.0015	0.4054	0.0566
602	0.0325	0.0330	0.0050	0.0005	0.1000	0.0154
805	0.0361	0.0368	0.0063	0.0007	0.1111	0.0194
1002	0.0394	0.0395	0.0077	0.0001	0.0130	0.0025
1201	0.0412	0.0417	0.0092	0.0005	0.0543	0.0121
1403	0.0437	0.0432	0.0107	-0.0005	-0.0467	-0.0114
1598	0.0446	0.0442	0.0122	-0.0004	-0.0330	-0.0090
1798	0.0447	0.0448	0.0137	0.0001	0.0073	0.0022
2005	0.0450	0.0450	0.0153	0	0	0

4.2.3.3 Parameterisation of Pure Methane Adsorption on Turkey's Shale Sample at 25 ^{o}Cusing Langmuir Isotherm

The variation of P/V with P for pure methane adsorption on Turkey's shale sample at 25 ^{o}C is shown in **Table 4.21** and the best fit line of the plot of P/V versus P (shown in **Figure 4.10**) yields the equation:

$$y = 18.261x + 7081.4 \tag{4.14}$$

where

$$\text{slope } m = 18.261 = {}^{1}/_{V_L} \tag{4.15}$$

and y-axis intercept

$$C = 7081.4 = \left(\frac{1}{V_L}\right) P_L \tag{4.16}$$

Here, Langmuir volume $\boldsymbol{V_L}$ and Langmuir pressure $\boldsymbol{P_L}$ are respectively obtained as **0.0548 mmol/g** and**387.79 psia**. Hence, pure methane adsorption on Turkey's shale sample at 25 ^{o}C is modelled as:

$$\boldsymbol{V(mmol/g) = 0.0548\left(\frac{P}{P+387.79}\right)} \tag{4.17}$$

where P is pressure (psia) and Langmuir constant

$$b = \frac{1}{P_L} = 0.002579 \text{ psia}^{-1} \tag{4.18}$$

Table 4.21: Parameters for plotting Langmuir isotherm for pure

methane adsorption on Turkey's shale sample at 25 ^{o}C

Experimental		$\frac{Pressure}{Volume}$, P/V (psia/mmol/g)
Pressure, P (psia)	**Gibbs adsorption, V (mmol/g)**	
190	0.0197	9645
403	0.0265	15207
602	0.0325	18523
805	0.0361	22230
1002	0.0394	25431
1201	0.0412	29150
1403	0.0437	32105
1598	0.0446	34739
1798	0.0447	40224
2005	0.0450	44556

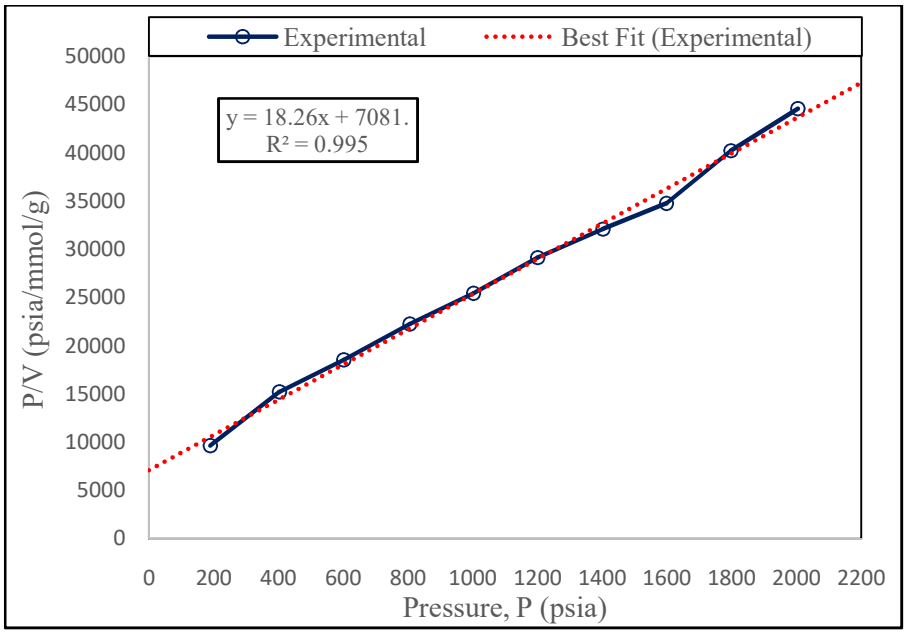

Figure 4.10: Plot of P/V versus P for pure methane adsorption on Turkey's shale sample at 25 ^{o}C

4.2.3.4 Prediction of Pure Methane Adsorption on Turkey's Shale Sample at 25 ^{o}C using Langmuir Isotherm

Prediction of pure methane adsorption on Turkey's shale sample at 25 ^{o}C using Langmuir isotherm, and the corresponding deviation (error) analysis parameters are presented in **Table 4.22**.

Here, weighted root mean square (WRMS) = 0.2652, weighted average absolute deviation (WAAD) = 0.1628, percent average absolute deviation (%AAD) = 2.5440, root mean square error (RMSE) = 0.0009 mmmol/g and R^2 value = 0.9891.

Table 4.22: Prediction of pure methane adsorption on Turkey's shale sample at 25 ^{o}C using Langmuir isotherm

Pressure, P (psia)	Gibbs adsorption, V (mmol/g)		Deviation (Error) Analysis			
	Experimental	Langmuir Isotherm	σ_{Exp} (mmol/g)	$V_{Cal} - V_{Exp}$ (mmol/g)	$\frac{V_{Cal} - V_{Exp}}{\sigma_{Exp}}$	$\frac{V_{Cal} - V_{Exp}}{V_{Exp}}$
190	0.0197	0.0180	0.0024	-0.0017	-0.7083	-0.0863
403	0.0265	0.0279	0.0037	0.0014	0.3784	0.0528
602	0.0325	0.0333	0.0050	0.0008	0.1600	0.0246
805	0.0361	0.0370	0.0063	0.0009	0.1429	0.0249
1002	0.0394	0.0395	0.0077	0.0001	0.0130	0.0025
1201	0.0412	0.0414	0.0092	0.0002	0.0217	0.0049
1403	0.0437	0.0429	0.0107	-0.0008	-0.0748	-0.0183
1598	0.0446	0.0441	0.0122	-0.0005	-0.0410	-0.0112
1798	0.0447	0.0451	0.0137	0.0004	0.0292	0.0089
2005	0.0450	0.0459	0.0153	0.0009	0.0588	0.0200

4.2.3.5 Generalisation of the Developed Isotherm forPure Methane Adsorption on Turkey's Shale Sample at 25 ^{o}C

To validate and generalise the developed isotherm, adsorption predictions by Langmuir and the developed isotherm are correlated with the experimental data. The generalisation of the developed isotherm for pure methane adsorption on Turkey's shale sample at 25 ^{o}C is shown in **Table 4.23** and **Figure 4.11**.

Table 4.23: Generalisation of the developed isotherm for pure methane adsorption on Turkey's shale sample at 25 ^{o}C

Pressure, P (psia)	Gibbs adsorption, *V* (mmol/g)		
	Experimental	Developed	Langmuir

		Isotherm	Isotherm
190	0.0197	0.0201	0.0180
403	0.0265	0.0280	0.0279
602	0.0325	0.0330	0.0333
805	0.0361	0.0368	0.0370
1002	0.0394	0.0395	0.0395
1201	0.0412	0.0417	0.0414
1403	0.0437	0.0432	0.0429
1598	0.0446	0.0442	0.0441
1798	0.0447	0.0448	0.0451
2005	0.0450	0.0450	0.0459

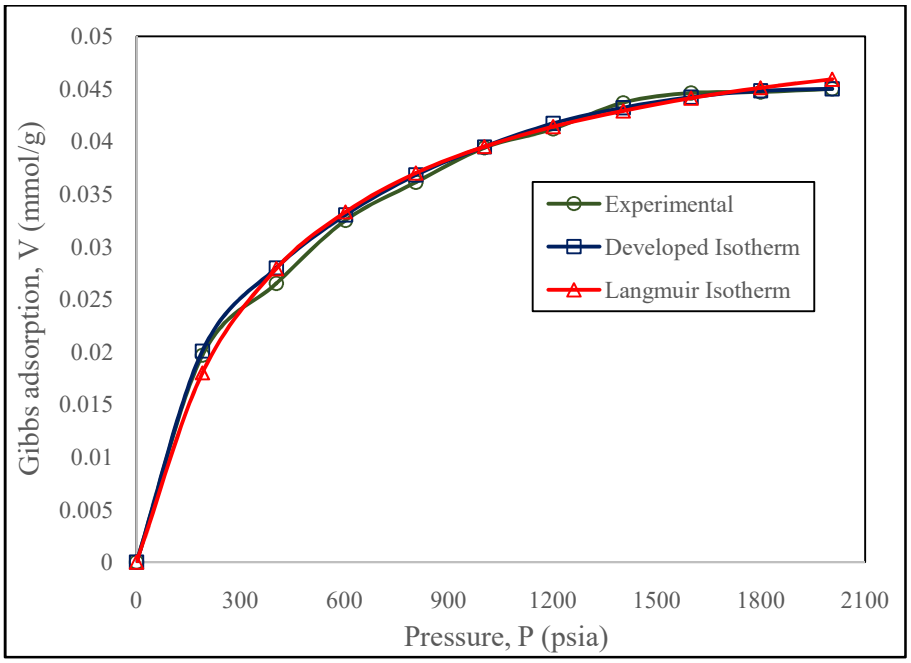

Figure 4.11: Generalisation of the developed isotherm for pure methane adsorption on Turkey's shale sample at 25 ^{o}C

4.2.3.6 Comparison of High-Pressure Adsorption Prediction for Pure Methane Adsorption on Turkey's Shale Sample at 25 ^{o}C

Langmuir and the developed isotherms predictions of pure methane adsorption on Turkey's shale sample at 25 ^{o}C for high-pressure range are compared in **Table 4.24** and **Figure 4.12**.

The developed isotherm predicts a maximum adsorbed volume of **0.0450 mmol/g** at an adsorption saturation pressure of **2005psia**. However, by Langmuir isotherm prediction,

a maximum adsorbed volume of **0.0548 mmol/g** is attained at an infinite adsorption saturation pressure. **Figure 4.12** shows that adsorption prediction by Langmuir isotherm is not reliable at higher pressures because of its inefficiency in defining the onset of adsorption saturation pressure; this contributes to an overestimation of maximum adsorbed volume.

Table 4.24: Langmuir and the developed isotherms predictionsof pure methane adsorption on Turkey's shale sampleat 25 ^{o}C for high-pressure range

Pressure, P (psia)	**Gibbs adsorption, *V* (mmol/g)**	
	Developed Isotherm	**Langmuir Isotherm**
190	0.0201	0.0180
602	0.0330	0.0333
1002	0.0395	0.0395
1403	0.0432	0.0429
1798	0.0448	0.0451
2005	0.0450	0.0459
2400	0.0450	0.0472
2800	0.0450	0.0481
3200	0.0450	0.0489
3600	0.0450	0.0495
4000	0.0450	0.0500

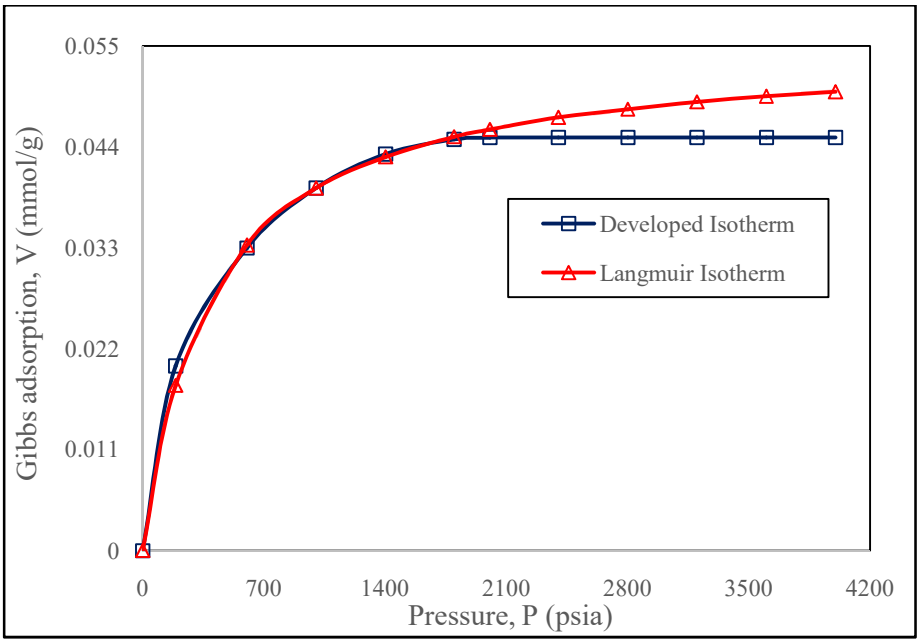

Figure 4.12: Langmuir and the developed isotherms predictions of pure methaneadsorption on Turkey's shale sample at 25 ^{o}Cfor high-pressure range

4.2.4Pure Nitrogen Adsorption on Dry Activated Carbon Sample at 328.2 K

4.2.4.1 Parameterisation of Pure Nitrogen Adsorption on Dry Activated Carbon Sample at 328.2 K using the Developed Isotherm

Plotting the experimental isotherm from **Table 4.4** and matching it with the relative adsorbed volume-relative pressure curve (see **Figure 3.3**) shows the adsorbate-adsorbent resistance parameter n to be in the range of 0.35 to 0.45.

For each n, the corresponding parameters $b = \frac{V_{last}}{V_{max}}$ and $c = \frac{P_{last}}{P_s}$ were featured. Using *Excel* spreadsheet, the corresponding $V_{max} = \frac{V_{last}}{b}$ and $P_s = \frac{P_{last}}{c}$, and the pressure and adsorbed volume P_β, V_β at the inflexion point β where $\Delta\left(\frac{V}{V_{max}}\right) = \Delta\left(\frac{P}{P_s}\right)$ on the isotherms were evaluated. The parameter n = 0.35 yields the P_β, V_β values (see **Table 4.25**) that correlate with the experimental adsorption isotherm as shown in **Figure 4.13**.

The $\boldsymbol{P_\beta}$, $\boldsymbol{V_\beta}$ values of **3.55 MPa** and **2.241 mmol/g** correlate with the experimental isotherm (see **Figure 4.13**), and the corresponding $\boldsymbol{P_s}$, $\boldsymbol{V_{max}}$ values of **13.70 MPa** and **3.108 mmol/g** are thus considered as the developed isotherm parameters for the experimental adsorption data.

Hence, pure nitrogen adsorption on activated carbon sample at 328.2K is modelled as:

$$\boldsymbol{V(mmol/g)} = \begin{Bmatrix} \mathbf{3.108}\left\{\frac{\boldsymbol{P}}{\mathbf{13.70}} + \left(\mathbf{1} - \frac{\boldsymbol{P}}{\mathbf{13.70}}\right)\left(\frac{\boldsymbol{P}}{\mathbf{13.70}}\right)^{\mathbf{0.35}}\right\}, for\ P < 13.70\ MPa \\ \mathbf{3.108},\ for\ P \geq 13.70\ MPa \end{Bmatrix} \quad (4.19)$$

where maximum adsorbed volume V_{max} = 3.108 mmol/g, adsorption saturation pressure P_s = 13.70 MPa, and n = 0.35 is a parameter that defines dry activated carbon resistance to pure nitrogen adsorption at 328.2 K.

Table 4.25: Adsorption saturation data for establishing the boundary conditions of the developed isotherm for pure nitrogen adsorption on dry activated carbon sample at 328.2 K. (Here, V_{last} = 3.108 mmol/g and P_{last} = 13.70 MPa)

$b = \frac{V_{last}}{V_{max}}$	n = 0.35				
	$c = \frac{P_{last}}{P_s}$	$V_{max} = \frac{V_{last}}{b}$ (mmol/g)	$P_s = \frac{P_{last}}{c}$ (MPa)	$V_\beta = 0.7500 V_{max}$ (mmol/g)	$P_\beta = \frac{1}{2} P_s$ (MPa)
0.955	0.6636	3.254	20.64	2.346	5.35
0.960	0.6815	3.327	20.10	2.334	5.21
0.965	0.7009	3.221	19.54	2.328	5.07
0.970	0.7218	3.204	18.98	2.310	4.92
0.975	0.7449	3.188	18.39	2.299	4.77
0.980	0.7706	3.171	17.78	2.287	4.61
0.985	0.8002	3.155	17.12	2.275	4.44
0.990	0.8358	3.139	16.39	2.263	4.25
0.005	0.8829	3.124	15.52	2.253	4.02
1.000	1.0000	**3.108**	**13.70**	**2.241**	**3.55**

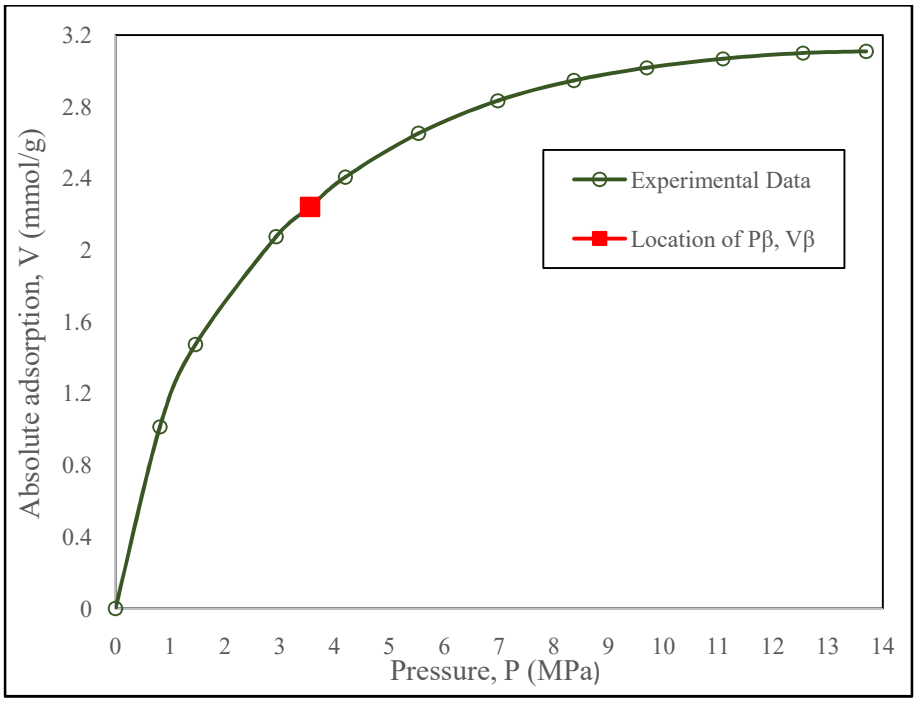

Figure 4.13: Location of P_β, V_β correlation on the experimental isotherm for pure nitrogen adsorption on activated carbon sample at 328 K

4.2.4.2 Prediction of Pure Nitrogen Adsorption on Dry Activated Carbon Sample at 328.2 K using the Developed Isotherm

Prediction of pure nitrogen adsorption on dry activated carbon sample at 328.2 K using the developed isotherm, and the corresponding deviation (error) analysis parameters are presented in **Table 4.26.**

Here, weighted root mean square, WRMS = 2.1947, weighted average absolute deviation, WAAD = 1.2844, percent average absolute deviation, %AAD = 3.7000, root mean square error, RMSE = 0.0892 mmmol/g and R^2 value = 0.9947.

Table 4.26: Prediction of pure nitrogen adsorption on dry activated carbon sample at 328.2 K using the developed isotherm

Pressure, P (MPa)	Absolute adsorption, V (mmol/g)		Deviation (Error) Analysis			
	Experimental	Developed Isotherm	σ_{Exp} (mmol/g)	V_{Cal} - V_{Exp} (mmol/g)	$\frac{V_{Cal} - V_{Exp}}{\sigma_{Exp}}$	$\frac{V_{Cal} - V_{Exp}}{V_{Exp}}$
0.81	1.015	1.270	0.041	0.255	6.219	0.251
1.46	1.473	1.599	0.040	0.126	3.150	0.085
2.93	2.075	2.089	0.039	0.014	0.359	0.007
4.19	2.407	2.376	0.039	-0.031	-0.795	-0.013
5.53	2.651	2.604	0.039	-0.047	-1.205	-0.018
6.98	2.834	2.787	0.039	-0.047	-1.205	-0.017
8.36	2.946	2.916	0.039	-0.030	-0.769	-0.010
9.69	3.018	3.004	0.040	-0.014	-0.350	-0.005
11.08	3.068	3.065	0.039	-0.003	-0.077	-0.001
12.54	3.100	3.100	0.040	0	0	0
13.70	3.108	3.108	0.040	0	0	0

4.2.4.3 Parameterisation of Pure Nitrogen Adsorption on Dry Activated Carbon Sample at 328.2 K using Langmuir Isotherm

The variation of $^{P}/_{V}$ with P for pure nitrogen adsorption on activated carbon sample at 328.2 K is shown in **Table 4.27** and the best fit line of the plot of $^{P}/_{V}$ versus P(shown in **Figure 4.14**) yields the equation:

$$y = 0.2758x + 0.5722 \tag{4.20}$$

where

$$\text{slope } m = 0.2758 = {}^{1}/_{V_L} \tag{4.21}$$

and y-axis intercept

$$C = 0.5722 = \left(\frac{1}{V_L}\right) P_L \tag{4.22}$$

Here, Langmuir volume $\boldsymbol{V_L}$ and Langmuir pressure $\boldsymbol{P_L}$ are respectively obtained as **3.626 mmol/g** and **2.075 MPa**. Hence, pure nitrogen adsorption on dry activated carbon sample at 328.2 K is modelled as:

$$\boldsymbol{V(mmol/g) = 3.626\left(\frac{P}{P+2.075}\right)} \tag{4.23}$$

where P is pressure (MPa) and Langmuir constant

$$b = \frac{1}{P_L} = 0.482 \text{ MPa}^{-1} \tag{4.24}$$

Table 4.27: Parameters for plotting Langmuir isotherm for pure nitrogen adsorption on dry activated carbon sample at 328.2 K

Experimental	$\boldsymbol{\frac{Pressure}{\quad}}$,

Pressure, P (MPa)	**Absolute adsorption, V (mmol/g)**	P/V **(MPa/mmol/g)**
0.81	1.015	0.7980
1.46	1.473	0.9912
2.93	2.075	1.4120
4.19	2.407	1.7408
5.53	2.651	2.0860
6.98	2.834	2.4629
8.36	2.946	2.8377
9.69	3.018	3.2107
11.08	3.068	3.6115
12.54	3.100	4.0452
13.70	3.108	4.4080

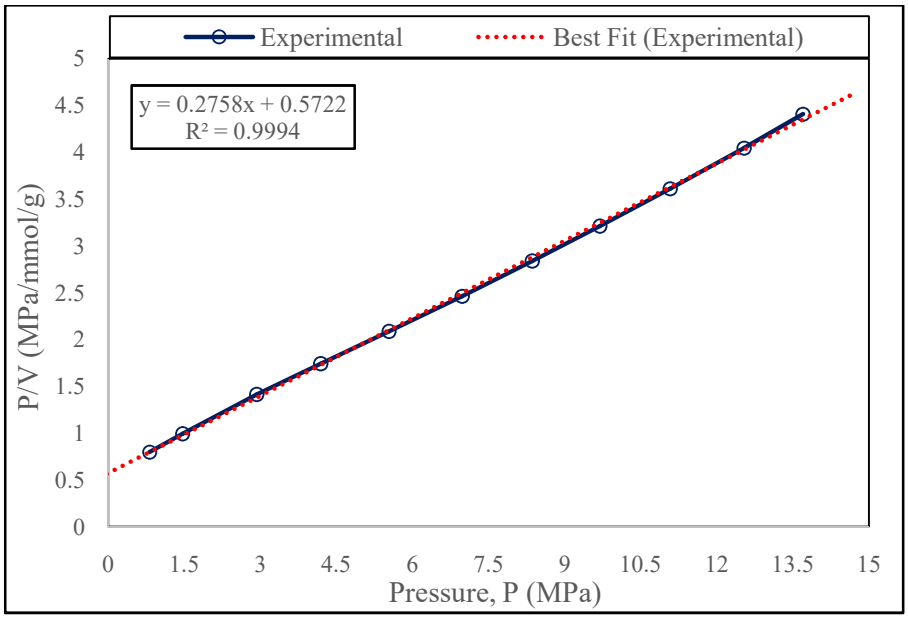

Figure 4.14: Plot of P/V versus P for pure nitrogen adsorption on activated carbon sample at 328 K

4.2.4.4 Prediction of Pure Nitrogen Adsorption on Dry Activated Carbon Sample at 328.2 K using Langmuir Isotherm

Prediction of pure nitrogen adsorption on dry activated carbon sample at 328.2 K using Langmuir isotherm, and the corresponding deviation (error) analysis parameters are presented in **Table 4.28.**

Here, weighted root mean square, WRMS = 0.7540, weighted average absolute deviation, WAAD = 0.6600, percent average absolute deviation, %AAD = 1.0545, root mean square error, RMSE = 0.0297 mmmol/g and R^2 value = 0.9983.

Table 4.28: Prediction of pure nitrogen adsorption on dry activated carbon sample at 328.2 K using Langmuir isotherm

Pressure, P (MPa)	Absolute adsorption, V (mmol/g)		Deviation (Error) Analysis			
	Experimental	Langmuir Isotherm	σ_{Exp} (mmol/g)	V_{Cal} - V_{Exp} (mmol/g)	$\frac{V_{Cal} - V_{Exp}}{\sigma_{Exp}}$	$\frac{V_{Cal} - V_{Exp}}{V_{Exp}}$
0.81	1.015	1.018	0.041	0.003	0.073	0.003
1.46	1.473	1.498	0.040	0.025	0.625	0.017
2.93	2.075	2.123	0.039	0.048	1.231	0.023
4.19	2.407	2.425	0.039	0.018	0.462	0.007
5.53	2.651	2.637	0.039	-0.014	-0.359	-0.005
6.98	2.834	2.795	0.039	-0.039	-1.000	-0.014
8.36	2.946	2.905	0.039	-0.041	-1.051	-0.014
9.69	3.018	2.986	0.040	-0.032	-0.800	-0.011
11.08	3.068	3.054	0.039	-0.014	0.359	-0.005
12.54	3.100	3.111	0.040	0.011	0.275	0.004
13.70	3.108	3.149	0.040	0.041	1.025	0.013

4.2.4.5 Generalisation of the Developed Isotherm for Pure Nitrogen Adsorption on Activated Carbon at 328.2 K

To validate and generalise the developed isotherm, adsorption predictions by Langmuir and the developed isotherm are correlated with the experimental data. The generalisation of the developed isotherm for pure nitrogen adsorption on dry activated carbon sample at 328.2 K is shown in **Table 4.29** and **Figure 4.15**.

Table 4.29: Generalisation of the developed isotherm for pure nitrogen adsorption on dry activated carbon sample at 328.2 K

Pressure, P (MPa)	**Absolute adsorption, *V* (mmol/g)**		
	Experimental	**Developed Isotherm**	**Langmuir Isotherm**
0.81	1.015	1.270	1.018
1.46	1.473	1.599	1.498
2.93	2.075	2.089	2.123
4.19	2.407	2.376	2.425
5.53	2.651	2.604	2.637
6.98	2.834	2.787	2.795
8.36	2.946	2.916	2.905
9.69	3.018	3.004	2.986
11.08	3.068	3.065	3.054
12.54	3.100	3.100	3.111
13.70	3.108	3.108	3.149

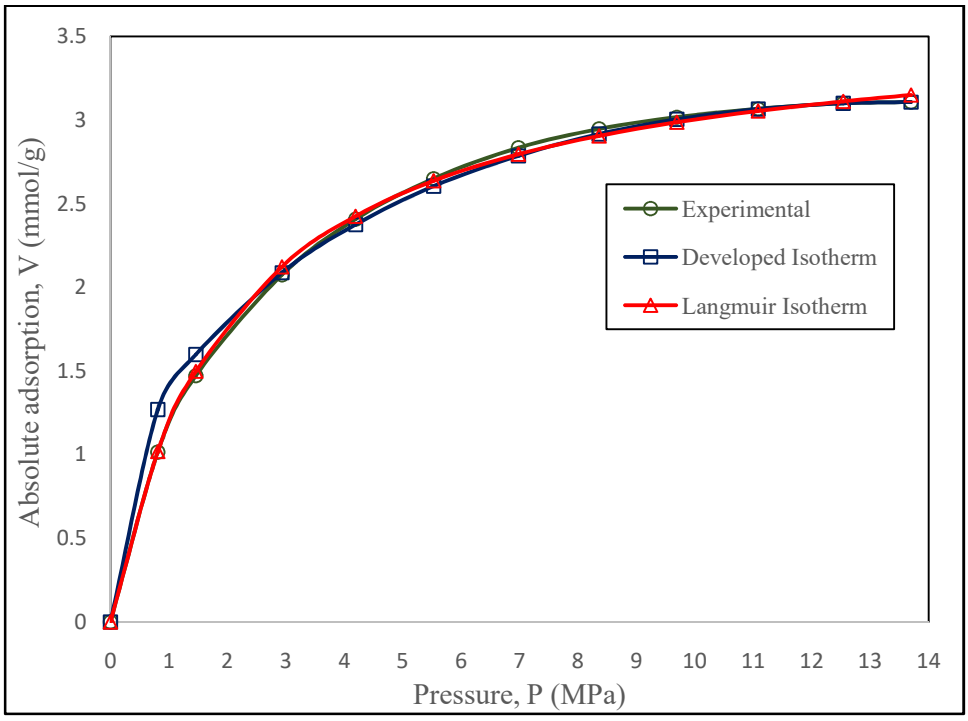

Figure 4.15: Generalisation of the developed isotherm for pure nitrogen adsorption on dry activated carbon sample at 328.2 K

4.2.4.6 Comparison of High-Pressure Adsorption Prediction for Pure Nitrogen Adsorption on Activated Carbon at 328.2 K

Langmuir and the developed isotherms predictions of pure nitrogen adsorption on dry activated carbon at 328.2 K for high-pressure range are compared in **Table 4.30** and **Figure 4.16**.

The developed isotherm predicts a maximum adsorbed volume of **3.108 mmol/g** at an adsorption saturation pressure of **13.70 MPa**. However, by Langmuir isotherm prediction, a maximum adsorbed volume of **3.626 mmol/g**is attained at an infinite adsorption saturation pressure.**Figure 4.16** shows that adsorption prediction by Langmuir isotherm is not reliable at higher pressures because of its inefficiency in defining the onset of adsorption saturation pressure; this contributes to an overestimation of maximum adsorbed volume.

Table 4.30: Langmuir and the developed isotherms predictions of pure nitrogen adsorption on dry activated carbon at 328.2 K for high-pressure range

Pressure, P (MPa)	**Absolute adsorption, V (mmol/g)**	
	Developed Isotherm	**Langmuir Isotherm**
0.81	1.270	1.018
2.93	2.089	2.123
5.53	2.604	2.637
8.36	2.916	2.905
11.08	3.065	3.054
13.70	3.108	3.149
16.00	3.108	3.210
18.00	3.108	3.251
20.00	3.108	3.285
22.00	3.108	3.313
24.00	3.108	3.337

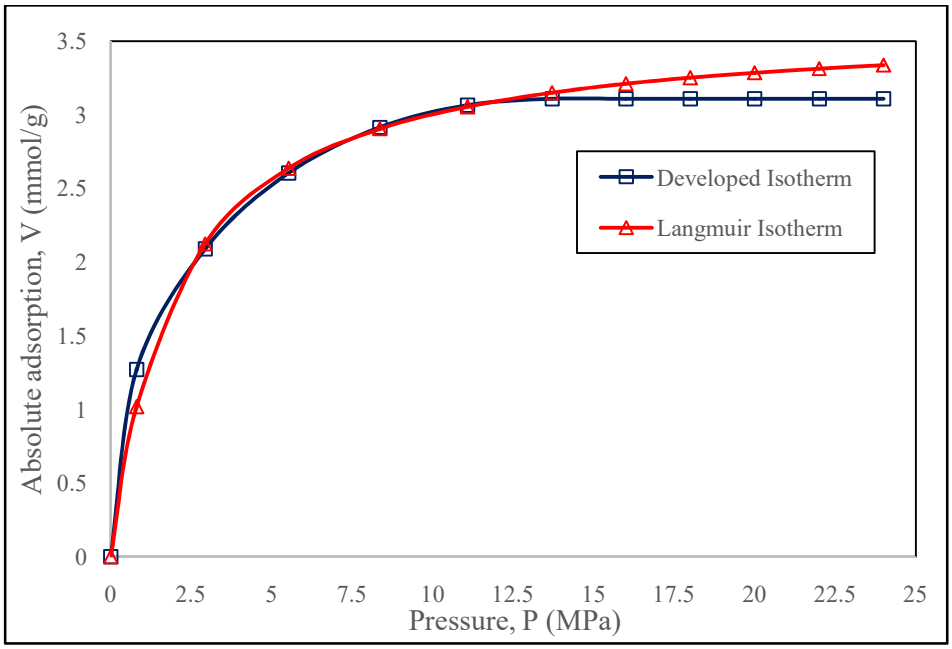

Figure 4.16: Langmuir and the developed isotherms predictions of pure nitrogen adsorption on dry activated carbon at 328.2 K for high-pressure range

4.2.5Pure Methane Adsorption on Dry Tiffany Mixed Coal Sample at 130 ^{o}F

4.2.5.1 Parameterisation of Pure Methane Adsorption on Dry Tiffany Mixed Coal Sample at 130 ^{o}Fusing the Developed Isotherm

Plotting the experimental isotherm from **Table 4.5** and matching it with the relative adsorbed volume-relative pressure curve (see **Figure 3.3**) shows the adsorbate-adsorbent resistance parameter n to be in the range of 0.45 to 0.55.

For each n, the corresponding parameters $b = \frac{V_{last}}{V_{max}}$ and $c = \frac{P_{last}}{P_s}$ were featured. Using *Excel* spreadsheet, the corresponding $V_{max} = \frac{V_{last}}{b}$ and $P_s = \frac{P_{last}}{c}$, and the pressure and adsorbed volume P_β, V_β at the inflexion point β where $\Delta\left(\frac{V}{V_{max}}\right) = \Delta\left(\frac{P}{P_s}\right)$ on the isotherms were evaluated. The parameter n = 0.50 yields the P_β, V_β values (see **Table 4.31**) that correlate with the experimental adsorption isotherm as shown in **Figure 4.17**.

The $\boldsymbol{P_\beta}$, $\boldsymbol{V_\beta}$ values of **765.0 psia** and **233.2 scf/ton** correlate with the experimental isotherm (see **Figure 4.17**), and the corresponding $\boldsymbol{P_s}$, $\boldsymbol{V_{max}}$ values of **2294.9 psia** and **324.7 scf/ton** are thus considered as the developed isotherm parameters for the experimental adsorption data.

Hence, pure methane adsorption on dry Tiffany mixed coal sample at 130 ^{o}F is modelled as:

$$\boldsymbol{V(scf/ton)} = \begin{Bmatrix} \mathbf{324.7}\left\{\frac{\boldsymbol{P}}{\mathbf{2294.9}} + \left(\mathbf{1} - \frac{\boldsymbol{P}}{\mathbf{2294.9}}\right)\left(\frac{\boldsymbol{P}}{\mathbf{2294.9}}\right)^{\mathbf{0.50}}\right\}, for\ P < 2294.9\ psia \\ \mathbf{324.7},\ for\ P \geq 2294.9\ psia \end{Bmatrix} \quad (4.25)$$

where maximum adsorbed volume V_{max} = 324.7 scf/ton, adsorption saturation pressure P_s = 2294.9 psia, and n = 0.50 is a parameter that defines dry Tiffany mixed coal sample resistance to pure methane adsorption at 130 ^{o}F.

Table 4.31: Adsorption saturation data for establishing the boundary conditions of the developed isotherm for pure methane adsorption on dry Tiffany mixed coal sample at 130 °F(Here, V_{last} = 316.6scf/ton and P_{last} = 1,796.9psia)

$b = \frac{V_{last}}{V_{max}}$	n = 0.50				
	$c = \frac{P_{last}}{P_s}$	$V_{max} = \frac{V_{last}}{b}$ (scf/ton)	$P_s = \frac{P_{last}}{c}$ (psia)	$V_\beta = 0.7182 V_{max}$ (scf/ton)	$P_\beta = \frac{1}{3} P_s$ (psia)
0.955	0.7120	331.5	2523.7	238.1	841.2
0.960	0.7278	329.8	2468.9	236.9	823.0
0.965	0.7447	328.1	2412.9	235.6	804.3
0.970	0.7629	326.4	2355.3	234.4	785.1
0.975	0.7830	**324.7**	**2294.9**	**233.2**	**765.0**
0.980	0.8052	323.1	2231.6	232.0	743.9
0.985	0.8307	321.4	2163.1	230.8	721.0
0.990	0.8612	319.8	2086.6	229.7	695.5
0.005	0.9013	318.2	1993.7	228.5	664.6
1.000	1.0000	316.6	1796.9	227.4	599.0

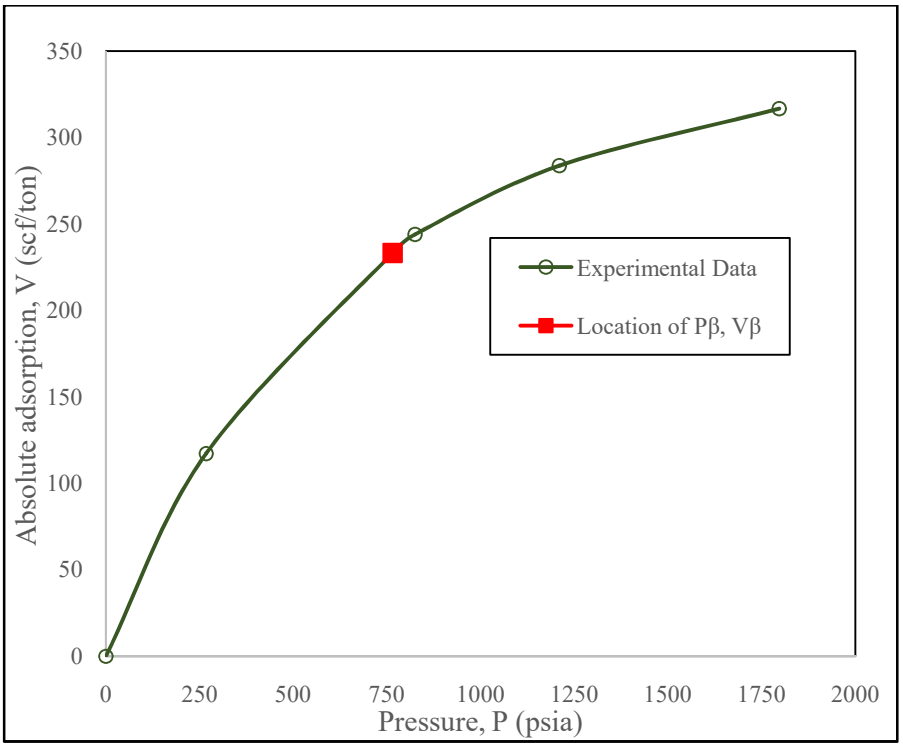

Figure 4.17: Location of P_β, V_β correlation on the experimental isotherm for pure methane adsorption on dry Tiffany mixed coal sample at 130 ^{o}F

4.2.5.2 Prediction of Pure Methane Adsorption on Dry Tiffany Mixed Coal Sample at 130 ^{o}F using the Developed Isotherm

Prediction of pure methane adsorption on dry Tiffany mixed coal sample at 130 ^{o}Fusing the developed isotherm, and the corresponding deviation (error) analysis parameters are presented in **Table 4.32**.

Here, weighted root mean square, WRMS = 2.2152, weighted average absolute deviation, WAAD = 1.2160, percent average absolute deviation, %AAD = 3.6250, root mean square error, RMSE = 7.8630 scf/ton and R^2 value = 0.9977.

Table 4.32: Prediction of pure methane adsorption on dry Tiffany mixed coal sample at 130 ^{o}Fusing the developed isotherm

Pressure, P (psia)	Absolute adsorption, V (scf/ton)		Deviation (Error) Analysis			
	Experimental	Developed Isotherm	σ_{Exp} (scf/ton)	V_{Cal} - V_{Exp} (scf/ton)	$\frac{V_{Cal} - V_{Exp}}{\sigma_{Exp}}$	$\frac{V_{Cal} - V_{Exp}}{V_{Exp}}$
255.9	117.0	132.5	3.510	15.5	4.416	0.132
824.9	243.9	241.4	7.317	-2.5	-0.342	-0.010
1210.2	283.6	282.7	8.508	-0.9	-0.106	-0.003
1796.9	316.6	316.6	9.498	0	0	0

4.2.5.3 Parameterisation of Pure Methane Adsorption on Dry Tiffany Mixed Coal Sample at 130 ^{o}F using Langmuir Isotherm

The variation of P/V with P for pure methane adsorption on dry Tiffany mixed coal sample at 130 ^{o}F is shown in **Table 4.33** and the best fit line of the plot of P/V versus P (shown in **Figure 4.18**) yields the equation:

$$y = 0.0023x + 1.5619 \tag{4.26}$$

where

$$\text{slope } m = 0.0023 = {}^{1}/_{V_L} \quad (4.27)$$

and y-axis intercept

$$C = 1.5619 = \left(\frac{1}{V_L}\right) P_L \quad (4.28)$$

Here, Langmuir volume $\boldsymbol{V_L}$ and Langmuir pressure $\boldsymbol{P_L}$ are respectively obtained as **434.78scf/ton**and **679.09 psia**. Hence,pure methane adsorption on dry Tiffany mixed coal sample at 130 ^{o}F is modelled as:

$$\boldsymbol{V(scf/ton) = 434.78\left(\frac{P}{P+679.09}\right)} \quad (4.29)$$

where P is pressure (psia) and Langmuir constant

$$b = \frac{1}{P_L} = 0.001473 \text{ psia}^{-1} \quad (4.30)$$

Table 4.33: Parameters for plotting Langmuir isotherm for pure methane adsorption on dry Tiffany mixed coal sample at 130 ^{o}F

Experimental		$\frac{Pressure}{Volume}$, P/V
Pressure, P (psiaa)	**Absolute adsorption, V (scf/ton)**	**(psia/scf/ton)**
255.9	117.0	2.1872
824.9	243.9	3.3821
1210.2	283.6	4.2673
1796.9	316.6	5.6756

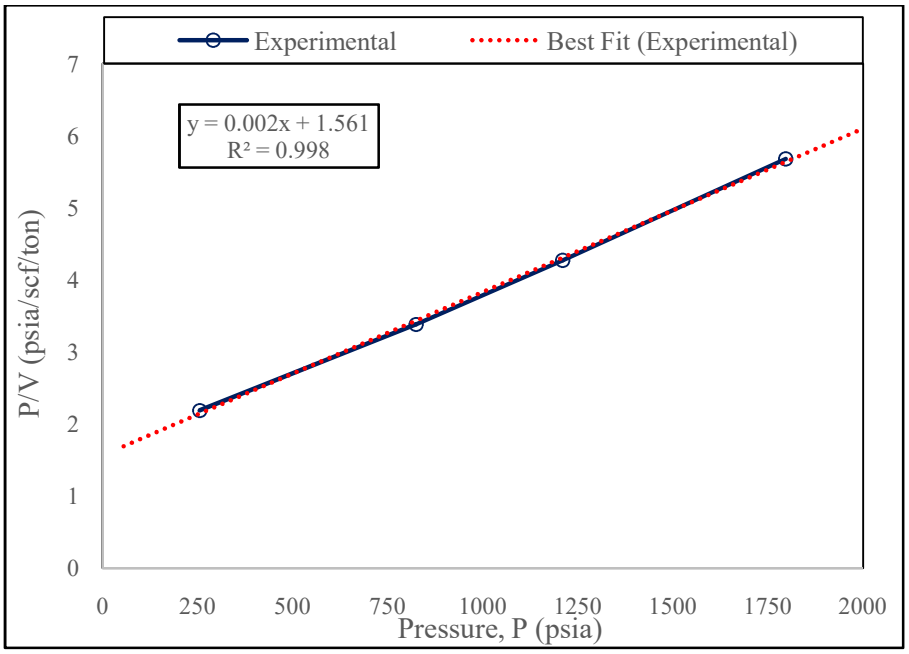

Figure 4.18: Plot of P/V versus P forpure methane adsorption on dry Tiffany mixed coal sample at 130 ^{o}F

4.2.5.4 Prediction of Pure Methane Adsorption on Dry Tiffany Mixed Coal Sample at 130 ^{o}F using Langmuir Isotherm

Prediction of pure methane adsorption on dry Tiffany mixed coal sample at 130 ^{o}Fusing Langmuir isotherm, and the corresponding deviation (error) analysis parameters are presented in**Table 4.34**.

Here, weighted root mean square, WRMS = 0.5572, weighted average absolute deviation, WAAD = 0.5058, percent average absolute deviation, %AAD = 1.5000, root mean square error, RMSE = 3.8852 scf/ton and R^2 value = 0.9989.

Table 4.34: Prediction of pure methane adsorption on dry Tiffany mixed coal sample at 130 ^{o}F using Langmuir isotherm

Pressure, P (psia)	Absolute adsorption, V (scf/ton)		Deviation (Error) Analysis			
	Experimental	Langmuir Isotherm	σ_{Exp} (scf/ton)	$V_{Cal} - V_{Exp}$ (scf/ton)	$\frac{V_{Cal} - V_{Exp}}{\sigma_{Exp}}$	$\frac{V_{Cal} - V_{Exp}}{V_{Exp}}$
255.9	117.0	119.0	3.510	2.000	0.570	0.017
824.9	243.9	238.5	7.317	-5.400	-0.738	-0.022
1210.2	283.6	278.5	8.508	-5.100	-0.599	-0.018
1796.9	316.6	315.5	9.498	-1.100	-0.116	-0.003

4.2.5.5 Generalisation of the Developed Isotherm for Pure Methane Adsorption on Dry Tiffany Mixed Coal Sample at 130 ^{o}F

To validate and generalise the developed isotherm, adsorption predictions by Langmuir and the developed isotherm are correlated with the experimental data. The generalisation of the developed isotherm for pure methane adsorption on dry Tiffany mixed coal sample at 130 ^{o}F is shown in **Table 4.35** and **Figure 4.19**.

Table 4.35: Generalisation of the developed isotherm for pure methane adsorption on dry Tiffany mixed coal sample at 130 ^{o}F

Pressure, P (psia)	**Absolute adsorption, *V* (scf/ton)**		
	Experimental	**Developed Isotherm**	**Langmuir Isotherm**
255.9	117.0	132.5	119.0
824.9	243.9	241.4	238.5
1210.2	283.6	282.7	278.5
1796.9	316.6	316.6	315.5

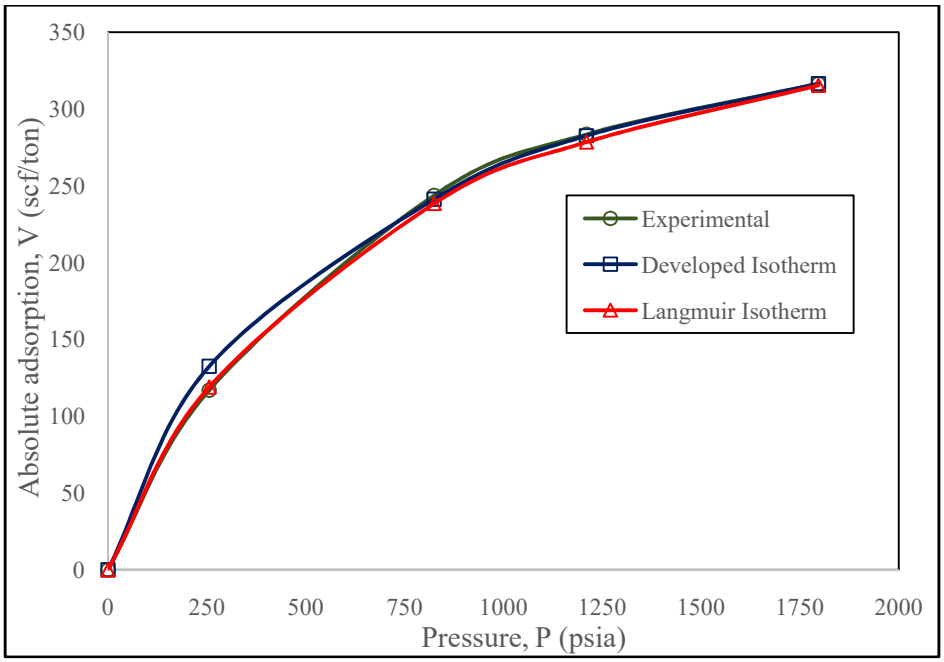

Figure 4.19: Generalisation of the developed isotherm for pure methane adsorption on dry Tiffany mixed coal sample at 130 ^{o}F

4.2.5.6 Comparison of High-Pressure Adsorption Prediction for Pure Methane Adsorption on Dry Tiffany Mixed Coal Sample at 130 ^{o}F

Langmuir and the developed isotherms predictions of pure methane adsorption on dry Tiffany mixed coal at130 ^{o}F for high-pressure range are compared in **Table 4.36** and **Figure 4.20**.

The developed isotherm predicts a maximum adsorbed volume of **324.7scf/ton** at an adsorption saturation pressure of **2294.9 psia**. However, by Langmuir isotherm prediction, a maximum adsorbed volume of **434.78scf/ton** is attained at an infinite adsorption saturation pressure. **Figure 4.20** shows that adsorption prediction by

Langmuir isotherm is not reliable at higher pressures because of its inefficiency in defining the onset of adsorption saturation pressure; this contributes to an overestimation of maximum adsorbed volume.

Table 4.36: Langmuir and the developed isotherms predictions of pure methane adsorption on dry Tiffany mixed coal sample at 130 ^{o}F for high-pressure range

Pressure, P (psia)	Absolute adsorption, V (scf/ton)	
	Developed Isotherm	Langmuir Isotherm
255.9	132.5	119.0
824.9	241.4	238.5
1210.2	282.7	278.5
1796.9	316.6	315.5
2294.9	324.7	335.5
2750	324.7	348.7
3250	324.7	359.6
3750	324.7	368.1

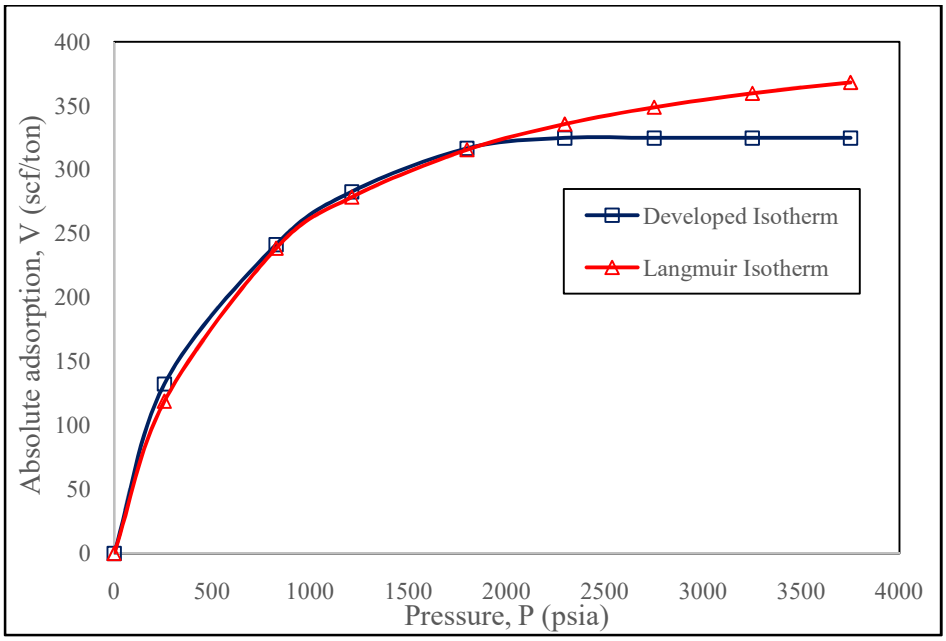

Figure 4.20: Langmuir and the developed isotherms predictions of pure methane adsorption on dry Tiffany mixed coal sample at 130 ^{o}F for high-pressure range

4.2.6Pure Nitrogen Adsorption on Dry Tiffany Mixed Coal Sample at 130 ^{o}F

4.2.6.1 Parameterisation of Pure Nitrogen Adsorption on Dry Tiffany Mixed Coal Sample at 130 ^{o}F using the Developed Isotherm

Plotting the experimental isotherm from **Table 4.6** and matching it with the relative adsorbed volume-relative pressure curve (see **Figure 3.3**) shows the adsorbate-adsorbent resistance parameter n to be in the range of 0.95 to 1.05.

For each n, the corresponding parameters$b = \frac{V_{last}}{V_{max}}$ and $c = \frac{P_{last}}{P_s}$ were featured. Using *Excel* spreadsheet, the corresponding $V_{max} = \frac{V_{last}}{b}$ and $P_s = \frac{P_{last}}{c}$, and the pressure and adsorbed volume P_β, V_β at the inflexion point β where $\Delta\left(\frac{V}{V_{max}}\right) = \Delta\left(\frac{P}{P_s}\right)$ on the isotherms were evaluated. The parameter n = 1.00 yields the P_β, V_β values (see **Table 4.37**) that correlate with the experimental adsorption isotherm as shown in **Figure 4.21**.

The $\boldsymbol{P_\beta}$, $\boldsymbol{V_\beta}$ values of **1227.8 psia** and **118.7 scf/ton** correlate with the experimental isotherm (see **Figure 4.21**), and the corresponding $\boldsymbol{P_s}$, $\boldsymbol{V_{max}}$ values of **2455.7 psia** and **158.3 scf/ton** are thus considered as the developed isotherm parameters for the experimental adsorption data.

Hence, pure nitrogen adsorption on dry Tiffany mixed coal sample at 130 ^{o}F is modelled as:

$$\boldsymbol{V(scf/ton)} = \begin{Bmatrix} \mathbf{158.3}\left\{\frac{\boldsymbol{P}}{\mathbf{2455.7}} + \left(\mathbf{1} - \frac{\boldsymbol{P}}{\mathbf{2455.7}}\right)\left(\frac{\boldsymbol{P}}{\mathbf{2455.7}}\right)^{\mathbf{1.00}}\right\}, for\ P < 2455.7\ psia \\ \mathbf{158.3},\ for\ P \geq 2455.7\ psia \end{Bmatrix} \quad (4.31)$$

where maximum adsorbed volume V_{max} = 158.3 scf/ton, adsorption saturation pressure P_s = 2455.7 psia, and n = 1.00 is a parameter that defines dry Tiffany mixed coal sample resistance to pure nitrogen adsorption at 130 ^{o}F.

Table 4.37: Adsorption saturation data for establishingthe boundary conditions of the developed isotherm for pure nitrogen adsorption on dry Tiffany mixed coal sample at 130 °F (Here, V_{last} = 147.2 scf/ton and , P_{last} = 1806.2 psia)

$b = \frac{V_{last}}{V_{max}}$	n = 1.00				
	$c = \frac{P_{last}}{P_s}$	$V_{max} = \frac{V_{last}}{b}$	$P_s = \frac{P_{last}}{c}$	$V_\beta = 0.7500 V_{max}$	$P_\beta = \frac{1}{2} P_s$
0.920	0.7172	160.0	2518.4	120.0	1259.2
0.925	0.7262	159.1	2487.2	119.3	1243.6
0.930	0.7355	**158.3**	**2455.7**	**118.7**	**1227.8**
0.935	0.7451	157.4	2424.1	118.0	1212.0
0.940	0.7551	156.6	2392.0	117.4	1196.0
0.945	0.7665	155.8	2359.5	116.8	1179.7
0.950	0.7764	154.9	2326.4	116.2	1163.2
0.955	0.7879	154.1	2292.4	115.6	1146.2
0.960	0.8000	153.3	2257.7	115.0	1128.8
0.965	0.8130	152.5	2221.6	114.4	1110.8
0.970	0.8268	151.7	2184.6	113.8	1092.3

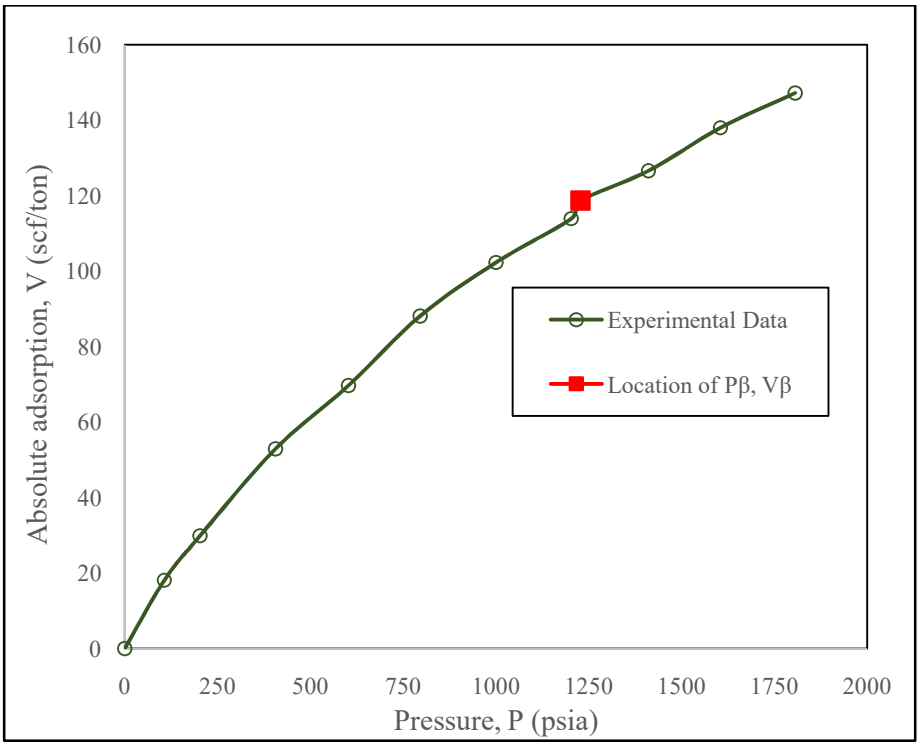

Figure 4.21: Location of P_β, V_β correlation on the experimental isotherm for pure nitrogen adsorption on dry Tiffany mixed coal sample at 130 ^{o}F

4.2.6.2 Prediction of Pure Nitrogen Adsorption on Dry Tiffany Mixed Coal Sample at 130 ^{o}F using the Developed Isotherm

Prediction of pure nitrogen adsorption on dry Tiffany mixed coal sample at 130 ^{o}F using the developed isotherm, and the corresponding deviation (error) analysis parameters are presented in **Table 4.38**.

Here, weighted root mean square, WRMS = 1.7020, weighted average absolute deviation, WAAD = 1.0389, percent average absolute deviation, %AAD = 6.2300, root mean square error, RMSE = 3.1127 scf/ton and R^2 value = 0.9989.

Table 4.38: Prediction of pure nitrogen adsorption on dry Tiffany mixed coal sample at 130 ^{o}F using the developed isotherm

Pressure, P (psia)	Absolute adsorption, V (scf/ton)		Deviation (Error) Analysis			
	Experimental	Developed Isotherm	σ_{Exp} (scf/ton)	$V_{Cal} - V_{Exp}$ (scf/ton)	$\frac{V_{Cal} - V_{Exp}}{\sigma_{Exp}}$	$\frac{V_{Cal} - V_{Exp}}{V_{Exp}}$
106.6	18.1	13.4	1.086	-4.7	-4.328	-0.260
202.9	29.9	25.1	1.794	-4.8	-2.676	-0.160
406.0	52.9	48.0	3.174	-4.9	-1.544	-0.093
602.7	69.7	68.2	4.182	-1.5	-0.359	-0.021
795.6	88.1	86.0	5.286	-2.1	-0.397	-0.024
1000.2	102.3	102.7	6.138	0.4	0.065	0.004
1202.5	113.9	117.1	6.834	3.2	0.468	0.028
1410.9	126.6	129.6	7.596	3.0	0.395	0.024
1604.9	138.0	139.3	8.280	1.3	0.157	0.009
1806.2	147.2	147.2	8.832	0	0	0

4.2.6.3 Parameterisation of Pure Nitrogen Adsorption on Dry Tiffany Mixed Coal Sample at 130 ^{o}F using Langmuir Isotherm

The variation of P/V with P for pure nitrogen adsorption on dry Tiffany mixed coal sample at 130 ^{o}F is shown in **Table 4.39** and the best fit line of the plot of P/V versus P (shown in **Figure 4.22**) yields the equation:

$$y = 0.0036x + 6.0837 \quad (4.32)$$

where

$$\text{slope } m = 0.0036 = {}^{1}/_{V_L} \quad (4.33)$$

and y-axis intercept

$$C = 6.0837 = \left(\frac{1}{V_L}\right) P_L \quad (4.34)$$

Here, Langmuir volume $\boldsymbol{V_L}$ and Langmuir pressure $\boldsymbol{P_L}$ are respectively obtained as **277.78scf/ton**and **1689.92 psia**. Hence,pure nitrogen adsorption on dry Tiffany mixed coal sample at 130 ^{o}F is modelled as:

$$\boldsymbol{V(scf/ton) = 277.78\left(\frac{P}{P+1689.92}\right)} \quad (4.35)$$

where P is pressure (psia) and Langmuir constant

$$b = \frac{1}{P_L} = 0.0005917 \text{ psia}^{-1} \quad (4.36)$$

Table 4.39: Parameters for plotting Langmuir isotherm for pure nitrogen adsorption on dry Tiffany mixed coal sample at 130 ^{o}F

Experimental		$\frac{Pressure}{Volume}$, P/V
Pressure, P (psia)	**Absolute adsorption, V (scf/ton)**	**(psia/scf/ton)**
106.6	18.1	5.8895
202.9	29.9	6.7860
406.0	52.9	7.6749
602.7	69.7	8.6471
795.6	88.1	9.0306
1000.2	102.3	9.7771
1202.5	113.9	10.5575
1410.9	126.6	11.1445
1604.9	138.0	11.6297
1806.2	147.2	12.2704

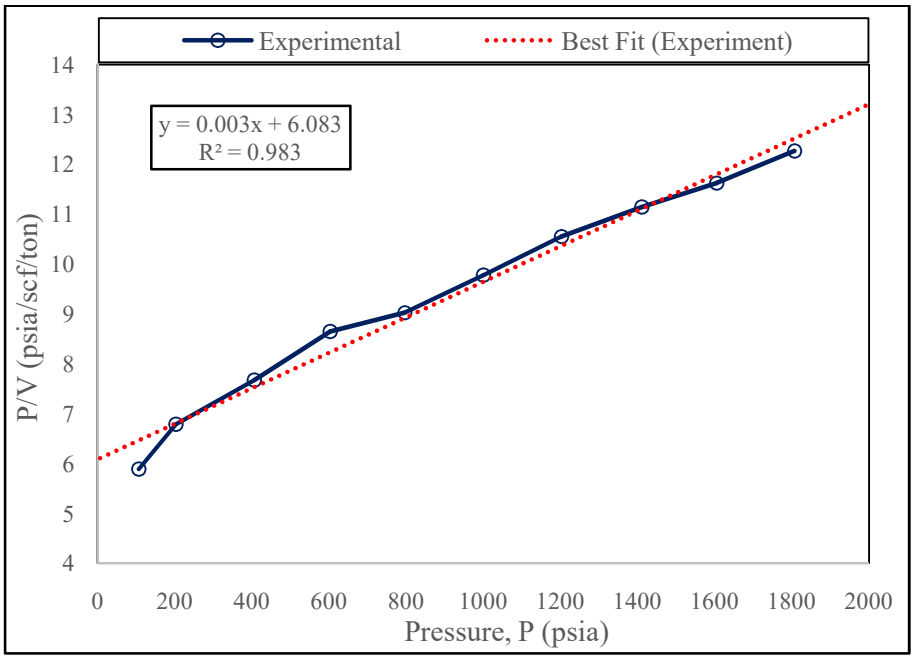

Figure 4.22: Plot of P/V versus P for purenitrogen adsorption on dry Tiffany mixed coal sample at 130 ^{o}F

4.2.6.4 Prediction of Pure Nitrogen Adsorption on Dry Tiffany Mixed Coal Sample at 130 ^{o}F using Langmuir Isotherm

Prediction of pure nitrogen adsorption on dry Tiffany mixed coal sample at 130 ^{o}F using Langmuir isotherm, and the corresponding deviation (error) analysis parameters are presented in **Table 4.40**.

Here, weighted root mean square, WRMS = 0.5712, weighted average absolute deviation, WAAD = 0.329, percent average absolute deviation, %AAD = 2.3500, root mean square error, RMSE = 1.987 scf/ton and R^2 value = 0.9980.

Table 4.40: Prediction of pure nitrogen adsorption on dry Tiffany mixed coal sample at 130 ^{o}F using Langmuir isotherm

Pressure, P (psia)	Absolute adsorption, V (scf/ton)		Deviation (Error) Analysis			
	Experimental	Langmuir Isotherm	σ_{Exp} (scf/ton)	$V_{Cal} - V_{Exp}$ (scf/ton)	$\frac{V_{Cal} - V_{Exp}}{\sigma_{Exp}}$	$\frac{V_{Cal} - V_{Exp}}{V_{Exp}}$
106.6	18.1	16.5	1.086	-1.600	-1.473	-0.088
202.9	29.9	29.8	1.794	-0.100	-0.056	-0.003
406.0	52.9	53.8	3.174	0.900	0.284	0.017
602.7	69.7	73.0	4.182	3.300	0.789	0.047
795.6	88.1	88.9	5.286	0.800	0.151	0.009
1000.2	102.3	103.3	6.138	1.000	0.163	0.010
1202.5	113.9	115.5	6.834	1.600	0.234	0.014
1410.9	126.6	126.4	7.596	-0.200	-0.026	-0.002
1604.9	138.0	135.3	8.280	-2.700	-0.326	-0.020
1806.2	147.2	143.5	8.832	-3.700	-0.419	-0.025

4.2.6.5 Generalisation of the Developed Isotherm for Pure Nitrogen Adsorption on Dry Tiffany Mixed Coal Sample at 130 ^{o}F

To validate and generalise the developed isotherm, adsorption predictions by Langmuir and the developed isotherm are correlated with the experimental data. The generalisation of the developed isotherm for pure nitrogen adsorption on dry Tiffany mixed coal sample at 130 ^{o}F is shown in **Table 4.41** and **Figure 4.23**.

Table 4.41: Generalisation of the developed isotherm for pure nitrogen adsorption on dry Tiffany mixed coal sample at 130 ^{o}F

Pressure, P (psia)	**Absolute adsorption, *V* (scf/ton)**		
	Experimental	**Developed Isotherm**	**Langmuir Isotherm**
106.6	18.1	13.4	16.5
202.9	29.9	25.1	29.8
406.0	52.9	48.0	53.8
602.7	69.7	68.2	73.0
795.6	88.1	86.0	88.9
1000.2	102.3	102.7	103.3
1202.5	113.9	117.1	115.5
1410.9	126.6	129.6	126.4
1604.9	138.0	139.3	135.3
1806.2	147.2	147.2	143.5

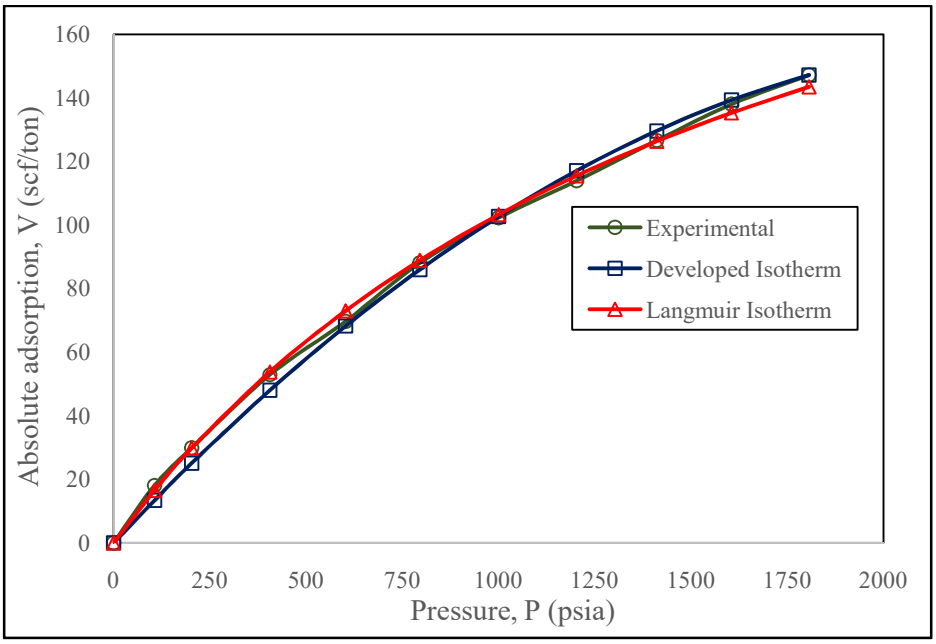

Figure 4.23: Generalisation of the developed isotherm for pure nitrogen adsorption on dry Tiffany mixed coal sample at 130 ^{o}F

4.2.6.6 Comparison of High-Pressure Adsorption Prediction for Pure Nitrogen Adsorption on Dry Tiffany Mixed Coal Sample at 130 ^{o}F

Langmuir and the developed isotherms predictions of pure nitrogen adsorption on dry Tiffany mixed coal at 130 ^{o}F for high-pressure range are compared in **Table 4.42** and **Figure 4.24**.

The developed isotherm predicts a maximum adsorbed volume of **158.3scf/ton** at an adsorption saturation pressure of **2455.7 psia**. However, by Langmuir isotherm prediction, a maximum adsorbed volume of **277.78scf/ton** is attained at an infinite adsorption saturation pressure. **Figure 4.24** shows that adsorption prediction by Langmuir isotherm is not reliable at higher pressures because of its inefficiency in defining the onset of adsorption saturation pressure; this contributes to an overestimation of maximum adsorbed volume.

Table 4.42: Langmuir and the developed isotherms predictions of pure nitrogen adsorption on dry Tiffany mixed coal sample at 130 ^{o}F for high-pressure range

Pressure, P (psia)	**Absolute adsorption, *V* (scf/ton)**	
	Developed Isotherm	**Langmuir Isotherm**
106.6	13.4	16.5
406.0	48.0	53.8
795.6	86.0	88.9
1202.5	117.1	115.5
1604.9	139.3	135.3
2006.5	153.0	150.8
2419.2	158.3	163.5
2809.5	158.8	173.4
3210.2	158.3	182.0
3623.8	158.3	189.4

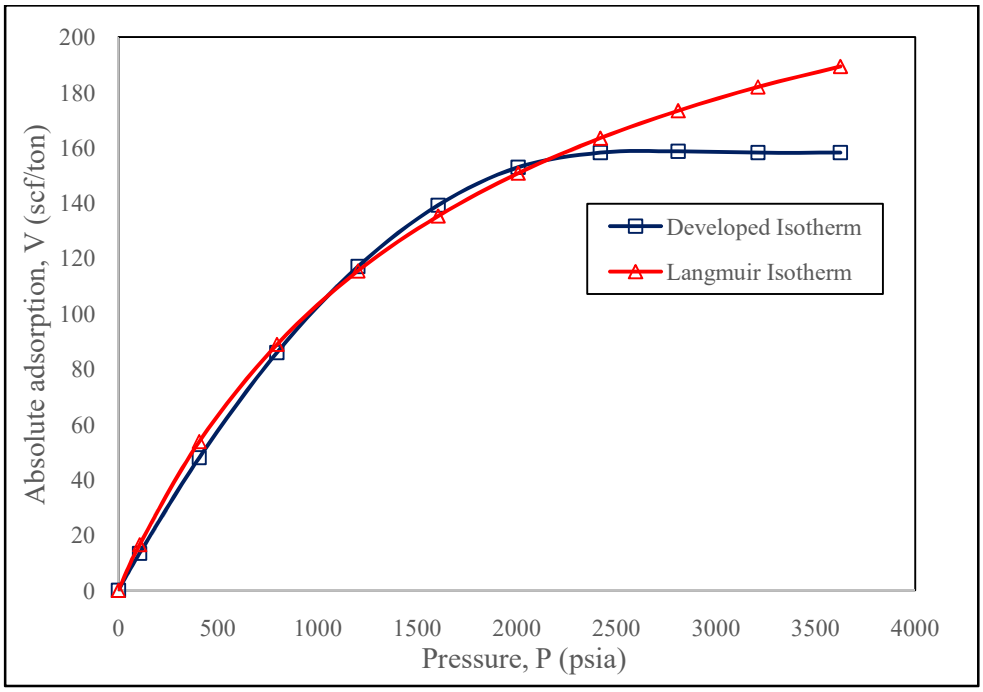

Figure 4.24: Langmuir and the developed isotherms predictions of pure nitrogen adsorption on dry Tiffany mixed coal sample at 130 ^{o}F for high-pressure range

4.3 COMPETITIVE (GAS MIXTURE) ADSORPTION

4.3.1 Methane and Nitrogen (Binary) Adsorption on Tiffany Mixed Coal Sample at 130 ^{o}F

In this study, using the developed isotherm, methane adsorption on Tiffany mixed coal sample at 130 ^{o}F is modelledas:

$$\boldsymbol{V(scf/ton)} = \begin{Bmatrix} \mathbf{324.7}\left\{\frac{\boldsymbol{P}}{\mathbf{2294.9}} + \left(\mathbf{1} - \frac{\boldsymbol{P}}{\mathbf{2294.9}}\right)\left(\frac{\boldsymbol{P}}{\mathbf{2294.9}}\right)^{\mathbf{0.50}}\right\}, for\ P < 2294.9\ psia \\ \mathbf{324.7},\ for\ P \geq 2294.9\ psia \end{Bmatrix} \quad (4.37)$$

where maximum adsorbed volume V_{max} = 324.7 scf/ton, adsorption saturation pressure P_s = 2294.9 psia, and n = 0.50 is a parameter that defines dry Tiffany mixed coal sample resistance to pure methane adsorption at 130 ^{o}F.

Langmuir isotherm modelling of the same methane adsorption on Tiffany mixed coal sample at 130 ^{o}F is expressed as:

$$\boldsymbol{V(scf/ton)} = \mathbf{434.78}\left(\frac{\boldsymbol{P}}{\boldsymbol{P}+\mathbf{679.09}}\right) \quad (4.38)$$

where P is pressure (psia) and Langmuir constant

$$b = \frac{1}{P_L} = 0.001473\ \text{psia}^{-1} \quad (4.39)$$

Using the developed isotherm, pure nitrogen adsorption on Tiffany mixed coal sample at 130 ^{o}F is modelled as:

$$\boldsymbol{V(scf/ton)} = \begin{Bmatrix} \mathbf{158.3}\left\{\frac{\boldsymbol{P}}{\mathbf{2455.7}} + \left(\mathbf{1} - \frac{\boldsymbol{P}}{\mathbf{2455.7}}\right)\left(\frac{\boldsymbol{P}}{\mathbf{2455.7}}\right)^{\mathbf{1.00}}\right\}, for\ P < 2455.7\ psia \\ \mathbf{158.3},\ for\ P \geq 2455.7\ psia \end{Bmatrix} \quad (4.40)$$

where maximum adsorbed volume V_{max} = 158.3 scf/ton, adsorption saturation pressure P_s = 2455.7 psia, and n = 1.00 isa parameter that defines dry Tiffany mixed coal sample resistance to pure nitrogen adsorptionat 130 ^{o}F.

Langmuir isotherm modelling of the samepure nitrogen adsorption on dry Tiffany mixed coal sample at 130 ^{o}F is modelled as:

$$\boldsymbol{V(scf/ton)} = \mathbf{277.78}\left(\frac{\boldsymbol{P}}{\boldsymbol{P}+\mathbf{1689.92}}\right) \quad (4.41)$$

where P is pressure (psia) and Langmuir constant

$$b = \frac{1}{P_L} = 0.0005917 \text{ psia}^{-1} \quad (4.42)$$

However, in practice, gas adsorption is often multi-component in nature and each gas competes for the same sorption sites. As stated earlier, with reference to the developedpure-component adsorption isotherm, the volume of the adsorbing specie i in a mixture of gases at an equilibrium pressure P is expressed as:

$$V_i = \frac{y_i(V_{max})_i}{\sum_{j=1}^{N} y_j(V_{max})_j}(V_{100\%})_i \quad (4.43)$$

wherey_i is the gas phase mole fraction (or the feed ratio) of the adsorbing specie i; $(V_{max})_i$ is the maximum adsorbed volume of the adsorbing specie i of 100% concentration; y_j is the gas phase mole fraction (or the feed ratio) of the respective adsorbing specie j; $(V_{max})_j$ is the maximum adsorbed volume of the respective adsorbing specie j of 100% concentration; $j = 1, \ldots\ldots N$; N is the number of gas specie (1 for pure-component, 2 for binary mixture, and 3 for ternary mixture); $(V_{100\%})_i$ is the volume of the adsorbing specie i of 100% concentration at the corresponding pressure.

The extended Langmuir isotherm (for mixture of gases) is expressed as:

$$V_i = (V_L)_i = \frac{y_i b_i P}{1+\sum_{j=i}^{N} y_j b_j P} \quad (4.44)$$

where y_i is the gas-phase mole fraction of the adsorbing specie i;$b_i$is equal to $\frac{1}{P_{L_i}}$, the temperature-dependent pure-component Langmuir model parameterof the adsorbing specie i;$(V_L)_i$ is the Langmuir (maximum) volume of the adsorbing specie i of 100% concentration;P is equilibrium pressure; and $j = 1, \ldots N$; $N$is the number of gas component (1 for pure-component, 2 for binary mixture, and 3 for ternary mixture).

For methane and nitrogen competitive adsorption on Tiffany mixed coal sample at 130 ^{o}F, the mixing rule for the developed isotherm is correlated with extended Langmuir isotherm and validated by the laboratory measurement presented by Gasem *et al.* (2002) for the purpose of generalising the extended version of the developed isotherm.

4.3.1.1 Adsorption of 50% Methane and 50% Nitrogen on Tiffany Mixed Coal Sample at 130 ^{o}F

The laboratory measurement of the competitive adsorption of 50% methane and 50% nitrogen on Tiffany mixed coal sample at 130 ^{o}F (Gasem *et al*., 2002) is shown in **Table 4.43** whine the graphical representation is shown in **Figure 4.25**.

The developed isotherm prediction of single-component adsorptions of methane and nitrogen, and the corresponding competitive adsorptions of 50% methane and 50% nitrogen on Tiffany mixed coal sample at 130 ^{o}F are shown in **Table 4.44**. However, the predicted competitive adsorptions are shown in **Figure 4.26**.

Also, Langmuir isotherm prediction of competitive adsorptions of 50% methane and 50% nitrogen on Tiffany mixed coal sample at 130 ^{o}F are shown in **Table 4.45** and **Figure 4.27**.

The correlation of the developed and Langmuir isotherms predictions of competitive adsorptions of 50% methane and 50% nitrogen on Tiffany mixed coal sample at 130 ^{o}F with laboratory measurement are shown in **Figure 4.28**.

The plot (**Figure 4.28**) shows that the developed isotherm prediction of competitive adsorption is better for cases where the adsorbent affinity for the adsorbate is high as displayed in the 50% methane adsorption. However, Langmuir isotherm prediction of competitive adsorption is better for cases where the adsorbent affinity for the adsorbate is low as displayed in the 50% nitrogen adsorption.

Table 4.43: Laboratory measurement of the competitive adsorption of 50% methane and 50% nitrogen on Tiffany mixed coal sample at 130 ^{o}F (Gasem *et al*., 2002)

Pressure,	**Absolute adsorption, *V* (scf/ton)**		
P (psia)	**50% Methane**	**50% Nitrogen**	**Total**
118.5	37.1	9.3	46.4
220.1	64.5	16.3	80.8
400.0	100.6	24.1	124.7
611.6	130.9	34.1	165.1
813.9	159.1	36.6	195.7
1005.9	177.1	43.3	220.4
1208.5	196.2	44.5	240.7
1409.7	209.5	49.3	258.7
1609.6	223.8	52.8	276.6
1812.8	231.9	60.6	292.5
2010.8	244.9	66.7	311.6

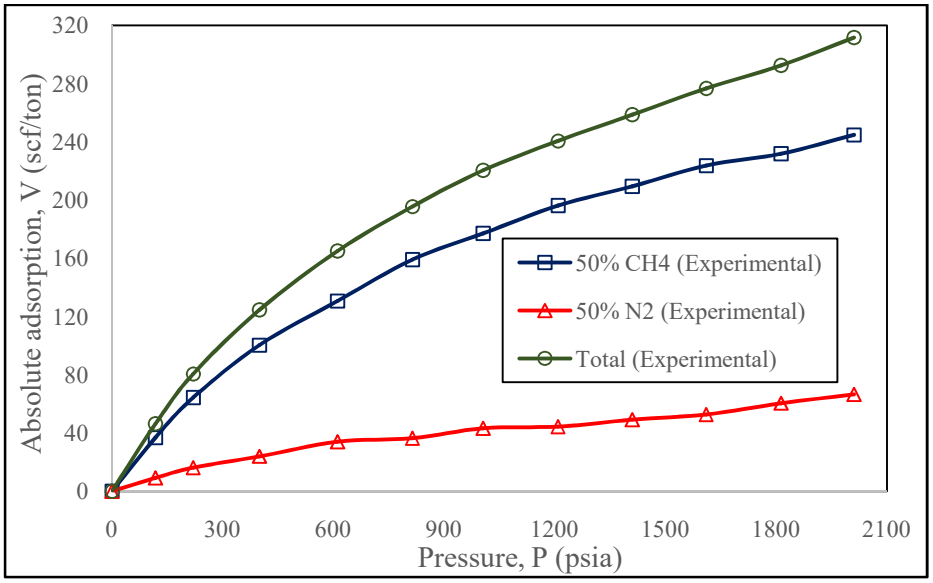

Figure 4.25: Plot of laboratory measurement of the competitive adsorption of 50% methane and 50% nitrogen on Tiffany mixed coal sample at 130 ^{o}F

Table 4.44: Developed isotherm prediction of single-component and competitive adsorptions of50% methane and 50% nitrogen on Tiffany mixed coal sample at 130 ^{o}F

Pressure, P (psia)	Absolute adsorption, *V* (scf/ton) (Developed Isotherm)				
	100% Methane	100% Nitrogen	50% Methane	50% Nitrogen	Total
118.5	86.73	14.9	58.3	4.9	63.2
220.1	122.0	27.1	82.0	8.9	90.9
400.0	168.5	47.4	113.3	15.5	128.8
611.6	209.5	69.0	140.4	22.6	163.0
813.9	239.9	87.5	161.7	28.7	190.4
1005.9	263.1	103.1	176.9	33.8	210.7
1208.5	282.5	117.5	189.9	38.5	228.4
1409.7	297.6	129.6	200.1	42.5	242.6
1609.6	308.9	139.5	207.7	45.7	253.4
1812.8	317.1	147.4	213.2	48.3	261.5
2010.8	322.1	153.1	216.5	50.2	266.7

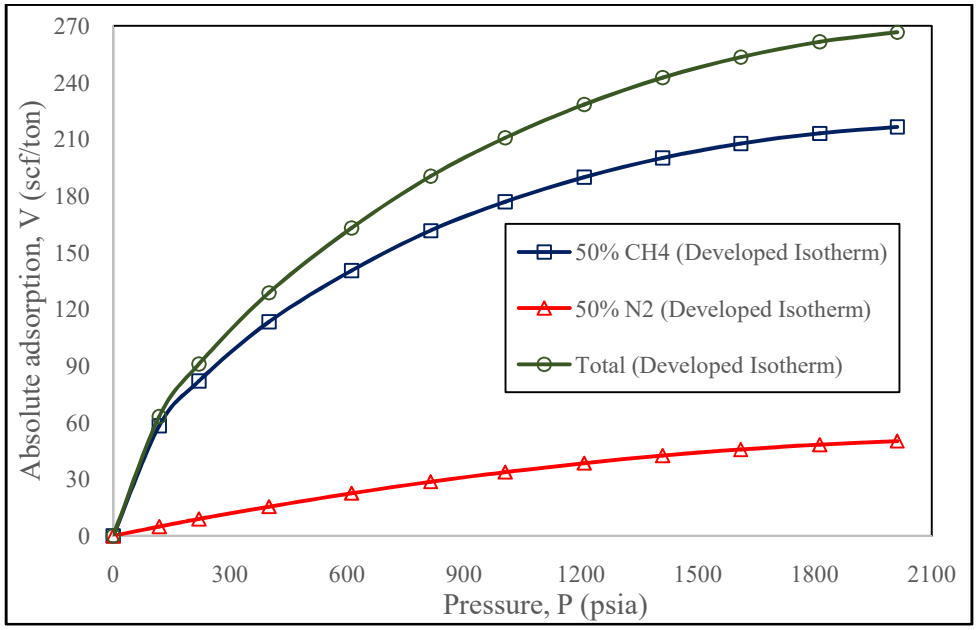

Figure 4.26: Developed isotherm prediction of competitive adsorption of methane andnitrogen on Tiffany mixed coal sample at 130 ^{o}F

Table 4.45: Langmuir isotherm prediction of competitive adsorptions of 50% methane and 50% nitrogen on Tiffany mixed coal sample at 130 ^{o}F

Pressure, P (psia)	**Absolute adsorption, *V* (scf/ton) (Langmuir Isotherm)**		
	50% Methane	**50% Nitrogen**	**Total**
118.5	33.8	8.7	42.5
220.1	57.4	14.7	72.1
400.0	90.6	23.3	113.9
611.6	120.0	30.8	150.8
813.9	141.6	36.3	177.9
1005.9	158.0	40.6	198.6
1208.5	172.2	44.2	216.4
1409.7	183.8	47.2	231.0
1609.6	193.6	49.7	243.3
1812.8	202.1	51.9	254.0
2010.8	209.3	53.7	263.0

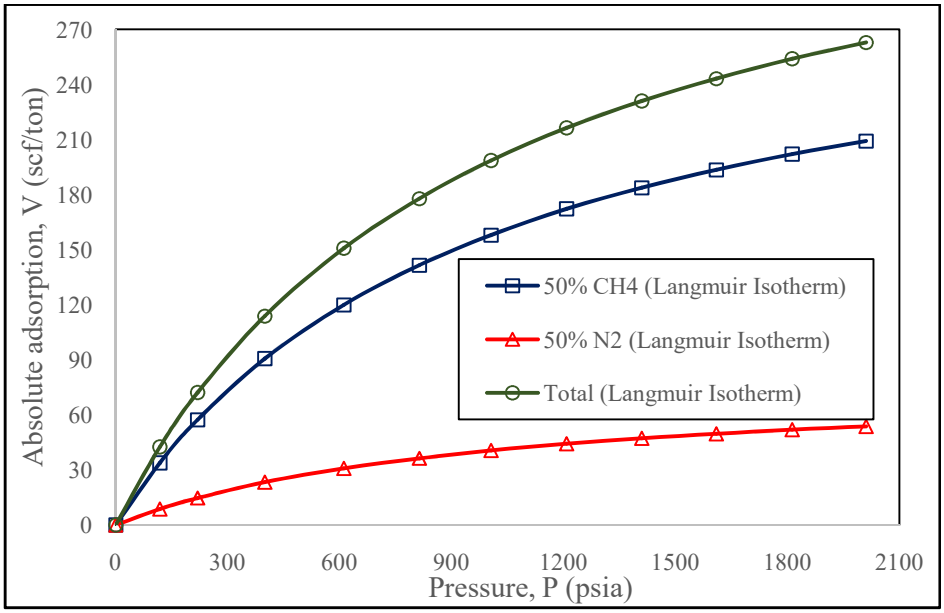

Figure 4.27: Langmuir isotherm prediction of competitive adsorption of methaneandnitrogen on Tiffany mixed coal sample at 130 ^{o}F

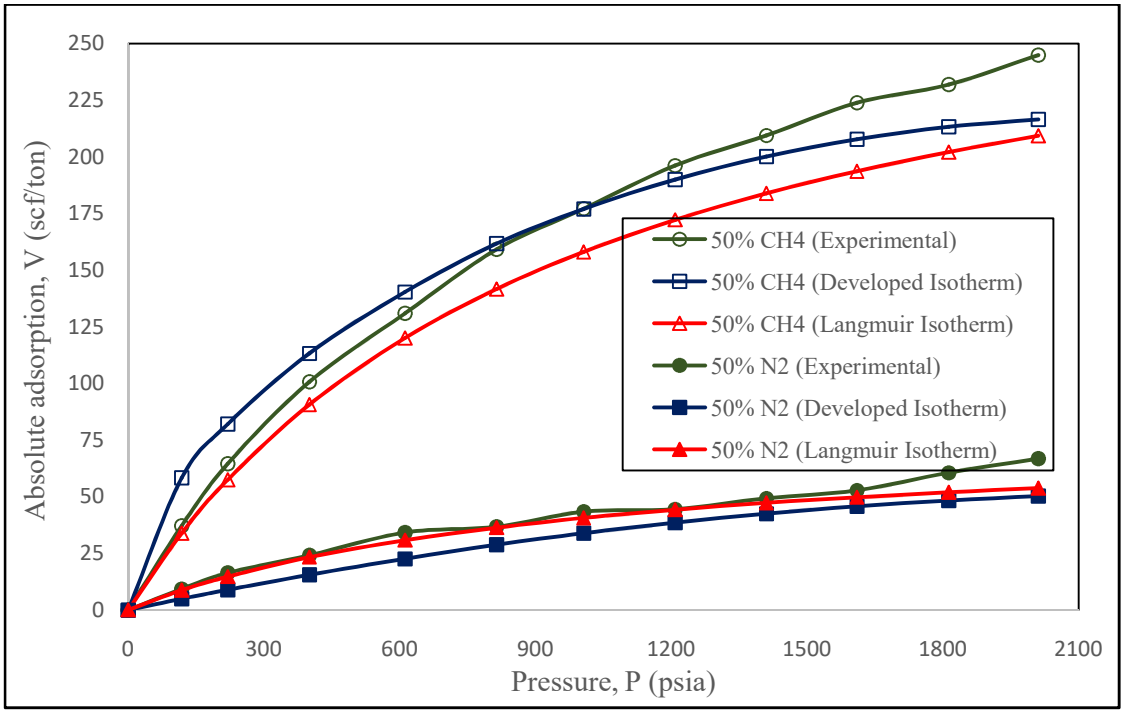

Figure 4.28: Correlation of predicted competitive adsorption ofmethane and nitrogen on Tiffany mixed coal sample at 130 ^{o}F with laboratory measurement

4.4NATURAL GAS ADSORPTION MODELLING FOR MARCELLUS, HAYNESVILLE AND BARNETT SHALE FORMATIONS

4.4.1 Langmuir Isotherm Modelling of Marcellus, Haynesville and Barnett Shale Natural Gas Adsorptions

Langmuir adsorption isotherm parameters for Marcellus, Haynesville and Barnett shale formations published in literature (Zuber *et al.*, 2002; Mengal & Watternbarger 2011; Boulis *et al*., 2012; Nobakht *et al.*, 2012; Ikewun & Ahmadi, 2012; Yu & Sepehrmoori, 2013; Yu & Sepehrmoori, 2014) are listed in **Table 4.46**.

Langmuir isotherm modelling of natural gas adsorption on Marcellus shale is expressed as:

$$\boldsymbol{V(scf/ton) = 200\left(\frac{P}{P+500}\right)} \quad (4.45)$$

where P is in psi.

Langmuir isotherm modelling of natural gas adsorption on Haynesville shale is expressed as:

$$\boldsymbol{V(scf/ton) = 60\left(\frac{P}{P+1500}\right)} \quad (4.46)$$

where P is in psi.

And Langmuir isotherm modelling of natural gas adsorption on Barnett shale is expressed as:

$$\boldsymbol{V(scf/ton) = 96\left(\frac{P}{P+650}\right)} \quad (4.47)$$

where P is in psi.

The corresponding pressure-adsorbed volume (P-V) data and the Langmuir isotherms are shown in **Table 4.47** and **Figure 4.29** respectively.

Table 4.46: Langmuir adsorption isotherm parameters for Marcellus, Haynesville and Barnett shale formations (Yu & Sepehrmoori, 2013; 2014)

Parameter	**Marcellus Shale**	**Haynesville Shale**	**Barnett Shale**
Langmuir volume (scf/ton)	200	60	96
Langmuir pressure (psi)	500	1500	650
Bulk density (g/cm^3)	2.46	2.60	2.58

Table 4.47: Langmuir isotherm predictions of natural gas adsorption on Marcellus, Haynesvilleand Barnett shale formations

Pressure, *P* (psi)	**Adsorption, *V* (scf/ton) (Langmuir Isotherm)**		
	Marcellus Shale at 175 ^{o}F	**Haynesville Shale at 300 ^{o}F**	**Barnett Shale at 180 ^{o}F**
250	66.67	8.57	26.67
500	100.00	15.00	41.74
750	120.00	20.00	51.43
1000	133.33	24.00	58.18
1250	142.86	27.27	63.16
1500	150.00	30.00	66.98
1750	155.56	32.30	70.00
2000	160.00	34.29	72.45
2250	163.64	36.00	74.48
2500	166.67	37.50	76.19
2750	169.23	38.82	77.65
3000	171.43	40.00	78.90
3250	173.33	41.05	80.00
3500	175.00	42.00	80.96
3750	176.47	42.86	81.82
4000	177.78	43.64	82.58
4250	178.95	44.35	83.26
4500	180.00	45.00	83.88
4750	180.95	45.60	84.44
5000	181.82	46.15	84.96

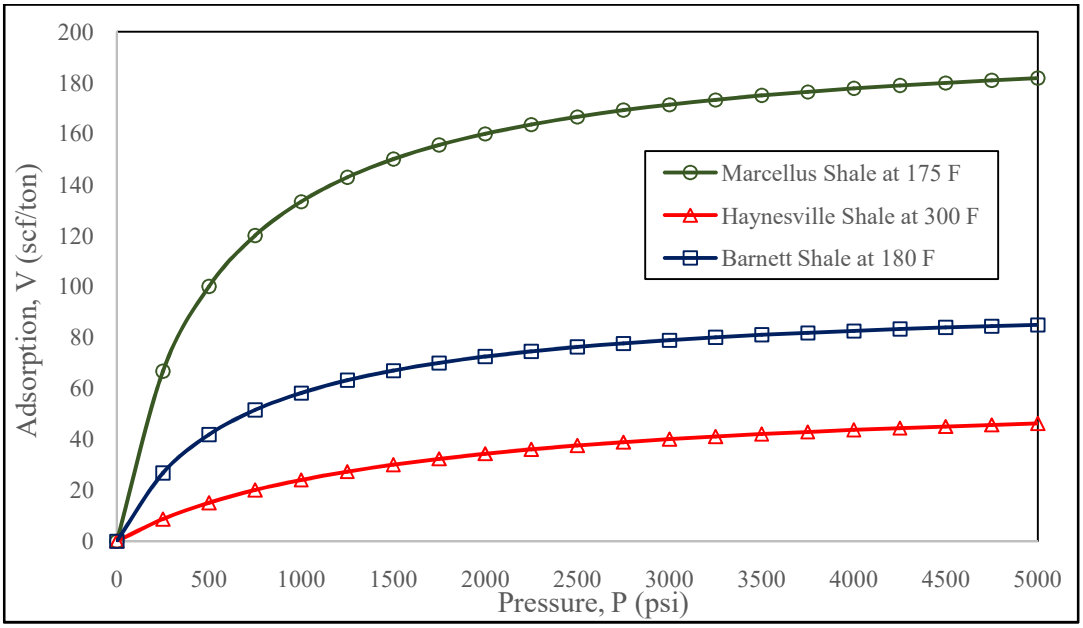

Figure 4.29: Langmuir isotherms of natural gas adsorption on Marcellus, Haynesville and Barnett shale formations

4.4.2Developed Isotherm Modelling of MarcellusShale Natural Gas Adsorptions

Aside the Langmuir isotherm prediction, the laboratory adsorption data of Marcellus shale is not yet published. However, Langmuir isotherm prediction has been established to be more reliable at lower pressure range.

The measured initial reservoir pressure of Marcellus shale in Eastern Gas Shale Project (EGSP) Well WV-6 is 3,500 psi (SPE Formation Evaluation, March, 1998; and Soeder, 2011). Hence, matching the lower pressure range ($0 \leq P \leq 1750$ psi) Langmuir isotherm representative of laboratory gas adsorption for Marcellus shale with the relative adsorbed volume-relative pressure curve (see **Figure 3.3**) shows the adsorbate-adsorbent resistance parameter n to be in the range of 0.35 to 0.45.

For each n, the corresponding parameters $b = \frac{V_{last}}{V_{max}}$ and $c = \frac{P_{last}}{P_s}$ were featured. Using *Excel* spreadsheet, the corresponding $V_{max} = \frac{V_{last}}{b}$ and $P_s = \frac{P_{last}}{c}$, and the pressure and adsorbed volume P_β, V_β at the inflexion point β where $\Delta\left(\frac{V}{V_{max}}\right) = \Delta\left(\frac{P}{P_s}\right)$ on the isotherms were evaluated. The parameter n = 0.35 yields the P_β, V_β values (see **Table 4.48**) that correlate with the isotherm representing laboratory adsorption as shown in **Figure 4.30**.

The $\boldsymbol{P_\beta}$, $\boldsymbol{V_\beta}$ values of **754.41 psi** and **119.97 scf/ton** correlate with the isotherm representing laboratory adsorption (see **Figure 4.30**), and the corresponding $\boldsymbol{P_s}$, $\boldsymbol{V_{max}}$ values of **2909.88psi** and **166.37scf/ton** are thus considered as the developed isotherm parameters for the representative of laboratory gas adsorption.

Hence, natural gas adsorption on Marcellus shale sample at 175 ^{o}F is modelled as:

$$\boldsymbol{V(scf/ton)} = \begin{Bmatrix} \mathbf{166.37}\left\{\frac{\boldsymbol{P}}{\mathbf{2909.88}} + \left(\mathbf{1} - \frac{\boldsymbol{P}}{\mathbf{2909.88}}\right)\left(\frac{\boldsymbol{P}}{\mathbf{2909.88}}\right)^{\mathbf{0.35}}\right\}, for\ P < 2909.88\ psi \\ \mathbf{166.37},\ for\ P \geq 2909.88\ psi \end{Bmatrix} \quad (4.48)$$

where maximum adsorbed volume V_{max} = 166.37 scf/ton, adsorption saturation pressure P_s = 2909.88 psi, and n = 0.35 is a parameter that defines Marcellus shale resistance to natural gas adsorption at 175 ^{o}F.

Table 4.48: Adsorption saturation data for establishing the boundary conditions of the developed isotherm for natural gas adsorption on Marcellus shale sample at 175 ^{o}F. (Here, V_{last} = 155.56scf/ton and P_{last} = 1750psi)

$b = \frac{V_{last}}{V_{max}}$	n = 0.35				
	$c = \frac{P_{last}}{P_s}$	$V_{max} = \frac{V_{last}}{b}$ (scf/ton)	$P_s = \frac{P_{last}}{c}$ (psi)	$V_\beta = 0.7211 V_{max}$ (scf/ton)	$P_\beta = \frac{7}{27} P_s$ (psi)
0.920	0.5621	169.09	3113.32	121.93	807.16
0.925	0.5746	168.17	3045.60	121.27	789.60
0.930	0.5877	167.27	2977.71	120.62	772.00
0.935	0.6014	**166.37**	**2909.88**	**119.97**	**754.41**
0.940	0.6157	165.49	2842.29	119.33	736.89
0.945	0.6308	164.61	2774.25	118.70	719.25
0.950	0.6467	163.75	2706.05	118.08	701.57
0.955	0.6636	162.89	2637.13	117.46	683.70
0.960	0.6815	162.04	2567.87	116.85	665.74
0.965	0.7009	161.20	2496.79	116.24	647.32
0.970	0.7218	160.37	2424.49	115.64	628.57
0.975	0.7449	159.55	2349.31	115.05	609.08
0.980	0.7706	158.73	2270.96	114.46	588.77
0.985	0.8002	157.93	2186.95	113.88	566.99
0.990	0.8358	157.13	2093.80	113.31	542.84
0.005	0.8829	156.34	1982.10	112.74	513.88
1.000	1.0000	155.56	1750.00	112.17	453.70

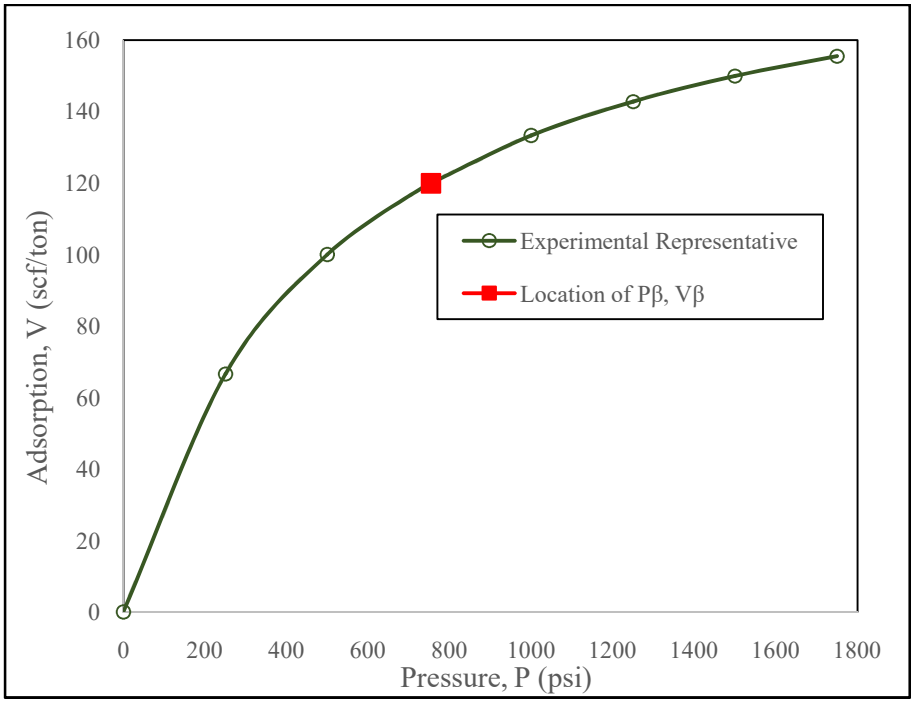

Figure 4.30: Location of P_β, V_β correlation on the isotherm representing laboratory adsorption of natural gas on Marcellus shale sample at 175 ^{o}F

4.4.3Comparison of Marcellus Shale Gas Adsorption Predictions by Langmuir and the Developed Isotherms

Predictions of natural gas adsorption on Marcellus shale formation for high pressure range by Langmuir and the developed isotherms are compared in **Table 4.49** and **Figure 4.31**.

For Marcellus shale formation, the developed isotherm predicts a maximum adsorbed volume of **166.37 scf/ton** at an adsorption saturation pressure of **2909.88 psi**. However, by Langmuir isotherm prediction, a maximum adsorbed volume of **200.00 scf/ton** is attained at an infinite adsorption saturation pressure.

Figure 4.31 shows that adsorption prediction by Langmuir isotherm is not reliable at higher pressures because of its inefficiency in defining the onset of adsorption saturation pressure; this contributes to an overestimation of maximum adsorbed volume.

Table 4.49: Marcellus shale gas adsorption predictions by Langmuirand the developed isotherms at 175 ^{o}F

Pressure, *P*	**Marcellus Shale Gas Adsorption, *V* (scf/ton)**	
(psi)	**Langmuir Isotherm**	**Developed Isotherm**
250	66.67	78.71
500	100.00	102.97
750	120.00	119.71
1000	133.33	132.31
1250	142.86	142.07
1500	150.00	149.68
1750	155.56	155.56
2000	160.00	159.97
2250	163.64	163.12
2500	166.67	165.16
2750	169.23	166.19
2909.88	170.67	166.37
3000	171.43	166.37
3250	173.33	166.37
3500	175.00	166.37
3750	176.47	166.37
4000	177.78	166.37
4250	178.95	166.37
4500	180.00	166.37
4750	180.95	166.37
5000	181.82	166.37

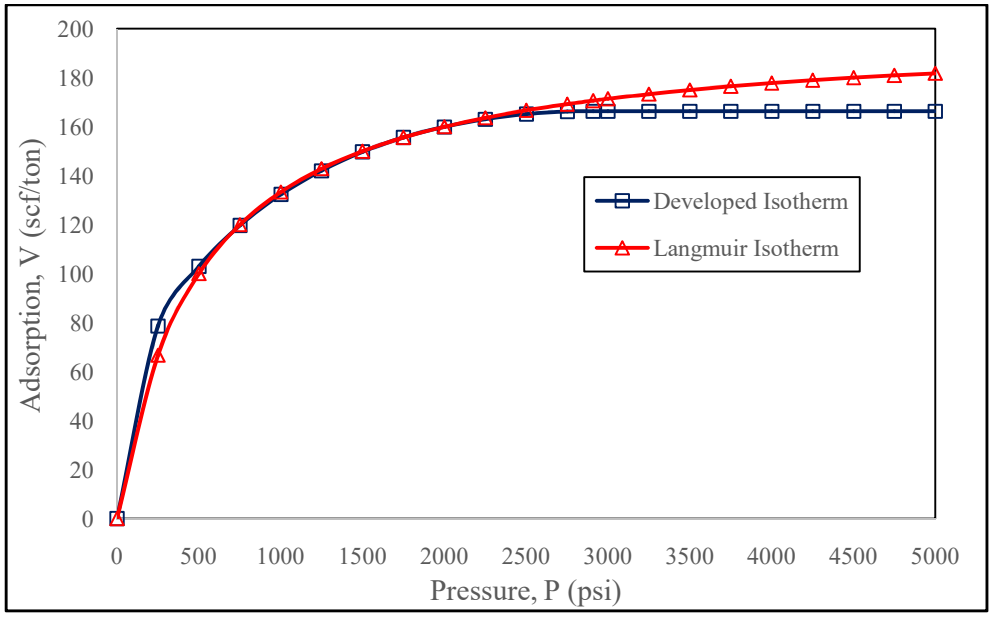

Figure 4.31: Marcellus shale gas adsorption predictions by Langmuir and the developed isotherms at 175 ^{o}F

4.4.4DevelopedIsotherm Modelling of Haynesville Shale Natural Gas Adsorptions

Aside the Langmuir isotherm prediction, the laboratory adsorption data of Haynesville shale is not yet published. However, Langmuir isotherm prediction has been established to be more reliable at lower pressure range.

The initial reservoir pressure of Haynesville shale formation is 12,000 psi (Kaiser and Yu, 2011; Male *et al*., 2015). Hence, matching the lower pressure range ($0 \leq P \leq 5000$ psi) Langmuir isotherm representative of laboratory gas adsorption for Haynesville shale with the relative adsorbed volume-relative pressure curve (see **Figure 3.3**) shows the adsorbate-adsorbent resistance parameter n to be in the range of 0.30 to 0.35.

For each n, the corresponding parameters $b = \frac{V_{last}}{V_{max}}$ and $c = \frac{P_{last}}{P_s}$ were featured. Using *Excel* spreadsheet, the corresponding $V_{max} = \frac{V_{last}}{b}$ and $P_s = \frac{P_{last}}{c}$, and the pressure and adsorbed volume P_β, V_β at the inflexion point β where $\Delta\left(\frac{V}{V_{max}}\right) = \Delta\left(\frac{P}{P_s}\right)$ on the isotherms were evaluated. The parameter n = 0.35 yields the P_β, V_β values (see **Table 4.50**) that correlate with the isotherm representing laboratory adsorption as shown in **Figure 4.32**.

The $\boldsymbol{P_\beta}$, $\boldsymbol{V_\beta}$ values of **2205.71 psi** and **35.78 scf/ton** correlate with the isotherm representing laboratory adsorption (see **Figure 4.32**), and the corresponding $\boldsymbol{P_s}$, $\boldsymbol{V_{max}}$ values of **8507.74psi** and **49.62scf/ton** are thus considered as the developed isotherm parameters for the representative of laboratory gas adsorption.

Hence, natural gas adsorption on Haynesville shale sample at 300 ^{o}F is modelled as:

$$\boldsymbol{V(scf/ton)} = \begin{Bmatrix} \mathbf{49.62}\left\{\frac{P}{8507.74} + \left(1 - \frac{P}{8507.74}\right)\left(\frac{P}{8507.74}\right)^{0.35}\right\}, for\ P < 8507.74\ psi \\ \mathbf{49.62},\ for\ P \geq 8507.74\ psi \end{Bmatrix} \quad (4.49)$$

where maximum adsorbed volume V_{max} = 49.62 scf/ton, adsorption saturation pressure P_s = 8507.74 psi, and n = 0.35 is a parameter that defines Haynesville shale resistance to natural gas adsorption at 300 ^{o}F.

Table 4.50: Adsorption saturation data for establishing the boundary conditions of the developed isotherm for natural gas adsorption on Haynesville shale sample at 300^{o}F. (Here, V_{last} = 46.15 scf/ton and P_{last} = 5000 psi)

$b = \frac{V_{last}}{V_{max}}$	n = 0.35				
	$c = \frac{P_{last}}{P_s}$	$V_{max} = \frac{V_{last}}{b}$ (scf/ton)	$P_s = \frac{P_{last}}{c}$ (psi)	$V_\beta = 0.7211 V_{max}$ (scf/ton)	$P_\beta = \frac{7}{27} P_s$ (psi)
0.920	0.5621	50.16	8895.21	36.17	2306.17
0.925	0.5746	49.89	8701.70	35.98	2255.73
0.930	0.5877	**49.62**	**8507.74**	**35.78**	**2205.71**
0.935	0.6014	49.36	8313.93	35.59	2155.46
0.940	0.6157	49.10	8120.84	35.41	2105.40
0.945	0.6308	48.84	7926.44	35.22	2055.00
0.950	0.6467	48.58	7731.56	35.03	2004.48
0.955	0.6636	48.32	7534.66	34.84	1953.43
0.960	0.6815	48.07	7336.76	34.66	1902.12
0.965	0.7009	47.82	7133.68	34.48	1849.47
0.970	0.7218	47.58	6927.13	34.31	1795.92
0.975	0.7449	47.33	6712.31	24.13	1740.23
0.980	0.7706	47.09	6488.45	33.96	1682.29
0.985	0.8002	46.85	6248.44	33.78	1619.97
0.990	0.8358	46.62	5982.29	33.62	1550.96
0.005	0.8829	46.38	5663.16	33.44	1468.23
1.000	1.0000	46.15	5000.00	33.28	1296.34

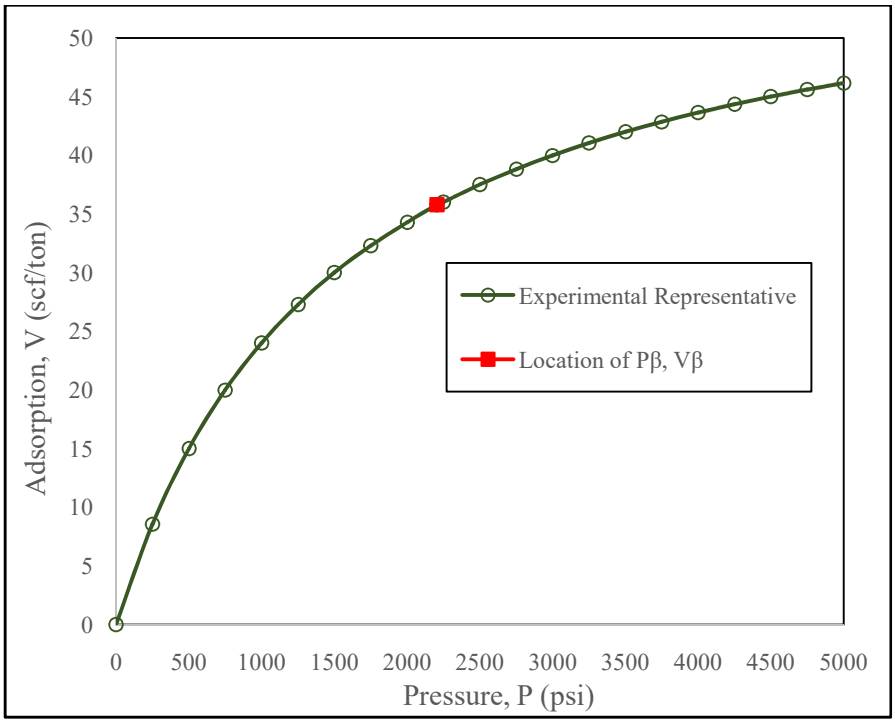

Figure 4.32: Location of P_β, V_β correlation on the isotherm representing laboratory adsorption of natural gas on Haynesville shale sample at 300°F

4.4.5Comparison of Haynesville Shale Gas Adsorption Predictions by Langmuir and the Developed Isotherms

Predictions of natural gas adsorption on Haynesville shale formation for high pressure range by Langmuir and the developed isotherms are compared in **Table 4.51**and**Figure 4.33**.

For Haynesville shale formation, the developed isotherm predicts a maximum adsorbed volume of **49.62 scf/ton** at an adsorption saturation pressure of **8507.74 psi**. However, by Langmuir isotherm prediction, a maximum adsorbed volume of **60.00 scf/ton** is attained at an infinite adsorption saturation pressure.

Figure 4.33 shows that adsorption prediction by Langmuir isotherm is not reliable at higher pressures because of its inefficiency in defining the onset of adsorption saturation pressure; this contributes to an overestimation of maximum adsorbed volume.

Table 4.51: Haynesville shale gas adsorption predictions by Langmuirand the developed isotherms at 300°F

Pressure, *P* (psi)	**Haynesville Shale Gas Adsorption, *V* (scf/ton)**	
	Langmuir Isotherm	**Developed Isotherm**
500	15.00	20.24
1000	24.00	26.53
1500	30.00	31.01
2000	34.29	34.53
2500	37.50	37.40
3000	40.00	39.80
3500	42.00	41.82
4000	43.64	43.52
4500	45.00	44.95
5000	46.15	46.15
5500	47.14	47.14
6000	48.00	47.94
6500	48.75	48.57
7000	49.41	49.04
7500	50.00	49.37
8000	50.53	49.56
8507.74	51.01	49.62
9000	51.43	49.62
9500	51.82	49.62
10000	52.17	49.62
10500	52.50	49.62
11000	52.80	49.62
11500	53.08	49.62
12000	53.33	49.62

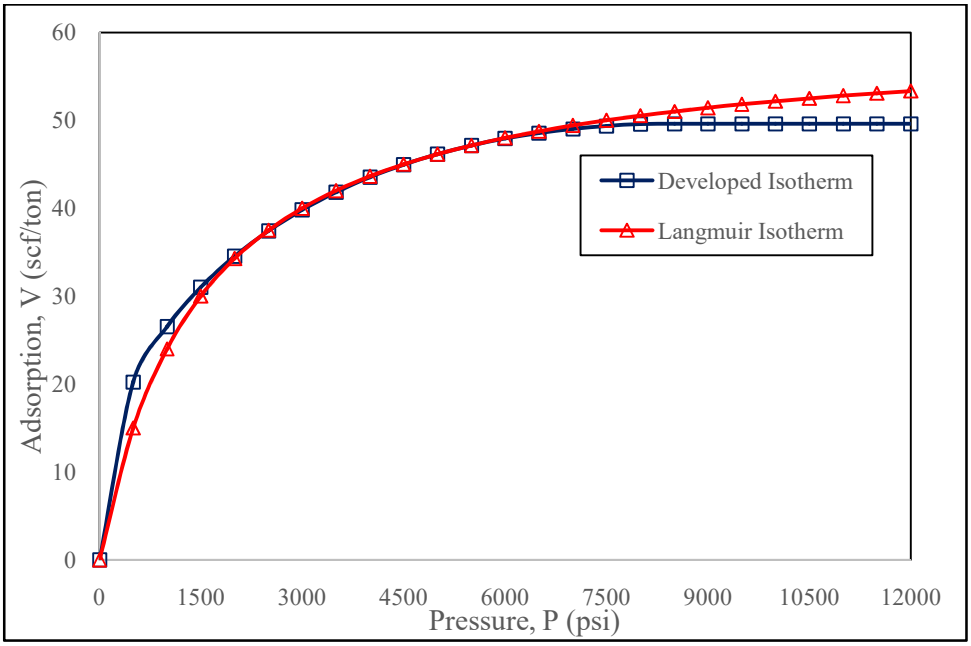

Figure 4.33: Haynesville shale gas adsorption predictions by Langmuir and the developed isotherms at 300°F

4.4.6DevelopedIsotherm Modelling of Barnett Shale Natural Gas Adsorptions

Aside the Langmuir isotherm prediction, the laboratory adsorption data of Barnett shale is not yet published. However, Langmuir isotherm prediction has been established to be more reliable at lower pressure range.

The initial reservoir pressure of Barnett shale formation is 3,900 psi (Bowker, 2007).Hence, matching the lower pressure range ($0 \leq P \leq 1750$ psi) Langmuir isotherm representative of laboratory gas adsorption for Barnett shale with the relative adsorbed volume-relative pressure curve (see **Figure 3.3**) shows the adsorbate-adsorbent resistance parameter n to be in the range of 0.50 to 0.60.

For each n, the corresponding parameters $b = \frac{V_{last}}{V_{max}}$ and $c = \frac{P_{last}}{P_s}$ were featured. Using *Excel* spreadsheet, the corresponding $V_{max} = \frac{V_{last}}{b}$ and $P_s = \frac{P_{last}}{c}$, and the pressure and adsorbed volume P_β, V_β at the inflexion point β where $\Delta\left(\frac{V}{V_{max}}\right) = \Delta\left(\frac{P}{P_s}\right)$ on the isotherms were evaluated. The parameter n = 0.55 yields the P_β, V_β values (see **Table 4.52**) that correlate with the isotherm representing laboratory adsorption as shown in **Figure 4.34**.

The $\boldsymbol{P_\beta}$, $\boldsymbol{V_\beta}$ values of **740.921 psi** and **51.158 scf/ton** correlate with the isotherm representing laboratory adsorption (see **Figure 4.34**), and the corresponding $\boldsymbol{P_s}$, $\boldsymbol{V_{max}}$ values of **2088.06psi** and **71.07scf/ton** are thus considered as the developed isotherm parameters for the representative of laboratory gas adsorption.

Hence, natural gas adsorption on Barnett shale sample at 180 ^{o}F is modelled as:

$$\boldsymbol{V(scf/ton)} = \begin{Bmatrix} \mathbf{71.07}\left\{\frac{P}{2088.06} + \left(1 - \frac{P}{2088.06}\right)\left(\frac{P}{2088.06}\right)^{0.55}\right\}, for\ P < 2088.06\ psi \\ \mathbf{71.07},\ for\ P \geq 2088.06\ psi \end{Bmatrix} \quad (4.50)$$

where maximum adsorbed volume V_{max} = 71.07 scf/ton, adsorption saturation pressure P_s = 2088.06 psi, and n = 0.55 is a parameter that defines Barnett shale resistance to natural gas adsorption at 180 ^{o}F.

Table 4.52: Adsorption saturation data for establishing the boundary conditions of the developed isotherm for natural gas adsorption on Barnett shale sample at 180 ^{o}F. (Here, V_{last} = 70.00 scf/ton and P_{last} = 1,750 psi)

$b = \frac{V_{last}}{V_{max}}$	n = 0.55				
	$c = \frac{P_{last}}{P_s}$	$V_{max} = \frac{V_{last}}{b}$ (scf/ton)	$P_s = \frac{P_{last}}{c}$ (psi)	$V_\beta = 0.7197 V_{max}$ (scf/ton)	$P_\beta = \frac{11}{31} P_s$ (psi)
0.920	0.6365	76.09	2749.41	54.76	975.60
0.925	0.6474	75.68	2703.12	54.46	959.17
0.930	0.6588	75.27	2656.34	54.17	842.57
0.935	0.6706	74.87	2609.60	53.88	925.99
0.940	0.6830	74.47	2562.22	53.59	909.17
0.945	0.6959	74.07	2514.72	53.31	892.32
0.950	0.7095	73.68	2466.53	53.03	875.22
0.955	0.7238	73.30	2417.79	52.75	857.92
0.960	0.7390	72.92	2368.06	52.48	840.28
0.965	0.7553	72.54	2316.96	52.21	822.15
0.970	0.7730	72.16	2263.91	51.94	803.32
0.975	0.7922	71.79	2209.04	51.67	783.85
0.980	0.8136	71.43	2150.93	51.41	763.25
0.985	0.8381	**71.07**	**2088.06**	**51.15**	**740.92**
0.990	0.8673	70.71	2017.76	50.89	715.98
0.005	0.9057	70.35	1932.21	50.63	685.62
1.000	1.0000	70.00	1750.00	50.38	620.97

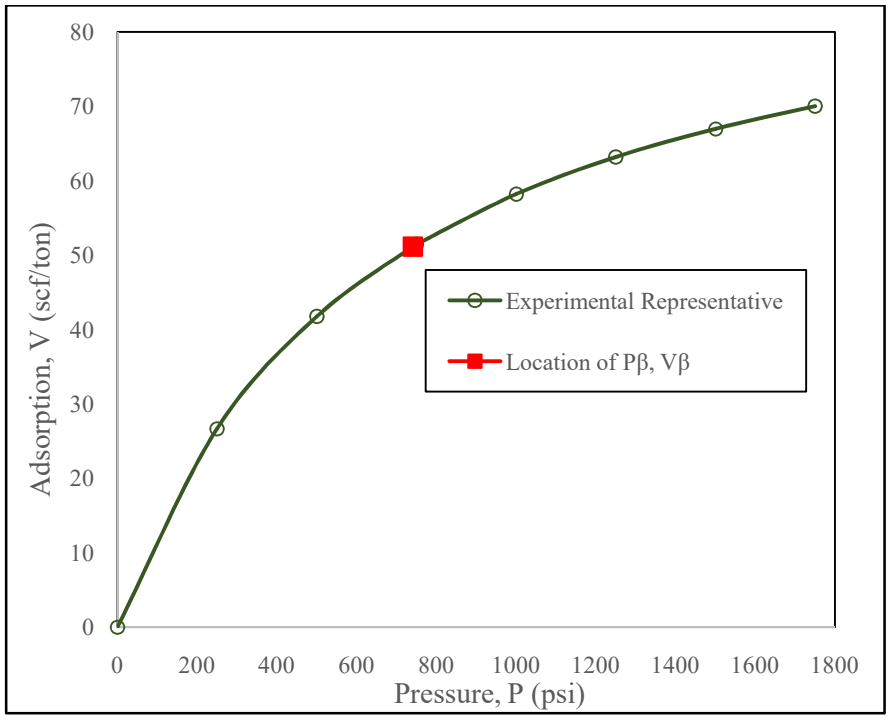

Figure 4.34: Location of P_β, V_β correlation on the isotherm representing laboratory adsorption of natural gas on Barnett shale sample at 180 ^{o}F

4.4.7Comparison of Barnett Shale Gas Adsorption Predictions by Langmuir and the Developed Isotherms

Predictions of natural gas adsorption on Barnett shale formation for high pressure range by Langmuir and the developed isotherms are compared in **Table 4.53**and**Figure 4.35**.

For Barnett shale formation, the developed isotherm predicts a maximum adsorbed volume of **71.07 scf/ton** at an adsorption saturation pressure of **2088.06 psi**. However, by Langmuir isotherm prediction, a maximum adsorbed volume of **96.00 scf/ton** is attained at an infinite adsorption saturation pressure.

Figure 4.35 shows that adsorption prediction by Langmuir isotherm is not reliable at higher pressures because of its inefficiency in defining the onset of adsorption saturation pressure; this contributes to an overestimation of maximum adsorbed volume.

Table 4.53: Barnett shale gas adsorption predictions by Langmuirand the developed isotherms at 180 ^{o}F

Pressure, *P* (psi)	**Barnett Shale Gas Adsorption, *V* (scf/ton)**	
	Langmuir Isotherm	**Developed Isotherm**
250	26.67	27.97
500	41.74	41.64
750	51.43	51.46
1000	58.18	58.74
1250	63.16	64.06
1500	66.98	67.74
1750	70.00	70.00
2000	72.45	71.00
2088.06	73.21	71.07
2250	74.48	71.07
2500	76.19	71.07
2750	77.65	71.07
3000	78.90	71.07
3250	80.00	71.07
3500	80.96	71.07
3750	81.82	71.07
4000	82.58	71.07
4250	83.26	71.07
4500	83.88	71.07
4750	84.44	71.07
5000	84.96	71.07

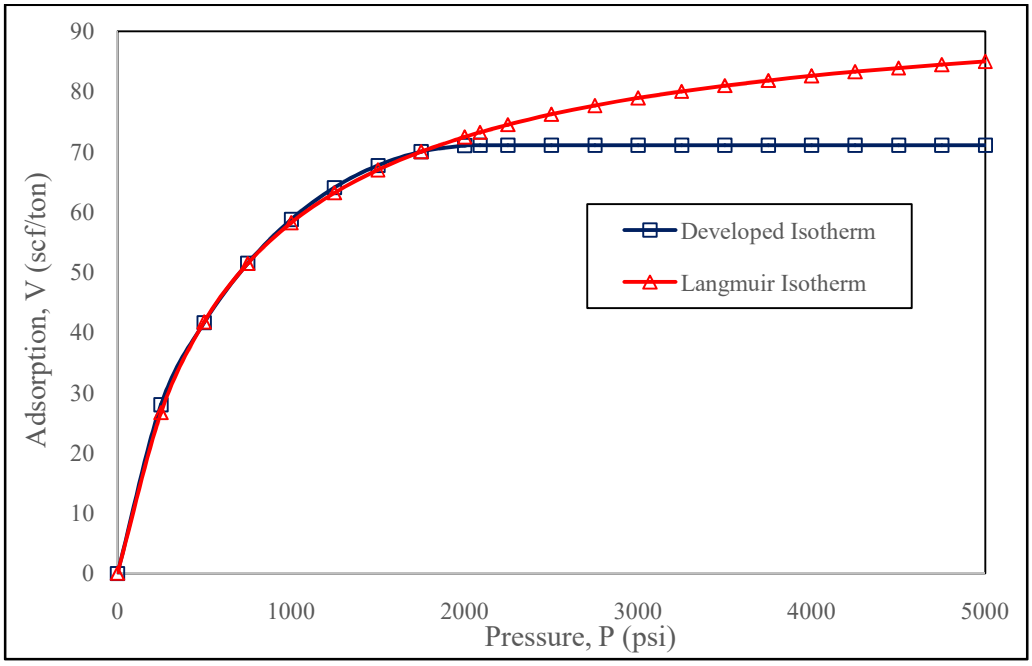

Figure 4.35: Barnett shale gas adsorption predictions by Langmuir and the developed isotherms at 180 ^{o}F

4.5 MARCELLUS SHALE GAS MATERIAL BALANCE ANALYSIS

4.5.1 Marcellus Shale Adsorption and Reservoir Data Used

The measured initial reservoir pressure of the Marcellus shale formation in Eastern Gas Shale Project (EGSP) Well WV-6 is 3,500 psig (SPE Formation Evaluation, March, 1998; and Soeder, 2011). Marcellus OGIP (free gas) was reported as 1,500 Tscf (US DoE, 2009).

The bulk of the OGIP cannot be recovered with current technologies. Engelder(2009) estimated Marcellus shale technically recoverable reservesas489 Tscf while undeveloped technically recoverable reserves was 410 Tscf (INTEK, 2009).Unproved technically recoverable reserves as of January, 2010 was estimated as 141 Tscf (US EIA, 2012) while undiscovered technically recoverable reserves was estimated as 84.2 Tscf (United States Geological Survey, 2011).

Marcellus shale reservoir area is 104,000 square miles (i.e. 269,359 km^2) (State Impact, 2017).Thus an average (net) thickness of 34 ft. is consideredin this work. Marcellus shale gas adsorption data is presented in **Table 4.54** while other reservoir data is shown in **Table 4.55**.

Table 4.54: Marcellus shale adsorption data

Parameter	**Symbol**	**Value**	**Unit**
Langmuir volume	V_L	200	scf/ton
Langmuir pressure	P_L	500	Psi
Maximum adsorbed volume (Developed isotherm)	V_{max}	166.37	scf/ton
Adsorption saturation pressure (Developed isotherm)	P_s	2909.88	psi
Adsorbate-adsorbent resistance parameter (Developed isotherm)	n	0.35	-

Table 4.55: Marcellus shale reservoir data
(SPE Formation Evaluation,March, 1998; US DoE, 2009; Soeder, 2011)

Parameter	Symbol	Value	Unit
Reservoir area	A	104,000	sq. mile
Reservoir area	A	269,359	sq. km.
Matrix porosity before fracturing	ϕ'_{mat}	0.10	-
Fracture porosity	ϕ_{frac}	0.04	-
Matrix permeability	k_{Darcy}	0.0003	mD
Initial gas saturation	S_{g_i}	0.70	-
Initial water saturation	S_{w_i}	0.30	-
Matrix (bulk) density	ρ_m	2.46	g/cm^3
Initial reservoir pressure	P_i	3,500	psig
Bottom hole pressure	P_{wf}	500	psig
Water compressibility	C_w	3.6×10^{-6}	psi^{-1}
Rock matrix compressibility	C_{matrix}	4.0×10^{-12}	psi^{-1}
Reservoir temperature	T	175	^oF
Gas gravity	γ_g	0.65	-

4.5.2Variation of Marcellus Shale Gas Compressibility Factor with Pressure

Marcellus shale gas reservoir temperature $T$of 175 ^{o}F (i.e. 635 ^{o}R) and a natural gas gravityγ_g of 0.65 are considered.Based on gas compositions (see **Table 2.8**), applying Sutton (1985) correlation$\left(0.57 < \gamma_g < 1.68\right)$ yields a pseudo-critical pressure P_{pc} of 670.13 psi (see **Equation 2.135**), pseudo-critical temperature T_{pc} of 365.11^{o}R (see **Equation 2.136**) and a pseudo-reduced temperature T_{pr} of 1.7392.

Standing and Katz Z-factors Z_{SK} are used as initial guesses in evaluating Dranchuk-Abou-Kassem Z-factors Z_{DAK}(see **Equation 3.87**) indicated as Z in **Table 4.56**. Here, the Dranchuk-Abou-Kassem Z-factorrepresents single-porosity gas reservoirs Z-factor at pressure *P*without pore compaction. The MAPPLE program for evaluating Marcellus shale Z-factorusing Dranchuk-Abou-Kassem (1975) eleven-constant equation of state is shown in **Appendix D**.

The pressure range considered for Marcellus shale is: $0 \leq P \leq 3{,}500$ psig. The initial formation volume factor of Marcellus shale gas:

$$B_{g_i} = \left(\frac{P_{sc}}{T_{sc}}\right)\frac{Z_i T}{P_i} \tag{4.51}$$

is evaluated as 4.6313 × 10^{-3} rcf/scf.

With ϕ_{frac} = 0, single-porosity Z-factor with pore compaction is evaluated as:

$$Z^* = Z\{1 - (1.5429E - 6)\Delta P\}^{-1} \tag{4.52}$$

With ϕ_{frac} = 0.04, Aguilera (2008) dual-porosity Z-factoris evaluated as:

$$Z'' = Z\{1 - (2.1479E - 6)\Delta P\}^{-1} \tag{4.53}$$

and the modified dual-porosity Z-factor is evaluated as:

$$Z^{**} = Z\{1 - (2.0983E - 6)\Delta P\}^{-1} \quad (4.54)$$

The variations of the Z-factors with pressure depletion are shown in **Table 4.56** and **Figure 4.36**. Correlating the modified dual-porosity Z-factor with Aguilera dual porosity Z-factor yields a R^2 value of 1.000.

Table 4.56: Variations of Marcellus shale gas Z, Z^*, Z'' and Z^{**} with pressurebased onϕ_{frac} of 0.04

P (psig)	P_{pr}	Z	ΔP (psig)	Z^*	Z'' (Aguilera)	Z^{**} (Modified)
3500	5.2229	0.9030	0	0.9030	0.9030	0.9030
3300	4.9244	0.8947	200	0.8950	0.8951	0.8951
3100	4.6260	0.8876	400	0.8881	0.8884	0.8883
2910	4.3424	0.8823	590	0.8831	0.8834	0.8834
2700	4.0291	0.8780	800	0.8791	0.8795	0.8795
2500	3.7306	0.8757	1000	0.8771	0.8776	0.8775
2300	3.4322	0.8753	1200	0.8769	0.8776	0.8775
2100	3.1337	0.8768	1400	0.8787	0.8794	0.8794
1900	2.8353	0.8804	1600	0.8826	0.8834	0.8834
1700	2.5368	0.8859	1800	0.8884	0.8893	0.8893
1500	2.2384	0.8934	2000	0.8962	0.8973	0.8972
1300	1.9399	0.9030	2200	0.9061	0.9073	0.9072
1100	1.6415	0.9143	2400	0.9177	0.9190	0.9189
900	1.3430	0.9272	2600	0.9309	0.9324	0.9323
700	1.0446	0.9415	2800	0.9456	0.9472	0.9471
500	0.7461	0.9570	3000	0.9615	0.9632	0.9631
300	0.4477	0.9736	3200	0.9784	0.9803	0.9802
100	0.1492	0.9910	3400	0.9962	0.9983	0.9981

0	0	1.0000	3500	1.0054	1.0076	1.0074

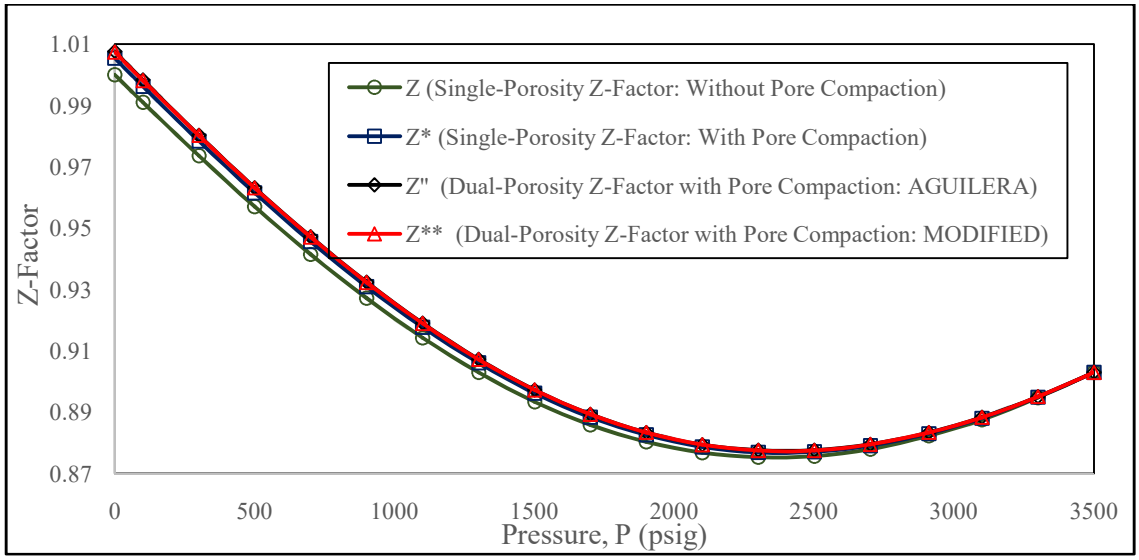

Figure 4.36: Variations of Z, $Z^{*}Z''$ and Z^{**} with pressure for Marcellus shale formation based on ϕ_{frac} of 0.04

4.5.3 Establishment of Marcellus Shale OGIPs from Plots of G_p versus P/Z^{**}

The variations of Marcellus shale gas P/Z^{**} and cumulative gas production G_p with pressure depletion based on ϕ_{frac} of 0.04 are shown in **Table 4.57**. Also, **Figure 4.37** shows the plots of Marcellus shale formation G_p versus P/Z^{**}based on ϕ_{frac} of 0.04. The original gas-in-place OGIP without adsorption consideration is evaluated as 1,480.4939 Tscf. However, the OGIPs that account for free and adsorbed gases based on the developed isotherm and Langmuir isotherm are 2,609.2751 Tscf and 2,667.8277 Tscf respectively.

When compared with the free gas-in-place, the adsorbed gas in Marcellus shale formation is observed to be significant due to the low reservoir temperature that yields low gasmolecular activation energy which favours adsorption.

From the material balance analysis, with pressure drawdown from 3,500 to 2,285 psig, technically recoverable reserves of 489 Tscf would be depletedin form of free gasG_p; the corresponding developed isotherm-based and Langmuir isotherm-based technically recoverable (total gas) reserves (in form of total gasG_p) were estimated as 509.2567 and 564.0901 Tscf respectively.

The plots of Marcellus shale formation G_p versus P/Z^{**} (based on ϕ_{frac} of 0.04) within the technically recoverable reserves depletion range is shown in **Figure 4.38**.

Table 4.57: Variation of Marcellus shale gas G_p with pressure based on ϕ_{frac} of 0.04

P (psig)	ΔP (psig)	P/Z^{**} (psig)	$1-\frac{P/Z^{**}}{P_i/Z_i}$	Cumulative Gas Production G_p (Tscf)		
				$G_{p_{Free}}$ Without Adsorption	$G_{p_{Total}}$ Developed Isotherm	$G_{p_{Total}}$ Langmuir Isotherm
3500	0	3875.97	0	0	0	0
3300	200	3686.74	0.0488	72.7102	72.7102	81.6375
3100	400	3489.81	0.0996	148.4004	148.4004	167.2470
2910	590	3294.09	0.1501	223.6435	223.6435	252.9911
2700	800	3069.93	0.2080	309.9124	312.0178	352.3973
2500	1000	2849.00	0.2650	394.8404	403.0686	451.3801
2300	1200	2621.08	0.3238	482.4502	501.1456	555.1441
2285	1215	2603.89	0.3282	**489.0000**	**509.2567**	**564.0901**
2100	1400	2388.00	0.3839	571.9970	605.8908	663.3294
1900	1600	2150.78	0.4451	663.1827	717.4766	776.2621
1700	1800	1911.62	0.5068	755.1135	835.5958	893.8927
1500	2000	1671.87	0.5687	847.3423	960.5504	1016.9614
1300	2200	1432.98	0.6303	939.1240	1092.5841	1146.4362
1100	2400	1197.08	0.6911	1029.7138	1232.3132	1284.1425
900	2600	965.35	0.7509	1118.8136	1381.4218	1433.8205
700	2800	739.10	0.8093	1205.8275	1542.4367	1601.6054
500	3000	519.16	0.8660	1290.3084	1720.4562	1799.1657
300	3200	306.06	0.9210	1372.2564	1927.5845	2032.7328

100	3400	100.19	0.9741	1451.3735	2206.3469	2412.5485
0	3500	0	1.0000	1489.9635	2618.7447	2677.2973

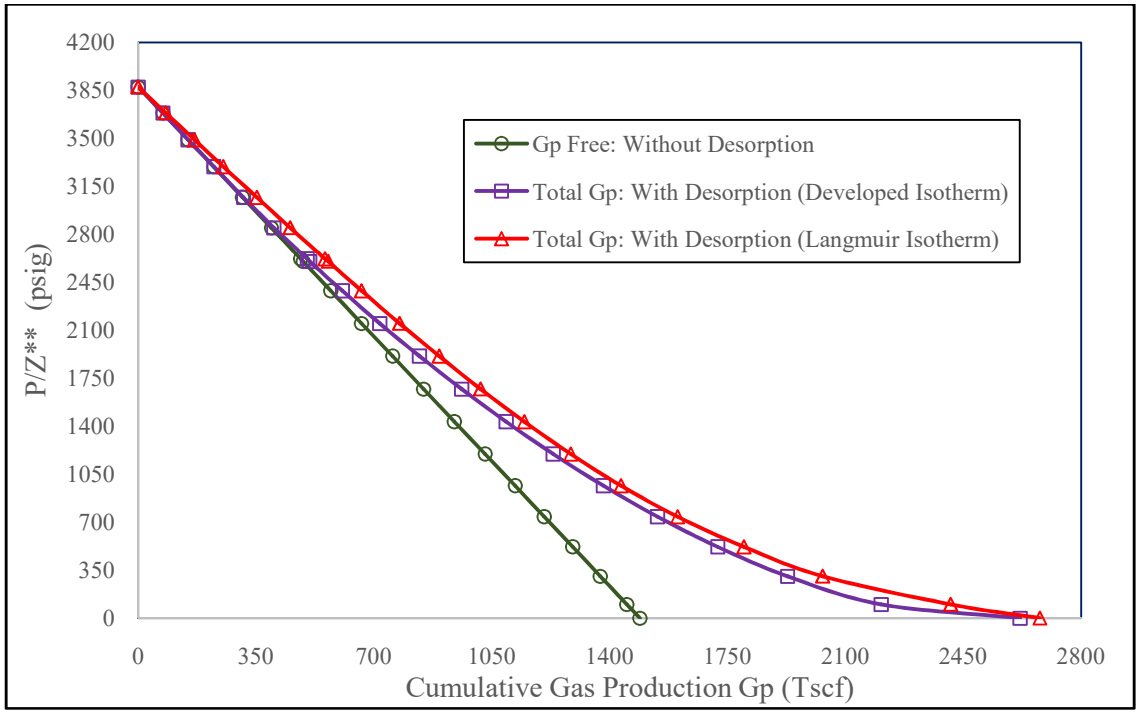

Figure 4.37: Plots of Marcellus shale G_p versus $^{P}/_{Z^{**}}$ based on ϕ_{frac} of 0.04

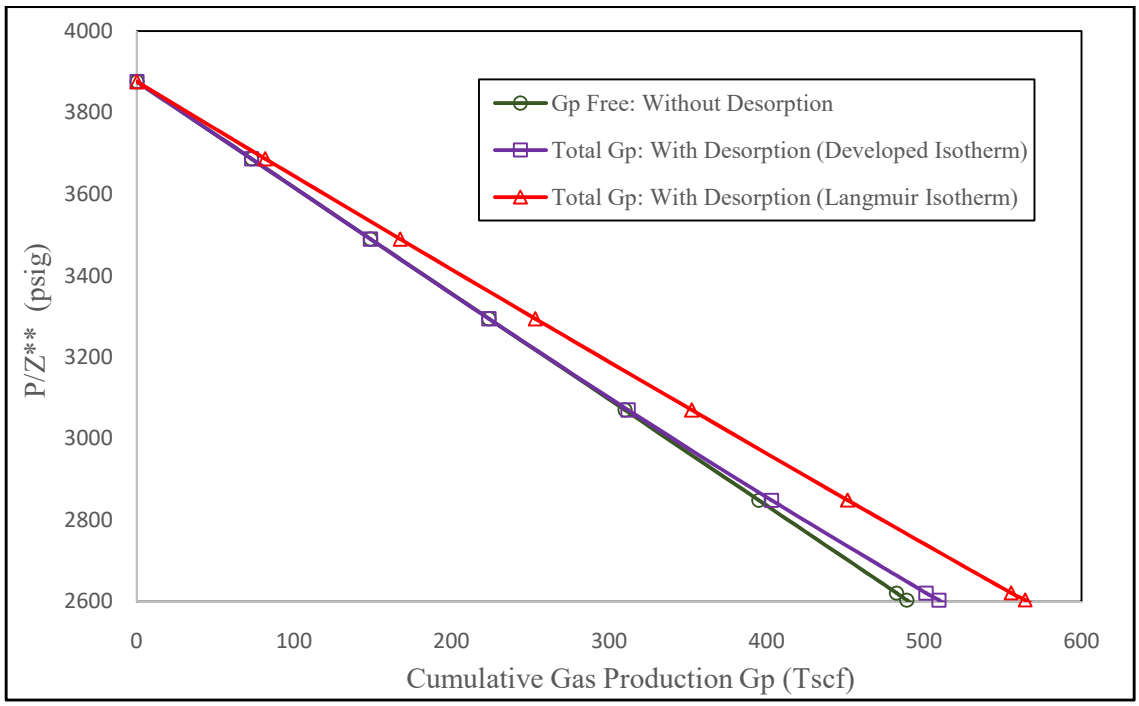

Figure 4.38: Plots of Marcellus shale G_p versus $^{P}/_{Z^{**}}$ (based on ϕ_{frac} of 0.04) for technically recoverable (free gas) reserves of 489 Tscf

4.5.4Variation of Marcellus Shale GIP with Pressure

The variation ofgas-in-place GIP with pressure for Marcellus shale formation with fracture porosity ϕ_{frac} of 0.04 is shown in **Table 4.58** while the plot is shown in **Figure 4.39**.However, the fractions of free and adsorbed GIP to total GIP for Marcellus shale formation with fracture porosity ϕ_{frac} of 0.04 is shown in **Table 4.59** while the plot is shown in **Figure 4.40**.

From **Figures 4.39** and **4.40**, with the developed isotherm-based MBE, pressure depletion from the initial reservoir condition of 3,500 to 2,554.81 psig reduces the free gas contributing capacity to production from 56.90% to 50.00%; further depletion to 100 psig reduces it to 9.36%. However, the adsorbed gas is observed to be the principal contributor to gas production below 2,554.81 psig. Pressure depletion from the initial reservoir condition to 2,554.81 psig causes the capacity to increase from 43.10% to 50.00%; while the capacity increases from 50.00% to 90.64% when pressure is depleted further down to 100 psig.

It is thus evident that adsorbed gas contribution to production is prevalent below a pressure of about 0.7299 the initial reservoir pressure. This confirms the remarkable proportion of adsorbed gas in Marcellus shale formation when compared with the free gas-in-place.

Table 4.58: Variation of Marcellus shale GIP with pressure based on ϕ_{frac} of 0.04

P (psig)	Gas-in-Place GIP (Tscf)				
	GIP_{Free} Without Adsorption	$GIP_{Adsorbed}$ Developed Isotherm	$GIP_{Adsorbed}$ Langmuir Isotherm	GIP_{Total} Developed Isotherm	GIP_{Total} Langmuir Isotherm
3500	1489.9635	1128.7812	1187.3338	2618.7447	2677.2973
3300	1417.2533	1128.7812	1178.4065	2546.0345	2595.6598
3100	1341.5631	1128.7812	1168.4872	2470.3443	2510.0503
2910	1266.3200	1128.7812	1157.9862	2395.1012	2424.3062
2700	1180.0511	1126.6758	1144.8489	2306.7269	2324.9000
2500	1095.1231	1120.5530	1130.7941	2215.6761	2225.9172
2300	1007.5133	1110.0858	1114.6399	2117.5991	2122.1532
2100	917.9665	1094.8874	1096.0014	2012.8539	2013.9679
1900	826.7808	1074.4873	1074.2544	1901.2681	1901.0352
1700	734.8500	1048.2989	1048.5546	1783.1489	1783.4046
1500	642.6212	1015.5731	1017.7147	1658.1943	1660.3359
1300	550.8395	975.3211	980.0216	1526.1606	1530.8611
1100	460.2497	926.1818	932.9051	1386.4315	1393.1548
900	371.1499	866.1730	872.3269	1237.3229	1243.4768
700	284.1360	792.1720	791.5559	1076.3080	1075.6919
500	199.6551	698.6334	678.4765	898.2885	878.1316
300	117.7071	573.4531	526.8574	691.1602	644.5645
100	38.5900	373.8078	226.1588	412.3978	264.7488

0	0	0	0	0	**0**

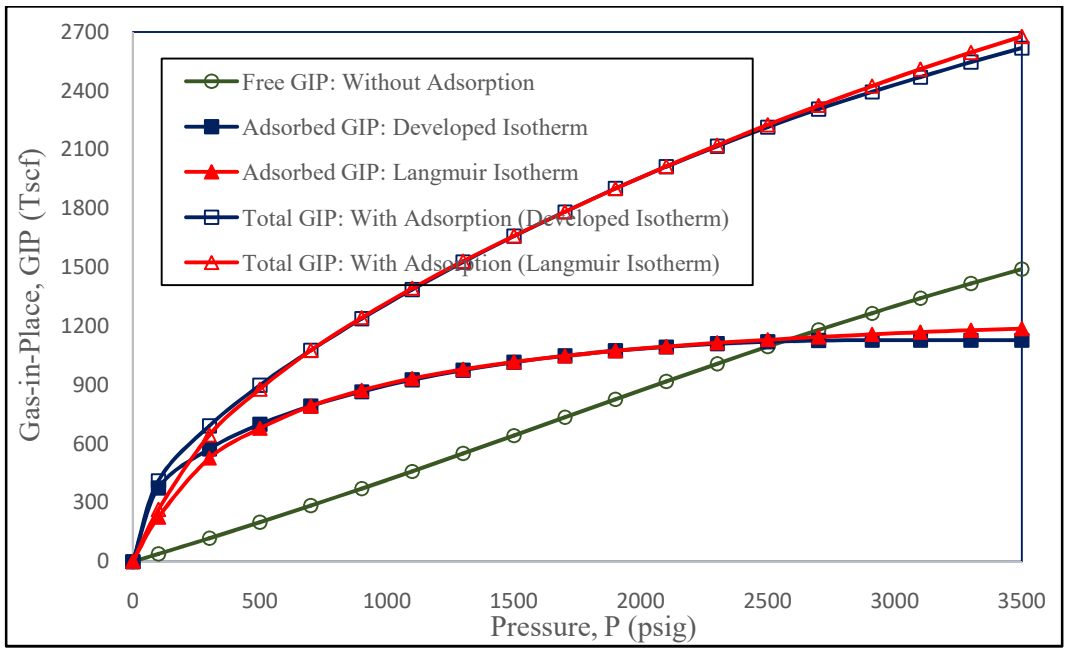

Figure 4.39: Plots of Marcellus shale GIP versus pressure based on ϕ_{frac} of 0.04

Table 4.59: Fractions of free and adsorbed GIP to total GIP for Marcellus shaleformation with fracture porosity ϕ_{frac} of 0.04

P (psig)	Fractions of Free and Adsorbed GIP to Total GIP			
	Developed Isotherm-Based		Langmuir Isotherm-Based	
	GIP_{Free}	$GIP_{Adsorbed}$	GIP_{Free}	$GIP_{Adsorbed}$
3500	0.5690	0.4310	0.5565	0.4435
3300	0.5567	0.4433	0.5460	0.4540
3100	0.5431	0.4569	0.5345	0.4655
2910	0.5287	0.4713	0.5223	0.4777
2700	0.5116	0.4884	0.5076	0.4924
2500	0.4943	0.5057	0.4920	0.5080
2300	0.4758	0.5242	0.4748	0.5252
2100	0.4561	0.5439	0.4558	0.5442
1900	0.4349	0.5651	0.4349	0.5651
1700	0.4121	0.5879	0.4120	0.5880
1500	0.3875	0.6125	0.3870	0.6130
1300	0.3609	0.6391	0.3598	0.6402
1100	0.3320	0.6680	0.3304	0.6696
900	0.3000	0.7000	0.2985	0.7015
700	0.2640	0.7360	0.2641	0.7359
500	0.2223	0.7777	0.2274	0.7726
300	0.1703	0.8297	0.1826	0.8174
100	0.0936	0.9064	0.1458	0.8542

0	-	-	-	-

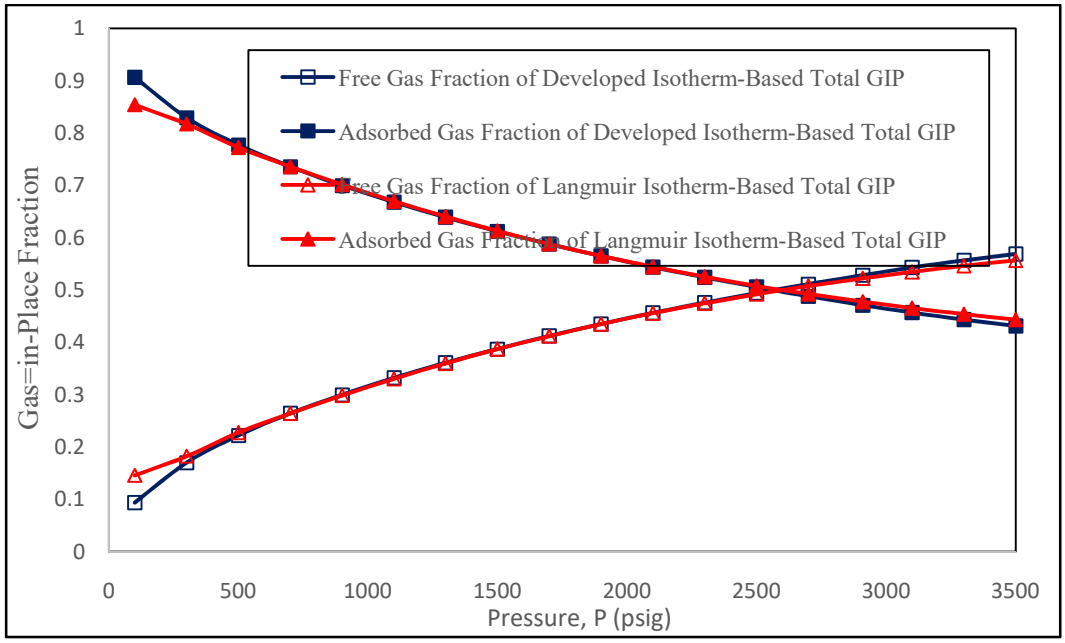

Figure 4.40: Fractions of free and adsorbed GIP to total GIP for Marcellus shale formation based on ϕ_{frac} of 0.04

4.5.5Effect of Fracture Porosity on Marcellus Shale Gas Production

The single-porosity gas reservoir Z-factor with pore compaction is evaluated as:

$$Z^* = Z\{1 - (1.5429E - 6)\Delta P\}^{-1} \quad (4.55)$$

The variations of Marcellus shale gas P/Z^{**} and cumulative gas production G_p with pressure depletion based on ϕ_{frac} of 0 and the developed isotherm are shown in **Table 4.60**.

For fracture porosity ϕ_{frac} of 0.02, the Z-factor for gas reservoir with pore volume reduction after fracturing:

$$Z^{**} = Z \cdot \{1 - (1.8206E - 6) \cdot \Delta P\}^{-1} \quad (4.56)$$

The variations of Marcellus shale gas P/Z^{**} and cumulative gas production G_p with pressure depletion based on ϕ_{frac} of 0.02 and the developed isotherm are shown in **Table 4.61**.

Also, for fracture porosity ϕ_{frac} of 0.06, the Z-factor for gas reservoir with pore volume reduction after fracturing:

$$Z^{**} = Z \cdot \{1 - (2.3761E - 6) \cdot \Delta P\}^{-1} \quad (4.57)$$

The variations of Marcellus shale gas P/Z^{**} and cumulative gas production G_p with pressure depletion based on ϕ_{frac} of 0.06 and the developed isotherm are shown in **Table 4.62**.

Fracture-induced increase in gas production from Marcellus shale (with reference to no-fracturing scenario) is shown in **Table 4.63**and **Figure 4.41**. Fracturing accelerates pressure depletion, and at a particular pressure, fracturing has increasing effect only on free gas production while gas desorption remains the same at that pressure.

As compared to the no-fracturing scenario, increases in gas production at fracture porosity levels of 0.02, 0.04 and 0.06 with pressure depletion are observed to be rising stepwise till respective constant peak values of about 0.2980 Tscf, 0.7450 Tscf and 1.0430 Tscf were attained with pressure depletions from 2,700 to 1,100 psig, 2,300 to 1,300 psig, and 2,300 to 1,100 psig. Thereafter, gas production increase was found to be declining stepwise towards the abandonment pressure range.

Table 4.60: Variation of Marcellus shale G_p with pressure based on ϕ_{frac} of 0 and the developed isotherm

P (psig)	ΔP (psig)	Z^*	P/Z^* (psig)	$1 - \frac{P/Z^*}{P_i/Z_i}$	Cumulative Gas Production G_p (Tscf)	
					$G_{p_{Free}}$	$G_{p_{Total}}$
3500	0	0.9030	3875.97	0	0	0
3300	200	0.8950	3687.15	0.0487	72.5612	72.5612
3100	400	0.8881	3490.60	0.0994	148.1024	148.1024
2910	590	0.8831	3295.21	0.1498	223.1966	223.1966
2700	800	0.8791	3071.32	0.2076	309.3164	311.4218
2500	1000	0.8771	2850.30	0.2646	394.2444	402.4726
2300	1200	0.8769	2622.88	0.3233	481.7052	500.4006
2100	1400	0.8787	2389.89	0.3834	571.2521	605.1459
1900	1600	0.8826	2152.73	0.4446	662.4378	716.7317
1700	1800	0.8884	1913.55	0.5063	754.3686	834.8509
1500	2000	0.8962	1673.73	0.5682	846.5972	959.8058
1300	2200	0.9061	1434.72	0.6298	938.3789	1091.8390
1100	2400	0.9177	1198.65	0.6907	1029.1178	1231.7172
900	2600	0.9309	966.81	0.7506	1118.3666	1380.9748
700	2800	0.9456	740.27	0.8090	1205.3804	1541.9896
500	3000	0.9615	520.02	0.8658	1290.0104	1720.1582
300	3200	0.9784	306.62	0.9209	1372.1074	1927.4355

100	3400	0.9962	100.38	0.9741	1451.3735	2206.3469
0	3500	1.0054	0	1.0000	1489.9635	2618.7447

Table 4.61: Variation of Marcellus shale G_p with pressure based on ϕ_{frac} of 0.02 and the developed isotherm

P (psig)	ΔP (psig)	Z^{**}	P/Z^{**} (psig)	$1-\frac{P/Z^{**}}{P_i/Z_i}$	Cumulative Gas Production G_p (Tscf)	
					$G_{p_{Free}}$	$G_{p_{Total}}$
3500	0	0.9030	3875.97	0	0	0
3300	200	0.8950	3687.15	0.0487	72.5612	72.5612
3100	400	0.8882	3490.20	0.0995	148.2513	148.2513
2910	590	0.8832	3294.84	0.1499	223.3455	223.3455
2700	800	0.8793	3070.62	0.2078	309.6144	311.7196
2500	1000	0.8773	2849.65	0.2648	394.5424	402/7706
2300	1200	0.8772	2621.98	0.3235	482.0032	500.6986
2100	1400	0.8790	2389.08	0.3836	571.5499	605.4437
1900	1600	0.8830	2151.75	0.4448	662.7358	717.0297
1700	1800	0.8888	1912.69	0.5065	754.6665	835.1488
1500	2000	0.8967	1672.80	0.5684	846.8952	960.1033
1300	2200	0.9066	1433.93	0.6300	938.6770	1092.1371
1100	2400	0.9183	1197.87	0.6909	1029.4158	1232.0152
900	2600	0.9316	966.07	0.7507	1118.5157	1381.1239
700	2800	0.9463	739.72	0.8091	1205.5295	1542.1387
500	3000	0.9623	519.59	0.8659	1290.1594	1720.3072

300	3200	0.9793	306.34	0.9210	1372.2564	1927.5845
100	3400	0.9972	100.28	0.9741	1451.3735	2206.3469
0	3500	1.0064	0	1.0000	1489.9635	2618.7447

Table 4.62: Variation of Marcellus shale G_p with pressure based on ϕ_{frac} of 0.06 and the developed isotherm

P (psig)	ΔP (psig)	Z^{**}	P/Z^{**} (psig)	$1-\frac{P/Z^{**}}{P_i/Z_i}$	Cumulative Gas Production G_p (Tscf)	
					$G_{p_{Free}}$	$G_{p_{Total}}$
3500	0	0.9030	3875.97	0	0	0
3300	200	0.8951	3686.74	0.0488	72.7102	72.7102
3100	400	0.8884	3489.42	0.0997	148.5493	148.5493
2910	590	0.8835	3293.72	0.1502	223.7925	223.7925
2700	800	0.8797	3069.23	0.2081	310.0614	312.1668
2500	1000	0.8778	2848.03	0.2652	395.1383	403.3665
2300	1200	0.8778	2620.19	0.3240	482.7482	501.4436
2100	1400	0.8797	2387.18	0.3841	572.2950	606.1888
1900	1600	0.8838	2149.81	0.4453	663.4807	717.7746
1700	1800	0.8897	1910.76	0.5070	755.4115	835.8938
1500	2000	0.8977	1670.94	0.5689	847.6403	960.8484
1300	2200	0.9077	1432.19	0.6305	939.4220	1092.8821
1100	2400	0.9195	1196.30	0.6914	1030.1608	1232.7602
900	2600	0.9330	964.63	0.7511	1119.1115	1381.7197
700	2800	0.9478	738.55	0.8094	1205.9764	1542.5856
500	3000	0.9639	518.73	0.8662	1290.6064	1720.7542
300	3200	0.9811	305.78	0.9211	1372.4054	1927.7335

100	3400	0.9991	100.09	0.9742	1451.5224	2206.4958
0	3500	1.0084	0	1.0000	1489.9635	2618.7447

Table 4.63: Fracture-induced increase in gas production from Marcellus shale (with reference to no-fracturing scenario)

P (psig)	Increase in Gas Production ΔG_p (Tscf) with Reference to No-Fracturing Scenario			
	ϕ_{frac} of 0	ϕ_{frac} of 0.02	ϕ_{frac} of 0.04	ϕ_{frac} of 0.06
3500	0	0	0	0
3300	0	0	0.1490	0.1450
3100	0	0.1489	0.2980	0.4469
2910	0	0.1489	0.4469	0.5959
2700	0	0.2980	0.5960	0.7450
2500	0	0.2980	0.5960	0.8939
2300	0	0.2980	0.7450	1.0430
2100	0	0.2978	0.7449	1.0429
1900	0	0.2980	0.7449	1.0429
1700	0	0.2979	0.7449	1.0429
1500	0	0.2980	0.7451	1.0431
1300	0	0.2981	0.7451	1.0431
1100	0	0.2980	0.5960	1.0430
900	0	0.1491	0.4470	0.7449
700	0	0.1491	0.4471	0.5960
500	0	0.1490	0.2980	0.5960
300	0	0.1490	0.1490	0.2980

100	0	0	0	0.1489
0	0	0	0	0

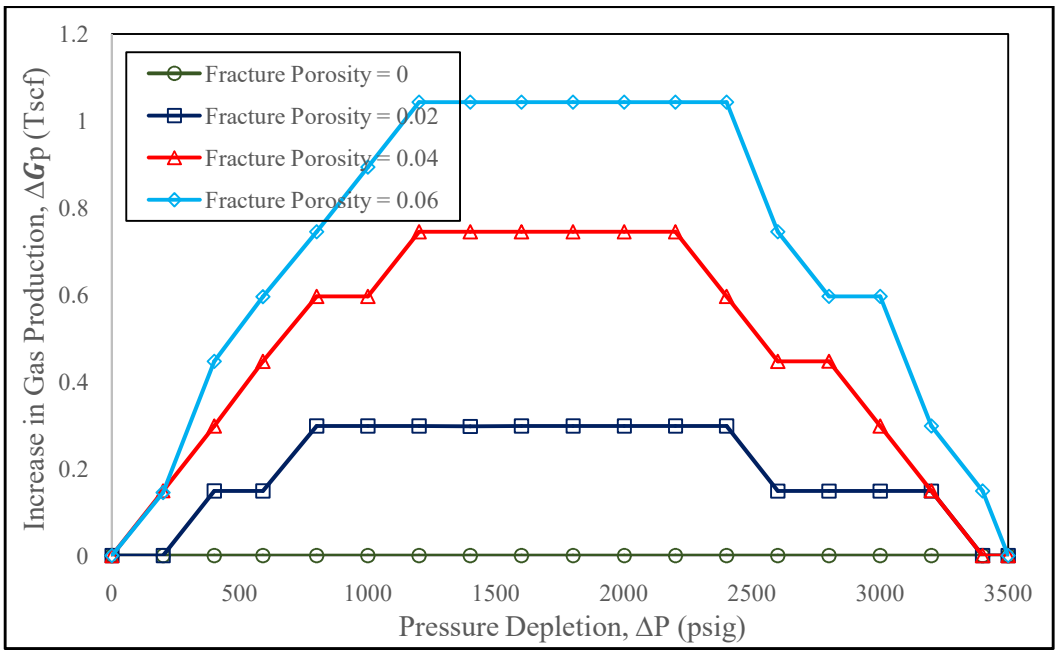

Figure 4.41: Fracture-induced increase in gas production from Marcellus shale (with reference to no-fracturing scenario)

4.6 MARCELLUS SHALE GAS PRODUCTION PERFORMANCE FORECAST

4.6.1Generation of Decline Rate Model from Production History

The variations of Marcellus shale gas production rate $q_g$with time (see **Figure 2.20 (**Chesapeake Energy, 2010)) is shown in **Table 4.64** and the plot is shown in **Figure 4.42**. The production rate at the first day is considered as 4,000 Mscf/d based on graphical extrapolation.

Thus variation of Marcellus shale gas production rateq_g with time is modelled as:

$$q_{g_{Well\ Forecast}^{Actual\ Total\ Gas}} = 4326.3\ t^{-0.5500}\ \text{Mscf/d} \tag{4.58}$$

where t is in months, the initial production rate (at the end of the first month) q_{g_1}= 4326.3 Mscf/d and production decline exponent $n = 0.5500$.

Table 4.64: Variations of Marcellus shale gas production rate q_g and cumulative gas production G_p with time

Time, t (month)	**Time, t (year)**	**Time, t (day)**	q_g **(Mscf/d)**	G_p **(MMscf)**
1	0.0833	30	3400	111.00
3	0.2500	90	2500	288.00
5	0.4167	150	1950	421.50
7	0.5833	210	1600	528.00
9	0.7500	270	1350	616.50
11	0.9167	330	1200	693.00
13	1.0833	390	1100	762.30
15	1.2500	450	1000	825.60
17	1.4167	510	950	884.10
19	1.5833	570	900	939.60
21	1.7500	630	840	991.80
23	1.9167	690	800	1041.00
25	2.0833	750	770	1088.10
27	2.2500	810	720	1132.80
29	2.4167	870	700	1175.40
31	2.5833	930	650	1215.90
33	2.7500	990	625	1254.15
35	2.9167	1050	615	1291.35
37	3.0833	1110	610	1328.10
39	3.2500	1170	600	1364.40
41	3.4167	1230	550	1398.90
43	3.5833	1290	525	1431.15
45	3.7500	1350	515	1462.35
47	3.9167	1410	505	1492.95
49	4.0833	1470	500	1523.10

51	4.2500	1530	495	1552.95
53	4.4167	1590	475	1582.05
55	4.5833	1650	450	1609.80
57	4.7500	1710	430	1636.20
59	4.9167	1770	425	1661.85

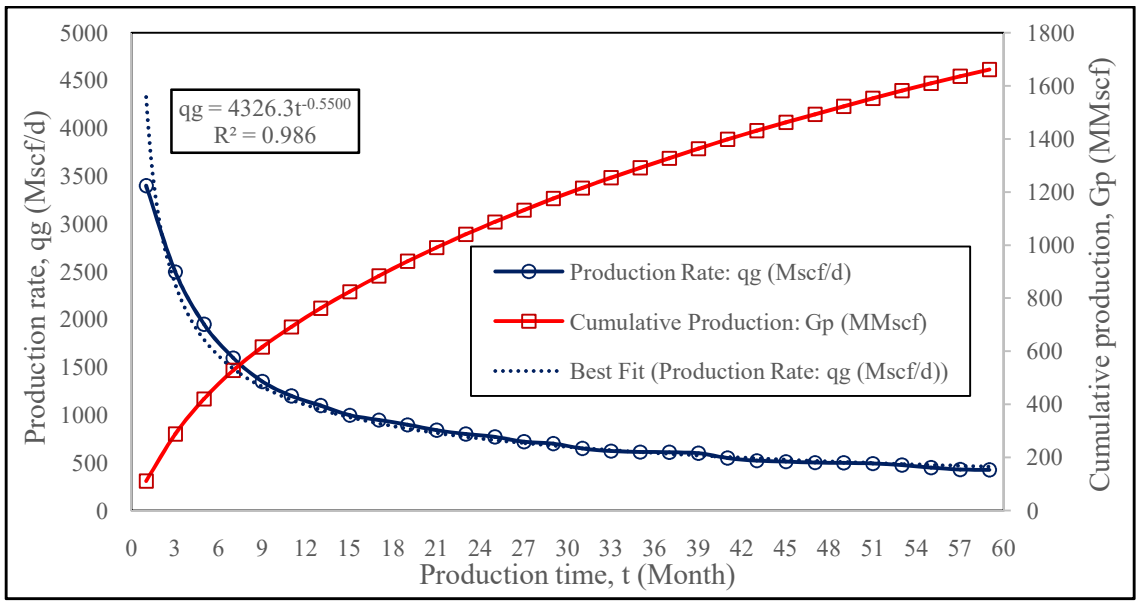

Figure 4.42: Plot of Marcellus shale gas q_g and G_p versus time t

4.6.2Development of Free and Total Gas Decline Rate Models for Production Performance Forecast

Flow rate $q = \frac{dG_p}{dP} * \frac{dP}{dt}$; however, pressure depletion in the well is the same both for free and total gas production. The decline rate exponent $n = \frac{C}{\left(\frac{dG_p}{dP}\right)}$(see **Equation 3.129**) where C is a constant of proportionality.

Therefore, the trend of $\frac{dG_p}{dP}$ (for pressure depletion from the initial reservoir pressure P_i to the wellbore flowing pressure P_{wf}in the improved material balance analysis MBA) forms the basis for comparing the production decline exponent n, and thus the flow rates $q_g$of free gas and total gas based on the developed isotherm, and total gas based on Langmuir isotherm.

In **Table 4.57**, for pressure depletion from initial reservoir pressure P_i to the wellbore flowing pressureP_{wf},

$$\left(\frac{dG_p}{dP}\right)_{Free\ Gas}^{MBA-Predicted} = 0.4301 \text{ Tscf/psig} \quad (4.59)$$

$$\left(\frac{dG_p}{dP}\right)_{(Developed\ Isotherm)}^{\substack{MBA-Predict \\ Total\ Gas}} = 0.5735 \text{ Tscf/psi} \quad (4.60)$$

and

$$\left(\frac{dG_p}{dP}\right)_{(Langmuir\ Isotherm)}^{\substack{MBA-Predict \\ Total\ Gas}} = 0.5997 \text{ Tscf/psi} \quad (4.61)$$

This shows that increase in estimated ultimate recovery (EUR) of Marcellus shale gas due to gas desorption based on the developed and Langmuir isotherms are 0.2500and 0.2828 respectively; where

$$\text{Increase in EUR} = \frac{\left(G_p^{Total\ Gas} - G_p^{Free\ Gas}\right)}{G_p^{Total\ Gas}} \tag{4.62}$$

Actual Marcellus shale OGIP (free gas) is 1,500 Tscf (US DoE, 2009); however, the MBA-predicted OGIP (free gas) is 1,489.9635 (see **Table 4.57**).

Therefore,

$$\left(\frac{Actual\ OGIP}{MBA-Predicted\ OGIP}\right)_{Free\ Gas} = 1.0067 \tag{4.63}$$

and

$$\left(\frac{dG_p}{dP}\right)_{Free\ Gas}^{Actual} = 1.0067 \times \left(\frac{dG_p}{dP}\right)_{Free\ Gas}^{MBA-Predicted} \tag{4.64}$$

Thus for pressure depletion from initial reservoir pressure P_i to the wellbore flowing pressureP_{wf},

$$\left(\frac{dG_p}{dP}\right)_{Free\ Gas}^{Actual} = 0.4330 \text{ Tscf/psig} \tag{4.65}$$

The developed isotherm has been established to truly represent Type I isotherm and predict actual adsorption or desorption, i.e.

$$V_{Gas\ Desorption}^{Experimental} \approx V_{Gas\ Desorption}^{Developed\ Isotherm} \tag{4.66}$$

However, the actual total gas production:

$$G_{p_{Total\ Gas}}^{Actual} = G_{p_{Free\ Gas}}^{Actual} + G_{p_{Desorbed\ Gas}}^{Actual} \tag{4.67}$$

Hence, for Marcellus shale formation,

$$G_{p_{Total\ Gas}}^{Actual} = 1.0067 \times \left(G_{p_{Free\ Gas}}^{MBA-Predicte}\right) + G_{p_{Desorbed\ Gas}}^{Developed\ Isotherm} \tag{4.68}$$

At P_{wf},

$$G_{p_{Total\ Gas}}^{Actual} = 1.0067\times (1290.3084) + 430.1478 = 1729.1013 \text{ Tscf} \quad (4.69)$$

and the corresponding

$$\left(\frac{dG_p}{dP}\right)_{Total\ Gas}^{Actual} = 0.5764 \text{ Tscf/psig} \quad (4.70)$$

The decline rate exponent

$$n = \frac{C}{\left(\frac{dG_p}{dP}\right)} \quad (4.71)$$

From the actual total gas forecast (see **Figure 4.42**),

$$n_{Well\ Forecast}^{Actual\ Total\ Gas} = 0.5500 \quad (4.72)$$

Therefore,

$$n_{Well\ Forecast}^{Actual\ Free\ Gas} = 0.5500\left(\frac{0.5764}{0.4330}\right) = 0.7321 \quad (4.73)$$

$$n_{Well\ Forecast}^{Total\ Gas\ (Developed\ Isotherm)} = 0.5500\left(\frac{0.5764}{0.5735}\right) = 0.5528 \quad (4.74)$$

and

$$n_{Well\ Forecast}^{Total\ Gas\ (Langmuir\ Isotherm)} = 0.5500\left(\frac{0.5764}{0.5997}\right) = 0.5286 \quad (4.75)$$

However, to correlate the production rate forecast with the production rate from field data, the respective model fitting factors

$$K = \left(\frac{q_{g_{Field\ Data}}^{Actual\ Total\ Gas}}{q_{g_{Well\ Forecast}}^{Actual\ Total\ Gas}}\right) \quad (4.76)$$

after the first time step must be considered. Hence, the variations of respective q_g with time are modelled as:

$$q_{g_{Well\ Forecast}}^{Actual\ Free\ Gas} = K\left(q_{g_1}t^{-0.7321}\right)\text{Mscf/d} \quad (4.77)$$

$$q_{g_{Well\ Forecast}}^{\substack{Total\ Gas \\ (Developed\ Isotherm)}} = K\left(q_{g_1}t^{-0.5528}\right)\text{Mscf/d} \quad (4.78)$$

and

$$q_{g_{Well\ Forecast}}^{\substack{Total\ Gas \\ (Langmuir\ Isotherm)}} = K\left(q_{g_1}t^{-0.5286}\right)\text{Mscf/d} \quad (4.79)$$

Beyond the production history, the last value of K is retained.

Marcellus shale gas production performance forecast (q_g) within and beyond well production history are shown in **Tables 4.65**and **4.66** respectively.

Table 4.65: Marcellus shale gas production performance forecast (q_g) within well production history

Time, t (month)	Actual Total Gas q_g (Field Data) (Mscf/d)	Actual Total Gas q_g Forecast (Mscf/d) n = 0.5500	Model Fitting Factor K	Free Gas q_g Forecast (Mscf/d)	Total Gas q_g Forecast (Developed Isotherm) (Mscf/d)	Total Gas q_g Forecast (Langmuir Isotherm) (Mscf/d)
1	3400	4326	-	4326	4326	4326
3	2500	2364	1.0575	2047	2492	2560
5	1950	1785	1.0924	1455	1941	2018
7	1600	1483	1.0789	1123	1592	1669
9	1350	1292	1.0449	905	1342	1415
11	1200	1157	1.0372	776	1192	1263
13	1100	1055	1.0426	690	1092	1162
15	1000	975	1.0256	611	993	1060
17	950	911	1.0428	567	942	1009
19	900	857	1.0502	526	892	958
21	840	811	1.0357	483	833	896
23	800	771	1.0376	452	793	856
25	770	737	1.0448	428	763	824
27	720	706	1.0198	395	713	773
29	700	679	1.0309	379	693	752
31	650	654	0.9939	348	644	700
33	625	632	0.9889	330	619	674
35	615	612	1.0049	322	609	664
37	610	594	1.0269	316	604	659

39	600	577	1.0399	308	594	649
41	550	561	0.9804	279	544	596
43	525	547	0.9598	265	519	569
45	515	533	0.9662	258	510	559
47	505	520	0.9712	251	500	549
49	500	509	0.9823	246	494	543
51	495	498	0.9940	242	489	538
53	475	487	0.9754	230	470	517
55	450	477	0.9434	217	445	491
57	430	468	0.9188	206	425	469
59	425	459	0.9259	203	420	464

Table 4.66: Marcellus shale gas production performance forecast (q_g) beyond well production history

Time, t (year)	Time, t (month)	Actual Total Gas q_g Forecast (Mscf/d) n =0.5500	Model Fitting Factor K	ActualTotal Gas q_g Projection (Mscf/d)	Free Gas q_g Forecast (Mscf/d)	Total Gas q_g Forecast (Developed Isotherm) (Mscf/d)	Total Gas q_g Forecast (Langmuir Isotherm) (Mscf/d)
6	72	412	0.9259	381	175	377	418
7	84	378	0.9259	350	156	346	385
8	96	351	0.9259	325	142	321	359
9	108	329	0.9259	305	130	301	337
10	120	311	0.9259	288	120	284	319
11	132	295	0.9259	273	112	269	303
12	144	281	0.9259	260	105	257	290
13	156	269	0.9259	249	99	246	278
14	168	258	0.9259	239	94	236	267
15	180	249	0.9259	230	89	227	257
16	192	240	0.9259	222	85	219	249
17	204	232	0.9259	215	82	212	241
18	216	225	0.9259	208	78	205	234
19	228	218	0.9259	202	75	199	227
20	240	212	0.9259	196	72	194	221
21	252	207	0.9259	191	70	188	215
22	264	201	0.9259	186	68	184	210
23	276	197	0.9259	182	65	179	205

24	288	192	0.9259	178	63	175	201
25	300	188	0.9259	174	62	171	196
26	312	184	0.9259	170	60	167	192
27	324	180	0.9259	167	58	164	189
28	336	176	0.9259	163	57	161	185
29	348	173	0.9259	160	55	158	182
30	360	170	0.9259	157	54	155	178

For production forecast within the production history, the plots of Marcellus shale gasq_g versus $t$are displayed on the same chart (**Figures 4.43)** for (i) the well production history (serving as the base case), (ii) the model results for free gas production (no desorption), (iii) the model results for total gas production based on the developed isotherm, and (iv) the decline rate model results for total gas production based on Langmuir isotherm.

With production history as base case, the developed isotherm-baseddecline rate model results for the gas well offeredbetter correlation than Langmuir isotherm-based results, with root mean square error (RMSE) of 6.6799 and 52.6459 Mscf/d respectively.

For the whole production performance forecast (i.e. within and beyond the production history), the plots of Marcellus shale gasq_g versus $t$are exhibited on the same chart (**Figure 4.44**) for (i) actual gas production and its projection (serving as the base case), (ii) the model results for free gas production (no desorption), (iii) the model results for total gas production based on the developed isotherm, and (iv) the model results for total gas production based on Langmuir isotherm.

For the 30-years production performance forecast, with production history and its projection as base case, the model results for total gas q_g based on the developed isotherm offer better correlation than the model results for total gas production based on Langmuir isotherm. The corresponding RMSE are 5.3333 and 42.7740 Mscf/d.

Marcellus shale gas production performance forecast (G_p) within and beyond well production history are shown in **Tables 4.67** and **4.68** respectively. For production forecast within the production history, the corresponding plots of Marcellus shale gasG_P versus $t$are shown in **Figures 4.45**. Also, for the whole production performance forecast (i.e. within and beyond the production history), the corresponding plots of Marcellus shale gasG_p versus $t$are shown in **Figures 4.46**.

Within and beyond the production history,the developed isotherm-based model results is observed to predict the actual gas well production $G_p$better than theLangmuir isotherm-based model resultsdo.

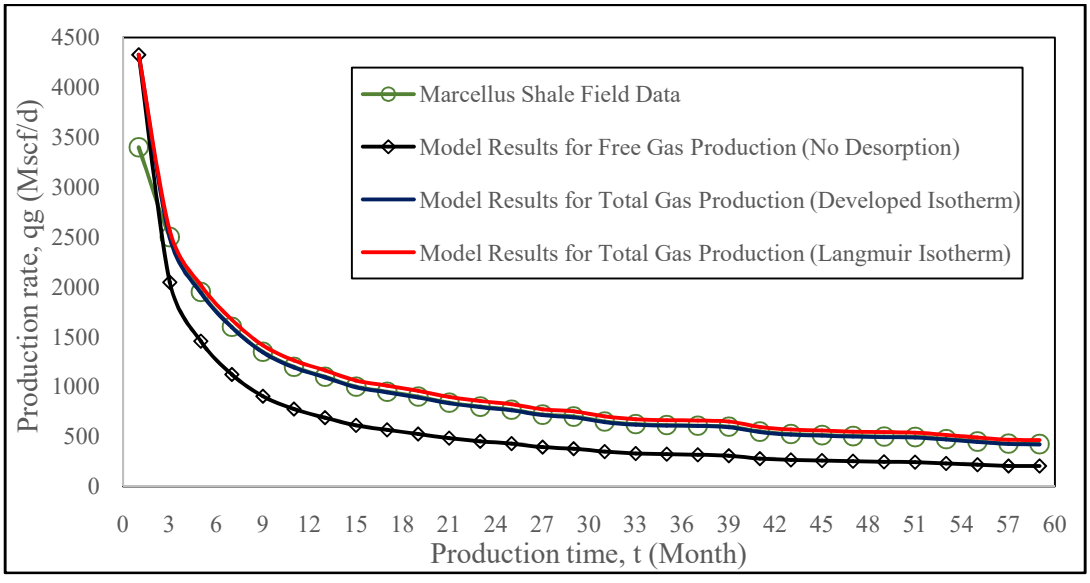

Figure 4.43: Correlation of Marcellus shale gas q_g model results

within the production history

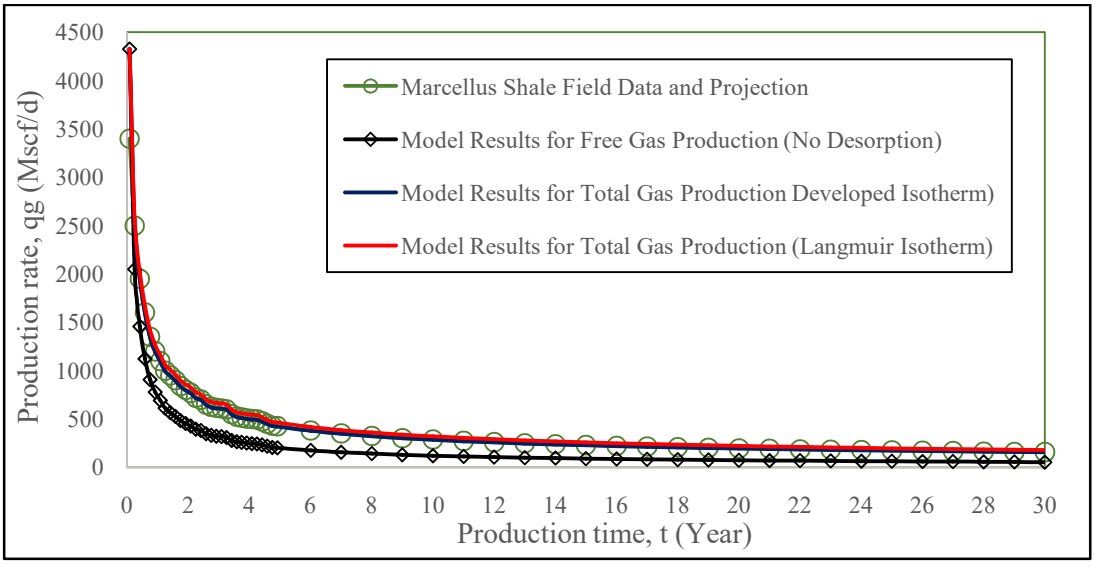

Figure 4.44: Correlation of Marcellus shale gas q_g model results for the whole production forecast

Table 4.67: Marcellus shale gas production performance forecast (G_p) within well production history

Time, t (year)	Time, t (month)	Time, t (day)	Actual Total Gas G_p (Field Data) (MMscf)	Free Gas G_p Forecast (MMscf)	Total Gas G_p Forecast (Developed Isotherm) (MMscf)	Total Gas G_p Forecast (Langmuir Isotherm) (MMscf)
0.0833	1	30	111.00	111.00	111.00	111.00
0.2500	3	90	288.00	235.81	287.08	294.91
0.4146	5	150	421.50	340.87	402.07	432.25
0.5833	7	210	528.00	418.21	526.06	542.86
0.7500	9	270	616.50	479.05	614.08	635.38
0.9167	11	330	693.00	529.48	690.10	715.72
1.0833	13	390	762.30	573.46	758.62	788.47
1.2500	15	450	825.60	612.49	821.17	855.13
1.4146	17	510	884.10	647.83	879.22	917.20
1.5833	19	570	939.60	680.62	934.24	976.21
1.7500	21	630	991.80	710.89	985.99	1031.83
1.9167	23	690	1041.00	738.94	1034.77	1084.39
2.0833	25	750	1088.10	765.34	1081.45	1134.79
2.2500	27	810	1132.80	790.03	1125.73	1182.70
2.4146	29	870	1175.40	813.25	1167.91	1228.45
2.5833	31	930	1215.90	835.06	1208.02	1272.01
2.7500	33	990	1254.15	855.40	1245.91	1313.23

2.9167	35	1050	1291.35	874.96	1282.75	1353.37
3.0833	37	1110	1328.10	894.10	1319.14	1393.06
3.2500	39	1170	1364.40	912.82	1355.08	1432.30
3.4146	41	1230	1398.90	930.43	1389.22	1469.65
3.5833	43	1290	1431.15	946.75	1421.11	1504.60
3.7500	45	1350	1462.35	962.44	1451.98	1538.44
3.9167	47	1410	1492.95	977.71	1482.28	1571.68
4.0833	49	1470	1523.10	992.62	1512.10	1604.44
4.2500	51	1530	1552.95	1007.26	1541.59	1636.87
4.4146	53	1590	1582.05	1021.42	1570.35	1668.52
4.5833	55	1650	1609.80	1034.83	1597.80	1698.76
4.7500	57	1710	1636.20	1047.52	1623.90	1727.56
4.9167	59	1770	1661.85	1059.79	1649.25	1755.55

Table 4.68: Marcellus shale gas production performance forecast (G_p) beyond well production history

Time, t (year)	Time, t (month)	Time, t (day)	Actual Total Gas G_p Projection (MMscf)	Free Gas G_p Forecast (MMscf)	Total Gas G_p Forecast (Developed Isotherm) (MMscf)	Total Gas G_p Forecast (Langmuir Isotherm) (MMscf)
6	72	2160	1819.02	1133.50	1804.67	1927.54
7	84	2520	1950.60	1193.08	1934.81	2072.08
8	96	2880	2072.10	1246.72	2054.87	2206.00
9	108	3240	2184.78	1295.68	2166.83	2331.28
10	120	3600	2290.80	1340.68	2272.13	2449.36
11	132	3960	2391.78	1382.44	2371.67	2561.32
12	144	4320	2487.72	1421.50	2466.35	2668.06
13	156	4680	2579.34	1458.22	2556.89	2770.30
14	168	5040	2667.18	1492.96	2643.65	2868.40
15	180	5400	2751.60	1525.90	2726.99	2962.72
16	192	5760	2832.96	1557.22	2807.27	3053.80
17	204	6120	2911.62	1587.28	2884.85	3142.00
18	216	6480	2987.76	1616.08	2959.91	3227.50
19	228	6840	3061.56	1643.62	3032.63	3310.48

20	240	7200	3133.20	1670.08	3103.37	3391.12
21	252	7560	3203.04	1695.64	3172.13	3469.60
22	264	7920	3271.08	1720.48	3239.09	3546.10
23	276	8280	3337.32	1744.42	3304.43	3620.80
24	288	8640	3402.12	1767.46	3368.15	3693.88
25	300	9000	3465.48	1789.96	3430.43	3765.34
26	312	9360	3527.40	1811.92	3491.27	3835.18
27	324	9720	3588.06	1833.16	3550.85	3903.76
28	336	10080	3647.46	1853.86	3609.35	3971.08
29	348	10440	3705.60	1874.02	3666.77	4037.14
30	360	10900	3762.66	1893.64	3723.11	4101.94

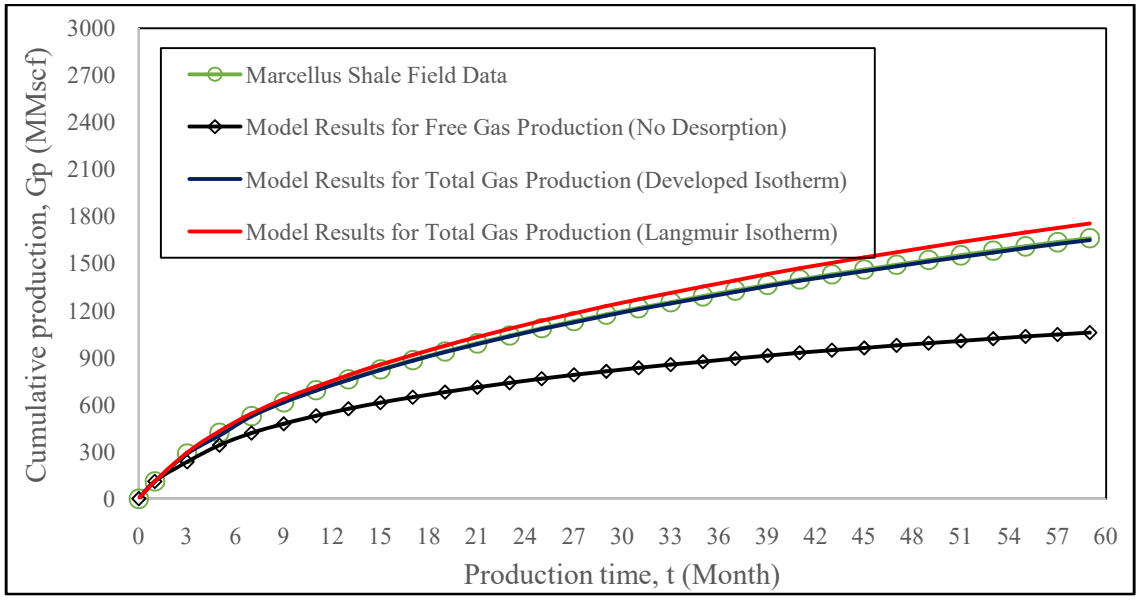

Figure 4.45: Correlation of Marcellus shale gas G_p model results within the production history

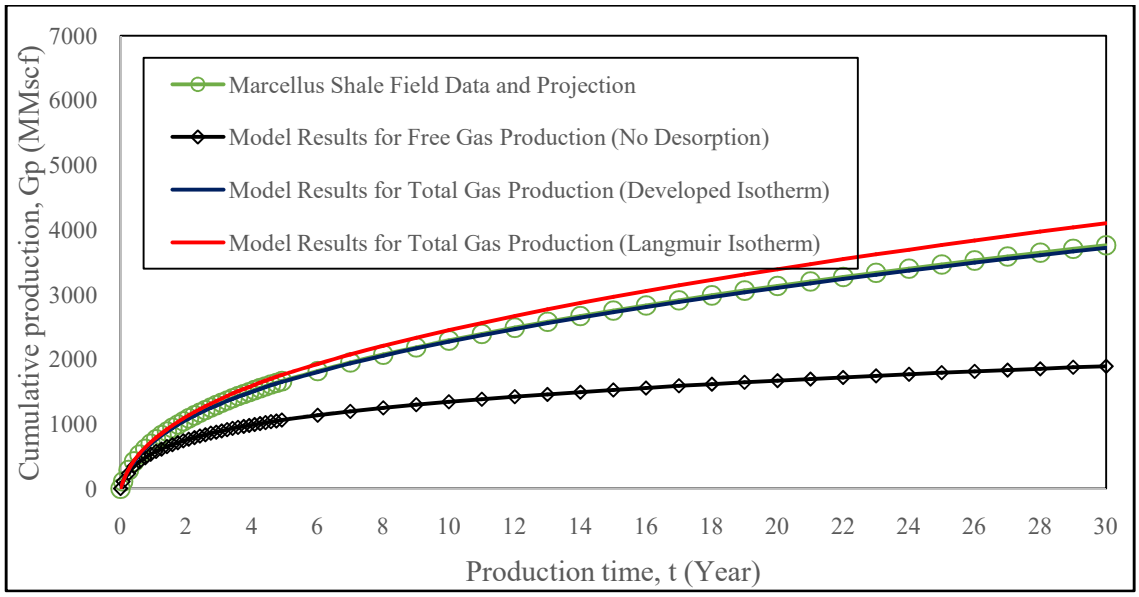

Figure 4.46: Correlation of Marcellus shale gas G_p model results for the whole production forecast

4.7 HAYNESVILLE SHALE GAS MATERIAL BALANCE ANALYSIS

4.7.1 Haynesville Shale Adsorption and Reservoir Data Used

The measured initial reservoir pressure of the Haynesville shale is 12,000 psig (Male *et al*., 2015). Haynesville OGIP (free gas) was reported as 717 Tscf (US DoE, 2009; and Browning *et al*., 2015). Haynesville shale has technically recoverable reserves of 75 Tscf (Institute for Energy Research, 2012). Unproved technically recoverable reserves as of January 2010 was estimated as 66 Tscf (US EIA, 2012).

Haynesville shale reservoir area is 9,000 square miles (i.e. 23,310 km^2) (US DoE, 2009). Hence, an average (net) thickness of 104 ft. (Institute for Energy Research, 2017) is considered in this work. Haynesville shale gas adsorption data is presented in **Table 4.69** while the reservoir data is shown in **Table 4.70**.

Table 4.69: Haynesville shale adsorption data

Parameter	Symbol	Value	Unit
Langmuir volume	V_L	60	scf/ton
Langmuir pressure	P_L	1,500	psi
Maximum adsorbed volume (Developed isotherm)	V_{max}	49.62	scf/ton
Adsorption saturation pressure (Developed isotherm)	P_s	8507.74	psi
Adsorbate-adsorbent resistance parameter (Developed isotherm)	n	0.35	-

Table 4.70: Haynesville shale reservoir data(US DoE, 2009; Male *et al*., 2015)

Parameter	Symbol	Value	Unit
Reservoir area	A	9,000	sq. mile
Reservoir area	A	23,310	sq. km.
Matrix porosity before fracturing	ϕ'_{mat}	0.085	-
Fracture porosity	ϕ_{frac}	0.04	-
Matrix permeability	k_{Darcy}	0.0003	mD
Initial gas saturation	S_{g_i}	0.70	-
Initial water saturation	S_{w_i}	0.30	-
Matrix (bulk) density	ρ_m	2.60	g/cm^3
Initial reservoir pressure	P_i	12,000	psig
Bottom hole pressure	P_{wf}	1500	psig
Water compressibility	C_w	3.6×10^{-6}	psi^{-1}
Rock matrix compressibility	C_{matrix}	3.0×10^{-12}	psi^{-1}
Reservoir temperature	T	300	^{o}F
Gas gravity	γ_g	0.65	-

4.7.2Variation of Haynesville Shale Gas Compressibility Factor with Pressure

Haynesville shale gasreservoir temperature T of 300^{o}F (i.e. 760^{o}R) and a natural gas gravity$\gamma_g$of 0.65 are considered. Based on gas compositions (see **Table 2.9**), applying Standing (1981) correlation $(\gamma_g < 0.75)$ for dry gas yields a pseudo-critical pressure P_{pc} of 660.91 psi (see **Equation 2.131**), pseudo-critical temperature T_{pc} of 373.97 ^{o}R (see **Equation 2.132**) and a pseudo-reduced temperature T_{pr} of 2.0322.

Standing and Katz Z-factors Z_{SK} are used as initial guesses in evaluating Dranchuk-Abou-Kassem Z-factors Z_{DAK}(see **Equation 3.87**) indicated as Z in **Table 4.71**. The MAPPLE program for evaluating Z-factor using Dranchuk-Abou-Kassem (1975) eleven-constant equation of state is shown in **Appendix D**.

The pressure range considered for Haynesville shale is: $0 \leq P \leq 12{,}000$ psig. The initial formation volume factor of Haynesville shale gas:

$$B_{g_i} = \left(\frac{P_{sc}}{T_{sc}}\right)\frac{Z_i T}{P_i} \quad (4.80)$$

is evaluated as 2.1653 × 10^{-3} rcf/scf.

With ϕ_{frac} = 0, single-porosity Z-factor with pore compaction is evaluated as:

$$Z^* = Z\{1 - (1.5429E - 6)\Delta P\}^{-1} \quad (4.81)$$

With ϕ_{frac} = 0.04, Aguilera (2008) dual-porosity Z-factor is evaluated as:

$$Z'' = Z\{1 - (2.2196E - 6)\Delta P\}^{-1} \quad (4.83)$$

and the modified dual-porosity Z-factor is evaluated as:

$$Z^{**} = Z\{1 - (2.2073E - 6)\Delta P\}^{-1} \quad (4.84)$$

The variations of the Z-factors with pressure depletion are shown in **Table 4.71** and **Figure 4.47**. Correlating the modified dual-porosity Z-factor with Aguilera dual porosity Z-factor yields a R^2 value of 1.000.

Table 4.71: Variations of Haynesville shale gas Z, Z^*, Z'' and Z^{**} with pressure based on ϕ_{frac} of 0.04

P (psig)	P_{pr}	Z	ΔP (psig)	Z^*	Z'' (Aguilera)	Z^{**} (Modified)

12000	18.1568	1.2094	0	1.2094	1.2094	1.2094
11250	17.0220	1.1931	750	1.1945	1.1951	1.1951
10500	15.8872	1.1780	1500	1.1807	1.1819	1.1819
9750	14.7524	1.1607	2250	1.1647	1.1665	1.1665
9000	13.6176	1.1415	3000	1.1468	1.1492	1.1491
8508	12.8732	1.1296	3492	1.1357	1.1384	1.1384
8250	12.4824	1.1205	3750	1.1270	1.1299	1.1298
7500	11.3480	1.0983	4500	1.1060	1.1094	1.1093
6750	10.2132	1.0754	5250	1.0842	1.0881	1.0880
6000	9.0784	1.0541	6000	1.0639	1.0683	1.0682
5250	7.9436	1.0297	6750	1.0405	1.0454	1.0453
4500	6.8088	1.0069	7500	1.0187	1.0239	1.0238
3750	5.6740	0.9818	8250	0.9945	1.0001	1.0000
3000	4.5392	0.9562	9000	0.9697	0.9757	0.9756
2250	3.4044	0.9436	9750	0.9580	0.9645	0.9644
1500	2.2696	0.9467	10500	0.9623	0.9693	0.9692
750	1.1348	0.9661	11250	0.9832	0.9908	0.9909
375	0.5674	0.9815	11625	0.9994	1.0075	1.0073
0	0	1.0000	12000	1.0189	1.0274	1.0273

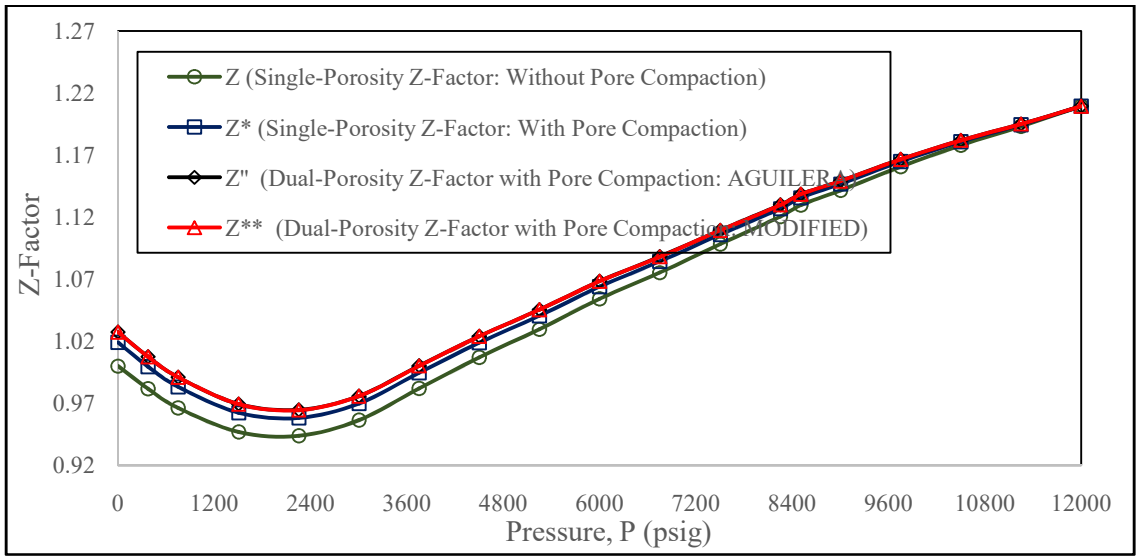

Figure 4.47: Variations of Z, $Z^{*}Z''$ and Z^{**} with pressure for Haynesville shale formation based on ϕ_{frac} of 0.04

4.7.3 Establishment of Haynesville Shale OGIPs from Plots of G_p versus $^{P}/_{Z^{**}}$

The variations of Haynesville shale gas $^{P}/_{Z^{**}}$ and cumulative gas production G_p with pressure depletion based on ϕ_{frac} of 0.04 are shown in **Table 4.72**. Also, **Figure 4.48** shows the plots of Haynesville shale formation G_p versus $^{P}/_{Z^{**}}$ based on ϕ_{frac} of 0.04.

The original gas-in-place OGIP without adsorption consideration is evaluated as 717.0420 Tscf. However, the OGIPs that account for free and adsorbed gases based on the developed isotherm and Langmuir isotherm are 811.8323 Tscf and 831.6614 Tscf respectively. When compared with the free gas-in-place, the adsorbed gas in Haynesville shale formation is observed to be small due to the high reservoir temperature that yields high gas molecular activation energy which has adverse effect on gas adsorption.

From the material balance analysis, with pressure drawdown from 12,000 to 10,501 psig, technically recoverable reserves of 75 Tscf would be depletedin form of free gasG_p; the corresponding developed isotherm-based and Langmuir isotherm-based technically recoverable (total gas) reserves (in form of total gasG_p) were estimated as 75.00and 76.59 Tscf respectively. The plots of Haynesville shale formation G_p versus P/Z^{**} (based on ϕ_{frac} of 0.04) within the technically recoverable reserves depletion range is shown in **Figure 4.49**.

Table 4.72: Variation of Haynesville shale gas G_p with pressure based on ϕ_{frac} of 0.04

P	ΔP	P/Z^{**}	$1 - \frac{P/Z^{**}}{}$	**Cumulative Gas Production G_p (Tscf)**

(psig)	(psig)	(psig)		$G_{p_{Free}}$ Without Adsorption	$G_{p_{Total}}$ Developed Isotherm	$G_{p_{Total}}$ Langmuir Isotherm
12000	0	9922.28	0	0	0	0
11250	750	9413.44	0.0513	36.7843	36.7843	37.5335
10501	1499	8884.44	0.1046	**75.0000**	**75.0000**	**76.5907**
10500	1500	8884.00	0.1046	75.0026	75.0026	76.5945
9750	2250	8358.34	0.1576	113.0058	113.0058	115.5529
9000	3000	7832.22	0.2106	151.0090	151.0090	154.6477
8508	3492	7473.65	0.2468	176.9660	176.9660	181.4058
8250	3750	7302.18	0.2641	189.3708	189.4015	194.2690
7500	4500	6761.02	0.3186	228.4495	228.9342	234.8173
6750	5250	6204.04	0.3747	268.6756	270.1994	276.7800
6000	6000	5616.93	0.4339	311.1245	314.3390	321.3129
5250	6750	5022.48	0.4938	354.0753	359.7180	366.8109
4500	7500	4395.39	0.5570	399.3924	408.3148	415.3117
3750	8250	3750.00	0.6221	446.0718	459.2861	466.0847
3000	9000	3075.03	0.6901	494.8307	513.5891	520.3017
2250	9750	2333.06	0.7649	548.4654	574.4150	581.5776
1500	10500	1547.67	0.8440	605.1835	640.7284	649.7577
750	11250	757.04	0.9237	662.3317	711.8237	726.0092
375	11625	372.28	0.9625	690.1389	750.3659	769.0990
0	12000	0	1.0000	717.0420	811.8323	818.9260

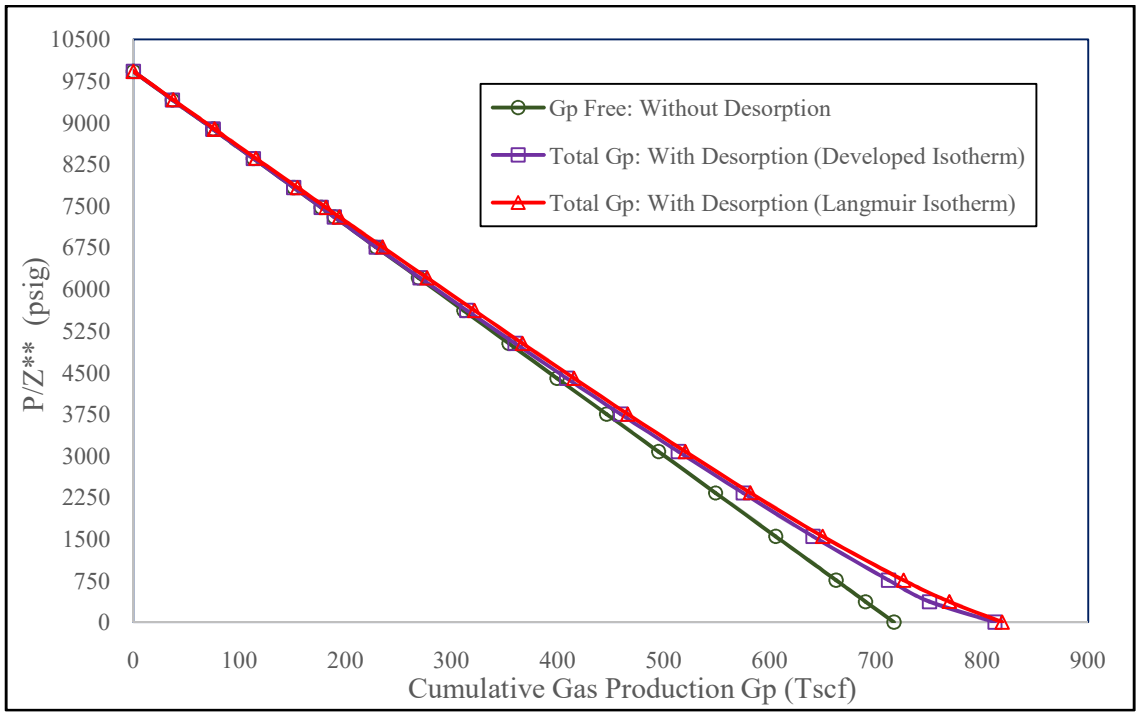

Figure 4.48: Plots of Haynesville shale G_p versus $^{P}/_{Z^{**}}$ based on ϕ_{frac} of 0.04

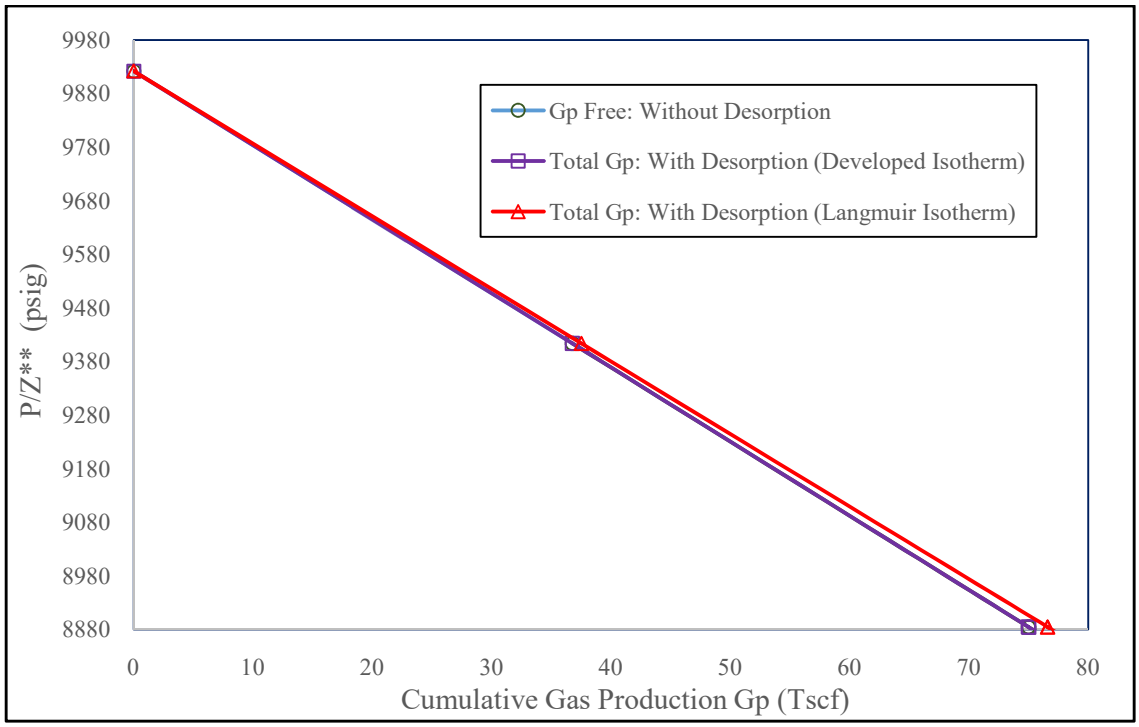

Figure 4.49: Plots of Haynesville shale G_p versus $^{P}/_{Z^{**}}$ (based on ϕ_{frac} of 0.04) for technically recoverable (free gas) reserves of 75 Tscf

4.7.4Variation of Haynesville Shale GIP with Pressure

The variation of gas-in-place GIP with pressure for Marcellus shale formation with fracture porosity ϕ_{frac} of 0.04 is shown in **Table 4.73** while the plot is shown in **Figure 4.50**.However, the fractions of free and adsorbed GIP to total GIP for

Haynesville shale formation with fracture porosity ϕ_{frac} of 0.04 is shown in **Table 4.74** while the plot is shown in **Figure 4.51**.

From **Figures 4.50** and **4.51**, with the developed isotherm-based MBE, pressure depletion from the initial reservoir condition of 12,000 psig to 588.70 psig reduces the free gas contributing capacity to production from 88.32% to 50.00%; further depletion to 375 psig reduces it to 43.76%. However, the adsorbed gas is observed to be the principal contributor to gas production below 588.70 psig. Pressure depletion from the initial reservoir condition to 588.70 psig causes the capacity to increase from 11.68% to 50.00%; while the capacity increases from 50.00% to 56.24% when pressure is depleted further down to 375 psig.

It is thus evident that adsorbed gas contribution to production is prevalent below a pressure of about 0.0491 the initial reservoir pressure. This confirms the small proportion of adsorbed gas in Haynesville shale formation when compared with the free gas-in-place.

Table 4.73: Variation of Haynesville shale GIP with pressure based on ϕ_{frac} of 0.04

P (psig)	Gas-in-Place GIP (Tscf)				
	GIP_{Free} Without Adsorption	$GIP_{Adsorbed}$ Developed Isotherm	$GIP_{Adsorbed}$ Langmuir Isotherm	GIP_{Total} Developed Isotherm	GIP_{Total} Langmuir Isotherm
12000	717.0420	94.7903	101.8840	811.8323	818.9260
11250	680.2577	94.7903	101.1348	775.0480	781.3926
10500	642.0394	94.7903	100.2921	736.8297	742.3314
9750	604.0362	94.7903	99.3369	698.8265	703.3731
9000	566.0330	94.7903	98.2452	660.8233	664.2782
8508	540.0760	94.7903	97.4403	634.8663	637.5163
8250	527.6712	94.7596	96.9857	622.4308	624.6569
7500	488.5925	94.3056	95.5163	582.8981	584.1088
6750	448.3664	93.2664	93.7796	541.6328	542.1450
6000	405.9175	91.5757	91.6956	497.4932	497.6131
5250	362.9666	89.1476	89.1485	452.1142	452.1151
4500	317.6496	85.8679	85.9646	403.5175	403.6142
3750	270.9702	81.5760	81.8710	352.5462	352.8412
3000	222.2113	76.0319	76.4130	298.2432	298.6243
2250	167.5766	68.8407	68.7717	236.4173	236.3483
1500	111.8585	59.2454	57.3097	171.1039	169.1682
750	54.7103	45.2984	38.2064	100.0087	92.9167
375	26.8891	34.5634	22.9239	61.4525	49.8130
0	0	0	0	0	0

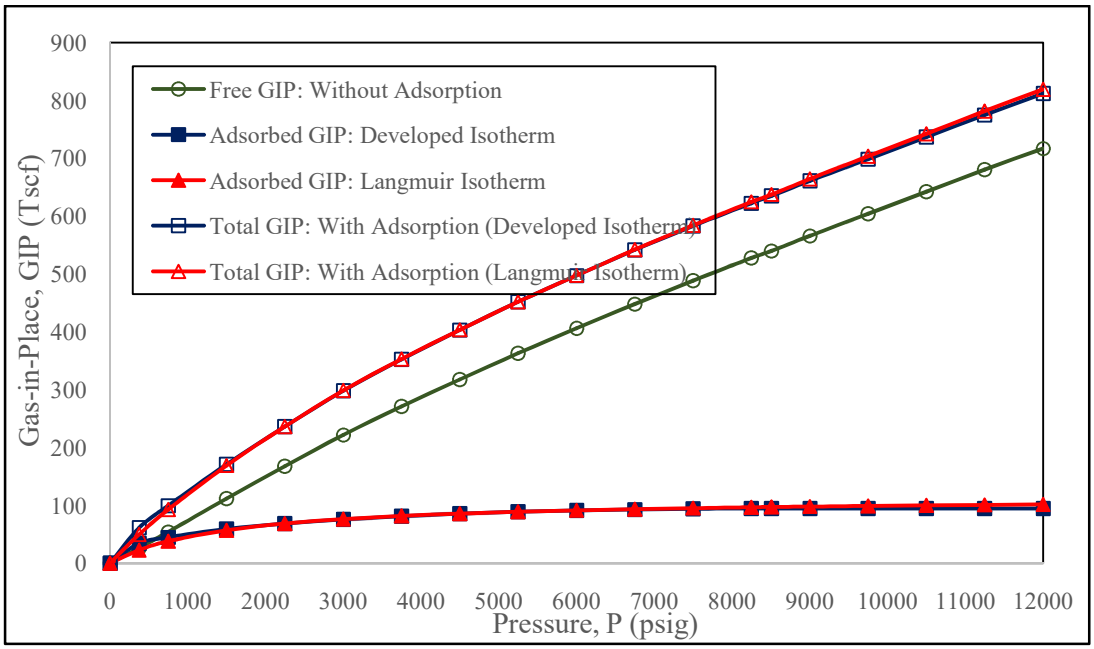

Figure 4.50: Plots of Haynesville shale GIP versus pressure based on ϕ_{frac} of 0.04

Table 4.74: Fractions of free and adsorbed GIP to total GIP for

Haynesville shale formation with fracture porosity ϕ_{frac} of 0.04

P **(psig)**	**Fractions of Free and Adsorbed GIP to Total GIP**			
	Developed Isotherm-Based		**Langmuir Isotherm-Based**	
	GIP_{Free}	$GIP_{Adsorbed}$	GIP_{Free}	$GIP_{Adsorbed}$
12000	0.8832	0.1168	0.8756	0.1244
11250	0.8777	0.1223	0.8706	0.1294
10500	0.8713	0.1287	0.8649	0.1351
9750	0.8644	0.1356	0.8588	0.1412
9000	0.8566	0.1434	0.8521	0.1479
8508	0.8507	0.1493	0.8472	0.1528
8250	0.8478	0.1522	0.8447	0.1553
7500	0.8382	0.1618	0.8365	0.1635
6750	0.8278	0.1722	0.8270	0.1730
6000	0.8159	0.1841	0.8157	0.1843
5250	0.8028	0.1972	0.8028	0.1972
4500	0.7872	0.2128	0.7870	0.2130
3750	0.7686	0.2314	0.7680	0.2320
3000	0.7451	0.2549	0.7441	0.2559
2250	0.7088	0.2912	0.7090	0.2910
1500	0.6537	0.3463	0.6612	0.3388
750	0.5471	0.4529	0.5888	0.4112
375	0.4376	0.5624	0.5398	0.4602
0	-	-	-	-

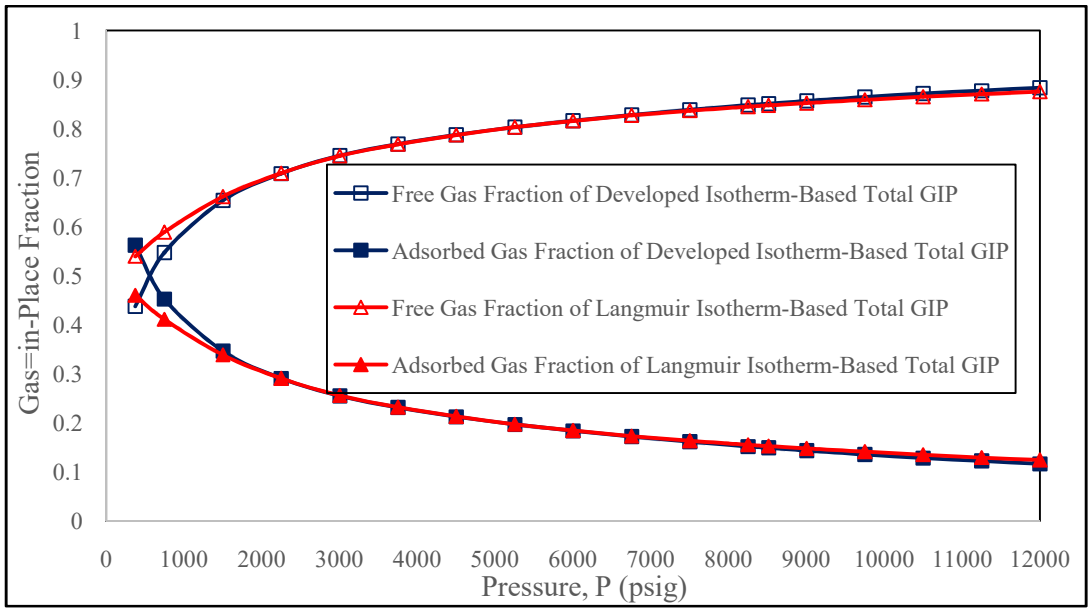

Figure 4.51: Fractions of free and adsorbed GIP to total GIP for Haynesville shale formation based on ϕ_{frac} of 0.04

4.7.5Effect of Fracture Porosity on Haynesville Shale Gas Production

The Z-factor for gas reservoir with pore volume reduction before fracturing is evaluated as:

$$Z^* = Z\{1 - (1.5429E - 6)\Delta P\}^{-1} \quad (4.85)$$

The variations of Haynesville shale gas ${}^{P}/_{Z^{**}}$ and cumulative gas production G_p with pressure depletion based on ϕ_{frac} of 0 and the developed isotherm are shown in **Table 4.75**.

For fracture porosity ϕ_{frac} of 0.02, the Z-factor for gas reservoir with pore volume reduction after fracturing:

$$Z^{**} = Z \cdot \{1 - (1.8751E - 6) \cdot \Delta P\}^{-1} \quad (4.86)$$

The variations of Marcellus shale gas ${}^{P}/_{Z^{**}}$ and cumulative gas production G_p with pressure depletion based on ϕ_{frac} of 0.02 and the developed isotherm are shown in **Table 4.76**.

Also, for fracture porosity ϕ_{frac} of 0.06, the Z-factor for gas reservoir with pore volume reduction after fracturing:

$$Z^{**} = Z \cdot \{1 - (2.5394E - 6) \cdot \Delta P\}^{-1} \quad (4.87)$$

The variations of Marcellus shale gas ${}^{P}/_{Z^{**}}$ and cumulative gas production G_p with pressure depletion based on ϕ_{frac} of 0.06 and the developed isotherm are shown in **Table 4.77**.

Fracture-induced increase in gas production from Haynesville shale (with reference to no-fracturing scenario) is shown in **Table 4.78**and **Figure 4.52**. Fracturing accelerates pressure depletion, and at a particular pressure, fracturing has increasing effect only on free gas production while gas desorption remains the same at that pressure.

As compared to the no-fracturing scenario, increases in gas production at fracture porosity levels of 0.02, 0.04 and 0.06 with pressure depletion were observed to be rising till respective constant peak values of 0.8605 Tscf, 1.6492 Tscf and 2.5097 Tscf were attained with pressure depletion from 6,000 to 5,250 psig. Thereafter, gas

production increase was observed to be declining towards the abandonment pressure range.

Haynesville shale formation OGIP is smaller than that of the Marcellus shale formation; however, increase in fracture porosity is found to have more increasing effect on free gas production in Haynesville shale formation than in Marcellus shale formation This is due to the fact that the relatively higher reservoir temperature in Haynesville shale formation yields higher gas molecular activation energy which favours free gas production.

Table 4.75: Variation of Haynesville shale G_p with pressure based on ϕ_{frac} of 0 and the developed isotherm

P (psig)	ΔP (psig)	Z^*	P/Z^* (psig)	$1-\frac{P/Z^*}{P_i/Z_i}$	Cumulative Gas Production G_p (Tscf)	
					$G_{p_{Free}}$	$G_{p_{Total}}$
12000	0	1.2094	9922.28	0	0	0
11250	750	1.1945	9418.17	0.0508	36.4257	36.4257
10500	1500	1.1807	8893.03	0.1037	74.3573	74.3573
9750	2250	1.1647	8371.25	0.1563	112.0737	112.0737
9000	3000	1.1468	7847.92	0.2091	149.9335	149.9335
8508	3492	1.1357	7491.41	0.2450	175.6753	175.6753
8250	3750	1.1270	7320.32	0.2622	188.0084	188.0391
7500	4500	1.1060	6781.19	0.3166	227.0155	227.5002
6750	5250	1.0842	6225.79	0.3725	267.0981	268.6219
6000	6000	1.0639	5639.63	0.4316	309.4753	312.6898
5250	6750	1.0405	5045.65	0.4915	352.4261	358.0687
4500	7500	1.0187	4417.39	0.5548	397.8149	406.7373
3750	8250	0.9945	3770.74	0.6200	444.5660	457.7803
3000	9000	0.9697	3093.74	0.6882	493.4683	512.2267
2250	9750	0.9580	2348.64	0.7633	547.3182	573.2678
1500	10500	0.9623	1558.77	0.8429	604.3947	639.9396
750	11250	0.9832	762.82	0.9231	661.9015	711.3935
375	11625	0.9994	375.23	0.9622	689.9378	750.1648
0	12000	1.0189	0	1.0000	717.0420	811.8323

Table 4.76: Variation of Haynesville shale G_p with pressure based on ϕ_{frac} of 0.02 and the developed isotherm

P (psig)	ΔP (psig)	Z^{**}	P/Z^{**} (psig)	$1-\frac{P/Z^{**}}{P_i/Z_i}$	Cumulative Gas Production G_p (Tscf)	
					$G_{p_{Free}}$	$G_{p_{Total}}$
12000	0	1.2094	9922.28	0	0	0
11250	750	1.1948	9415.80	0.0510	36.5691	36.5691
10500	1500	1.1813	8888.51	0.1042	74.7158	74.7158
9750	2250	1.1656	8364.79	0.1570	112.5756	112.5756
9000	3000	1.1480	7839.72	0.2099	150.5071	150.5071
8508	3492	1.1370	7482.85	0.2459	176.3206	176.3206
8250	3750	1.1284	7311.24	0.2631	188.6538	188.6845
7500	4500	1.1076	6771.40	0.3176	227.7325	228.2172
6750	5250	1.0861	6214.90	0.3736	267.8869	269.4107
6000	6000	1.0661	5627.99	0.4328	310.3358	313.5503
5250	6750	1.0429	5034.04	0.4927	353.2866	358.9292
4500	7500	1.0213	4406.15	0.5559	398.6037	407.5261
3750	8250	0.9972	3760.53	0.6210	445.2831	458.4974
3000	9000	0.9726	3084.52	0.6891	494.1136	512.8720
2250	9750	0.9612	2340.82	0.7641	547.8918	573.8414
1500	10500	0.9657	1553.28	0.8435	604.8249	640.3698
750	11250	0.9869	759.95	0.9234	662.1166	711.6086
375	11625	1.0034	373.73	0.9623	690.0095	750.2365
0	12000	1.0230	0	1.0000	717.0420	811.8323

Table 4.77: Variation of Haynesville shale G_p with pressure based on ϕ_{frac} of 0.06 and the developed isotherm

P (psig)	ΔP (psig)	Z^{**}	P/Z^{**} (psig)	$1-\frac{P/Z^{**}}{P_i/Z_i}$	Cumulative Gas Production G_p (Tscf)	
					$G_{p_{Free}}$	$G_{p_{Total}}$
12000	0	1.2094	9922.28	0	0	0
11250	750	1.1954	9411.08	0.0515	36.9277	36.9277
10500	1500	1.1825	8879.49	0.1051	75.3611	75.3611
9750	2250	1.1674	8351.89	0.1583	113.5077	113.5077
9000	3000	1.1503	7824.05	0.2115	151.6544	151.6544
8508	3492	1.1397	7465.12	0.2476	177.5396	177.5396
8250	3750	1.1313	7292.50	0.2650	190.0161	190.0468
7500	4500	1.1110	6750.67	0.3196	229.1666	229.6513
6750	5250	1.0899	6193.23	0.3758	269.4644	270.9882
6000	6000	1.0704	5605.38	0.4351	311.9850	315.1995
5250	6750	1.0477	5010.98	0.4950	354.9358	360.5784
4500	7500	1.0264	4384.26	0.5581	400.1811	409.1035
3750	8250	1.0028	3739.53	0.6231	446.7889	460.0032
3000	9000	0.9786	3065.60	0.6910	495.4760	514.2344
2250	9750	0.9676	2325.34	0.7656	548.9674	574.9170
1500	10500	0.9726	1542.26	0.8446	605.6137	641.1586
750	11250	0.9945	754.15	0.9240	662.5468	712.0388
375	11625	1.0114	370.77	0.9626	690.2246	750.4516
0	12000	1.0314	0	1.0000	717.0420	811.8323

Table 4.78: Fracture-induced increase in gas production from Haynesville shale with reference to no-fracturing scenario)

P (psig)	ΔP (psig)	Increase in Gas Production ΔG_p (Tscf) with Reference toNo-Fracturing Scenario			
		ϕ_{frac} of 0	ϕ_{frac} of 0.02	ϕ_{frac} of 0.04	ϕ_{frac} of 0.06
12000	0	0	0	0	0
11250	750	0	0.1434	0.3586	0.5020
10500	1500	0	0.3585	0.6453	1.0038
9750	2250	0	0.5019	0.9321	1.4340
9000	3000	0	0.5736	1.0755	1.7209
8508	3492	0	0.6453	1.2907	1.8643
8250	3750	0	0.6454	1.3624	2.0077
7500	4500	0	0.7170	1.4340	2.1511
6750	5250	0	0.7888	1.5775	2.3663
6000	6000	0	0.8605	1.6492	2.5097
5250	6750	0	0.8605	1.6492	2.5097
4500	7500	0	0.7888	1.5775	2.3662
3750	8250	0	0.7171	1.5058	2.2229
3000	9000	0	0.6453	1.3624	2.0077
2250	9750	0	0.5736	1.1472	1.6492
1500	10500	0	0.4302	0.7888	1.2190
750	11250	0	0.2151	0.4302	0.6453
375	11625	0	0.0717	0.2011	0.2868
0	12000	0	0	0	0

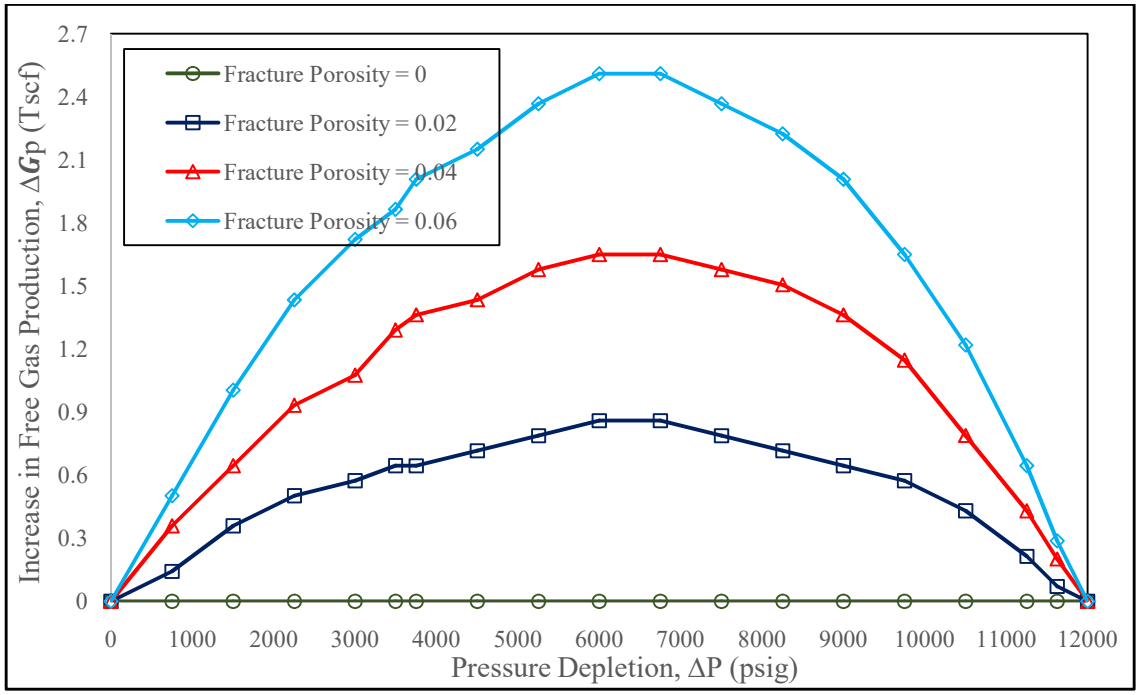

Figure 4.52: Fracture-induced increase in gas production from Haynesville shale (with reference to no-fracturing scenario)

4.8 HAYNESVILLE SHALE GAS PRODUCTION PERFORMANCE FORECAST

4.8.1Generation of Decline Rate Model from Production History

The variations of Haynesville shale gas production rate q_g (see **Figure 2.20 (**Chesapeake Energy, 2010)) is shown in **Table 4.79** and the plot is shown in **Figure 4.53**. The production rate at the first day is considered as 13,000 Mscf/d based on graphical extrapolation.

Thus variation of Haynesville shale gas production rateq_g with time is modelled as:

$$q_{g}{}_{Well\ Forecast}^{Actual\ Total\ Gas} = 11961\ t^{-0.6970}\ \text{Mscf/d} \quad (4.88)$$

where t is in months, the initial production rate (at the end of the first month) q_{g_1}= 11961 Mscf/d and production decline exponent $n = 0.6970$.

Table 4.79: Variations of Haynesville shale gas production rate q_g and cumulative gas production G_p with time

Time, t (month)	Time, t (year)	Time, t (day)	q_g (Mscf/d)	G_p (MMscf)
1	0.0833	30	10400	351.00
3	0.2500	90	5800	837.00
5	0.4167	150	4000	1131.00
7	0.5833	210	3150	1345.50
9	0.7500	270	2700	1521.00
11	0.9167	330	2400	1674.00
13	1.0833	390	2000	1806.00
15	1.2500	450	1850	1921.50
17	1.4167	510	1700	2028.00
19	1.5833	570	1600	2127.00
21	1.7500	630	1500	2220.00
23	1.9167	690	1400	2307.00
25	2.0833	750	1300	2388.00
27	2.2500	810	1250	2464.50
29	2.4167	870	1100	2535.00
31	2.5833	930	1050	2599.50
33	2.7500	990	1025	2661.75
35	2.9167	1050	1000	2722.50
37	3.0833	1110	950	2781.00
39	3.2500	1170	900	2836.50
41	3.4167	1230	885	2890.05
43	3.5833	1290	850	2942.10
45	3.7500	1350	800	2991.60
47	3.9167	1410	785	3039.15
49	4.0833	1470	780	3086.10
51	4.2500	1530	775	3132.75
53	4.4167	1590	750	3178.50
55	4.5833	1650	725	3222.75
57	4.7500	1710	700	3265.50
59	4.9167	1770	690	3307.20

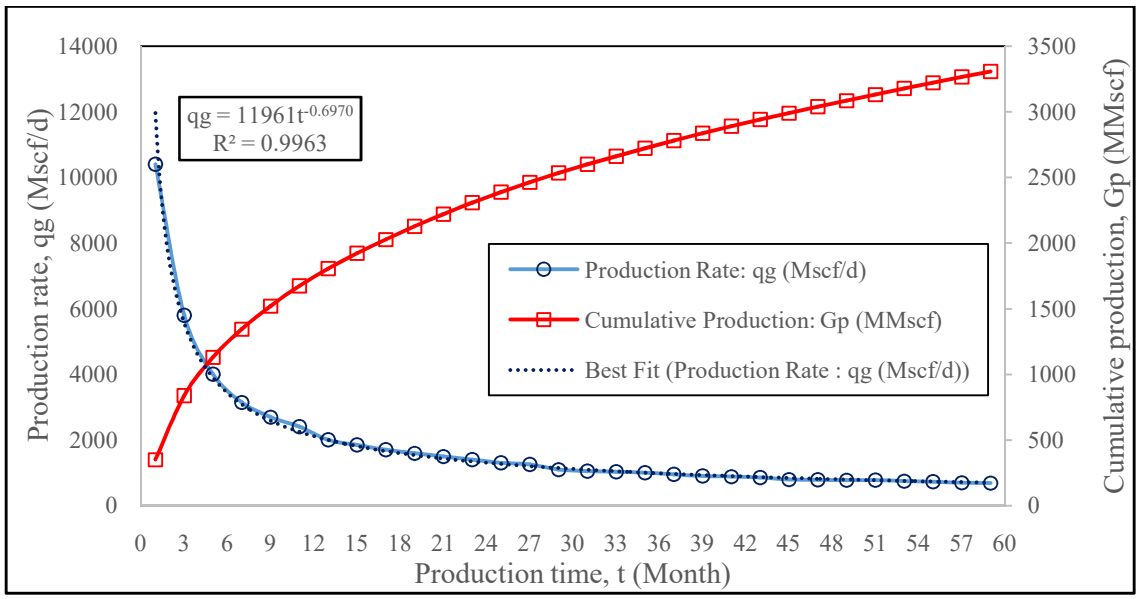

Figure 4.53: Plot of Haynesville shale gas q_g and G_p versus time t

4.8.2Development of Free and Total Gas Decline Rate Models for Production Performance Forecast

Flow rate $q = \frac{dG_p}{dP} * \frac{dP}{dt}$; however, pressure depletion in the well is the same both for free and total gas production. The decline rate exponent $n = \frac{C}{\left(\frac{dG_p}{dP}\right)}$(see **Equation 3.129**) where C is a constant of proportionality.And the trend of $\frac{dG_p}{dP}$ (for pressure depletion from the initial reservoir pressure P_i to the bottom hole pressure P_{wf}in the improved material balance analysis) forms the basis for comparing the production exponent n and thus the flow rates $q_g$of free gas, total gas based on the proposed isotherm, and total gas based on Langmuir isotherm.

In**Table 4.72**, for pressure depletion from the initial reservoir pressure P_i to the bottom hole pressure P_{wf},

$$\left(\frac{dG_p}{dP}\right)_{Free\ Gas}^{MBA-Predicted} = 0.0576 \text{ Tscf/psi} \quad (4.89)$$

$$\left(\frac{dG_p}{dP}\right)_{(Developed\ Isotherm)}^{\substack{MBA-Predicted \\ Total\ Gas}} = 0.0610 \text{ Tscf/psi} \quad (4.90)$$

and

$$\left(\frac{dG_p}{dP}\right)_{(Langmuir\ Isotherm)}^{\substack{MBA-Predicted \\ Total\ Gas}} = 0.0619 \text{ Tscf/psi} \quad (4.91)$$

This shows that increase in estimated ultimate recovery (EUR) of Haynesville shale gas due to gas desorption based on the developed and Langmuir isotherms are 0.0557and 0.0695respectively; here

$$\text{Increase in EUR} = \frac{\left(G_p^{Total\ Gas} - G_p^{Free\ Gas}\right)}{G_p^{Total\ Gas}} \quad (4.92)$$

Actual Haynesville shale OGIP (free gas) is 717 Tscf (US DoE, 2009); however, the MBA-predicted OGIP (free gas) is 717.0420 (see **Table 4.72**). Therefore,

$$\left(\frac{Actual\ OGIP}{MBA-Predicted\ OGIP}\right)_{Free\ Gas} = 0.9999 \tag{4.93}$$

and

$$\left(\frac{dG_p}{dP}\right)_{Free\ Gas}^{Actual} = 0.9999 \times \left(\frac{dG_p}{dP}\right)_{Free\ Gas}^{MBA-Predicted} \tag{4.94}$$

Thus for pressure depletion from initial reservoir pressure P_i to the wellbore flowing pressure P_{wf},

$$\left(\frac{dG_p}{dP}\right)_{Free\ Gas}^{Actual} = 0.0576 \text{ Tscf/psig} \tag{4.95}$$

The developed isotherm has been established to truly represent Type I isotherm and predicts actual adsorption or desorption, i.e.

$$V_{Gas\ Desorption}^{Experimental} \approx V_{Gas\ Desorption}^{Developed\ Isotherm} \tag{4.96}$$

However, the actual total gas production

$$G_{p\ Total\ Gas}^{Actual} = G_{p\ Free\ Gas}^{Actual} + G_{p\ Desorbed\ Gas}^{Actual} \tag{4.97}$$

Hence, for Haynesville shale formation,

$$G_{p\ Total\ Gas}^{Actual} = 0.9999 \times \left(G_{p\ Free\ Gas}^{MBA-Predicte}\right) + G_{p\ Desorbed\ Gas}^{Developed\ Isotherm} \tag{4.98}$$

At P_{wf},

$$G_{p\ Total\ Gas}^{Actual} = 0.9999 \times (605.1835) + 35.5449 = 640.6679 \text{ Tscf} \tag{4.99}$$

and the corresponding

$$\left(\frac{dG_p}{dP}\right)_{Total\ Gas}^{Actual} = 0.0610 \text{ Tscf/psig} \tag{4.100}$$

The production decline exponent

$$n = \frac{C}{\left(\frac{dG_p}{dP}\right)} \tag{4.101}$$

From the actual total gas forecast (see **Figure 4.41**),

$$n_{Well\ Forecast}^{Actual\ Total\ Gas} = 0.6970 \tag{4.102}$$

Therefore,

$$n_{Well\ Forecast}^{Actual\ Free\ Gas} = 0.6970\left(\frac{0.0610}{0.0576}\right) = 0.738 \tag{4.103}$$

$$n_{Well\ Forecast}^{Total\ Gas\ (Developed\ Isotherm)} = 0.6970\left(\frac{0.0610}{0.0610}\right) = 0.6970 \tag{4.104}$$

and

$$n_{Well\ Forecast}^{Total\ Gas\ (Langmuir\ Isotherm)} = 0.6970\left(\frac{0.0610}{0.0619}\right) = 0.6869 \tag{4.105}$$

However, to correlate the production rate forecast with the production rate from field data, the respective model fitting factors

$$K = \left(\frac{q_{g_{Field\ Data}}^{Actual\ Total\ Gas}}{q_{g_{Well\ Forecast}}^{Actual\ Total\ Gas}}\right) \tag{4.106}$$

after the first time step must be considered. Hence, the variations of respective q_g with time are modelled as:

$$q_{g_{Well\ Forecast}}^{Actual\ Free\ Gas} = K\left(q_{g_1}t^{-0.7381}\right)\text{Mscf/d} \tag{4.107}$$

$$q_{g_{Well\ Forecast}}^{Total\ Gas\ (Developed\ Isotherm)} = K\left(q_{g_1}t^{-0.6970}\right)\text{Mscf/d} \tag{4.108}$$

and

$$q_{g_{Well\ Forecast}}^{Total\ Gas\ (Langmuir\ Isotherm)} = K\left(q_{g_1}t^{-0.6869}\right)\text{Mscf/d} \tag{4.109}$$

Beyond the production history, the last value of K is retained.

Haynesville shale gas production performance forecast (q_g) within and beyond well production history are shown in **Tables 4.80**and **4.81** respectively.

For production forecast within the production history, the plots of Haynesville shale gasq_g versus $t$are displayed on the same chart (**Figure 4.54)** for (i) the well production history (serving as the base case), (ii) the model results for free gas production (no desorption), (iii) the model results for total gas production based on the developed isotherm, and (iv) the decline rate model results for total gas production based on Langmuir isotherm.

With production history as base case, the developed isotherm-baseddecline rate model results for the gas well offeredbetter correlation than Langmuir isotherm-based results, with RMSE of 0 and 44.0407 Mscf/d respectively.

For the whole production performance forecast (i.e. within and beyond the production history), the plots of Haynesville shale gasq_g versus $t$are exhibited on the same chart (**Figure 4.55**) for (i) actual gas production and its projection (serving as the base case), (ii) the model results for free gas production (no desorption), (iii) the model results for total gas production based on the developed isotherm, and (iv) the model results for total gas production based on Langmuir isotherm.

Table 4.80: Haynesville shale gas production performance forecast (q_g) within well production history

Time, t (month)	Actual Total Gas q_g (Field Data) (Mscf/d)	Total Gas q_g Forecast (Mscf/d) n = 0.6970	Model Fitting Factor K	Free Gas q_g Forecast (Mscf/d)	Total Gas q_g Forecast (Developed Isotherm) (Mscf/d)	Total Gas q_g Forecast (Langmuir Isotherm) (Mscf/d)
1	10400	11961	-	11961	11961	11961
3	5800	5562	1.0428	5543	5800	5865
5	4000	3896	1.0267	3743	4000	4065
7	3150	3081	1.0224	2908	3150	3213
9	2700	2586	1.0441	2467	2700	2761
11	2400	2244	1.0695	2222	2400	2464
13	2000	2001	0.9995	1800	2000	2053
15	1850	1811	1.0215	1656	1850	1902
17	1700	1660	1.0241	1514	1700	1750
19	1600	1536	1.0417	1418	1600	1649
21	1500	1433	1.0468	1323	1500	1547
23	1400	1345	1.0409	1230	1400	1445
25	1300	1269	1.0244	1139	1300	1343
27	1250	1203	1.0391	1091	1250	1292
29	1100	1144	0.9615	958	1100	1138
31	1050	1092	0.9615	911	1050	1087
33	1025	1046	0.9799	888	1025	1061
35	1000	1004	0.9960	863	1000	1036
37	950	965	0.9845	819	950	986
39	900	931	0.9667	774	900	936
41	885	899	0.9844	760	885	919
43	850	869	0.9781	729	850	883
45	800	842	0.9501	684	800	832
47	785	817	0.9608	671	785	816
49	780	794	0.9824	664	780	811
51	775	772	1.0039	660	775	806
53	750	751	0.9987	637	750	781
55	725	732	0.9904	615	725	755
57	700	714	0.9804	593	700	730

59	690	697	0.9900	584	690	719

Table 4.81: Haynesville shale gas production performance forecast (q_g) beyond well production history

Time, t (year)	Time, t (month)	Total Gas q_g Forecast (Mscf/d) n = 0.6970	Model Fitting Factor K	ActualTotal Gas q_g Projection (Mscf/d)	Free Gas q_g Forecast (Mscf/d)	Total Gas q_g Forecast (Developed Isotherm) (Mscf/d)	Total Gas q_g Forecast (Langmuir Isotherm) (Mscf/d)
6	72	607	0.9900	601	504	601	627
7	84	545	0.9900	540	449	540	564
8	96	497	0.9900	492	408	492	515
9	108	458	0.9900	453	373	453	475
10	120	425	0.9900	421	345	421	442
11	132	398	0.9900	394	322	394	414
12	144	374	0.9900	370	302	370	390
13	156	354	0.9900	350	285	350	369
14	168	336	0.9900	333	269	333	351
15	180	320	0.9900	317	256	317	334
16	192	306	0.9900	303	245	303	320
17	204	294	0.9900	291	234	291	307
18	216	282	0.9900	279	224	279	295
19	228	272	0.9900	269	215	269	284
20	240	262	0.9900	259	207	259	274
21	252	253	0.9900	250	200	250	265
22	264	245	0.9900	243	193	243	257
23	276	238	0.9900	236	187	236	249
24	288	231	0.9900	229	181	229	242
25	300	224	0.9900	222	176	222	235
26	312	218	0.9900	216	170	216	229
27	324	213	0.9900	211	166	211	223
28	336	207	0.9900	205	161	205	218
29	348	202	0.9900	200	157	200	213
30	360	198	0.9900	196	153	196	208

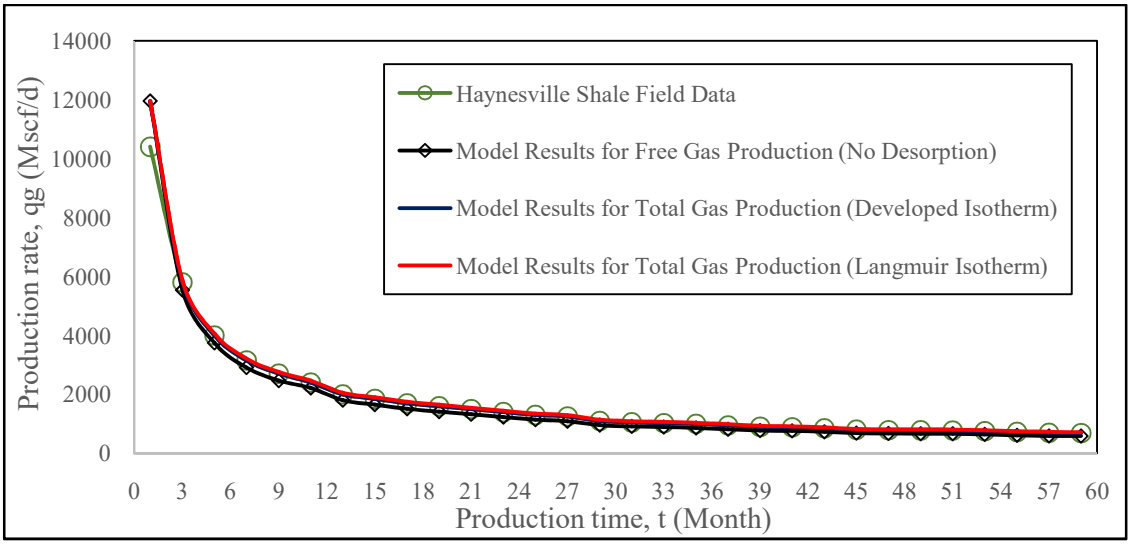

Figure 4.54: Correlation of Haynesville shale gas q_g model results within the production history

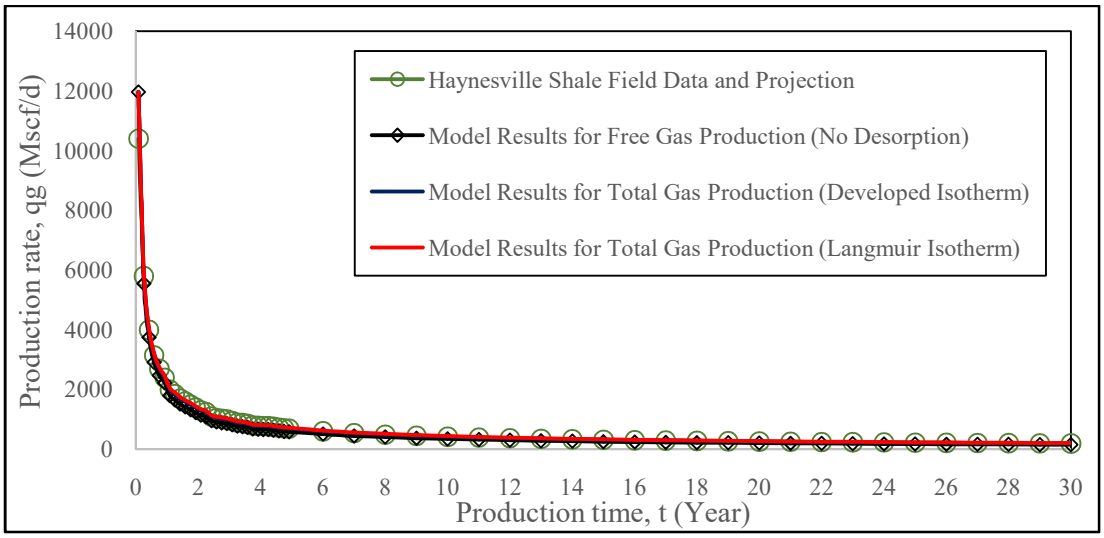

Figure 4.55: Correlation of Haynesville shale gas q_g model results for the whole production forecast

For the 30-years production performance forecast, with production history and its projection as base case, the model results for total gas q_g based on the developed isotherm offer better correlation than the model results for total gas production based on Langmuir isotherm. The corresponding RMSE are 0 and 34.4149 Mscf/d.

Haynesville shale gas production performance forecast (G_p) within and beyond well production history are shown in **Tables 4.82**and **4.83** respectively.

For production forecast within the production history, the corresponding plots of Haynesville shale gasG_P versus $t$are shown in **Figure 4.56**. Also, for the whole production performance forecast (i.e. within and beyond the production history), the corresponding plots of Haynesville shale gasG_p versus $t$are shown in **Figure 4.57**.

Within and beyond the production history,the developed isotherm-based model results is observed to predict the actual gas well production $G_p$better than theLangmuir isotherm-based model resultsdo.

Table 4.82: Haynesville shale gas production performance forecast (G_p) within well production history

Time, t (year)	Time, t (month)	Time, t (day)	Actual Total Gas G_p (Field Data) (MMscf)	Free Gas G_p Forecast (MMscf)	Total Gas G_p Forecast (Developed Isotherm) (MMscf)	Total Gas G_p Forecast (Langmuir Isotherm) (MMscf)
0.0833	1	30	351.00	351.00	351.00	351.00
0.2500	3	90	837.00	799.91	837.00	846.38
0.4146	5	150	1131.00	1078.49	1131.00	1144.28
0.5833	7	210	1345.50	1278.02	1345.50	1362.62
0.7500	9	270	1521.00	1439.27	1521.00	1541.84
0.9167	11	330	1674.00	1579.94	1674.00	1698.59
1.0833	13	390	1806.00	1700.60	1806.00	1834.10
1.2500	15	450	1921.50	1804.28	1921.50	1952.75
1.4146	17	510	2028.00	1899.38	2028.00	2062.31
1.5833	19	570	2127.00	1987.34	2127.00	2164.28
1.7500	21	630	2220.00	2069.57	2220.00	2260.16
1.9167	23	690	2307.00	2146.16	2307.00	2349.92
2.0833	25	750	2388.00	2217.23	2388.00	2433.56
2.2500	27	810	2464.50	2284.13	2464.50	2512.61
2.4146	29	870	2535.00	2345.60	2535.00	2585.51
2.5833	31	930	2599.50	2401.67	2599.50	2652.26
2.7500	33	990	2661.75	2455.64	2661.75	2716.70
2.9167	35	1050	2722.50	2508.17	2722.50	2779.61
3.0833	37	1110	2781.00	2558.63	2781.00	2840.27
3.2500	39	1170	2836.50	2606.42	2836.50	2898.74
3.4146	41	1230	2890.05	2652.44	2890.05	2955.20
3.5833	43	1290	2942.10	2697.11	2942.10	3009.26
3.7500	45	1350	2991.60	2739.50	2991.60	3060.71
3.9167	47	1410	3039.15	2780.15	3039.15	3110.15
4.0833	49	1470	3086.10	2820.20	3086.10	3158.96
4.2500	51	1530	3132.75	2859.92	3132.75	3207.47
4.4146	53	1590	3178.50	2898.83	3178.50	3255.08
4.5833	55	1650	3222.75	2936.39	3222.75	3301.16
4.7500	57	1710	3265.50	2972.63	3265.50	3345.71

4.9167	59	1770	3307.20	3007.94	3307.20	3389.18

Table 4.83: Haynesville shale gas production performance forecast (G_p)beyond well production history

Time, t (year)	Time, t (day)	Actual Total Gas G_p Projection (MMscf)	Free Gas G_p Forecast (MMscf)	Total Gas G_p Forecast (Developed Isotherm) (MMscf)	Total Gas G_p Forecast (Langmuir Isotherm) (MMscf)
6	2160	3558.94	3220.10	3558.94	3651.65
7	2520	3764.32	3391.64	3764.32	3866.03
8	2880	3950.08	3545.90	3950.08	4060.25
9	3240	4120.18	3686.48	4120.18	4238.45
10	3600	4277.50	3815.72	4277.50	4403.51
11	3960	4424.20	3935.78	4424.20	4557.59
12	4320	4561.72	4048.10	4561.72	4702.31
13	4680	4691.32	4153.76	4691.32	4838.93
14	5040	4814.26	4253.48	4814.26	4968.53
15	5400	4931.26	4347.98	4931.26	5091.83
16	5760	5042.86	4438.16	5042.86	5209.55
17	6120	5149.78	4524.38	5149.78	5322.41
18	6480	5252.38	4606.82	5252.38	5430.77
19	6840	5351.02	4685.84	5351.02	5534.99
20	7200	5446.06	4761.80	5446.06	5635.43
21	7560	5537.68	4835.06	5537.68	5732.45
22	7920	5626.42	4905.80	5626.42	5826.41
23	8280	5712.64	4974.20	5712.64	5917.49
24	8640	5796.34	5040.44	5796.34	6005.87
25	9000	5877.52	5104.70	5877.52	6091.73
26	9360	5956.36	5166.98	5956.36	6175.25

27	9720	6033.22	5227.46	6033.22	6256.61
28	10080	6108.10	5286.32	6108.10	6335.99
29	10440	6181.00	5343.56	6181.00	6413.57
30	10900	6252.28	5399.36	6252.28	6489.35

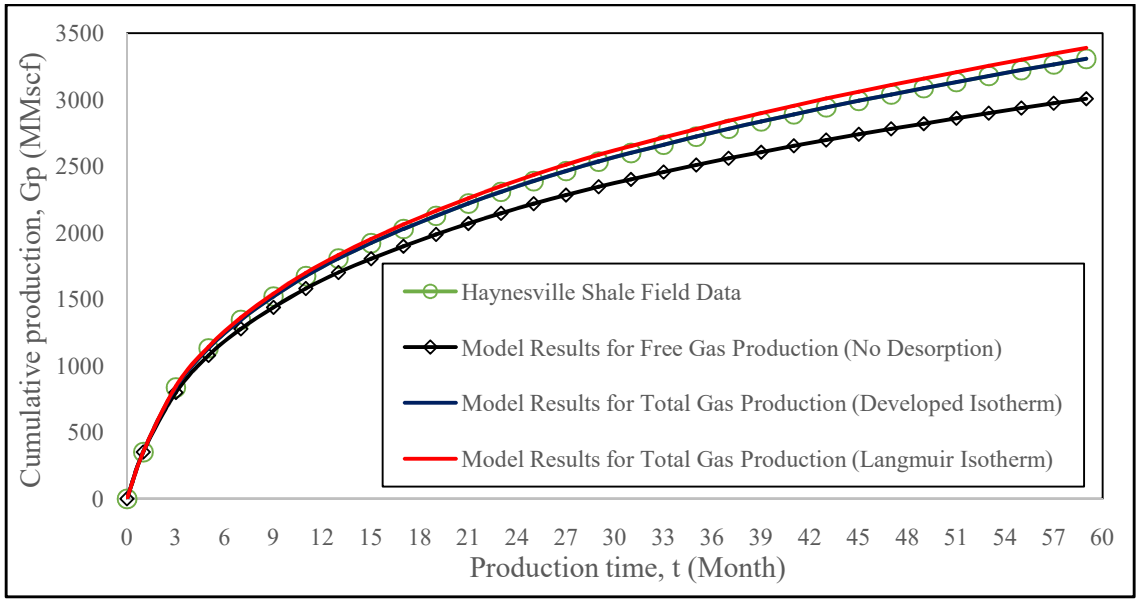

Figure 4.56: Correlation of Haynesville shale gas G_p model results within the production history

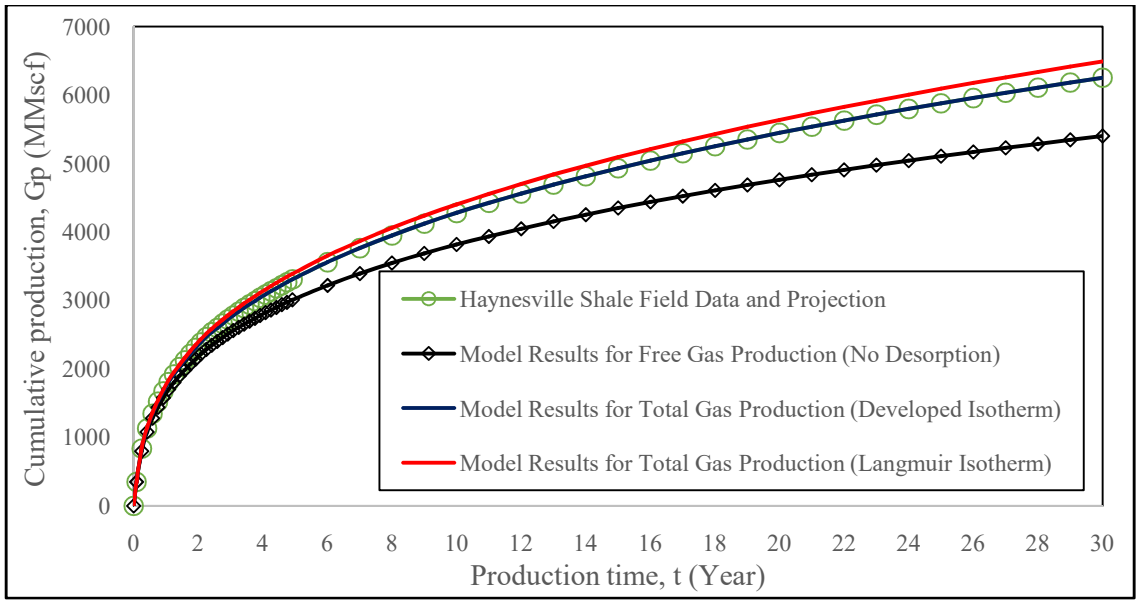

Figure 4.57: Correlation of Haynesville shale gas G_p model results for the whole production forecast

4.9BARNETT SHALE GASMATERIAL BALANCE ANALYSIS

4.9.1 Barnett Shale Adsorption and Reservoir Data Used

The measured initial reservoir pressure of the Barnett shale formation is 3,900 psi (Bowker, 2007). Barnett OGIP (free gas) was reported as 327 Tscf (US DoE, 2009). Barnett shale has technically recoverable reserves of 44 Tscf (US DoE, 2009; and Bureau of Economic Geology Annual Report, 2016).

Barnett shale reservoir area is 5,000 square miles (i.e. 12,950 km^2) (US DoE, 2009). Hence, an average (net) thickness of 317 ft. is considered in this work. Barnett shale gas adsorption data is presented in **Table 4.84** while the reservoir data is shown in **Table 4.85**.

Table 4.84: Barnett shale adsorption data

Parameter	**Symbol**	**Value**	**Unit**
Langmuir volume	V_L	96	scf/ton
Langmuir pressure	P_L	650	psi
Maximum adsorbed volume (Developed isotherm)	V_{max}	71.07	scf/ton
Adsorption saturation pressure (Developed isotherm	P_s	2088.06	psi
Adsorbate-adsorbent resistance parameter (Developed isotherm)	n	0.55	-

Table 4.85: Barnett shale reservoir data(Bowker, 2007; US DoE, 2009)

Parameter	Symbol	Value	Unit
Reservoir area	A	5,000	sq. mile
Reservoir area	A	12,950	sq. km.
Matrix porosity before fracturing	ϕ'_{mat}	0.045	-
Fracture porosity	ϕ_{frac}	0.02	-
Matrix permeability	k_{Darcy}	0.0003	mD
Initial gas saturation	S_{g_i}	0.70	-
Initial water saturation	S_{w_i}	0.30	-
Matrix (bulk) density	ρ_m	2.58	g/cm^3
Initial reservoir pressure	P_i	3,900	psig
Bottom hole pressure	P_{wf}	550	psig
Water compressibility	C_w	3.6×10^{-6}	psi^{-1}
Rock matrix compressibility	C_{matrix}	3.0×10^{-12}	psi^{-1}
Reservoir temperature	T	180	^{o}F
Gas gravity	γ_g	0.65	-

4.9.2Variation of Barnett Shale Gas Compressibility Factor with Pressure

Barnett shale gas reservoir temperature T of 180°F (i.e. 640°R) and a natural gas gravity γ_g of 0.65 are considered.Based on gas compositions (see **Table 2.10**), applying Standing (1981) correlation $(\gamma_g < 0.75)$ for dry gas yields a pseudo-critical pressure P_{pc} of 660.91 psi (see **Equation 2.131**), pseudo-critical temperature T_{pc} of 373.97 °R (see **Equation 2.132**) and a pseudo-reduced temperature T_{pr} of 1.71140.

Standing and Katz Z-factors Z_{SK} are used as initial guesses in evaluating Dranchuk-Abou-Kassem Z-factors Z_{DAK} (see **Equation 3.87**) indicated as Z in **Table 4.86**. The MAPPLE program for evaluating Z-factor using Dranchuk-Abou-Kassem (1975) eleven-constant equation of state is shown in **Appendix D**.

The pressure range considered for Barnett shale is: $0 \leq P \leq 3{,}900$ psig. The initial formation volume factor of Barnett shale gas:

$$B_{g_i} = \left(\frac{P_{sc}}{T_{sc}}\right)\frac{Z_i T}{P_i} \tag{4.110}$$

is evaluated as 4.2614×10^{-3} rcf/scf.

With ϕ_{frac} = 0, single-porosity Z-factor with pore compaction is evaluated as:

$$Z^* = Z\{1-(1.5429E-6)\Delta P\}^{-1} \tag{4.111}$$

With ϕ_{frac} = 0.02, Aguilera (2008) dual-porosity Z-factor is evaluated as:

$$Z'' = Z\{1-(2.1847E-6)\Delta P\}^{-1} \tag{4.112}$$

and the modified dual-porosity Z-factor is evaluated as:

$$Z^{**} = Z\{1-(2.1978E-6)\Delta P\}^{-1} \tag{4.113}$$

The variations of the Z-factors with pressure depletion are shown in **Table 4.86** and **Figure 4.58**. Correlating the modified dual-porosity Z-factor with Aguilera dual porosity Z-factor yields a R^2 value of 1.000.

Table 4.86: Variations of Barnettshale gas Z, Z^*, Z'' and Z^{**} with pressure based on ϕ_{frac} of 0.02

P (psig)	P_{pr}	Z	ΔP (psig)	Z^*	Z'' (Aguilera)	Z^{**} (Modified)
3900	5.9009	0.9186	0	0.9186	0.9186	0.9186
3600	5.4470	0.9020	300	0.9024	0.9026	0.9026
3300	4.9931	0.8878	600	0.8886	0.8890	0.8890
3050	4.6148	0.8784	850	0.8795	0.8800	0.8800
2800	4.2366	0.8714	1100	0.8729	0.8735	0.8735
2550	3.8583	0.8671	1350	0.8689	0.8697	0.8697
2300	3.4800	0.8660	1600	0.8681	0.8690	0.8691
2088	3.1593	0.8676	1812	0.8700	0.8710	0.8711
1800	2.7235	0.8738	2100	0.8766	0.8778	0.8779
1550	2.3452	0.8830	2350	0.8862	0.8876	0.8876
1300	1.9670	0.8955	2600	0.8991	0.9006	0.9006
1050	1.5887	0.9110	2850	0.9150	0.9167	0.9167
800	1.2104	0.9292	3100	0.9337	0.9355	0.9356
550	0.8322	0.9495	3350	0.9544	0.9565	0.9565
300	0.4539	0.9717	3600	0.9771	0.9794	0.9794
150	0.2270	0.9856	3750	0.9913	0.9937	0.9938
0	0	1.0000	3900	1.0060	1.0086	1.0086

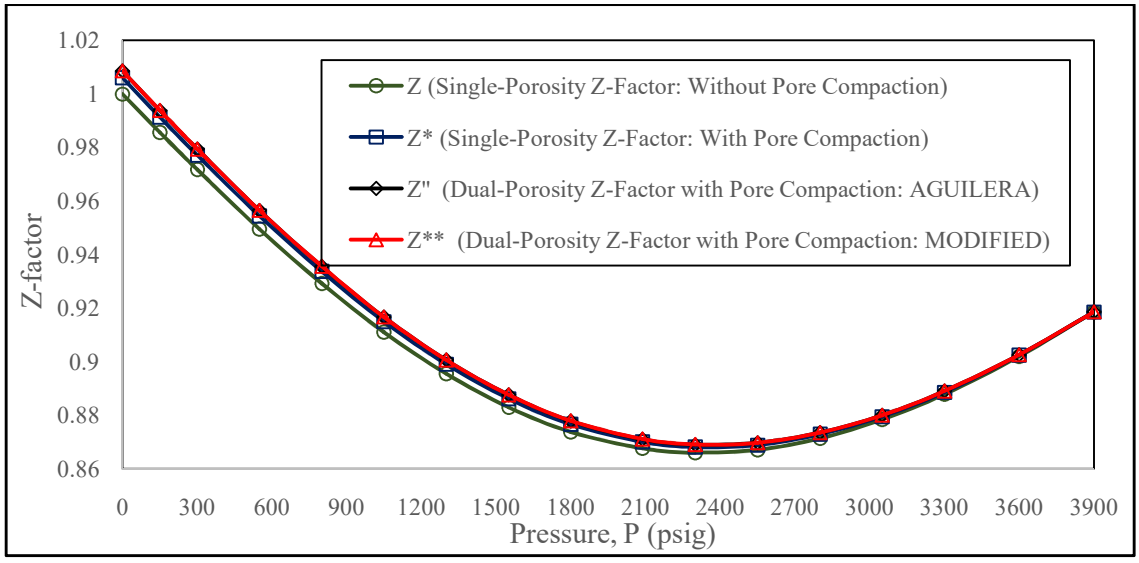

Figure 4.58: Variationsof Z, $Z^{*}Z''$ and Z^{**} with pressure for Barnett shale formation based on ϕ_{frac} of 0.02

4.9.3 Establishment of Barnett Shale OGIPs from Plots of G_p versus P/Z^{**}

The variations of Barnett shale gas P/Z^{**} and cumulative gas production G_p with pressure depletion based on ϕ_{frac} of 0.02 are shown in **Table 4.87**. Also, **Figure 4.59** shows the plots of Barnett shale formation G_p versus P/Z^{**} based on ϕ_{frac} of 0.02. The original gas-in-place OGIP without adsorption consideration is evaluated as 326.6310 Tscf.

However, the OGIPs that account for free and adsorbed gases based on the developed isotherm and Langmuir isotherm are 554.7667 Tscf and 590.7693 Tscf respectively. When compared with the free gas-in-place, the adsorbed gas in Barnett shale formation is observed to be substantial due to the low reservoir temperature that yields low gas molecular activation energy which favours adsorption.

From the material balance analysis, with pressure drawdown from 3,900 to 3,261 psig, technically recoverable reserves of 44 Tscf would be depletedin form of free gasG_p; the corresponding developed isotherm-based and Langmuir isotherm-based technically recoverable (total gas) reserves (in form of total gasG_p) were estimated as 44.00and 51.19 Tscf respectively. The plots of Barnett shale formation G_p versus P/Z^{**} (based on ϕ_{frac} of 0.02) within the technically recoverable reserves depletion range is shown in **Figure 4.60**.

Table 4.87: Variation of Barnett shale gas G_p with pressure based on ϕ_{frac} of 0.02

P (psig)	ΔP (psig)	P/Z^{**} (psig)	$1-\frac{P/Z^{**}}{P_i/Z_i}$	Cumulative Gas Production G_p (Tscf)		
				$G_{p_{Free}}$ Without Adsorption	$G_{p_{Total}}$ Developed Isotherm	$G_{p_{Total}}$ Langmuir Isotherm
3900	0	4245.59	0	0	0	0
3600	300	3988.48	0.0606	19.7938	19.7938	22.9013
3300	600	3712.04	0.1257	41.0575	41.0575	47.7445
3261	639	3673.67	0.1347	**44.0000**	**44.0000**	**51.1927**
3050	850	3465.91	0.1836	59.9694	59.9694	70.0828
2800	1100	3205.49	0.2450	80.0246	80.0246	94.0609
2550	1350	2932.04	0.3094	101.0596	101.0596	119.6318
2300	1600	2646.42	0.3767	123.0419	123.0419	146.9188
2088	1812	2396.97	0.4354	142.2151	142.2151	171.3494
1800	2100	2050.58	0.5170	168.8682	171.3357	206.6022
1550	2350	1746.28	0.5887	192.2877	201.1742	239.3132
1300	2600	1443.48	0.6600	215.5764	235.3308	274.2738
1050	2850	1145.41	0.7302	238.5059	274.2130	312.3092
800	3100	855.07	0.7986	260.8475	318.5489	354.9657
550	3350	575.01	0.8646	282.4051	369.7696	405.3028
300	3600	306.31	0.9278	303.0482	431.2035	469.8724
150	3750	150.94	0.9644	315.0029	476.9982	521.3610
0	3900	0	1.0000	326.6310	554.7667	590.7693

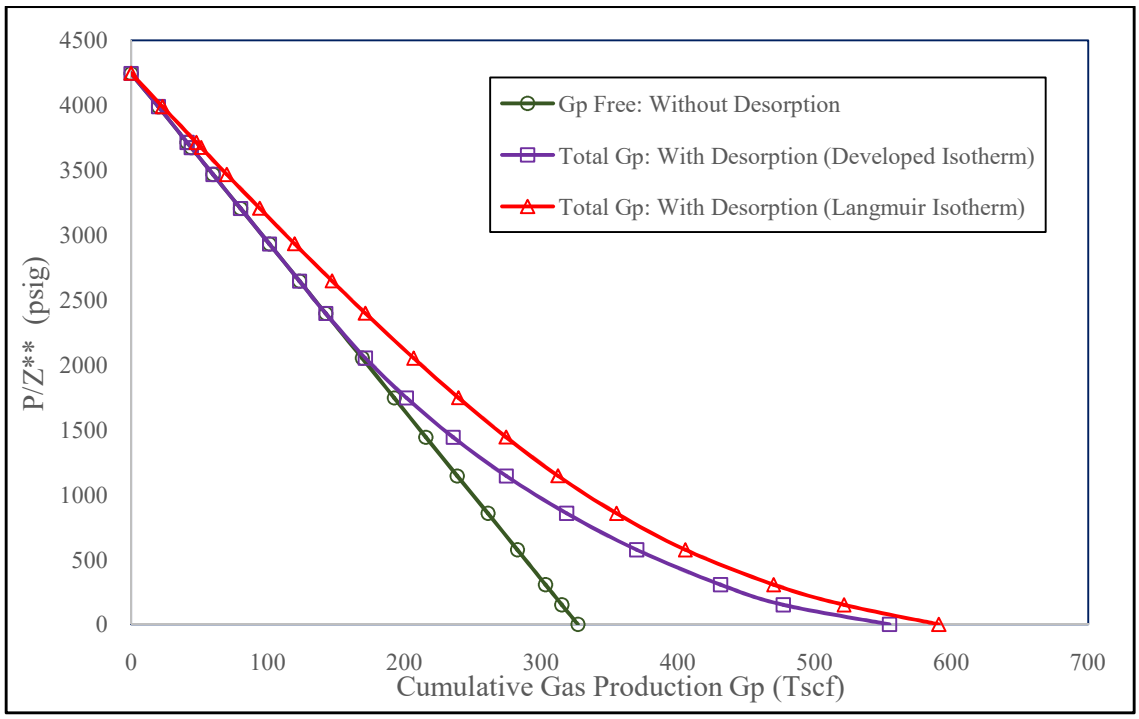

Figure 4.59: Plots of Barnett shale G_p versus $^{P}/_{Z^{**}}$ based on ϕ_{frac} of 0.02

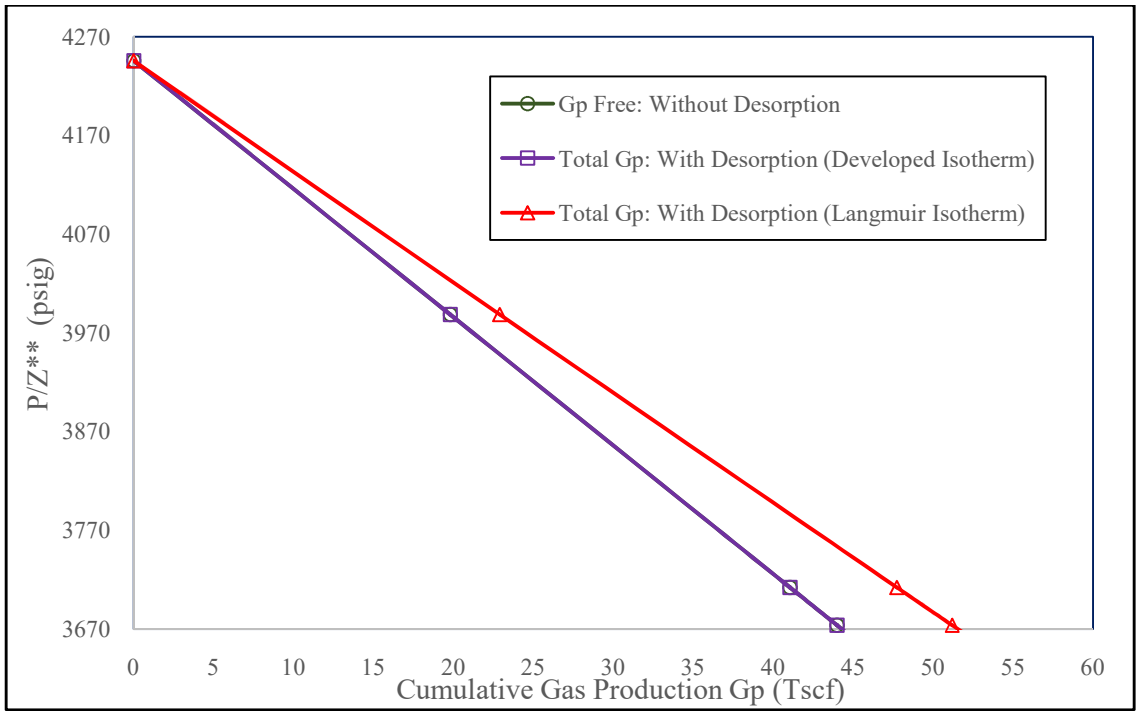

Figure 4.60: Plots of Barnett shale G_p versus $^{P}/_{Z^{**}}$ (based on ϕ_{frac} of 0.02) for technically recoverable (free gas) reserves of 44 Tscf

4.9.4Variation of Barnett Shale GIP with Pressure

The variation of gas-in-place GIP with pressure for Barnett shale formation with fracture porosity ϕ_{frac} of 0.02 is shown in **Table 4.88** while the plot is shown in **Figure 4.61**. However, the fractions of free and adsorbed GIP to total GIP for Barnett shale formation with fracture porosity ϕ_{frac} of 0.02 is shown in **Table 4.89** while the plot is shown in **Figure 4.62**.

From **Figures 4.61** and **4.62**, with the developed isotherm-based MBE, pressure depletion from the initial reservoir condition of 3,900 psig to 2,581.39 psig reduces the free gas contributing capacity to production from 58.88% to 50.00%; further depletion to 150 psig reduces it to 14.95%. However, the adsorbed gas is found to be the principal contributor to gas production below 2,581.39 psig. Pressure depletion from the initial reservoir condition to 2,581..9 psig causes the capacity to increase from 41.12% to 50.00%; while the capacity increases from 50.00% to 85.05% when pressure is depleted further down to 150 psig.

It is thus evident that adsorbed gas contribution to production is prevalent below a pressure of about 0.6620 the initial reservoir pressure. This confirms the remarkable proportion of adsorbed gas in Barnett shale formation when compared with the free gas-in-place.

Table 4.88: Variation of Barnett shale GIP with pressure based on ϕ_{frac} of 0.02

P (psig)	Gas-in-Place GIP (Tscf)				
	GIP_{Free} Without Adsorption	$GIP_{Adsorbed}$ Developed Isotherm	$GIP_{Adsorbed}$ Langmuir Isotherm	GIP_{Total} Developed Isotherm	GIP_{Total} Langmuir Isotherm
3900	326.6310	228.1357	264.1383	554.7667	590.7693
3600	306.8372	228.1357	261.0308	534.9729	567.8680
3300	285.5735	228.1357	257.4513	513.7092	543.0248
3050	266.6616	228.1357	254.0249	494.7973	520.6865
2800	246.6064	228.1357	250.1020	474.7421	496.7084
2550	225.5714	228.1357	245.5661	453.7071	471.1375
2300	203.5891	228.1357	240.2614	431.7248	443.8505
2088	184.4159	228.1357	235.0040	412.5516	419.4199
1800	157.7628	225.6682	226.4043	383.4310	384.1671
1550	134.3433	219.2492	217.1128	353.5925	351.4561
1300	111.0546	208.3813	205.4409	319.4359	316.4955
1050	88.1251	192.4286	190.3350	280.5537	278.4601
800	65.7835	170.4343	170.0201	236.2178	235.8036
550	44.2259	140.7712	141.2406	184.9971	185.4665
300	23.5828	99.9804	97.3141	123.5632	120.8969
150	11.6281	66.1404	57.7802	77.7685	69.4083
0	0	0	0	0	0

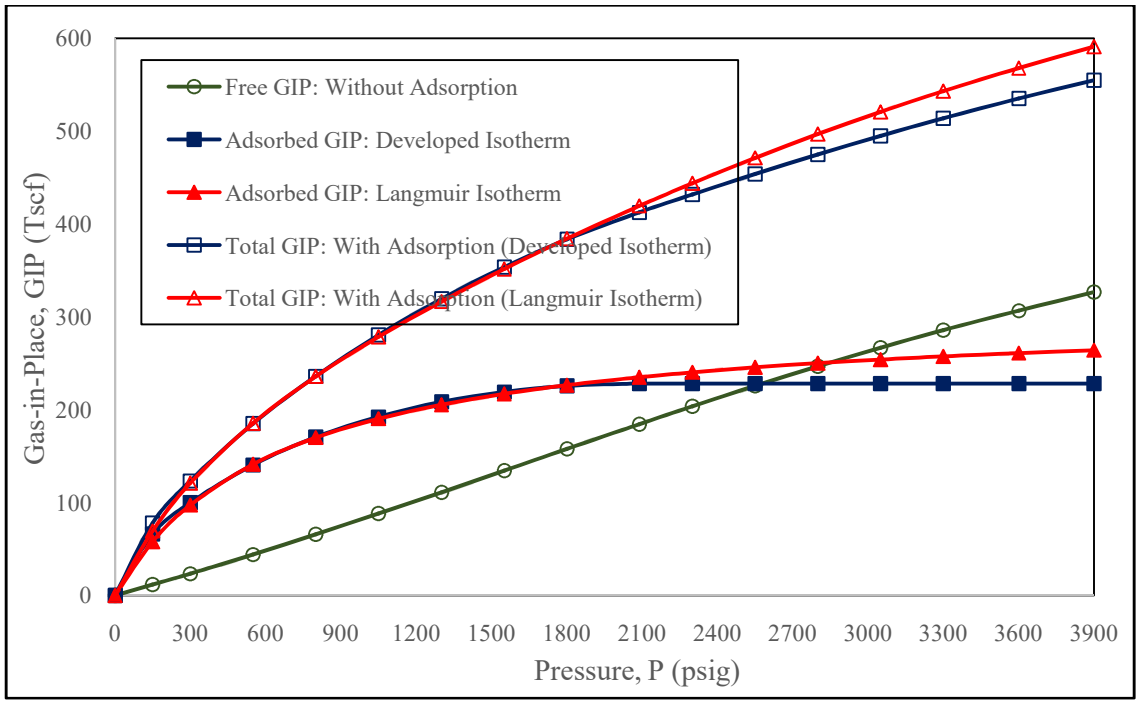

Figure 4.61: Plots of Barnett shale GIP versus pressure based on ϕ_{frac} of 0.02

Table 4.89: Fractions of free and adsorbed GIP to total GIP for Barnett shale formation with fracture porosity ϕ_{frac} of 0.02

P (psig)	Fractions of Free and Adsorbed GIP to Total GIP			
	Developed Isotherm-Based		Langmuir Isotherm-Based	
	GIP_{Free}	$GIP_{Adsorbed}$	GIP_{Free}	$GIP_{Adsorbed}$
3900	0.5888	0.4112	0.5529	0.4471
3600	0.5736	0.4264	0.5403	0.4597
3300	0.5559	0.4441	0.5259	0.4741
3050	0.5389	0.4611	0.5121	0.4879
2800	0.5195	0.4805	0.4965	0.5035
2550	0.4972	0.5028	0.4788	0.5212
2300	0.4716	0.5284	0.4587	0.5413
2088	0.4470	0.5530	0.4397	0.5603
1800	0.4115	0.5885	0.4107	0.5893
1550	0.3799	0.6201	0.3822	0.6178
1300	0.3477	0.6523	0.3509	0.6491
1050	0.3141	0.6859	0.3165	0.6835
800	0.2785	0.7215	0.2790	0.7210
550	0.2391	0.7609	0.2385	0.7615
300	0.1909	0.8091	0.1951	0.8049
150	0.1495	0.8505	0.1675	0.8325
0	-	-	-	-

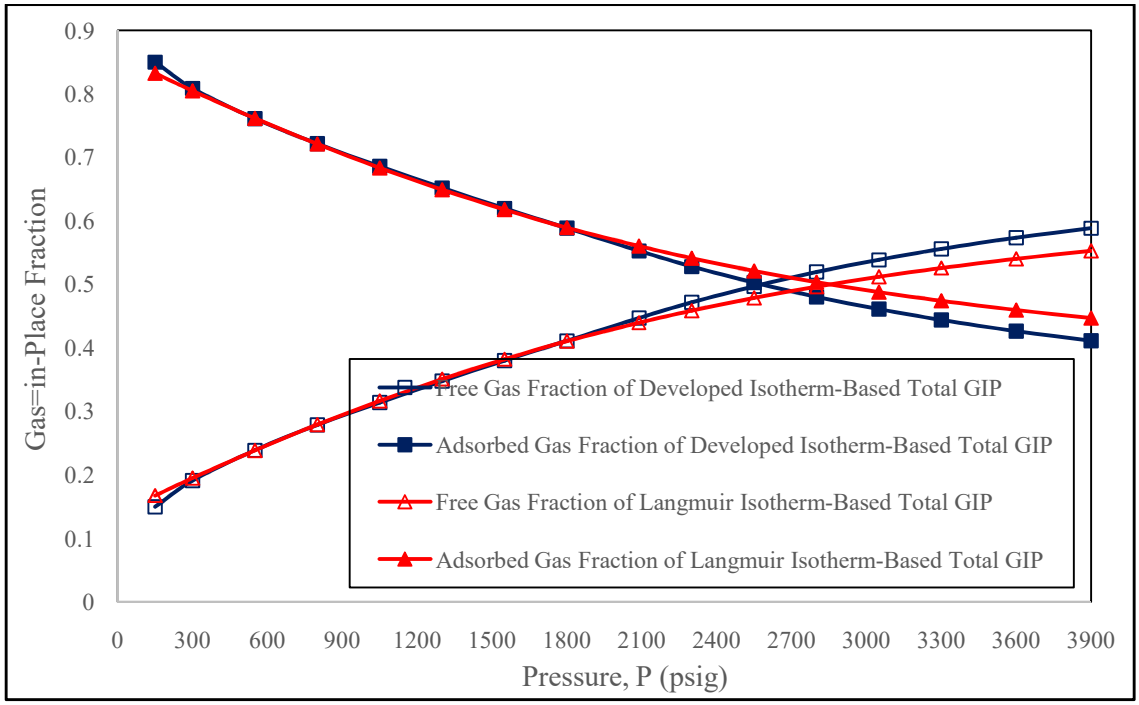

Figure 4.62: Fractions of free and adsorbed GIP to total GIP for Barnett shale formation based on ϕ_{frac} of 0.02

4.9.5Effect of Fracture Porosity on Barnett Shale Gas Production

The single-porosity gas reservoir Z-factor g is evaluated as:

$$Z^* = Z\{1 - (1.5429E - 6)\Delta P\}^{-1} \quad (4.114)$$

The variations of Barnett shale gas $^{P}/_{Z^{**}}$ and cumulative gas production G_p with pressure depletion based on ϕ_{frac} of 0 and the developed isotherm are shown in **Table 4.90**.

For fracture porosity ϕ_{frac} of 0.04, the modified dual-porosity Z-factor is evaluated as:

$$Z^{**} = Z \cdot \{1 - (2.8526E - 6) \cdot \Delta P\}^{-1} \quad (4.115)$$

The variations of Barnett shale gas $^{P}/_{Z^{**}}$ and cumulative gas production G_p with pressure depletion based on ϕ_{frac} of 0.04 and the developed isotherm are shown in **Table 4.91**.

Also, for fracture porosity ϕ_{frac} of 0.06, the modified dual-porosity Z-factor is evaluated as:

$$Z^{**} = Z \cdot \{1 - (3.5075E - 6) \cdot \Delta P\}^{-1} \quad (4.116)$$

The variations of Barnett shale gas $^{P}/_{Z^{**}}$ and cumulative gas production G_p with pressure depletion based on ϕ_{frac} of 0.06 and the developed isotherm are shown in **Table 4.92**.

Fracture-induced increase in gas production from Barnett shale (with reference to no-fracturing scenario) is shown in **Table 4.83**and **Figure 4.63**. Fracturing accelerates

pressure depletion, and at a particular pressure, fracturing has increasing effect only on free gas production while gas desorption remains the same at that pressure.

As compared to the no-fracturing scenario, increase in gas production at fracture porosity levels of 0.02, 0.04 and 0.06 with pressure depletion are observed to be rising till respective constant peak values of 0.2286 Tscf, 0.4573 Tscf and 0.6859 Tscf were attained at 2,300 to 1,550 psig, at 2088 to 1,800 psig, and at 1,800 psig. Thereafter, gas production increase was found to be declining towards the abandonment pressure range.

Table 4.90: Variation of Barnett shale G_p with pressure based on ϕ_{frac} of 0 and the developed isotherm

P (psig)	ΔP (psig)	Z^*	P/Z^* (psig)	$1-\frac{P/Z^*}{P_i/Z_i}$	Cumulative Gas Production G_p (Tscf)	
					$G_{p_{Free}}$	$G_{p_{Total}}$
3900	0	0.9186	4245.59	0	0	0
3600	300	0.9024	3989.36	0.0604	19.7285	19.7285
3300	600	0.8886	3713.71	0.1253	40.9269	40.9269
3050	850	0.8795	3467.88	0.1832	59.8388	59.8388
2800	1100	0.8729	3207.70	0.2445	79.8613	79.8613
2550	1350	0.8689	2934.75	0.3088	100.8636	100.8636
2300	1600	0.8681	2649.46	0.3760	122.8133	122.8133
2088	1812	0.8700	2400.00	0.4347	141.9865	141.9865
1800	2100	0.8766	2053.39	0.5163	168.6396	171.1071
1550	2350	0.8862	1749.04	0.5880	192.0590	200.9456
1300	2600	0.8991	1445.89	0.6594	215.3805	235.1349
1050	2850	0.9150	1147.54	0.7297	238.3426	274.0497
800	3100	0.9337	856.81	0.7982	260.7169	318.4183
550	3350	0.9544	576.28	0.8643	282.3072	369.6717
300	3600	0.9771	307.03	0.9277	303.0156	431.1709
150	3750	0.9913	151.32	0.9644	315.0029	476.9982

0	3900	1.0060	0	1.0000	326.6310	554.7667

Table 4.91: Variation of Barnett shale G_p with pressure based on ϕ_{frac} of 0.04 and the developed isotherm

P (psig)	ΔP (psig)	Z^{**}	P/Z^{**} (psig)	$1-\frac{P/Z^{**}}{P_i/Z_i}$	Cumulative Gas Production G_p (Tscf)	
					$G_{p_{Free}}$	$G_{p_{Total}}$
3900	0	0.9186	4245.59	0	0	0
3600	300	0.9028	3987.59	0.0608	19.8592	19.8592
3300	600	0.8893	3710.78	0.1260	41.1555	41.1555
3050	850	0.8805	3463.94	0.1841	60.1328	60.1328
2800	1100	0.8741	3203.29	0.2455	80.1879	80.1879
2550	1350	0.8704	2929.69	0.3099	101.2229	101.2229
2300	1600	0.8700	2643.68	0.3773	123.2379	123.2379
2088	1812	0.8721	2394.22	0.4361	142.4438	142.4438
1800	2100	0.8791	2047.55	0.5177	169.0969	171.5644
1550	2350	0.8890	1743.53	0.5893	192.4837	201.3702
1300	2600	0.9022	1440.92	0.6606	215.7724	235.5269
1050	2850	0.9185	1143.17	0.7307	238.6693	274.3764
800	3100	0.9375	853.33	0.7990	260.9782	318.6796
550	3350	0.9587	573.69	0.8649	282.5031	369.8676
300	3600	0.9818	305.56	0.9280	303.1135	431.2688

150	3750	0.9963	150.56	0.9645	315.0356	477.0309
0	3900	1.0112	0	1.0000	326.6310	554.7667

Table 4.92: Variation of Barnett shale G_p with pressure based on ϕ_{frac} of 0.06 and the developed isotherm

P (psig)	ΔP (psig)	Z^{**}	P/Z^{**} (psig)	$1-\frac{P/Z^{**}}{P_i/Z_i}$	Cumulative Gas Production G_p (Tscf)	
					$G_{p_{Free}}$	$G_{p_{Total}}$
3900	0	0.9186	4245.59	0	0	0
3600	300	0.9029	3987.15	0.0609	19.8918	19.8918
3300	600	0.8897	3709.11	0.1264	41.2862	41.2862
3050	850	0.8810	3461.97	0.1846	60.2961	60.2961
2800	1100	0.8748	3200.73	0.2461	80.3839	80.3839
2550	1350	0.8712	2927.00	0.3106	101.4516	101.4516
2300	1600	0.8709	2640.95	0.3779	123.4338	123.4338
2088	1812	0.8731	2391.48	0.4367	142.6398	142.6398
1800	2100	0.8803	2044.76	0.5184	169.3255	171.7930
1550	2350	0.8903	1740.99	0.5899	192.6796	201.5661
1300	2600	0.9037	1438.53	0.6612	215.9684	235.7228
1050	2850	0.9202	1141.06	0.7312	238.8326	274.5397
800	3100	0.9394	851.61	0.7994	261.1088	318.8102
550	3350	0.9608	572.44	0.8652	282.6011	369.9656
300	3600	0.9841	304.85	0.9282	303.1789	431.3342
150	3750	0.9987	150.19	0.9646	315.0682	477.0635

0	3900	1.0139	0	1.0000	326.6310	554.7667

Table 4.93: Fracture-induced increase in gas production from Barnett shale (with reference to no-fracturing scenario)

P (psig)	Increase in Gas Production ΔG_p (Tscf) with Reference to No-Fracturing Scenario			
	ϕ_{frac} of 0	ϕ_{frac} of 0.02	ϕ_{frac} of 0.04	ϕ_{frac} of 0.06
3900	0	0	0	0
3600	0	0.0653	0.1307	0.1633
3300	0	0.1306	0.2286	0.3593
3050	0	0.1306	0.2577	0.4246
2800	0	0.1633	0.3266	0.5226
2550	0	0.1960	0.3593	0.5880
2300	0	0.2286	0.4246	0.6205
2088	0	0.2286	0.4573	0.6533
1800	0	0.2286	0.4573	0.6859
1550	0	0.2286	0.4246	0.6205
1300	0	0.1959	0.3919	0.5879
1050	0	0.1633	0.3267	0.4900
800	0	0.1306	0.2612	0.3919
550	0	0.0979	0.1959	0.2939
300	0	0.0326	0.0979	0.1633

150	0	0	0.0327	0.0653
0	0	0	0	0

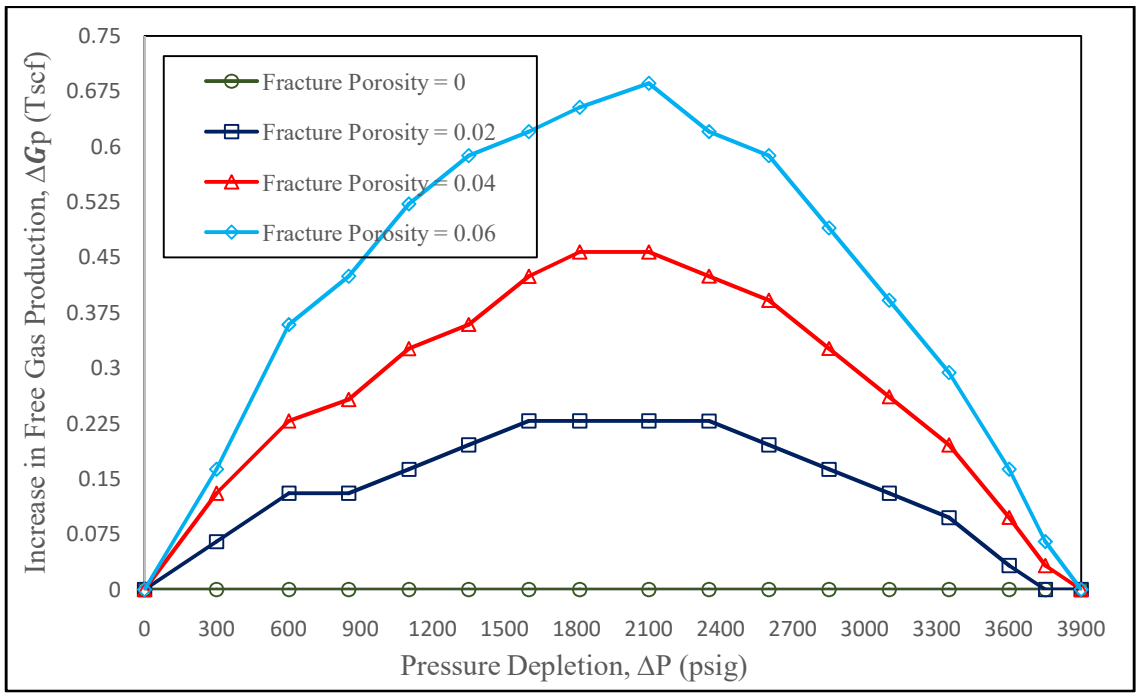

Figure 4.63: Fracture-induced increase in gas production from Barnett shale (with reference to no-fracturing scenario)

4.10 BARNETT SHALE GAS PRODUCTION PERFORMANCE FORECAST

4.10.1Generation of Decline Rate Model from Production History

The variations of Barnett shale gas production rate q_g (see **Figure 2.20 (**Chesapeake Energy, 2010) is shown in **Table 4.94** and the plot is shown in **Figure 4.64**. The production rate at the first day is considered as 2,600 Mscf/d based on graphical extrapolation.

Thus variation of Barnett shale gas production rateq_g with time is modelled as:

$$q_{g_{Well\ Forecast}^{Actual\ Total\ Gas}} = 2973.3\ t^{-0.5920}\ \text{Mscf/d} \qquad (4.117)$$

where t is in months, the initial production rate (at the end of the first month) q_{g_1}= 2973.3 Mscf/d and production exponent $n = 0.5920$.

Table 4.94: Variations of Barnett shale gas production rate q_g and cumulative gas production G_p with time

Time, t (month)	Time, t (year)	Time, t (day)	q_g (Mscf/d)	G_p (MMscf)
1	0.0833	30	2180	71.70
3	0.2500	90	1600	185.10
5	0.4167	150	1270	271.20
7	0.5833	210	1000	339.30
9	0.7500	270	850	394.80
11	0.9167	330	760	443.10
13	1.0833	390	700	486.90
15	1.2500	450	630	526.80
17	1.4167	510	590	563.40
19	1.5833	570	560	597.90
21	1.7500	630	530	630.60
23	1.9167	690	500	661.50
25	2.0833	750	475	690.75
27	2.2500	810	450	718.50
29	2.4167	870	430	744.90
31	2.5833	930	415	770.25
33	2.7500	990	400	794.70
35	2.9167	1050	375	817.95
37	3.0833	1110	360	840.00
39	3.2500	1170	330	860.70
41	3.4167	1230	300	879.60
43	3.5833	1290	290	897.30
45	3.7500	1350	285	914.55

47	3.9167	1410	280	931.50
49	4.0833	1470	275	948.15
51	4.2500	1530	270	964.50
53	4.4167	1590	265	980.55
55	4.5833	1650	260	996.30
57	4.7500	1710	255	1011.75
59	4.9167	1770	250	1026.90

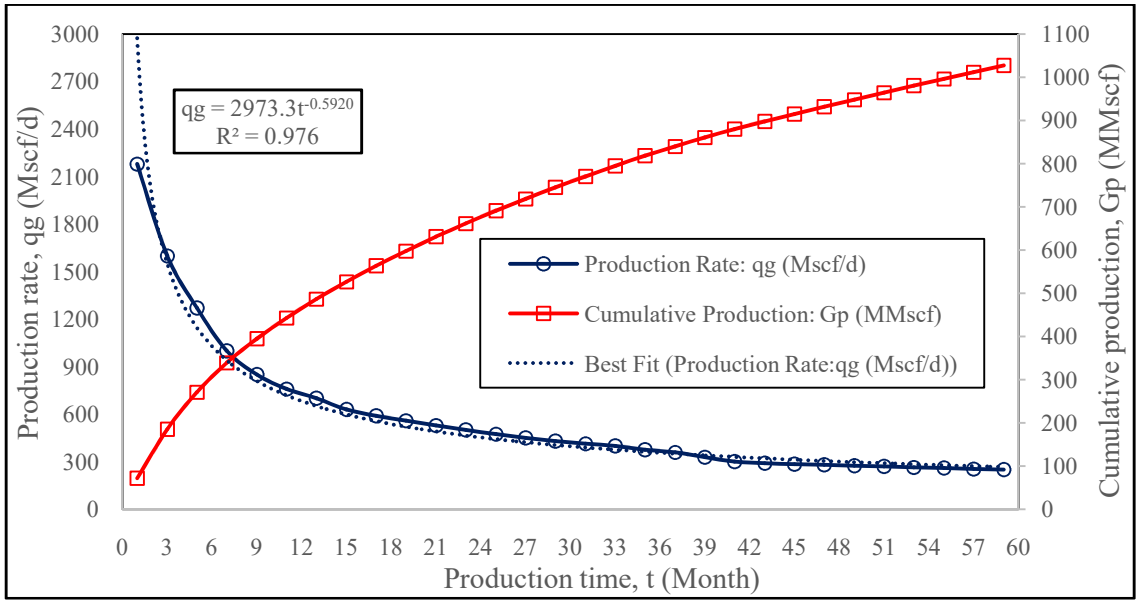

Figure 4.64: Plot of Barnett shale gas q_g and G_p versus time t

4.10.2Development of Free and Total Gas Decline Rate Models for Production Performance Forecast

Flow rate $q = \frac{dG_p}{dP} * \frac{dP}{dt}$; however, pressure depletion in the well is the same both for free and total gas production. The decline rate exponent $n = \frac{C}{\left(\frac{dG_p}{dP}\right)}$(see **Equation 3.129**) where C is a constant of proportionality.And the trend of $\frac{dG_p}{dP}$(for pressure depletion from the initial reservoir pressure P_i to the wellbore flowing pressure P_{wf}in the improved material balance analysis)forms the basis for comparing the production exponent n and thus the flow rates $q_g$of free gas, total gas based on the developed isotherm, and total gas based on Langmuir isotherm.

In **Table 4.87**, for pressure depletion from the initial reservoir pressure P_i to the wellbore flowing pressure P_{wf},

$$\left(\frac{dG_p}{dP}\right)^{MBA-Predict}_{Free\ Gas} = 0.0843 \text{ Tscf/psi} \quad (4.118)$$

$$\left(\frac{dG_p}{dP}\right)^{MBA-Predic}_{\substack{Total\ Gas \\ (Developed\ Isotherm)}} = 0.1104 \text{ Tscf/psi} \quad (4.119)$$

and

$$\left(\frac{dG_p}{dP}\right)^{MBA-Predi}_{\substack{Total\ Gas \\ (Langmuir\ Isotherm)}} = 0.1210 \text{ Tscf/psi} \quad (4.120)$$

This shows that increase in estimated ultimate recovery (EUR) of Barnett shale gas due to gas desorption based on the developed and Langmuir isotherms are 0.2364and 0.3033 respectively; here

$$\text{Increase in EUR} = \frac{\left(G_p^{Total\ Gas} - G_p^{Free\ Gas}\right)}{G_p^{Total\ Gas}} \tag{4.121}$$

Actual Barnett shale OGIP (free gas) is 327 Tscf (US DoE, 2009); however, the MBA-predicted OGIP (free gas) is 326.6310 Tscf (see **Table 4.87**). Therefore,

$$\left(\frac{Actual\ OGIP}{MBA-Predict\quad OGIP}\right)_{Free\ Gas} = 1.0011 \tag{4.122}$$

and

$$\left(\frac{dG_p}{dP}\right)_{Free\ Gas}^{Actual} = 1.0011 \times \left(\frac{dG_p}{dP}\right)_{Free\ Gas}^{MBA-Predicted} \tag{4.123}$$

Thus for pressure depletion from initial reservoir pressure P_i to the wellbore flowing pressure P_{wf},

$$\left(\frac{dG_p}{dP}\right)_{Free\ Gas}^{Actual} = 0.0844 \text{ Tscf/psig} \tag{4.124}$$

The developed isotherm has been establishedto truly represent Type I isotherm and predicts actual adsorption or desorption, i.e.

$$V_{Gas\ Desorption}^{Experimental} \approx V_{Gas\ Desorption}^{Developed\ Isotherm} \tag{4.125}$$

However, the actual total gas production,

$$G_{p\ Total\ Gas}^{Actual} = G_{p\ Free\ Gas}^{Actual} + G_{p\ Desorbed\ Gas}^{Actual} \tag{4.126}$$

Hence, for Barnett shale formation,

$$G_{p\ Total\ Gas}^{Actual} = 1.0011 \times \left(G_{p\ Free\ Gas}^{MBA-Predicte}\right) + G_{p\ Desorbed\ Gas}^{Developed\ Isotherm} \tag{4.127}$$

At P_{wf},

$$G_{p_{Total\ Gas}}^{Actual} = 1.0011 \times (282.4051) + 87.3645 = 370.0802 \text{ Tscf} \quad (4.128)$$

and the corresponding

$$\left(\frac{dG_p}{dP}\right)_{Total\ Gas}^{Actual} = 0.1105 \text{ Tscf/psi} \quad (4.129)$$

The decline rate exponent

$$n = \frac{C}{\left(\frac{dG_p}{dP}\right)} \quad (4.130)$$

From the actual total gas forecast for the well (see **Figure 4.64**)

$$n_{Well\ Forecast}^{Actual\ Total\ Gas} = 0.5920 \quad (4.131)$$

Therefore,

$$n_{Well\ Forecast}^{Actual\ Free\ Gas} = 0.5920\left(\frac{0.1105}{0.0844}\right) = 0.7751 \quad (4.132)$$

$$n_{Well\ Forecast}^{Total\ Gas\ (Developed\ Isotherm)} = 0.5920\left(\frac{0.1105}{0.1104}\right) = 0.5925 \quad (4.133)$$

and

$$n_{Well\ Forecast}^{Total\ Gas\ (Langmuir\ Isotherm)} = 0.5920\left(\frac{0.1105}{0.1210}\right) = 0.5406 \quad (4.134)$$

However, to correlate the production rate forecast with the production rate from field data, the respective model fitting factors

$$K = \left(\frac{q_{g_{Field\ Data}}^{Actual\ Total\ Gas}}{q_{g_{Well\ Forecast}}^{Actual\ Total\ Gas}}\right) \quad (4.135)$$

after the first time step must be considered. Hence, the variations of respective q_g with time are modelled as:

$$q_{g_{Well\ Forecast}}^{Actual\ Free\ Gas} = K\left(q_{g_1} t^{-0.7751}\right) \text{Mscf/d} \quad (4.136)$$

$$q_{g_{Well\ Forecast}}^{\substack{Total\ Gas \\ (Developed\ Isotherm)}} = K\left(q_{g_1}t^{-0.5925}\right)\text{Mscf/d} \qquad (4.137)$$

and

$$q_{g_{Well\ Forecast}}^{\substack{Total\ Gas \\ (Langmuir\ Isotherm)}} = K\left(q_{g_1}t^{-0.5406}\right)\text{Mscf/d} \qquad (4.138)$$

Beyond the production history, the last value of K is retained.

Barnett shale gas production performance forecast (q_g) within and beyond well production history are shown in **Tables 4.95**and **4.96** respectively.

Table 4.95: Barnett shale gas production performance forecast (q_g) within well production history

Time, t (month)	Actual Total Gas q_g (Field Data) (Mscf/d)	Total Gas q_g Forecast (Mscf/d) n = 0.5920	Model Fitting Factor K	Free Gas q_g Forecast (Mscf/d)	Total Gas q_g Forecast (Developed Isotherm) (Mscf/d)	Total Gas q_g Forecast (Langmuir Isotherm) (Mscf/d)
1	2180	2973	-	2973	2973	2973
3	1600	1552	1.0309	1308	1599	1692
5	1270	1147	1.1072	946	1269	1379
7	1000	940	1.0638	700	999	1104
9	850	810	1.0494	568	849	951
11	760	719	1.0570	490	759	860
13	700	651	1.0753	438	699	799
15	630	598	1.0535	384	630	725
17	590	556	1.0611	351	589	682
19	560	520	1.0769	327	559	652
21	530	490	1.0816	304	530	620
23	500	465	1.0753	281	499	587
25	475	442	1.0747	264	475	561
27	450	422	1.0663	246	450	534
29	430	405	1.0617	232	429	511
31	415	389	1.0668	221	415	496
33	400	375	1.0667	211	400	479
35	375	362	1.0359	196	375	451
37	360	351	1.0256	186	359	433

39	330	340	0.9706	169	329	398
41	300	330	0.9091	152	299	363
43	290	321	0.9034	146	289	352
45	285	312	0.9135	142	285	347
47	280	304	0.9210	139	280	342
49	275	297	0.9259	135	274	336
51	270	290	0.9310	131	269	330
53	265	283	0.9364	128	265	326
55	260	277	0.9386	125	260	320
57	255	271	0.9410	122	255	314
59	250	266	0.9398	118	249	308

Table 4.96: Barnett shale gas production performance forecast (q_g) beyond well production history

Time, t (year)	Time, t (month)	Total Gas q_g Forecast (Mscf/d) n = 0.5920	Model Fitting Factor K	ActualTotal Gas q_g Projection (Mscf/d)	Free Gas q_g Forecast (Mscf/d)	Total Gas q_g Forecast (Developed Isotherm) (Mscf/d)	Total Gas q_g Forecast (Langmuir Isotherm) (Mscf/d)
6	72	236	0.9398	222	102	222	277
7	84	216	0.9398	203	90	202	255
8	96	199	0.9398	187	81	187	237
9	108	186	0.9398	175	74	174	222
10	120	175	0.9398	164	68	164	210
11	132	165	0.9398	155	63	155	199
12	144	157	0.9398	148	59	147	190
13	156	150	0.9398	141	56	140	182
14	168	143	0.9398	134	53	134	175
15	180	137	0.9398	129	50	129	169
16	192	132	0.9398	124	47	124	163
17	204	128	0.9398	120	45	120	158
18	216	123	0.9398	116	43	116	153
19	228	119	0.9398	112	42	112	148
20	240	116	0.9398	109	40	109	144
21	252	113	0.9398	106	38	106	141

22	264	109	0.9398	102	37	103	137
23	276	107	0.9398	101	36	100	134
24	288	104	0.9398	98	35	98	131
25	300	102	0.9398	96	34	95	128
26	312	99	0.9398	93	33	93	125
27	324	97	0.9398	91	32	91	123
28	336	95	0.9398	89	31	89	120
29	348	93	0.9398	87	30	87	118
30	360	91	0.9398	86	29	85	116

For production forecast within the production history, the plots of Barnett shale gas q_g versus t are displayed on the same chart (**Figure 4.65)** for (i) the well production history (serving as the base case), (ii) the model results for free gas production (no desorption), (iii) the model results for total gas production based on the developed isotherm, and (iv) the decline rate model results for total gas production based on Langmuir isotherm.

With production history as base case, the developed isotherm-based decline rate model results for the gas well offered better correlation than Langmuir isotherm-based results, with RMSE of 0.7656 and 80.7971 Mscf/d respectively.

For the whole production performance forecast (i.e. within and beyond the production history), the plots of Barnett shale gas q_g versus t are exhibited on the same chart (**Figure 4.66**) for (i) actual gas production and its projection (serving as the base case), (ii) the model results for free gas production (no desorption), (iii) the model results for total gas production based on the developed isotherm, and (iv) the model results for total gas production based on Langmuir isotherm.

For the 30-years production performance forecast, with production history and its projection as base case, the model results for total gas q_g based on the developed

isotherm offer better correlation than the model results for total gas production based on Langmuir isotherm. The corresponding RMSE are 0.6804 and 64.9808 Mscf/d.

Barnett shale gas production performance forecast (G_p) within and beyond well production history are shown in **Tables 4.97** and **4.98** respectively. For production forecast within the production history, the corresponding plots of Barnett shale gasG_P versus $t$are displayed on the same chart in **Figure 4.67**. Also, for the whole production performance forecast (i.e. within and beyond the production history), the corresponding plots of Barnett shale gasG_p versus $t$are exhibited on the same chart in **Figures 4.68**.

Within and beyond the production history,the developed isotherm-based model results is observed to predict the actual gas well production $G_p$better than theLangmuir isotherm-based model resultsdo.

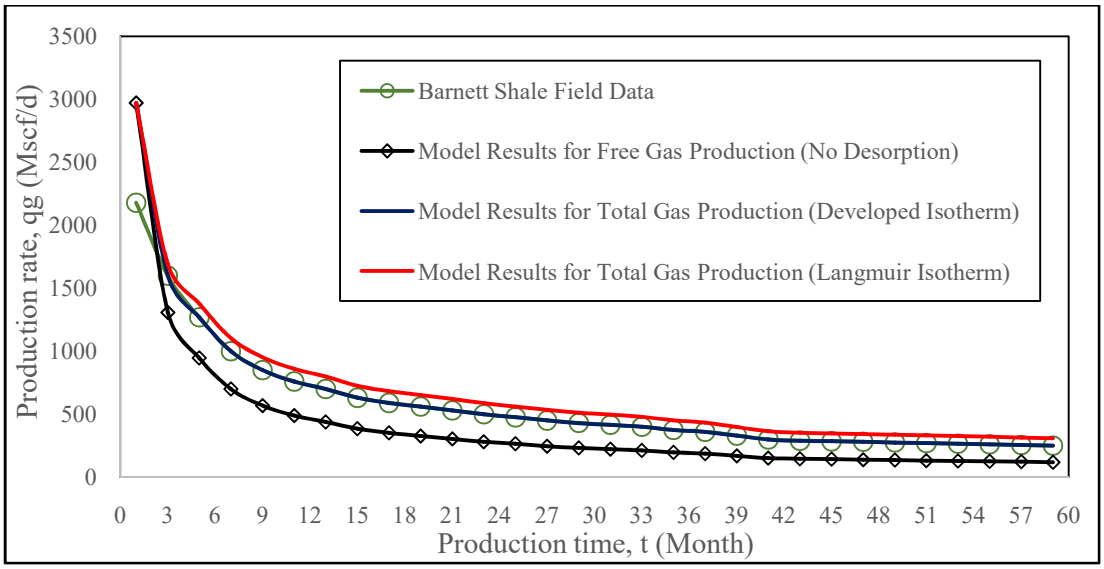

Figure 4.65: Correlation of Barnett shale gas q_g model results within the production history

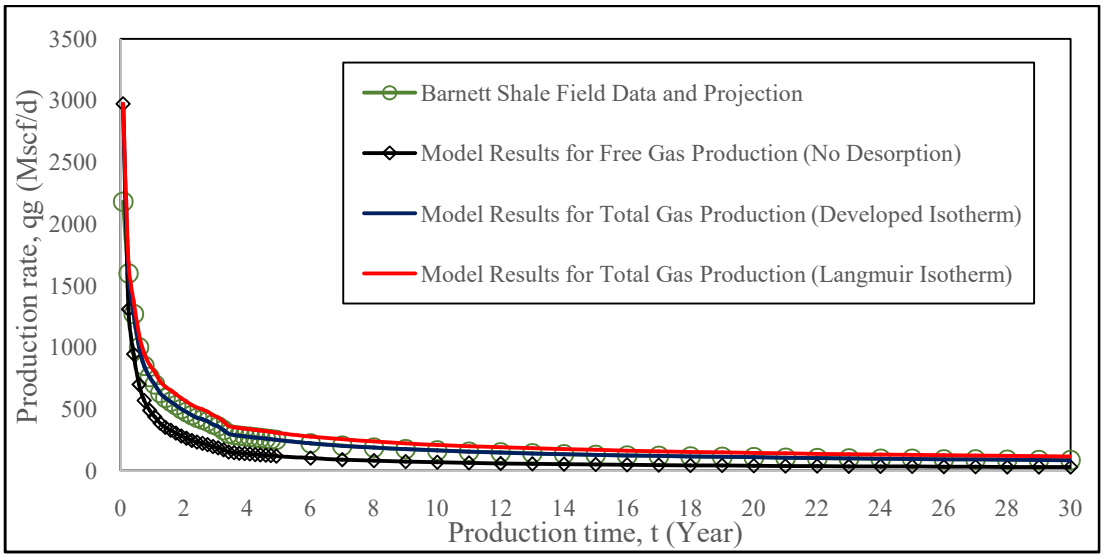

Figure 4.66: Correlation of Barnett shale gas q_g model results for the whole production forecast

Table 4.97: Barnett shale gas production performance forecast (G_p) within well production history

Time, t (year)	Time, t (month)	Time, t (day)	Actual Total Gas G_p (Field Data) (MMscf)	Free Gas G_p Forecast (MMscf)	Total Gas G_p Forecast (Developed Isotherm) (MMscf)	Total Gas G_p Forecast (Langmuir Isotherm) (MMscf)
0.0833	1	30	71.70	71.70	71.70	71.70

0.2500	3	90	185.10	151.32	184.98	195.74
0.4146	5	150	271.20	218.94	271.02	287.87
0.5833	7	210	339.30	268.32	339.06	362.36
0.7500	9	270	394.80	306.36	394.50	424.01
0.9167	11	330	443.10	338.10	442.74	478.34
1.0833	13	390	486.90	365.94	486.33	528.11
1.2500	15	450	526.80	390.60	526.20	573.83
1.4146	17	510	563.40	412.65	562.77	616.04
1.5833	19	570	597.90	432.99	597.21	656.06
1.7500	21	630	630.60	451.92	629.88	694.22
1.9167	23	690	661.50	469.47	660.75	730.43
2.0833	25	750	690.75	485.82	689.97	764.87
2.2500	27	810	718.50	501.12	717.72	797.72
2.4146	29	870	744.90	515.46	744.09	829.07
2.5833	31	930	770.25	529.05	769.41	859.28
2.7500	33	990	794.70	542.01	793.86	888.53
2.9167	35	1050	817.95	554.22	817.11	916.43
3.0833	37	1110	840.00	565.68	839.13	942.95
3.2500	39	1170	860.70	576.33	859.77	967.88
3.4146	41	1230	879.60	585.96	878.61	990.71
3.5833	43	1290	897.30	594.90	896.25	1012.16
3.7500	45	1350	914.55	603.54	913.47	1033.13
3.9167	47	1410	931.50	611.97	930.42	1053.80
4.0833	49	1470	948.15	620.19	947.04	1074.14
4.2500	51	1530	964.50	628.17	963.33	1094.12
4.4146	53	1590	980.55	635.94	979.35	1113.80
4.5833	55	1650	996.30	643.53	995.10	1133.18
4.7500	57	1710	1011.75	650.94	1010.55	1152.20
4.9167	59	1770	1026.90	658.14	1025.67	1170.86

Table 4.98: Barnett shale gas production performance forecast (G_p) beyond well production history

Time, t (year)	Time, t (day)	Actual Total Gas G_p Projection (MMscf)	Free Gas G_p Forecast (MMscf)	Total Gas G_p Forecast (Developed Isotherm) (MMscf)	Total Gas G_p Forecast (Langmuir Isotherm) (MMscf)

6	2160	1118.94	701.04	1117.52	1284.94
7	2520	1195.44	735.60	1193.84	1380.70
8	2880	1265.64	766.38	1263.86	1469.26
9	3240	1330.80	794.28	1328.84	1551.88
10	3600	1391.82	819.84	1389.68	1629.64
11	3960	1449.24	843.42	1447.10	1703.26
12	4320	1503.78	865.38	1501.46	1773.28
13	4680	1555.80	886.08	1553.12	1840.24
14	5040	1605.30	905.70	1602.44	1904.50
15	5400	1652.64	924.24	1649.78	1966.42
16	5760	1698.18	941.70	1695.32	2026.18
17	6120	1742.10	958.26	1739.24	2083.96
18	6480	1784.58	974.10	1781.72	2139.94
19	6840	1825.62	989.40	1822.76	2194.12
20	7200	1865.40	1004.16	1862.54	2246.68
21	7560	1904.10	1018.20	1901.24	2297.98
22	7920	1941.54	1031.70	1938.86	2348.02
23	8280	1978.08	1044.84	1975.40	2396.80
24	8640	2013.90	1057.62	2011.04	2444.50
25	9000	2048.82	1070.04	2045.78	2491.12
26	9360	2082.84	1082.10	2079.62	2536.66
27	9720	2115.96	1093.80	2112.74	2581.30
28	10080	2148.36	1105.14	2145.14	2625.04
29	10440	2180.04	1116.12	2176.82	2667.88
30	10900	2211.00	1126.74	2207.78	2710.00

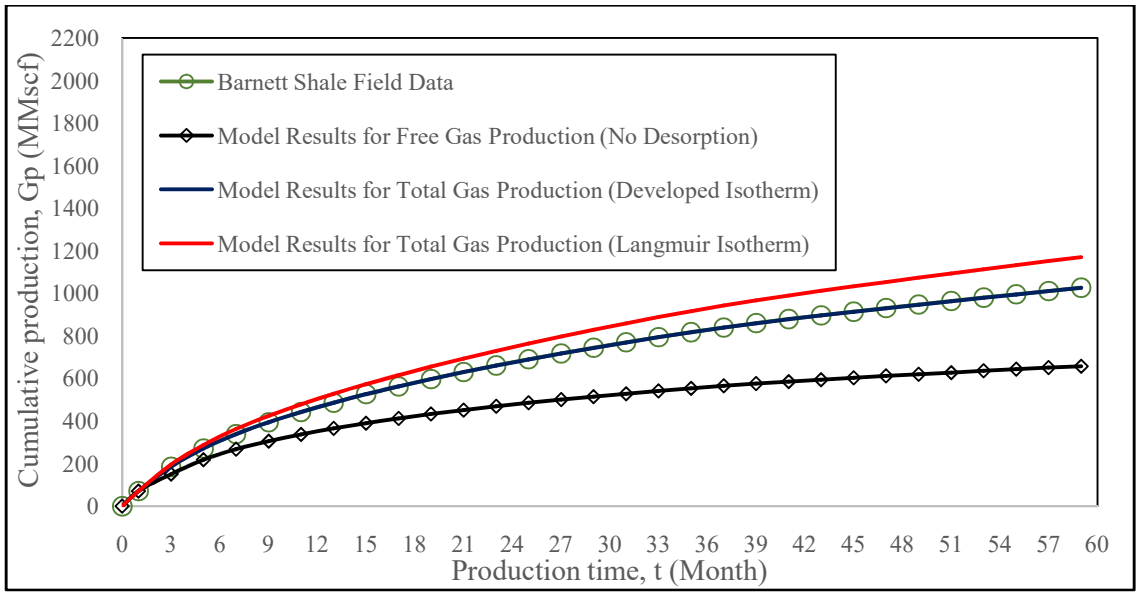

Figure 4.67: Correlation of Barnett shale gas G_p model results within the production history

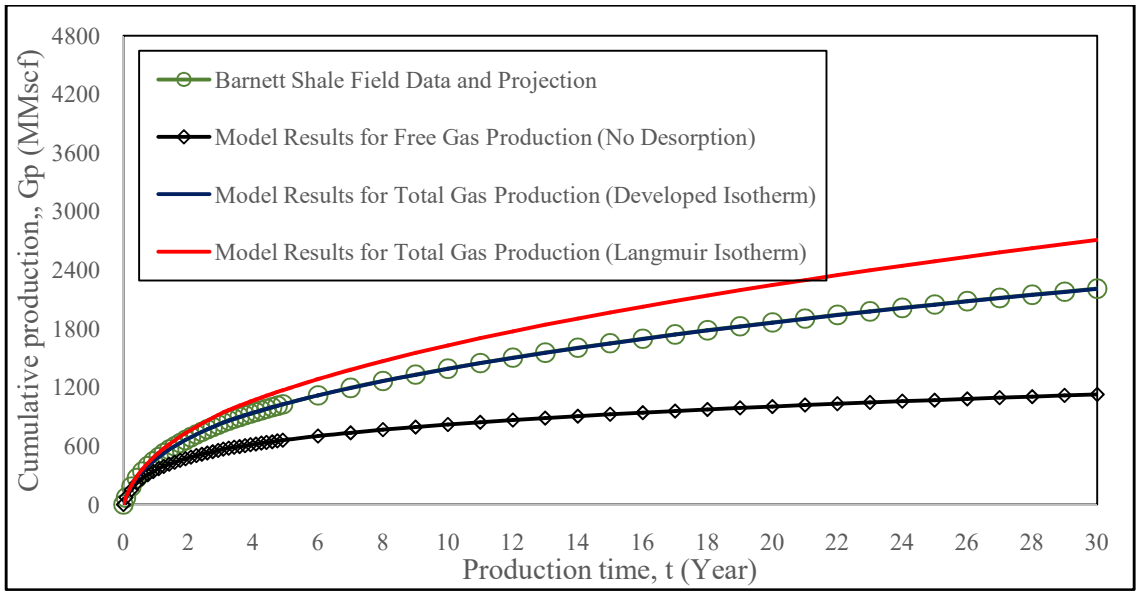

Figure 4.68: Correlation of Barnett shale gas G_p model results for the whole production forecast

CHAPTER FIVE

CONCLUSIONS AND RECOMMENDATIONS

5.1 CONCLUSIONS

From the research undertaken, the following have been concluded:

(1) A Type I adsorption isotherm was developed that defines the onset of adsorption saturation pressure (P_s); thus offering a correction to Langmuir isotherm's over-

estimation at higher pressures. The developed isotherm, $V = \begin{Bmatrix} V_{max}\left\{\frac{P}{P_s} + \left(1 - \frac{P}{P_s}\right)\left(\frac{P}{P_s}\right)^n\right\}, for\ P < P_s\ i.e. undersaturated\ adsorption \\ V_{max},\ for\ P \geq P_s\ i.e. saturated\ adsorption \end{Bmatrix}$ shows that maximum adsorbed volume(V_{max}) is maintained during pressure depletion to P_s, below which gas desorption begins.

(2) For secondary low-pressure adsorption data, the developed adsorption isotherm offers better correlation than Langmuir isotherm in modelling pure carbon dioxide adsorption on BPL activated carbon sample at 28.3 ^{o}C, within the pressure range of 5 to 419 psia; and pure methane adsorption on BPL activated carbon sample at 28.3 ^{o}C, within the pressure range of 23 to 443 psia. Also, for secondary low-pressure methane adsorption data of Turkey's shale sample within 190 to 2,005 psia at 25 ^{o}C, a V_{max} of 0.0450 mmol/g at a P_s of 2,005 psia and a Langmuir volume $(V_L)$of 0.0548 mmol/g at infinite P_s were predicted by the developed and Langmuir isotherms with R^2 values of 0.997 and 0.989, respectively.

(3) The modified Z-factor, $Z^{**} = Z \cdot \left\{1 - \left(1 - \phi_{frac} + \frac{\phi_{frac}}{\phi'_{mat}}\right)\left(\frac{C_w S_{w_i} + C_{matrix}}{S_{g_i}}\right) \cdot \Delta P\right\}^{-1}$ where$Z$,C_w, S_{w_i}, C_{matrix} and S_{g_i} aresingle-porosity Z-factor at pressure P without pore compaction, water compressibility, initial water saturation, matrix compressibility and initial gas saturation, respectively. For Marcellus shale formation, correlating the modified Z-factor with Aguilera Z-factor gives a R^2 value of 1.000.

(4) Original free gas-in-place ($OGIP_{Free}$), original total gas-in-place $\left(OGIP_{(Total)}\right)$ based on the developedisotherm and original total gas-in-place $\left(OGIP_{(Total)}\right)$based on Langmuir isotherm were evaluated using reservoir and adsorption data from shale gas formations published in the literature. For Marcellus shale, the respective OGIPs are 1,489.9635, 2,618.7447 and 2,677.2973 Tscf. Also, for Haynesville shale, the respective OGIPs are 717.0420, 811.8323 and 818.9260 Tscf. For Barnett shale, the respective OGIPs are 326.6310, 554.7667 and 590.7693 Tscf. These reveal the contribution of Langmuir's over-estimation of adsorption.

(5) For Marcellus shale, with pressure drawdown from 3,500 to 2,285 psig, technically recoverable reserves of 489 Tscf would be depletedin form of free gasG_p; the corresponding developed isotherm-based and Langmuir isotherm-based total gas G_p were estimated as 509.2567 and 564.0901 Tscf, respectively. For Haynesville shale, with pressure drawdown from 12,000 to 10,501 psig, technically recoverable reserves of 75 Tscf would be depletedin form of free gasG_p; the corresponding developed isotherm-based and Langmuir isotherm-based total gas G_p were estimated as 75.00and 76.59 Tscf, respectively. For Barnett shale,with pressure drawdown from 3,900 to 3,261 psig, technically recoverable reserves of 44 Tscf would be depletedin form of free gasG_p; the corresponding developed isotherm-based and Langmuir isotherm-based total gas G_p were estimated as 44.00and 51.19 Tscf, respectively. This showed that Langmuir isotherm over-estimates gas desorption.

(6) For Marcellus shaleat 2,300 psig, the cumulative gas productions G_p obtained from the developed isotherm-based MBE for ϕ_{frac} of 0, 0.02, 0.04 and 0.06 are500.4006,500.6986, 501.1456 and 501.4436 Tscf, respectively. For Haynesville shale at 10,500 psig, the corresponding cumulative gas productions are74.3573,74.7158, 75.0026 and 75.3611 Tscf. And for Barnett shale at 3,300 psig, the corresponding cumulative gas productions are40.9269,41.0575, 41.1555 and 41.2864 Tscf. Thus increase in fracture porosity ϕ_{frac} was found to have increasing effect on cumulative gas production G_p.

(7) The trend of the average change of cumulative gas production G_p with pressure (for pressure depletion from the initial reservoir pressure P_i to the bottom hole pressure(P_{wf}) in the improved material balance analysis forms the basis for comparing the production exponent n and thus the flow rates q_g of free gas, total gas based on the developed isotherm, and total gas based on Langmuir isotherm. The respective $\frac{dG_p}{dP}$, the rate decline model generated from production history, and the model fitting factor K were used in obtaining free gas, developed isotherm-basedtotal gas and Langmuir isotherm-based total gas decline rate models for production performance forecast.

(8) Using production history of 59 months as base case, the developed isotherm-based decline rate model results offered better correlation than Langmuir isotherm-based model results, with Root Mean Square Errors (RMSE) of 6.680 and 52.646 Mscf/d, respectively for Marcellus shale formation; 0 and 44.041 Mscf/d, respectively for Haynesville shale formation; and 0.766 and 80.797 Mscf/d, respectively for Barnett shale formation. However, production forecast of 30 years, using the production history and its projection as base case, yields corresponding RMSE of 5.333 and 42.774 Mscf/d, respectively for Marcellus shale formation;0 and 34.4149 Mscf/d, respectively for Haynesville shale formation; and 0.6804 and 64.9808 Mscf/d, respectively for Barnett shale formation.

(9) This study is very valuable because reliable reserves estimation is an important component of effective production forecast, economic assessment, fiscal planning and decision-making in reservoir development.

5.2 RECOMMENDATIONS

Recommendations are made as follows:

(1) For further studies, other adsorption isotherms with limitations should be reviewed and improved versions of the models should be developed.

(2) For local content development, laboratory adsorption of methane on crushed Nigerian shale samples should be done to determine the natural gas adsorption capacities of Nigerian shale formations.

(3) Nigerian shale formations should be developed for natural gas production.

(4) Sequel to this, material balance analysis and production forecast should be carried out forNigerian shale formations based on their adsorption capacities and production history.

REFERENCES

Adamson, A.W. and Gast, A.P. 1997.*Physical Chemistry of Surfaces*.6th Ed. New York: Wiley-Interscience Publisher.

Aguilera, R. 2008. Effect of Fracture Compressibility on Gas-In-Place Calculations of Stress-Sensitive Naturally Fractured Reservoirs. SPE Paper 100451.

Aharoni, C. and Sparks, D.L. 1991. *Kinetics of Soil Chemical Reaction - A Theoretical Treatment*.Eds. D.L. Sparks & D.L. Suarez.Rate of Soil Chemical Processes. Soil Science Society of America. Madison, WI. 1-18.

Aharoni, C. and Ungarish, M. 1977. Kinetics of Activated Chemisorption. Part 2. Theoretical Models.*Journal of Chemical Society. Faraday Transactions.* 73: 456-464.

Ahmaruzzaman, M.D. 2008. Adsorption of Phenolic Compounds on Low-Cost Adsorbents: A Review.*Advanced Colloid and Interface Science*. 143.1-2: 48-67.

Ahmed, T.H. 1989.*Hydrocarbon Phase Behavior*.Houston TX: Gulf Publishing Co.

Ahmed, T.H. 1989.*Reservoir Engineering Handbook*.2nd Ed. Boston: Gulf Professional Publishing.

Ahmed, T. and McKinney, P.D.2005. *Advanced Reservoir Engineering*. Gulf Professional Publishing. Elsevier.

Altin, O., Ozbelge, H.O. and Dogu, T. 1998. Use of General Purpose Adsorption Isotherms for Heavy Metal-Clay Mineral Interactions.*Journal of Colloid and Interface Science*. 198: 130-140.

Angus, S., Armstrong, B. andde Reuck, K.M.1978.*International Thermodynamic Table of the Fluid State-5: Methane*.IUPAC Chemical Data Series No. 16.New York: Pergamon Press.

Angus, S., de Reuck, K.M. and Armstrong, B. 1979.*International Thermodynamic Table of the Fluid State-6: Nitrogen*. IUPAC Chemical Data Series No. 20.New York: Pergamon Press.

Aranovich, G.L. and Donohue, M.D. 1996. Adsorption of Supercritical Fluids.*Journal of Colloid and Interface Science*. 180.2: 537-541.

Aranovich, G.L. and Donohue, M.D. 1997. Prediction of Multilayer Adsorption using Lattice Theory.*Journal of Colloid and Interface Science*.180.1: 101-108.

Aranovich, G.L. and Donohue, M.D. 2001.Surface Compression in Adsorption Systems Physicochemical and Engineering Aspects.*Colloids and Surface*. 187-188. 95-108.

Arps, J.J. 1945. Analysis of Decline Curvesin Petroleum Development and Technology.*Transactions of the American Institute of Mining and Metallurgical Engineers (AIME).*160: 228-247.SPE-945228-G. New York.

Arri, L.E. and Yee, D. 1992. Modelling Coal-bed Methane Production with Binary Gas Sorption. SPE Paper 24363 presented at the *SPE Rocky Mountain Regional Meeting*. Casper, WY. USA.

Arumugam, A. 2004. High-Pressure Adsorption of Pure Coalbed Methane Gases on Dry Coals. M.S. Thesis. Oklahoma State University. Stillwater, Oklahoma. USA.

Avbovbo, A.A. and Ayoola, O. 1981.Petroleum Prospects of Southern Nigeria's Anambra Basin.*Oil and Gas Journal*. May 4, 1981. 334-342.

Bailey, A. 2008. Appalachia to the Rescue: Could Devonian Shales Deep Under the Appalachians Supply Trillions of Cubic Feet of Much Needed Natural Gas for the U.S.? *Petroleum News*. Retrieved 5 April, 2008.

Beggs, H.D and Brills, J.P. 1974. Two-Phase Flow in Pipes. University of Tulsa, Tulsa, OK. USA.

Bergen, F., van Pagnier, H.J.M., David, P. and Kross, B.M. 2000.*Inventory of the Potential for Enhanced Coalbed Methane Production with Carbon Dioxide Disposal*. TNO. Utrecht. The Netherlands.

Blasingame, T.A. 1988. Review Materials: Properties of Reservoir Fluids. Texas A&M University,

Boulis, A., Jayakumar, R., Lalehrokh, F. and Lawal, H. 2012. Improved Methodologies for More Accurate Shale Gas Assessment. Paper SPE 154981.*Americas Unconventional Resources Conference*. Pittsburgh, PA. USA.

Bowker, K.A. April 2007. Barnett Shale Gas Production, Fort Worth Basin: Issues and Discussion.*AAPG Bulletin*. 91.4: 523-533.

Browning, J., Ikonnikova, S., Male, F., Gulen, G., Smye, K., Horvath, S., Grote, C., Patzeck, T., Potter, E. and Tinker, S.W. 2015. Study Forecasts Gradual Haynesville Production Recovery before Final Decline.*Oil and Gas Journal.* Dec 2015 Issue.

Brunauer, S., Emmett, P.H. and Teller, E. 1938.*Journal of American Chemical Society*. 6: 309.

Bullin, K. and Krouskop, P. 2008.Composition Variety Complicates Processing Plans for US Shale Gas. *Annual Forum of Gas Processors Association*. Houston, Texas. USA. Oct. 7, 2008.

Bumb, A.C. and McKee, C.R. 1986. Gas-Well Testing in the Presence of Desorption for Coalbed Methane and Devonian Shales. Paper SPE 15227 presented at *SPE Unconventional Gas Technology Symposium*. Louisville, Kentucky. May 18-21.

Bureau of Economic Geology, 2016.*Annual Report 2016*. University of Texas at Austin.

Busch, A., Alles, S., Genterblum, Y., Prinz, D., Dewhurst, D.N, Raven, M.D., Stanjek, H. and Kross, B.M. 2008. Carbon Dioxide Storage Potential of Shales.*International Journal of Greenhouse Control*. 2.3: 297-308.

Bustin, R.M., Bustin, A.M.M., Cui, A., Ross, D. and Pathi, V.M. 2008. Impact of Shale Properties on Pore Structure and Storage Characteristics. *SPE Shale Gas Production Conference*.

Catuneanua, O., Wopfnerb,H., Erikssonc,P.G., Cairncrossd, B., Rubidgee,B.S., Smith,R.M.H. and Hancox,P.J. 2005. The Karoo Basins of South-Central Africa.*Journal of African Earth Sciences*. 43.1-3: 211-253.

Chen, J.H., Wong, D.S.H., Tan, C.S., Subramanian, R., Lira, C.T. and Orth, M. 1997. Adsorption and Desorption of Carbon Dioxide onto and from Activated Carbon at High Pressures.*Ind. Eng. Chem. Res*. 36.7: 2808-2815.

Chen, J.S. 2007. Simplified Local-Density Modeling of Pure and Multi-Components Gas Adsorption on Dry and Wet Coals. MSc Thesis. Oklahoma State University. Stillwater, Oklahoma. USA.

Chesapeake Energy Corporation. 2010.*CHK Play Comparison*.

Civan, A.F., Devegowda, D. and Sigal, R. 2010. Accurate Simulation of Shale Gas Reservoir. Paper SPE 135564 presented at *Annual Technical Conference and Exhibition*. Florence. Italy. 19-22 September 2010.

Clarkson, C.R., Bustin, R.M. and Levy, J.H. 1997. Application of the Mono/Multilayer and Adsorption Potential Theories to Coal Methane Adsorption Isotherms at Elevated Temperature and Pressure.*Carbon*. 35.12: 1689-1705.

Clarkson, C.R. and Bustin, R.M. 2000. Binary Gas Adsorption/Desorption Isotherms: Effect of Moisture and Coal Composition upon Carbon Dioxide Selectivity over Methane.*International Journal of Coal Geology*. 42.4: 241-271.

Crain, E.R. 2011.Unicorns in the Garden of Good and Evil: Part 4- Shale Gas.Retrieved from: www.spec2000.net/00-publications. Accessed on October 7, 2012.

Dabrowski, A. 2001. Adsorption - from Theory to Practice.*Advances in Colloid Interface Science*. 93: 135-224.

Day, S., Duffy, G., Sakurovs, R. and Weir, S. 2008. Effect of Coal Properties on CO_2 Sorption Capacity under Supercritical Conditions.*International Journal of Greenhouse Gas Control*. 2.3: 342-352.

de Boer, J.H. 1953.*The Dynamical Character of Adsorption*.London: Oxford University Press.

DeGance, A.E. 1992. Multicomponent High-Pressure Adsorption Equilibria on Carbon Substrates: Theory and Data. *Fluid Phase Equilibria*. 78: 99.

Dhima, A., de Hemptinne, J. and Jose, J. 1999. Solubility of Hydrocarbons and CO_2 Mixtures in Water under High Pressure.*Ind. & Eng. Chem. Res*. 38.8: 3144-3161.

Dranchuk, P.M., Purvis, R.A. and Robinson, D.B. 1974. Computer Calculation of Natural Gas Compressibility Factors using the Standing and Katz Correlation. *Institute of Petroleum Technical Series*.IP 74-008.

Dranchuk, P.M. and Abou-Kassem, J.H. 1975. Calculation of Z-Factors for Natural Gases using Equations of State.*Journalof Canadian Petroleum Technology*. July-September 1975. 14.3: 34.

Duarte, J.C., Vinas, E.C. and Ciancaglini, M. 2014. Material Balance Analysis of Naturally or Artificially Fractured Shale Gas Reservoirs to Maximize Final Recovery. SPE Paper 169480-MS presented at the *SPE Latin American and Caribbean Petroleum Engineering Conference*. Maracaibo. Venezuela. May 21-23.

Dubinin, M.M. 1960. The Potential Theory of Adsorption of Gases and Vapours for Adsorbent with Energetically Non-Uniform Surface.*Chem. Rev*. 60: 235-266.

Dubinin, M.M. 1966.*Chemistry and Physics of Carbon*.Ed. Walker P.L. New York: Marcel Dekker Inc. 2: 51-120.

Dubinin, M.M. and Astakhov, V.A. 1971. Description of Adsorption Equilibria of Vapours on Zeolites over Wide Range of Temperature and Pressure.*Advances in Chemistry Series*. 102: 69-85.

Dubinin, M.M. and Radushkevich, L.V. 1977. The Equation of the Characteristic Curve of the Activated Charcoal.*Proc. Acad. Sci. USSR Phys. Chem. Sect*. 55: 331-337.

Ehinola, O.A and Sonibare, O.O. 2005. Hydrocarbon Potential and Thermal Maturity of Nkporo from Lower Benue Trough, Nigeria.*Journal of Applied Sciences*. 5: 689-695.

Elovich, S.Y. and Larinov, O.G. 1962. Theory of Adsorption from Solution of Non-Electrolytes on Solid: (I) Equation Adsorption from Solutions and the Analysis of Its Simplest Form and (II) Verification of the Equation of Adsorption Isotherm from Solutions.*Izv. Akad. Nauk. SSSR, Otd. Khim. Nauk*. 2: 209-216.

Elsharkawy, A.M., Hashem, Y.K. and Alikhan, A.A. 2000. Compressibility Factor for Gas Condensate Reservoirs. Paper SPE 59702.

Elsharkawy, A.M. and Elkamel, A. 2001. The Accuracy of Predicting Compressibility Factor for Sour Natural Gases.*Petroleum Science and Technology*. 19.5-6: 711-731.

Engelder, T. 2009. Marcellus Technically Recoverable Reserves. Marcellus Center for Outreach and Research. Pennsylvania State University. University Park, PA 16802-6813. USA.

Ertekin, T., King, G.A. and Schwerer, F.C. 1986. Dynamic Gas Slippage: A Unique Dual-Mechanism Approach to the Flow of Gas in Tight Formations. SPE-12045-PA.*SPE Formation Evaluation*. Feb. 1986.

Fathi, E., Tinni, A. and Akkutlu, I.Y. 2012.Corretion to Klinkenberg Slippage Theory for Gas Flow in Nano-Capillaries.*International Journal of Coal Geology*.10.3: 51-59.

Fathi, E. and Akkutlu, I.Y. 2013. Lattice Boltzmann Method for Simulation of Natural Gas in Kerogen.*SPE Journal*. 18.1.

Feast, G., Wu, K., Walton, J., Cheng, Z. and Chen, B.2015. Modeling and Simulation of Natural Gas Production from Unconventional Shale Reservoirs.*International Journal of Clean Coal and Energy*. 4: 23-32.

Fitzgerald, J.E., Sudibandriyo, M., Pan, Z., Robinson, R.L. and Gasem, K.A.M. 2004. Modeling the Adsorption of Pure Gases on Coals with SLD Model.*Carbon*. 41.12: 2203-2216.

Fitzgerald, J.E. 2005. Adsorption of Pure and Multi-Component Gases of Importance to Enhanced Coalbed Methane Recovery: Measurement and Simplified Local-Density Modeling. Ph.D Dissertation. Oklahoma State University. Stillwater, Oklahoma. USA.

Fitzgerald, J.E., Pan, Z., Sudibandriyo, M., Robinson, R.L. Jr., Gasem, K.A.M. and Reeves, S. 2005. Adsorption of Methane, Nitrogen, Carbon Dioxide and their Mixtures on Wet Tiffany Coal.*Fuel*. 84.18: 2351-2363.

Fowler, R.H. and Guggenheim, E.A. 1939. Statistical Thermodynamics.London: Cambridge University Press. 431-450.

Freundlich, H.M.F.1906. Adsorption in Solution.*J. Phys. Chem*. 57: 385-471.

Gasem, K.A.M.,Robinson, R.L. Jr. and Reeves, S.R. 2002. Adsorption of Pure Methane, Nitrogen and Carbon Dioxide and their Mixtures on San Juan Basin Coal. DE-FC26-00NT40924 Paper prepared for the U.S. Department of Energy.

Gasem, K.A.M., Robinson, R.L. Jr., Fitzgerald, J.E., Pan, Z. and Sudibandriyo, M. 2003. Sequestering Carbon Dioxide in Coalbeds. DE-FC26-98FT40426 Paper prepared for the U.S. Department of Energy.

Gasem, K.A.M., Robinson, R.L. Jr., Mohammad, S.A., Chen, J.S. and Fitzgerald, J.E. 2008. Improved Adsorption Models for Coalbeds Methane Production and CO_2 Sequestration. Final Technical Report for 2005-2007 prepared for Advanced Resources International.

Gasem, K.A.M., Mohammad, S.A. and Robinson, R.L. Jr. 2009. Modeling Coalbed Methane Adsorption and CO_2 Sequestration.*Encyclopaedia of Chemical Processing*. DOI:10.1081/E-ECHP-120043857.

Geoscience News and Information. 2016. www.geology.com

Ghiaci,M., Abbaspur, A., Kia, R. and Seyedeyn-Azad, F. 2004. Equilibrium Isotherm Studies for the Sorption of Benzene, Toluene and Phenol onto Organo-zeolites and As-synthesized MCM -41.*Sep. Purif. Technol.* 40: 217-229.

Gregg,S.J. and Sing, K.S.W. 1982.*Adsorption, Surface Area and Porosity*.London:Academic Press Inc. UK.

Gunay,A., Arslankaya, E. and Tosun, I. 2007. Lead Removal from Aqueous Solution by Natural and Preheated Clinoptilolite: Adsorption Equilibrium and Kinetics.*Journal ofHazardous Materials.* 146: 362-371.

Guo, B. and Ghalambor, A. 2005.*Natural Gas Engineering Handbook*.Houston, TX:Gulf Publishing Company. USA.

Haghseresht, F. and Lu, G. 1998. Adsorption Characteristics of Phelonic Compounds onto Coal-Reject-Derived Adsorbents.*Energy Fuels*. 12: 1100-1107.

Hall, F.E. 1993. Adsorption of Pure and Multicomponent Gases on Wet Fruitland Coal. M.S Thesis. Oklahoma State University. Stillwater, Oklahoma. USA.

Hall, F., Zhou, C., Gasem, K.A.M. and Robinson R.L. Jr. 1994. Adsorption of Pure Methane, Nitrogen and Carbon Dioxide, and their Binary Mixtures on Wet Fruitland Coal. SPE Paper 29194 presented at the *SPE Eastern Conference & Exhibition, Charleston,* South Carolina. USA.

Hall, K.R. and Yarbrough, L. June 1973. A New Equation of State for Z-Factor Calculations.*Oil and Gas*. 82.

Halsey, G.D. 1952. The Role of Surface Heterogeneity.*Adv. Cata.*4: 259-269.

Harkins, W.D. and Jura, G.J. 1943. *Chem. Phys*.11: 430.

Harpalani, S., Prusty, B.K. and Dutta P. 2006. Methane/CO_2 Sorption Modeling for Coalbed Methane Production and CO_2 Sequestration.*Energy Fuels.*20.4: 1591-1599.

Harper, J.A., Laughrey, C.D., Kostelnik, J., Gold, D.P. and Doden, A.G. 2004. Trenton and Black River Carbonates in the Union Furnace Area of Blair and Huntingdon Counties, Pennsylvania: Introduction. Field Trip Guidebook for the Eastern Section AAPG Annual Meeting. September 10, 2003 and PAPG Spring Field Trip. May 26, 2004. *Pennsylvania Geological Survey*. (Retrieved 14 June, 2008).

Heller, R.J. and Zoback, M.D. 2011. Adsorption, Swelling and Viscous Creep of Synthetic Clay Samples.45th US Rock Mechanics/Geomechanics Symposium. San Francisco, CA. USA.

Heller, R. and Zoback, M. 2014. Adsorption of Methane and Carbon Dioxide on Gas Shale and Pure Mineral Samples.*Journal of Unconventional Oil and Gas Resources*.8: 14-24.

Henderson, D. 1992.*Fundamentals of Inhomogeneous Fluids*.New York: Marcel Dekker Inc.

Hill, R.J., Jarvie, D.M., Zumberge, J., Henry, M. and Pollastro, R.M. 2007.Oil and Gas Geochemistry and Petroleum Systems of the Fort WorthBasin.*AAPG Bulletin*. 91.4: 445-473.

Hill, T.L. 1946. Theory of Multimolecular Adsorption from a Mixture of Gases.*J. Chem. Phys.*14: 268.

Ho, Y.S., Porter, J.F. and McKay, G. 2002. Equilibrium Isotherm Studies for the Sorption of Divalent Metal Ions onto Peat, Copper, Nickel and Lead Single Component Systems.*Water Air and Soil Pollution*. 141: 1-33.

Hocker, T., Aranovch, G.L. and Donohue, M.D. 1999. Monolayer Adsorption for the Subcritical Lattice Gas and Partially Miscible Binary Mixtures.*Journal of Colloid and Interface Science.*211.1: 61-80

Honig, J.M. and Mueller, C.R. 1962, Adaptation of Lattice Vacancy Theory to Gas Adsorption Phenomena. *J. Phys. Chem*. 66: 1305–1308.

Hoory, S.E. and Prausnitz, J.M. 1967. Monolayer Adsorption of Gas Mixtures on Homogeneous and Heterogeneous Solids.*Chemical Engineering Science.*22.7: 1025-1033.

Horsfall, M. and Spiff, A.I. 2005. Equilibrium Sorption Study of Al^{3+}, CO^{2+} and Ag^{2+} in Aqueous Solutions by Fluted Pumpkin (*Telfairia occidentalis hook*) Waste Biomass. *Acta Chim. Slov.* 52: 174-181.

House of Common Library. 2010. Key Issues for the New Parliament.

Idowu, J.O. and Ekweozor, C. M. 1993. Petroleum Potential of Cretaceous Shales in the Upper Benue Trough.*Nigeria. Journal of Petroleum Geology*. 16.3: 249-264.

Ikewun, P. and Ahmadi, M. 2012. Production Optimization and Forecasting of Shale Gas Wells using Simulation Models and Decline Curve Analysis. Paper SPE 153914 presented at the *SPE Western Regional Meeting*. Bakersfield, CA. USA. March 19-23.

Ikoku, C.U. 1992.*Natural Gas Production Engineering*.Malabar, Florida: Krieger Publishing Company. USA.

Institute for Energy Research. 2012. Haynesville Shale Fact Sheet.

Institute for Energy Research. 2017.www.instituteforenergyresearch.org

INTEK. 2009. Shale Report.

International Union of Pure and Applied Chemistry (IUPAC). 1985.

Jenkins, C.D., MacNaughton, DeGolyer and Boyer C.M. 2008.Coalbed-and Shale-Gas Reservoirs.*Journal of Petroleum Technology.*92.

Jones, S. C. 1972. A Rapid Accurate Unsteady-State Klinkenberg Parameter.*SPE Journal*. 383–397.

Jones, F.O. and Owens, W.W. 1980. A Laboratory Study of Low Permeability Gas Sands.*Journal of Petroleum Technology.*32.9: 1631-1640.

Jossens, L., Prausnitz, J.M., Fritz, W., Schlunder, E.U. and Myers, A.L. 1978. Thermodynamics of Multi-Solute Adsorption from Dilute Aqueous Solutions.*Chem. Eng. Sci.* 33: 1097-1107.

Kaiser, M.J. and Yu, Y. 2011. Louisiana Haynesville Shale-1: Characteristics, Production Potential of Haynesville Shale Wells Described. Louisiana State University Baton Rouge. USA.

Kang, S.M., Fathi, E., Ambrose, R.J., Akkutlu, I.Y. and Sigal, R.F. 2010. Carbon Dioxide Storage Capacity of Organic-Rich Shales. SPE Paper 134583. 1-17.

Keller, J. and Staudt, R. 2005.*Gas Adsorption Equilibria: Experimental Method and Adsorption Isotherm*.Boston: Springer Science and Business Media, Inc.USA.

Kim, Y., Kim, C., Choi, I., Rengraj, S. and Yi, J. 2004. Arsenic Removal using Mesoporous Alumina prepared via a Templating Method.*Environ. Sci. Technol.* 38: 924-931.

King, A.D. Jr. and Coan, C.R. 1971. Solubility of Water in Compressed Carbon Dioxide, Nitrous Oxide and Ethane - Evidence for Hydration of Carbon Dioxide and Nitrous Oxide in the Gas Phase.*Journal of American Chemical Society.*93.8: 1857-1862.

King, G.R. 1990. Material Balance Techniques for Coal Seam and Devonian Shale Gas Reservoirs. SPE Paper 20730 presented at the *65th Annual Technical Conference and Exhibition*. New Orleans, Louisiana. USA. September 23-26.

Kiselev, A.V. 1958. Vapor Adsorption in the Formation of Adsorbate Molecule Complexes on the Surface.*Kolloid Zhur.*20: 338-348.

Klinkenberg, L. J. 1941.The Permeability of Porous Media to Liquids and Gases. American PetroleumInstitute.*Drilling and Productions Practices*. 200–213.

Koble, R.A. and Corrigan, T.E. 1952. Adsorption Isotherms for Pure Hydrocarbon.*Ind. Eng. Chem.* 44: 383-387.

Koretsky, M.D. 2004.*Engineering and Chemical Thermodynamics*.New Jersey: John Wiley and SonsInc. 177-180.

Kumar, K.V. and Sivanesan, S. 2007. Sorption Isotherm for Safranin onto Rice Husk: Comparison of Linear and Non-Linear Methods. *Dyes Pigments.* 72: 130-133.

Lako, P.2002. Option for CO_2 Sequestration and Enhanced Fuel Supply. Monograph in the Framework of the VLEEM Project ECN-C-01-113.

Lancaster, D.E., Holditch, S.A. and Hill, D.G. 1993.A Multi-Laboratory Comparison of Isotherm Measurements on Antrim Shale Samples.SCA Conference Paper Number 9303. Otsego County, Michigan. USA.

Langmuir, I. 1916. The Constitution and Fundamental Properties of Solids and Liquids.*Journal of American Chemical Society.*38.11: 2221-2295.

Langmuir, I. 1918. The Adsorption of Gases on Plane Surfaces of Glass, Mica and Platinum.*Journal of American Chemical Society.* 40.9: 1361-1403.

Lee, L.L. 1988.*Molecular Thermodynamics of Non-Ideal Fluids*.Stoneham, MA: Butterworth Inc. USA.

Lee, D.S. 2010. A Critical Evaluation of Unconventional Gas Recovery from the Marcellus Shale, Northeastern United States.Presented at the *44th US Rock Mechanics Symposium and 5th US-Canada Rock Mechanics Symposium* held in Salt Lake, UT. June 27-30, 2010.

Loucks, R.G., Reed, R.M., Ruppel, S.C. and Jarvie, D.M. 2009. Morphology, Genesis, and Distribution of Nanometer-Scale Pores in Siliceous Mudstones of the Mississippi Barnet Shale.*J. Sediment. Res*. 79.12: 848-861.

Male, F., Islam, A.W., Patzek, T.W., Ikonnikova, S., Browning, J. and Marder, M.P. 2015. Analysis of Gas Production from Hydraulically Fractured Wells in the Haynesville Shale using Scaling Methods.*Journal of Unconventional Oil and Gas Resources.* 10: 11-17.

Manik, J. 2002. Development and Validation of Compositional Coalbed Simulator.*Journal of Canadian Petroleum Technology*. 41.4: 39-45.

Markham, E.D. and Benton, A.F. 1931. The Adsorption of Gas Mixtures by Silica.*Journal of American Chemical Society.* 53: 497.

Mattot, I.S. 2007.*Isofit Documentation and User's Guide Version 1.2*. State University of New York at Buffalo. USA.

McCarty, R.D. 1972. Thermophysical Properties of Helium-4 from 2 to 1500K with Pressure to 100 Atmospheres.*National Bureau of Standards Technical Note 631.* U.S. Department of Commerce.

Mengal, S.A. 2010. Accounting for Adsorbed Gas and Its Effects on Production Behavior of Shale Gas Reservoirs. M.Sc Thesis. Texas A&M University.

Mengal, S.A. and Watterbanger,R.A. 2011. Accounting for Adsorbed Gas in Shale Gas Reservoirs", SPE Paper 141085 presented at the *SPE Middle East Oil and Gas Show and Conference*. Manama. Bahrain. September 25-28.

Merey, S. 2013. Experimental Analysis of Adsorption Capacities and Behaviours of Shale Samples. M.Sc Thesis. Middle East Technical University, Turkey.

Merey, S. and Sinayuc, C. 2015. Analysis of Carbon Dioxide Sequestration in Shale Gas Reservoirs by Using Experimental Adsorption Data and Adsorption Models. Paper presented at the *56th Canadian Chemical Engineering Conference*. Calgary, Alberta. Canada. October 4-7.

Moghadam, S., Jeje, O. and Mattar, L. 2009. Advanced Gas Material Balance in Simplified Format. Paper PETSOC 2009-149 presented at the *10th Canadian International Petroleum Conference (CICP)*. Calgary, Alberta. Canada. June 16-18.

Mohammad, S.A. 2009. Adsorption Modeling of Coalbed Gases and the Effects of Water on Their Adsorption Behavior. Ph.D Thesis. Faculty of the Graduate College. Oklahoma State University. Oklahoma. USA.

Mohammad, S.A., Chen, J.S.,RobinsonR.L. Jr., and Gasem,K.A.M. 2009. Generalized Simplified Local-Density/Peng-Robinson Model for Adsorption of Pure and Mixed Gases on Coals.Energy and Fuels. 23.12: 6259.

Moore, W.J. 1972.*Physical Chemistry.*Prentice-Hall, Inc.

Myers, A.L. and Prausnitz, J.M. 1965. Thermodynamics of Mixed-Gas Adsorption.*AIChE Journal*. 11.1: 121-127.

Myers, R. 2008. Marcellus Shale Update. Independent Oil and Gas Association of West Virginia.

National Energy Technology Laboratory (NETL) of the US Department of Energy. 2013. Modern Shale Gas Development in the United States: An Update. September, 2013.

New Scientist. 2012. Frack Responsibly and Risks - and Quakes - are Small. January 2012.

Nitta, T., Shigetomi, T., Kuro-Oka, M. and Katayam, T. 1984. An Adsorption Isotherm of Multi-Site Occupancy Model for Homogeneous Surface.*Journal of Chemical Engineering of Japan*. 17.1: 39-45.

Nobakht, M., Clarkson, C.R. and Kaviani, D. 2012. New and Improved Methods for Performing Rate-Transient Analysis of Shale Gas Reservoirs. *SPE Reservoir Evaluation and Engineering*.15.3: 335-350.

Nuttall, B.C., Eble, C.F., Drahovzal, J.A. and Bustin, R.M. 2005. Analysis of Devonian Black Shales in Kentucky for Potential Carbon Sequestration and Enhanced Natural Gas Production. Final Report - Kentucky Geological Survey. University of Kentucky.DE-FC26-02NT41442. www.uky.edu/KGS/emsweb/devsh/final_report.pdf.

Obaje, N.G. and Abaa, S.I. 1996. Potential for Coal-Derived Gaseous Hydrocarbons in the Middle Benue Trough of Nigeria.*Journal of Petroleum Geology.* 19.1: 77-94.

Obaje, N.G., Wehner, H.and Scheeder, G. 2004. Hydrocarbon Prospectivity of Nigeria's Inland Basins: From the Viewpoint of Organic Geochemistry and Organic Petrology.*AAPG Bulletin*. 88.3: 325-353.

Oil and Gas Journal. Digital Magazine. 2016.

Oluwajana, O.A. and Ehinola, O.A. 2018.Potential Shale Resource Plays in South-Eastern Nigeria: Petroleum System Modelling and Microfabric Perspectives. *Journal of African Earth Sciences*. 138: 247-257.

Ono, S. and Kondo, S. 1960.*Molecular Theory of Surface Tension*.Berlin, Germany: Springer Publishers.

Pan, Z. 2004. Modeling of Gas Adsorption using Two-Dimensional Equations of State. Ph.D Dissertation. Oklahoma State University. Stillwater, Oklahoma. USA.

Perez-Marin, A.B., Zapata, V.M., Ortuno, J.F., Aguilar, M.,Saez, J., and Llorens, M. 2007. Removal of Cadmium from Aqueous Solutions by Adsorption onto Orange Waste.*Journal of Hazardous Materials.* B139: 122-131.

Piper, L.D. Jr., McCain, W.D. Jr. and Corredor, J.H. 1993. Compressibility Factors for Naturally Occurring Petroleum Gases. Paper SPE 26668.

Polanyi, M. 1932. Theories of Adsorption of Gases: A General Survey and Some Additional Remarks.*Transactions of Faraday Society.* 28: 316.

Potential Gas Committee. 2013. Potential Supply of Natural Gas in the United States. http://potentialgas.org/press-release

Promote UK. 2011.

Rangarajan, B., Lira, C.T. and Subramanian, R. 1995. Simplified Local Density Model for Adsorption over Large Pressure Ranges.*AIChE Journal.* 41.4: 838-845.

Redlich, O. and Peterson, D.L. 1959. A Useful Adsorption Isotherm.*J. Phys. Chem*. 63: 1024-1026.

Reid, R.C., Prausnitz, J.M. and Poling, B.E. 1987.*The Properties of Gases and Liquids*. New York: McGraw-Hill Inc. USA.

Rice, D.D. 1997. Coalbed Methane - An Untapped Energy Resources and an Environmental Concern.*U.S. Geological Survey Fact Sheet.* FS-019-97.

Ross, D.J. and Bustin, R.M. 2008. The Importance of Shale Composition and Pore Structure upon Gas Storage Potential of Shale Gas Reservoirs.*Marine and Petroleum. Geology.* 26.6: 916-927.

Saulsberry, J.L., Schafer, P.S. and Schraufnagel, R.A. 1996.A Guide to Coalbed MethaneReservoir Engineering. Gas Research Institute Report GRI-94/0397. Chicago,Illinois.

Schilthuis, R. 1936. Active Oil and Reservoir Energy.*Trans. AIME*. 118: 33.

Seidle, J.P. 1991. Long-Term Gas Deliverabiliy of a Dewatered Coalbed. SPE Paper 21488 presented at the *SPE Gas Technology Symposium*. Houston, Texas. USA. January 23-25.

Shi, J.Q. and Durucan, S. 2010. Exponential Growth in San Juan Basin Fruitland Coalbed Permeability with Reservoir Drawdown: Model Match and Insights.*SPE Reservoir Evaluation and Engineering.* 914-925.

Silin, D. and Knaefsey, T. 2011. Gas-Shale: from Nanometer-Scale to Well Modeling. CSUG/SPE Paper 149489 presented at the *Canadian Unconventional Resources Conference*. Calgary, Alberta. Canada. November 15-17.

Sips, R. 1948. Combined Form of Langmuir and Freundlich Equations.*J. Chem. Phys.* 16: 490-495.

Soeder, D.J. 2011. Petrophysical Characterization of the Marcellus and other Gas Shales.*AAPG Eastern Section Meeting*.

Soeder, D.J. 2011. Resource and Environmental Studies on the Marcellus Shale.*Savage River Watershed Association Meeting*. Frostburg, MD. National Energy Technology Laboratory. US Dept. of Energy.6 January.

Sondergeld, C.H., Ambrose, R.J., Rai, C.S. and Moncrieff, J. 2010. Micro-Structural Studies of Gas Shales.*SPE Unconventional Gas Conference*.

Song, B., Economides, M.J. and Economides, C.J. 2011. Design of Multiple Fracture Horizontal Wells in Shale Gas Reservoirs. SPE Paper 140555 presented at *SPE Hydraulic Fracturing Technology Conference and Exhibition*. The Woodlands, Texas. USA.

Soule, A.D. 1998. Studies of Gas Adsorption on Activated Carbon and Cherry Flavor Recovery from Cherry Pits. M.S Thesis. Michigan State University. East Lansing, Michigan. USA.

Soule, A.D., Smith, C.A., Yang, X. and Lira, C.T. 2001. Adsorption Modeling with the ESD Equation of State.*Langmuir.* 17.10: 2950-2957.

Span, R. and Wagner, W. 1996. A New Equation of State for Carbon Dioxide Covering the Fluid Region from the Triple-Point Temperature 1100K at Pressure up to 800MPa.*Journal of Phys. Chem. Ref. Data*. 25: 1509-1590.

SPE Formation Evaluation. March, 1998.

Standing, M.B. and Katz, D.L. 1942. Density of Natural Gases.*Trans. AIME* 146: 140-149.

Standing, M.B. 1981.*Volumetric and Phase Behaviour of Oil Field Hydrocarbon Systems*. 9th Edition. Society of Petroleum Engineers of AIME. Dallas, TX. USA.

State Impact. 2017. The Marcellus Shale Explained. Pennsylvania.

Stevens, S.H., Spector, D. and Riemer, P. 1998. Enhanced Coalbed Methane Recovery using CO_2 Injection: Worldwide Resources and CO_2 Sequestration Potential. *SPE International Conference*. Beijing. China. November 1998.

Stevenson, M.D., Pinczewski, W.V., Somers, M.L. and Bagio, S.E. 1991. Adsorption/Desorption of Multicomponent Gas Mixtures at In-Seam Conditions. SPE Paper 23026 presented at the *SPE Asia-Pacific Conference*. Perth. Australia.

Subramanan, R., Pyada, H. and Lira, C.T. 1995. Engineering Model for Adsorption of Gases onto Flat Surfaces and Clustering in Supercritical Fluids.*Ind. Eng. Chem. Res.* 34.11: 3830.

Sudibandriyo, M. 2003. Generalized Ono-Kondo Lattice Model for High Pressure Adsorption on Carbon Adsorbents. Ph.D Thesis. Oklahoma State University. Stillwater, Oklahoma. USA.

Sudibandriyo, M., Pan, Z. Fitzgerald, J.E., Robinson, R.L. and Gasem, K.A.M. 2003. Adsorption of Methane, Nitrogen, Carbon Dioxide and their Binary Mixtures on Dry Activated Carbon at 318.2K and Pressure up to 13.6MPa.*Langmuir.*19.13: 5323-5331.

Sudibandriyo, M.,Mohammad, S.A., Robinson, R.L.J. and Gasem, K.A.M. 2010. Ono-Kondo Lattice Model for High-Pressure Adsorption: Pure Gases.*Fluid Phase Equilibria*. 229: 238-251.

Sudibandriyo, M.,Mohammad, S.A., Robinson, R.L.Jr. and Gasem, K.A.M. 2011. Ono-Kondo Lattice Model for High-Pressure Mixed-Gas Adsorption on Activated Carbons and Coals.*Energy and Fuels*. 25: 3355-3367.

Sutton, R.P. 1985. Compressibility Factors for High Molecular Weight Reservoir Gases. Paper SPE 14265 presented at *60th Annual Technical Conference and Exhibition of the SPE*. Las Vegas. USA. September 22-25.

Takacs, G.1976. Comparisons Made for Computer Z-Factor Calculations.*Oil and Gas Journal.* 64-66.

Temkin, M.I. and Pyzhev, V. 1940. Kinetics of Ammonia Synthesis on Promoted Iron Catalyst/*Acta Phys. Chem. USSR.* 12: 327-356.

Toth, J. 1971. State Equations of the Solid Gas Interface Layer.*Acta Chem Acad. Hung*. 69: 311-317.

UNEP. 2006. Africa Environmental Outlook 2: Our Environment Our Wealth. UNEP Job No. DEW/0801/NA. United Nations Environment Programme. 48-74.

United States Geological Survey. August 2011.

U.S. Department of Energy, Office of Fossil Energy and National Energy Technology Laboratory. 2009. Modern Shale Gas Development in the United States: A Primer. DE-FG26-04NT15455.

U.S. Energy Information Administration. April 2010.

U.S. Energy Information Administration. June 2012. Annual Energy Outlook.

U.S. Energy Information Administration. June 2013. Annual Energy Outlook.

U.S. Energy Information Administration. 2015.Technically Recoverable Shale Oil and Shale Gas Resources: An Assessment of 137 Shale Formations in41 Countries Outside the United States. 6.http://www.eia.gov/analysis/studies/worldshalegas/

U.S. Energy Information Administration. 2016. Annual Energy Outlook.

Ustinov, E.A., Do, D.D., Herbst, A., Staudt, R. and Harting, P. 2002. Modelling of Gas Adsorption Equilibrium over a Wide Range of Pressure: A Thermodynamic Approach Based on Equation of State.*Journal of Colloid Interface Science*. 250.1: 49-62.

Valenzuela, D.P., Myers, A.L., Talu, O. and Zwiebel, I. 1998. Adsorption of Gas Mixtures Effect of Energetic Heterogeneity.*AIChem J*. 34: 397-402.

van der Waals, J.D. 1873. On the Continuity of the Gaseous and Liquid States. Doctoral Dissertation. Universiteit Leiden.

Vijarayaghavan, K., Padmesh, T.V.N., Palanivelu, K.and Velan, M. 2006. Biosorption of Nickel (II) Ions onto Sargassum Wightii: Application of Two-Parameter and Three-Parameter Isotherm Models.*Journal of Hazardous Materials.* B133: 304-308.

Volmer, M.Z. 1925.*Phys. Chem*. 115: 253.

Wang, F.P. and Reed, R.M. 2009. Pore Network and Fluid Flow in Gas Shales.*SPE Annual Technical Conference and Exhibition*.

Wang, S., Elsworth, D. and Liu, J. 2012.A Mechanistic Model for Permeability Evolution in Fractured Reservoirs.*Journal of Geophysical Research.* 117.B06205.

Warren, J.E. and Root, P.J. 1963. The Behavior of Naturally Fractured Reservoirs.*SPE Journal.* 245-255.

Weibe, R. and Gaddy, V. 1940. The Solubility of Carbon Dioxide in Water at Various Temperatures from 12 ^{o} to 40 ^{o}C and at Pressures to 500 Atmospheres Critical Phenomena.*Journal of American Chemical Society.* 62: 815-817

Wickens, D.V. and Cole, D.2018. Shale Gas Potential of the Permian Karoo Basin: Stratigraphy and Sedimentology of the Lower Ecca, Burial Metamorphism and Dolerite Intrusion.*AAPG International Conference and Exhibition (ICE)*. Cape Town. South Africa. Monday, 29 October-Thursday, 1 November 2018.

Wihert, E. and Aziz, K. 1972. Calculation of Z's for Sour Gases.*Hydrocarbon Processing*. 51:5.

Wood, G.O. 2001. Affinity Coefficients of the Polanyi/Dubinin Adsorption Isotherm Equations-A Review with Compilations and Correlations.*Carbon.* 39: 343-356.

Wong, Y.C., Szeto, Y.S., Cheung, W.H. and McKay, G. 2004. Adsorption of Acid Dyes on Chitosan-Equilibrium Isotherm Analyses.*Process Biochem*. 39: 693-702.

Wu, Y.S., Li, J., Ding, D.Y., Wang, C. and Di, Y. 2013. A Generalized Framework Model for Simulation of Gas Production in Unconventional Gas Reservoirs. SPE Paper 163609 presented at the *SPE Reservoir Simulation Symposium*. The Woodlands, Texas. USA. February 18-20.

Yang, R.T. 1987.*Gas Separation by Adsorption Processes*.Boston: Butterworth Publishing Inc. USA.

Yu, W. and Sepehrnoori, K. 2013. Simulation of Gas Desorption and Geomechanic Effects for Unconventional Gas Reservoirs. SPE Paper 165377 presented at the *SPE Western Region and AAPG Pacific Section Meeting/Joint Technical Conference*. Monterey, California. USA. April 19-25.

Yu, W. and Sepehrmoon, K. 2014. Simulation of Gas Desorption and Geomechanic Effects for Unconventional Gas Reservoirs.*Fuel*. 116: 455-464.

Zeldowitsch, J. 1934. Adsorption Site Energy Distribution.*Acta Phys. Chem. USSR.* 1: 961-973.

Zhong, H. 2011. Flow of Gas and Water in Hydraulically Fractured Shale Gas Reservoirs.*EPA HF Workshop*. Arlington, Virginia. USA. March 28-29.

Zhou, C., Hall, F., Gasem, K.A.M. and Robinson, R.L. Jr. 1994. Predicting Gas Adsorption using Two-Dimensional Equations of State.*Ind. Eng. Chem. Res.* 33.5: 1280-1289.

Zhou, C., Hall, F., Gasem, K.A.M. and Robinson, R.L. Jr. 1994. Predicting Gas Adsorption using Two-Dimensional Equations of State., *Ind. Eng. Chem. Res.* 33.5: 1280-1289.

Zuber, M.D., Williamson, J.R., Hill, D.G., Sawyer, W.K. and Frantz, J.H. 2002. A Comprehensive Reservoir Evaluation of a Shale Reservoir - The New Albany Shale.SPE Paper 164509 presented at the *SPE Annual Technical Conference and Exhibition.* San Antonio, Texas. USA. September 29-October 2.

3-Legs Resources. 2011. An Introduction to Shale Gas.*Course Hero Online Classes*.

APPENDICES

APPENDIX A

Derivation of Gas Material Balance Equation (MBE) for Non-Fractured Gas Reservoirs (Schilthuis, 1936)

The general (or traditional) gas material balance equation (MBE) (Schilthuis, 1936) is stated as:

$$G \cdot \left(B_g - B_{g_i}\right) + \Delta V_m + \Delta V_{mw} + W_e = G_p B_g + W_p B_w \qquad \text{(A.1)}$$

where $G \cdot \left(B_g - B_{g_i}\right)$ is gas expansion, G is free gas initially in place i.e. original gas initially in place OGIP, B_{g_i} is gas formation volume factor (rcf/scf) evaluated at initial pressure P_i i.e. before expansion, B_g is gas formation volume factor (rcf/scf) evaluated at pressure P i.e. after expansion, ΔV_m is pore compaction, ΔV_{mw} is matrix water expansion, W_e is water influx, G_p is cumulative gas production (scf), W_p is cumulative water produced (stb) and B_w is water formation volume factor.

It should be noted that pore compressibility is:

$$C_p = \frac{1}{V_p} \cdot \frac{\Delta V_m}{\Delta P} \qquad \text{(A.2)}$$

Andmatrix water compressibility is:

$$C_w = \frac{1}{V_w} \cdot \frac{\Delta V_{mw}}{\Delta P} \qquad \text{(A.3)}$$

where V_p, V_w and ΔP are pore volume, matrix water volume and pressure depletion respectively.

Hence,

$$G \cdot \left(B_g - B_{g_i}\right) + C_p V_p \Delta P + C_w V_w \Delta P + W_e = G_p B_g + W_p B_w \qquad \text{(A.4)}$$

The free gas initially in place $G$is expressed as:

$$G = \frac{V_p(1-S_w)}{B_{g_i}} \quad \text{(A.5)}$$

i.e.

$$V_p = \frac{G \cdot B_{g_i}}{(1-S_w)} \quad \text{(A.6)}$$

where S_w is matrix water saturation.

Matrix water volume is expressed as:

$$V_w = V_p \cdot S_w \quad \text{(A.7)}$$

$$V_w = \frac{G \cdot B_{g_i} S_w}{(1-S_w)} \quad \text{(A.8)}$$

Hence,

$$G \cdot \left(B_g - B_{g_i}\right) + G \cdot \left(\frac{C_p \cdot B_{g_i}}{(1-S_w)} + \frac{C_w \cdot B_{g_i} S_w}{(1-S_w)}\right) \Delta P + W_e = G_p B_g + W_p B_w \quad \text{(A.9)}$$

$$G \cdot \left(B_g - B_{g_i}\right) + \frac{G \cdot B_{g_i}}{(1-S_w)} \cdot \left(C_p + C_w S_w\right) \Delta P + W_e = G_p B_g + W_p B_w \quad \text{(A.10)}$$

Assuming a volumetric gas reservoir (i.e. where there is no water influx or water production), $W_e = W_p = 0$. Then,

$$G \cdot \left(B_g - B_{g_i}\right) + \frac{G \cdot B_{g_i}}{(1-S_w)} \cdot \left(C_p + C_w S_w\right) \Delta P = G_p B_g \quad \text{(A.11)}$$

Also, assuming an insignificant rock compaction effect, $\Delta V_m = \Delta V_{mw} = 0$, then,

$$G \cdot \left(B_g - B_{g_i}\right) = G_p B_g \quad \text{(A.12)}$$

Dividing **Equation A.12** through by $G \cdot B_g$ yields:

$$\frac{G_p}{G} = 1 - \frac{B_{g_i}}{B_g} \quad \text{(A.13)}$$

but

$$\frac{B_{g_i}}{B_g} = \frac{Z_i}{P_i} \frac{P}{Z} \quad \text{(A.14)}$$

thus

$$\frac{G_p}{G} = 1 - \frac{{}^{P}/_{Z}}{{}^{P_i}/_{Z_i}} \qquad \text{(A.15)}$$

where Z_i and Z are the respective Z-factors at initial pressure P_i and pressure P in a single-porosity (or non-fractured) reservoir.

$${}^{P}/_{Z} = {}^{P_i}/_{Z_i}\left(1 - \frac{G_p}{G}\right) \qquad \text{(A.16)}$$

The straight line plot of ${}^{P}/_{Z}$ versus cumulative production G_p is used in estimating the free gas initially in place G i.e. original gas initially in place OGIP.

APPENDIX B

Derivation of Langmuir Adsorption Isotherm

As stated earlier, Langmuir isotherm describes a progressively increasing surface adsorption as a function of pressure up until the entire surface area is covered with a single layer of molecules and no further adsorption can occur. The physical depiction of adsorption in Langmuir isotherm is shown in **Figure C.1**.

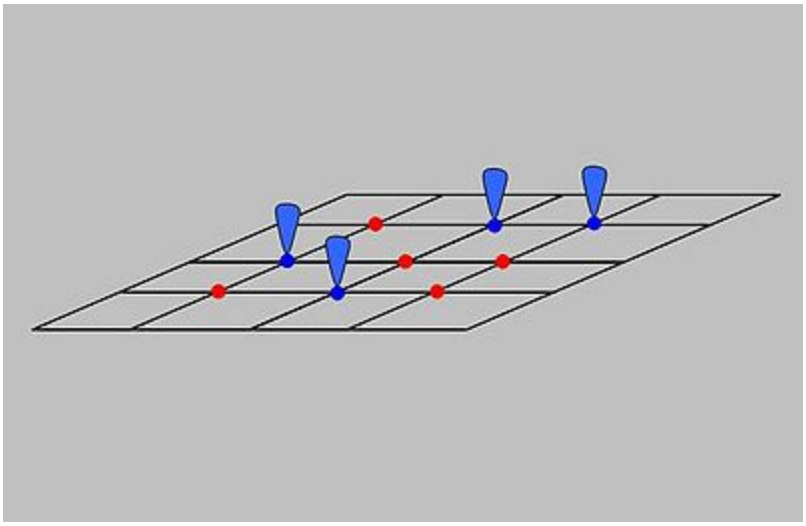

Figure B.1: Physical depiction of adsorption in Langmuir isotherm. (Langmuir, 1916). Here, the occupied surface sites are denoted as blue clips while vacant surface sites are denoted as red spots on the surface

B.1 Assumptions

The basic assumptions made here are similar to those of Langmuir isotherm. The model assumes an ideal surface where:

1. Solid surface is composed of localised adsorption sites, and each site can only hold one adsorbate molecule
2. Adsorption sites are energetically equivalent i.e. the surface is homogeneous and all sites are identical
3. Saturation coverage is attained when all sites are completely occupied
4. There are no adsorbate-adsorbate interactions between neighbouring adsorption sites
5. Adsorption of molecules is of monolayer type

6. Adsorption is reversible i.e. desorption occurs during pressure depletion, and
7. Adsorption coverage is independent of the enthalpy of adsorption

B.2 Isotherm Derivation

Considering fluid phase F, vacant surface sites$[S]$, and occupied surface sites $[F_{ads}]$ (number/area); the rates of adsorption and desorption of fluid molecules are R_{ads} and R_{des} respectively.

Rate of adsorption is proportional to the partial pressure P_f of the fluid over the surface and the concentration of vacant sites $[S]$ (number/area):

$$R_{ads} = K_{ads} \cdot P_f \cdot [S] \quad \text{(B.1)}$$

where K_{ads} is adsorption rate coefficient.

Rate of desorption is proportional to the concentration of sites filled with fluid molecules $[F_{ads}]$ (number/area):

$$R_{des} = K_{des} \cdot [F_{ads}] \quad \text{(B.2)}$$

where$K_{des}$is desorption rate coefficient

If adsorption coverage is assumed to be independent of the enthalpy of adsorption, then the dynamic equilibrium parameter K_{eq}^{f}has a constant value and it is referred to as Langmuir dynamic equilibrium constant.

At dynamic equilibrium, rate of adsorption equals rate of desorption. Hence,

$$K_{eq}^{f} = \frac{K_{ads}}{K_{des}} = \frac{[F_{ads}]}{P_f \cdot [S]} \quad \text{(B.3)}$$

Concentration of all sites$[S_T]$is the sum of the concentrations of vacant and occupied sites (number/area):

$$[S_T] = [S] + [F_{ads}] \quad \text{(B.4)}$$

With reference to (B.3),

$$[S_T] = \frac{[F_{ads}]}{K_{eq}^{f} \cdot P_f} + [F_{ads}] \tag{B.5}$$

$$[S_T] = [F_{ads}] \left\{ \frac{1 + K_{eq}^{f} \cdot P_f}{K_{eq}^{f} \cdot P_f} \right\} \tag{B.6}$$

The fraction of the surface sites occupied by fluid $[F]$ is defined as:

$$\theta = \frac{[F_{ads}]}{[S_T]} \tag{B.7}$$

Hence,

$$\theta = \frac{[F_{ads}]}{[S_T]} = \frac{K_{eq}^{f} \cdot P_f}{1 + K_{eq}^{f} \cdot P_f} \tag{B.8}$$

Expressing the partial pressureP_f as P, the occupied surface site $[F_{ads}]$ as the volume of fluid adsorbed V_{ads}, the concentration of all sites$[S_T]$ as the Langmuir volume V_L, (the maximum fluid adsorbable), and the Langmuir dynamic equilibrium constant K_{eq}^{f} as b; the fractional loading of the surface sites is then expressed as:

$$\theta = \frac{V_{ads}}{V_L} = \frac{bP}{1 + bP} \tag{B.9}$$

$$V_{ads} = V_L \cdot \frac{bP}{1 + bP} \tag{B.10}$$

Equation (B.10) is the Langmuir adsorption isotherm where b is the Langmuir dynamic equilibrium constant determined as $\frac{1}{P_L}$andP_L is the Langmuir pressure(the pressure at a volume $\frac{V_L}{2}$). Therefore, Langmuir isotherm could be expressed as:

$$V_{ads} = V_L \cdot \frac{P}{P + P_L} \tag{B.11}$$

APPENDIX C

Derivation of Pressure P_β and Adsorbed Volume V_β at Inflexion Pointβ where$\Delta\left(\frac{V}{V_{max}}\right) = \Delta\left(\frac{P}{P_s}\right)$ on the Developed Isotherm

With reference to **Equation 3.16**,

$$\frac{dP_a}{dP} = \frac{d}{dP}\left\{(P_s - P)\left(\frac{P}{P_s}\right)^n\right\} \tag{C.1}$$

$$\frac{dP_a}{dP} = \frac{d}{dP}\left\{\left(\frac{P_s}{{P_s}^n}\right)P^n - \left(\frac{1}{{P_s}^n}\right)P^{n+1}\right\} \tag{C.2}$$

$$\frac{dP_a}{dP} = n\left(\frac{P_s}{{P_s}^n}\right)P^{n-1} - (n+1)\left(\frac{1}{{P_s}^n}\right)P^n \tag{C.3}$$

However, $\frac{dP_a}{dP} = 0$ at inflexion point β where$\Delta\left(\frac{V}{V_{max}}\right) = \Delta\left(\frac{P}{P_s}\right)$ on the developed isotherm. Hence, at pressure P_β,

$$n\left(\frac{{P_\beta}^n}{{P_s}^n}\right)\left(\frac{P_s}{P_\beta}\right) = (n+1)\left(\frac{{P_\beta}^n}{{P_s}^n}\right) \tag{C.4}$$

$$n\left(\frac{P_s}{P_\beta}\right) = (n+1) \tag{C.5}$$

$$P_\beta = \left(\frac{n}{n+1}\right)P_s \tag{C.6}$$

and

$$V_\beta = V_{max}\left\{\frac{P_\beta}{P_s} + \left(1 - \frac{P_\beta}{P_s}\right)\left(\frac{P_\beta}{P_s}\right)^n\right\} \tag{C.7}$$

APPENDIX D

MAPPLE Program Code for Evaluating Z-Factor at Different Pressure Levels using the Dranchuk and Abou-Kassem (1975) Correlation

MAPPLE PROGRAM CODE

```
>rho[r]:=0.27*P[pr]/(z*T[pr]):
>C[1](T[pr]):=(((A[1])+((A[2])/(T[pr]))+((A[3])/(T[pr])^3))+((A[4])/(T[pr])^4))+((A[5])/(T[pr])^5):
>C[2](T[pr]):=A[6]+(A[7]/T[pr])+((A[8]/(T[pr])^2)):
>C[3](T[pr]):=A[9]*(((A[7]/T[pr])+((A[8])/(T[pr])^2))):
>C[4[i]](rho,T[pr]):=1+(A[11]*(rho[r])^2):
>C[4[ii]](rho,T[pr]):=((rho[r])^2/(T[pr])^3):
>C[4[iii]](rho,T[pr]):=exp(-(A[11]*(rho[r])^2)):
>C[4](rho,T[pr]):=A[10]*(C[4[i]](rho,T[pr]))*(C[4[ii]](rho,T[pr]))*(C[4[iii]](rho,T[pr])):
>Z:=1+(C[1](T[pr])*rho[r])+(C[2](T[pr])*(rho[r])^2),(C[3](T[pr])*(rho[r])^5)+(C[4](rho,T[pr])):
>F(z[i]):=z-Z:
>F(z[ii]):=eval(eval(eval(eval(eval(eval(eval(eval(eval(eval(eval(F(z[i]),A[1]=0.3265),A[2]=-1.0700),A[3]=-0.5339),A[4]=0.01569),A[5]=-0.05165),A[6]=0.5475),A[7]=0.7361),A[8]=0.1844),A[9]=0.1056),A[10]=0.6134),A[11]=0.7210),T[pr]=2.0322):
>F(z):=eval(F(z[ii]),P[pr]=12.8762):
>fsolve(F(z)):
>Z[i]:=F(z):
>Q[i]:=diff(Z[i],z):
>H[i]:=eval(Z[i],z=1.127965508):
>K[i]:=eval(Q[i],z=1.127965508):
>Z[i+1]:=1-(H[i]/K[i]);
>Error[i]:=Z[i+1]-1.127965508
```